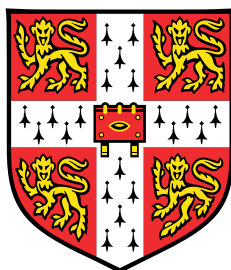


An Experimental and Theoretical Investigation into Mg-ion Battery Electrodes using Nuclear Magnetic Resonance Spectroscopy



Jeongjae Lee

Supervisor: Professor Clare Grey

Advisor: Dr Siân Dutton

Department of Chemistry
University of Cambridge

This dissertation is submitted for the degree of
Doctor of Philosophy

Trinity College

May 2019

To my loving parents and my grandparents, who always supported me in doing science

Declaration

This dissertation is the result of my own work and includes nothing which is the outcome of work done in collaboration except as declared in the Acknowledgement and specified in the text.

It is not substantially the same as any that I have submitted, or, is being concurrently submitted for a degree or diploma or other qualification at the University of Cambridge or any other University or similar institution except as declared in the Acknowledgement and specified in the text. I further state that no substantial part of my dissertation has already been submitted, or, is being concurrently submitted for any such degree, diploma or other qualification at the University of Cambridge or any other University or similar institution except as declared in the Acknowledgement and specified in the text.

This dissertation contains fewer than 65,000 words including appendices, bibliography, footnotes, tables and equations and has fewer than 150 figures.

Jeongjae Lee
May 2019

Acknowledgements

No thesis (good or bad) is made alone, and luckily I have had the chance to work with one of the most brilliant minds in this field:

Firstly, I would like to thank my supervisor, Professor Clare Grey, for all her help in guiding me through the work presented in this thesis. This thesis would not have existed without her insights and support, both scientific and non-scientific. In the darkest hours of the night where things seemed hopeless, the help from Clare led me out into the bright sun and kept me running; and I cannot thank her enough for being my supervisor despite the frequent deviation from my path.

A significant portion of this thesis is on the synthesis and magnetism of inorganic compounds. On this ground, the help of my advisor, Dr Siân Dutton, was indispensable. From advices in synthesis techniques to discussion on exotic magnetism, her comments and insights made this thesis sitting at the crossroads between physics and chemistry.

Different people guided me with different parts of this thesis. I would like to thank Dr Ieuan Seymour for his guidance in introducing me to many fields of computational chemistry, including (but not limited to!) *ab initio* calculations and transition state searching. Dr Bartomeu Monserrat performed and analysed some of the electronic structures in Chapter 5 and I am grateful to him for all his help and advice. I would also like to thank Dr Zigeng Liu, who has guided me in my attempts in performing electrochemistry and also did most of the NMR work which formed the basis of Chapter 5. Professor Andrew Pell, who is one of the most brilliant NMR spectroscopists I have met (with a sense of British humour!), gave the insight and helped me setting up many advanced NMR experiments performed in this study. I would like to thank all four for their kindness in helping me learn and perform.

The members of various Grey Group teams also need to be properly acknowledged: Evan Keyzer, Hugh Glass, Josh Lewis, Sunita Dey (Team Mg)—despite me working on a completely different project from them using NMR, their comments and ideas have much helped in shaping of this thesis.

Insights (and the caffeination) from weekly coffee meetings in Team Theory was helpful in many computational work performed: I would like to thank Derek Middlemiss, David

Halat, Roberta Pigliapochi, Erlendur Jónsson, Céline Merlet, John Kattirtzi, and Matthew Cliffe for all their discussions over a cup of coffee every Friday afternoon.

Many of my Korean friends in and out of the Grey lab have been a big emotional aid to my 9-year life in Cambridge: Gunwoo Kim, Yumi Kim, Yuji Kim, Donghwi Ko, Mia Kim, Seung-woo Kim, Sanggil Han, Minkoo Ahn. Some as co-workers and others as good friends, I have had the honour to receive their contributions to both scientific and non-scientific parts of my life.

Special thanks must be given to Paromita Mukherjee and Michael Hope for proofreading and providing helpful comments on the chapters, as well as training me on the SQUID (Paromita) and providing a sample of VO₂ (Michael).

Finally, I would like to thank all Grey group members. I really enjoyed working in the Grey Group for the past five years with all the amazing science and occasional cheese.

The computational work carried out in this thesis was performed on three different clusters: the group cluster Odyssey, Scientific Data & Computing Center at Brookhaven National Laboratory, and ARCHER, the UK national supercomputing cluster. I am grateful to all the admins in their efforts in managing the cluster.

Abstract

This thesis presents a combined experimental and theoretical approach on studying Mg-ion battery electrode materials, where Nuclear Magnetic Resonance (NMR) spectroscopy plays a central role in identifying the local structure and dynamics of the magnesium ions. Density Functional Theory (DFT) techniques are used extensively to (i) calculate and rationalise the observed NMR shifts, (ii) provide insights into the dynamics involved in such electrode materials, and (iii) guide the synthesis of candidate electrode materials.

This work begins by a systematic study of ^{25}Mg solid-state NMR in paramagnetic oxides, where the presence of transition metals makes them suitable for applications in high-voltage cathode materials. DFT methods for predicting and rationalising the paramagnetic NMR shifts are developed, with experimental verifications on synthesised samples. Feasibility of using advanced NMR pulse sequences such as Rotor-Assisted Population Transfer and Magic Angle Turning is demonstrated on such systems to afford enhanced resolution and sensitivity.

This approach of combined NMR and DFT techniques is then applied to two of magnesium vanadates for high-voltage cathode applications. In particular, DFT-based thermodynamic energies are used to rationally design the synthetic steps leading to the said vanadate materials, followed by DFT prediction of the migration barriers. The prepared material was subject to experimental characterisation using NMR and diffraction techniques, with an initial cycling data in an electrochemical cell.

In the final part, a combined experimental and ab initio investigation on Mg_3Bi_2 , a promising Mg-ion battery anode material, is presented. Previous reports on variable-temperature ^{25}Mg NMR spectroscopy is validated by DFT calculations on the migration barrier and defect energetics. Mechanistic insights on the migration mechanism are presented using the hybrid eigenvector-following transition state searching method, where the relativistic effects of heavy bismuth is shown to influence the migration barrier. We show that the defect formation energy of a Mg vacancy is critical in the apparent Mg diffusion barrier, which is heavily influenced by sample preparation conditions.

List of Publications

Chapter 3 contains materials from the publication:

Lee, J.; Seymour, I. D.; Pell, A. J.; Dutton, S. E. and Grey, C. P. A systematic study of ^{25}Mg NMR in paramagnetic transition metal oxides: applications to Mg-ion battery materials. *Phys. Chem. Chem. Phys.* **2017**, 19, 613–625.

Chapter 5 contains materials from the publication:

Lee, J.; Monserrat, B.; Seymour, I. D.; Liu, Z.; Dutton, S. E. and Grey, C. P. An *ab initio* investigation on investigation on the electronic structure, defect energetics, and magnesium kinetics in Mg_3Bi_2 . *J. Mater. Chem. A* **2018**, 6, 16983–16991.

Liu, Z.; **Lee, J.**; Xiang, G. Glass, H. F. J.; Keyzer, E. N.; Dutton, S. E. and Grey, C. P. Insights into the electrochemical performances of Bi anodes for Mg ion batteries using ^{25}Mg NMR spectroscopy. *Chem. Commun.* **2017**, 4, 743–746.

Other publications not included in this thesis:

Keyzer, E. N.; **Lee, J.**; Liu, Z.; Bond, A. D.; Wright, D. S.; and Grey, C. P. A general synthetic methodology to access magnesium aluminate electrolyte systems for Mg batteries. *J. Mater. Chem. A* **2019**, 7, 2677-2685.

Li, Q.; Liu, Z.; Zheng, F.; Liu, R.; **Lee, J.**; Xu, G.-L.; Zhong, G.; Hou, X.; Fu, R.; Chen, Z.; Amine, K.; Mi, J.; Wu, S.; Grey, C. P. and Yang, Y. Identifying the Structural Evolution of the Sodium Ion Battery $\text{Na}_2\text{FePO}_4\text{F}$ Cathode. *Angew. Chem. Int. Ed.* **2018**, 57, 11918–11923.

Cliffe, M. J.; **Lee, J.**; Paddison, J. A. M.; Schott, S.; Mukherjee, P.; Gaultois, M. W.; Manuel, P. Siringhaus, H.; Dutton, S. E. and Grey, C. P. Low-dimensional quantum magnetism in $\text{Cu}(\text{NCS})_2$: A molecular framework material. *Phys. Rev. B* **2018**, 97, 144421.

Pecher, O.; Halat, D. M.; **Lee, J.**; Liu, Z.; Griffith, K. J.; Braun, M. and Grey, C. P. Enhanced efficiency of solid-state NMR investigations of energy materials using an external automatic tuning/matching (eATM) robot. *J. Magn. Reson.* **2017**, 275, 127–136.

Table of contents

List of figures	xvii
List of tables	xxv
1 Introduction	1
1.1 Introduction to Mg-ion Batteries	1
1.1.1 The Working Principles of Rechargeable Batteries	1
1.1.2 Motivation for Secondary Mg-ion Batteries	3
1.1.3 Challenges of Developing MIB Systems	4
1.2 ²⁵ Mg NMR Spectroscopy Applied to MIBs	5
1.2.1 Motivation and Challenges for Using ²⁵ Mg NMR for Studying MIBs	5
1.2.2 Previous Reports on ²⁵ Mg NMR Spectroscopy for MIB Materials .	6
1.3 Investigated Oxide Structures	9
1.3.1 Mg ₆ MnO ₈	10
1.3.2 Spinel Structures	11
1.4 Outlook and Structure of This Thesis	17
2 Background Theory	19
2.1 Density Functional Theory	19
2.1.1 The Hartree-Fock Approximation	19
2.1.2 The Hohenberg-Kohn-Sham Approach	21
2.1.3 The Hubbard- <i>U</i> Method	22
2.1.4 Hybrid Functionals	24
2.1.5 Basis Sets in DFT Calculations	25
2.1.6 Solid-state DFT	26
2.2 Relativistic Quantum Chemistry: a Brief Introduction	26
2.2.1 Relativity and the Dirac Equation	26

2.2.2	Relativistic Corrections: the Mass-velocity and Darwin Terms . . .	27
2.2.3	Relativistic Corrections at the Core and Valence: Spin-orbit Coupling	30
2.2.4	The Zeroth-Order Regular Approximation	30
2.2.5	Handling of Relativistic Corrections: VASP <i>versus</i> CASTEP	31
2.3	Transition State Searching: The HEF Method	32
2.3.1	Transition States: Definition and the Motivation for Searching Them	32
2.3.2	The Hybrid Eigenvector-following Method	33
2.4	Nuclear Magnetic Resonance	35
2.4.1	Physical Basis of NMR Interactions	35
2.4.2	Solid-state NMR and Magic Angle Spinning	42
2.4.3	Pulse Sequences	45
2.5	Magnetism and the Paramagnetic NMR Shifts	50
2.5.1	The Basics of Electron Magnetism	50
2.5.2	Magnetic Measurements with a SQUID Magnetometer	51
2.5.3	Electron-Nucleus Interactions in Paramagnetic Systems	52
2.5.4	<i>Ab initio</i> Calculation of the Magnetic Coupling Parameter J	55
2.5.5	<i>Ab initio</i> Calculation of Paramagnetic NMR Parameters from the Curie-Weiss Law	56
2.6	Carbothermal Reaction: Thermodynamics	57
2.6.1	Using Carbon as a Reducing Agent	57
2.6.2	<i>Ab initio</i> Computation of G for Solids	59
2.7	X-ray Diffraction Techniques	62
2.7.1	Powder Diffraction	62
2.7.2	Rietveld Refinement	62
3	A Systematic Study of ^{25}Mg NMR in Paramagnetic Transition Metal Oxides	63
3.1	Introduction	63
3.2	Experimental	64
3.2.1	Sample Preparation	64
3.2.2	Magnetic Measurements	64
3.2.3	^{25}Mg NMR	65
3.2.4	<i>Ab Initio</i> Calculations	65
3.3	Results and Discussion	69
3.3.1	Diffraction and Magnetic characterisation	69
3.3.2	^{25}Mg NMR	79

3.3.3	DFT Calculation of NMR and Magnetic Parameters	90
3.3.4	Shift Mechanism and the Fermi Contact Pathways	92
3.4	Conclusion and Outlook	96
4	Carbothermal Synthesis and Characterisation of MgV₂O₅, a Potential Mg-ion Battery Cathode Material	97
4.1	Introduction	97
4.2	Methods	98
4.2.1	Materials Synthesis	98
4.2.2	Magnetic Measurements	99
4.2.3	²⁵ Mg NMR Spectroscopy	99
4.2.4	Computational Methods	100
4.2.5	Electrochemical Testing	102
4.3	Results	102
4.3.1	Calculation of Mg-ion Migration Barrier	103
4.3.2	Rational Design of Synthetic Steps by DFT	109
4.3.3	Characterisation of MgV ₂ O ₅	115
4.3.4	Electrochemical Cycling of MgV ₂ O ₅	122
4.3.5	Computation of Magnetic and NMR Parameters	126
4.3.6	Characterisation of MgV ₂ O ₄ Prepared Through the CTR method . .	130
4.4	Discussion	137
4.4.1	Implications of the CTR Method for Other Oxides	137
4.4.2	Discussion on the Initial MgV ₂ O ₅ Electrochemistry	137
4.4.3	MgV ₂ O ₄ : Sample Dependence on the Preparation Method	139
4.5	Conclusion and Further Work	140
5	An Investigation on the Electronic Structure, Defect Energetics, and Magnesium Kinetics in Mg₃Bi₂	143
5.1	Introduction	143
5.2	Methodology	144
5.2.1	Computational Details	144
5.2.2	Calculation of NMR Parameters	145
5.2.3	Transition State Searching	146
5.3	Results and Discussion	147
5.3.1	Crystal Structure	147
5.3.2	Electronic Structure	148

5.3.3	Calculation of the ^{25}Mg NMR Shifts	151
5.3.4	Defect Energetics	154
5.3.5	Mg Migration Kinetics	156
5.4	Conclusion	161
6	Conclusion and Further Work	163
	References	167
	Appendix A Post ball-mill analysis of MgV_2O_5	179
A.1	SEM	179
A.2	XRD	181
	Appendix B EDX data of lithium counterelectrode from charged VO_2 cell	183

List of figures

1.1	A schematic illustration of a MIB system under work.	2
1.2	Structure of Mg_6MnO_8 , shown with oxygen polyhedra around the metal ions.	10
1.3	Compositional phase diagram (at 0 K) of the Mg–V–O system, calculated using the Materials Project.[65, 66]. PBE+U functional was used with $U = 3.25$ eV for V. Stable phases at 0 K are also labelled on the diagram. MgV_2O_5 exists at only 0.026 eV above the hull.	14
1.4	Structures of the α -, δ -, and metastable ε -polymorphs of MgV_2O_5 . Reproduced from Sai Gautam <i>et al.</i> [67]	16
2.1	Total energy as a function of electron count in the system. Black line gives the analytical DFT energy, red line gives the exact energy, and the blue line gives the parabolic energy difference given by the U -correction. Figure adopted from [81].	23
2.2	Schematic illustration of the HEF method for TS searching. Detailed explanations are presented in the main text. Saddle point figure was adopted from Wikipedia under a CC-BY 3.0 license.	34
2.3	Schematic illustration of the pulse-acquire experiment on a 2-level system. Both spin state and vector formalisms are shown.	36
2.4	Schematic energy levels (not drawn to scale) in the presence of quadrupolar coupling, illustrated for $\gamma < 0$ and $I = 5/2$ (the case for ^{25}Mg).	41
2.5	Schematic illustration of MAS experiments.	43
2.6	(a) Hahn-echo pulse sequence. (b) RAPT-echo pulse sequence. (c) QMAT pulse sequence.	49
2.7	Illustration of different spin density transfer mechanisms in TM – O – Li bonds, with 90° and 180° bond angles. Figure reproduced from Carlier <i>et al.</i> [144]	54

2.8	Illustration of calculating J by a broken symmetry supercell approach. In (a), the total energy equals $E_a = E_0 + 8J_1$. In (b), the total energy equals $E_b = E_0$. Subtracting the energies yields $J_1 = (E_a - E_b)/8$	55
2.9	Ellingham diagram, reproduced from the original construction by Ellingham.[145]	60
3.1	^{25}Mg bond pathway (P) contributions and TM–TM J couplings.	68
3.2	X-ray powder diffraction pattern and Rietveld refinement data for Mg_6MnO_8 . The positions of allowed reflections are indicated by the tick marks.	70
3.3	Inverse magnetic susceptibility per mol Mn, $1/\chi$, as a function of temperature for Mg_6MnO_8	71
3.4	X-ray powder diffraction pattern and Rietveld refinement data for MgCr_2O_4 . The positions of allowed reflections are indicated by the tick marks.	74
3.5	Inverse magnetic susceptibility per mol Cr, $1/\chi$, as a function of temperature for MgCr_2O_4	75
3.6	X-ray powder diffraction pattern for the SS- MgV_2O_4 . The positions of allowed reflections are indicated by the tick marks.	76
3.7	X-ray powder diffraction pattern for MgMn_2O_4 . Collected data (red), refined data (black), and differences (lower panel) are shown. The positions of allowed reflections are indicated by the tick marks. 7.9 wt % of Mg_6MnO_8 phase was detected.	78
3.8	Inverse magnetic susceptibility per mol Mn, $1/\chi$, as a function of temperature for MgMn_2O_4	79
3.9	(a) ^{25}Mg spin echo spectrum of Mg_6MnO_8 (14 kHz MAS, 81712 transients), with fitted central transition lineshape including contributions from both the paramagnetic shift anisotropy and the quadrupolar interaction (parameters are listed in Table 3.7). (b) Magic angle turning (MAT) spectrum of Mg_6MnO_8 (20 kHz MAS, 128 slices in the F1 dimension with 2.23 μs delay increment, 3072 transients acquired in each slice). RAPT pulses were applied before the MAT pulses to enhance the signal-to-noise ratio.	81

3.10	(a) ^{25}Mg spin echo signal intensities of Mg_6MnO_8 with increasing offset frequency of the saturating pulse trains in the RAPT experiment. (b) Enhancement of spin echo signal intensity using the RAPT pulse. Saturating pulses were applied at a modulation frequency of 270 kHz. Both experiments were performed at MAS spin rate of 14 kHz. 1024 transients were acquired in each spectrum.	82
3.11	^{25}Mg NMR spectra of Mg_6MnO_8 , recorded with the rotor-synchronised Hahn echo and Double Frequency Sweep (DFS) pulse sequences. Signal-to-noise enhancement of around 1.5 is observed for the isotropic shift. A 36 kHz-strength DFS sweep pulse starting from an offset of 1000 kHz and ending at 100 kHz was applied for 2040 μs . 51200 transients were acquired in each case with recycle delays of 0.01 s.	83
3.12	Simulated ^{25}Mg NMR spectra of Mg_6MnO_8 , with different Euler angles β between the anisotropic hyperfine tensor and the EFG tensor in the simulation.	84
3.13	^{25}Mg spin echo spectrum of MgCr_2O_4 at a MAS spin rate of 10 kHz. 20480 transients were acquired. The broad feature seen around 2700 ppm is due to probe background.	85
3.14	86
3.15	^{25}Mg spin echo spectrum of SS- MgV_2O_4 (solid-state route) at MAS spin rate of 10 kHz. 505600 transients were acquired with recycle delays of 0.1 s.	86
3.16	^{25}Mg spin echo spectrum of MgMn_2O_4 at MAS spin rate of 14 kHz. Mg_6MnO_8 secondary phase signals are shown with asterisks (*). 3550928 transients were acquired. (a) Comparison between experimental and fitted spectrum. Fitted parameters are listed in Table 3.7. (b) Enhancement of spin echo signal intensity with RAPT pulse sequence. RAPT modulation pulses were applied at 240 kHz. 1024000 transients were acquired in each spectrum.	88
3.17	3-dimensional spin density maps. Yellow denotes positive spin; blue denotes negative spin. Bounding box refers to the unit cell and solid lines connecting atoms refer to the metal-oxygen bonds. Bond pathway contributions P to the spin density are shown in red.	95
4.1	Determination of rotationally invariant Hubbard U of V^{4+} in MgV_2O_5 by a linear response method by varying the site potential α . SC and non-SC refer to self-consistent and non-self-consistent calculations, respectively.	103

4.2	(a) Energy profiles of a single Mg vacancy hop between 6-fold coordinated (stable) and 5-fold coordinated (metastable) sites. For the HSE06 calculations, only a handful of points along the PBE+ <i>U</i> diffusion path was selected to calculate the single point energies. All energies are referenced to their lowest respective state. (b) Metastable 5-coordinated, (c) transition state, and (d) stable 6-coordinated Mg site along the diffusion pathway. Colour scheme: orange(Mg), red(V).	105
4.3	(a) Local geometry around the Mg in its transition state, fully magnesiated MgV ₂ O ₅ . (b) Local geometry around the Mg in its transition state, fully demagnesiated V ₂ O ₅ . All units are in Å. Mg–O bond distances closer than 3.2 Å are represented by a bond.	107
4.4	(a) Energy profiles of a single Mg hop between 6-fold coordinated (stable) and 5-fold coordinated (metastable) sites. For HSE06 calculations, only a handful of points along the PBE+ <i>U</i> diffusion path was selected to calculate the single point energies. All energies are referenced to their lowest respective state. (b) Metastable 5-coordinated, (c) transition state, and (d) stable 6-coordinated Mg site along the diffusion pathway. Colour scheme: orange(Mg), red(V).	108
4.5	Reaction scheme to synthesise MgV ₂ O ₅ and MgV ₂ O ₄ <i>via</i> the CTR approach.	110
4.6	Free energy ΔG vs. temperature <i>T</i> plot, or Ellingham diagram, of the various oxidation reactions involved in syntheses of MgV ₂ O ₅ and MgV ₂ O ₄ phases, calculated from DFT. All values are under standard 1 atm partial pressures. The two carbon lines cross at $T = 973$ K (700 °C). To allow a direct calculation of ΔG , the values are normalised with respect to 1 mol of O ₂ .	111
4.7	DFT-based free energy ΔG of the CTR reactions to produce MgV ₂ O ₅ and MgV ₂ O ₄ phases at 900 K as a function of CO ₂ partial pressure ρ_{CO_2} . The two lines cross at $\rho_{\text{CO}_2} = 10^{-2}$ atm. The values are normalised with respect to 1 mol of MgV ₂ O ₆	112
4.8	DFT-based free energy ΔG of the oxidation reactions involving MgV ₂ O ₅ and MgV ₂ O ₄ phases at 1200 K as a function of O ₂ partial pressure ρ_{O_2} . Equilibrium ρ_{O_2} of Cu oxidation is also shown as a dashed line at 10^{-8} atm. The values are normalised with respect to 1 mol of MgV ₂ O ₆	115
4.9	Refined powder X-ray diffraction data of MgV ₂ O ₅ as prepared by the CTR method. Refined parameters are shown in Table 4.1. Reflections for MgV ₂ O ₅ (50979) and VO ₂ (34033) are taken from the ICSD.	117

4.10	Thermogravimetric data of the magnesium acetate (nominally tetrahydrate) precursor used in the synthesis of MgV_2O_6	118
4.11	(a) ^{25}Mg spin echo spectrum of the as-synthesised MgV_2O_5 , measured under 20 kHz MAS and a 0.1 s recycle delay. Fitted parameters are shown in Table 4.3. (b) Structure of MgV_2O_5 , showing the 6-fold Mg coordination environment as polyhedra.	119
4.12	Enhancement profile of the integrated signal intensity in MgV_2O_5 using the RAPT pulse sequence, as a function of the Gaussian offset v_{off} . All samples were measured under 20 kHz MAS and a 0.1 s recycle delay.	120
4.13	^{25}Mg spectra of as-synthesised MgV_2O_5 , measured with a normal spin echo and a RAPT-spin echo pulse sequences. Both were measured under 20 kHz MAS and 0.1 s recycle delay.	120
4.14	^{25}Mg spectra of ball-milled MgV_2O_5 , measured under normal spin echo and RAPT-spin echo. Both were measured under 20 kHz MAS and a 0.1 s recycle delay.	122
4.15	(a) Electrochemical cycling data of ball-milled MgV_2O_5 , charged vs Li. (b) Glass fibre separator and lithium disc after disassembly of the coin cell shown in (a). (c) Powder X-ray diffraction data of charged cathode. Broad background at 20° is due to Kapton sample holder.	124
4.16	(a) Electrochemical cycling data of VO_2 , charged vs Li. (b) Lithium disc after disassembly of the coin cell. (c) Powder X-ray diffraction data and Le Bail fit of charged VO_2 . Broad background at 20° is due to Kapton sample holder. Self-standing films were provided by Michael Hope.	125
4.17	(a) Zero field cooled molar susceptibility χ and (b) Zero field cooled inverse molar susceptibility $1/\chi$ of MgV_2O_5 as measured by SQUID magnetometry. Linear fitting was performed from 200 K to 300 K.	127
4.18	(a) Illustration of the V–V exchange interactions J_n up to the fourth nearest neighbour in MgV_2O_5 . Dark blue colour refers to vanadium. (b) Dominant exchange mechanisms for the J_1 (left) and $J_{2,3}$ (right).	129
4.19	X-ray powder diffraction pattern for CTR- MgV_2O_4 (carbothermal route). The positions of allowed reflections are indicated by the tick marks.	132
4.20	Inverse magnetic susceptibility per mol V, $1/\chi$, as a function of temperature for the CTR- MgV_2O_4 sample prepared <i>via</i> a carbothermal route.	133

4.21	^{25}Mg spin echo spectrum of CTR- MgV_2O_4 (carbothermal route) at MAS spin rate of 10 kHz. Positions of the isotropic resonances are indicated. 628400 transients were acquired with recycle delays of 0.1 s.	135
5.1	(a) Crystal structure of Mg_3Bi_2 . Positions of tetrahedrally coordinated Mg (orange sphere, Tet) and octahedrally coordinated Mg (green sphere, Oct) are shown. Bismuth atoms sit on the line vertices (not shown for clarity). (b) Schematic illustration of the Mg_3Bi_2 structure (on the left) showing the possible diffusion pathways involving the tetrahedral and the octahedral interstitial sites ('Tet Int' and 'Oct Int').	147
5.2	Density of states plot of Mg_3Bi_2 using the PBE and HSE06 exchange-correlation functionals. Local atomic DOS projections inside the sphere defined by the Wigner-Seitz radii (1.63 and 1.52 Å for Bi and Mg, respectively) are also shown. All energies were referenced to the highest occupied state.	150
5.3	Band structure plots of Mg_3Bi_2 using the PBE (left) and HSE06 (right) exchange-correlation functionals without (grey) and with (red) spin-orbit coupling (SOC). The Fermi level is located at the zero of energy.	150
5.4	Density-of-states (DOS) plot for Mg_3Bi_2 , generated using CASTEP. Three cases are considered: nonrelativistic (NR), scalar relativistic (SR) using the ZORA method, and full relativistic (FR) including the SOC. All energies were referenced to the highest occupied state. Site- and orbital-decomposed DOS under SOC is not supported in the version of CASTEP used.	152
5.5	Relaxed cell structures using the (a) scalar relativistic ZORA approximation, and (b) nonrelativistic Schrödinger equation, projected along the a -direction. Here, Mg(oct) sits on layer A and Mg(tet) sits on layer B.	153
5.6	Diffusion profile of Mg ion for selected pathways as illustrated in Figure 5.1b. (a) Scalar relativistic, (b) full relativistic, with SOC included. Energies are referenced to the bulk energy of each 120-atom supercell with one V_{oct} defect.	158
A.1	(a) SEM image of pristine MgV_2O_5 before ball-milling. (b) SEM image of MgV_2O_5 after ball-milling.	180
A.2	(a) XRD pattern of pristine MgV_2O_5 before ball-milling. (b) XRD pattern of MgV_2O_5 after ball-milling.	181

B.1	EDX data of the lithium disc from the coin cell after charging of VO ₂	183
-----	---	-----

List of tables

3.1	Synthesis conditions of samples.	64
3.2	Rietveld refined parameters from the PXRD data of Mg_6MnO_8	70
3.3	Magnetic characterisation data of compounds studied. μ_{eff} refers to the effective magnetic moment in Bohr magneton (μ_B) per TM ion, Θ refers to the Weiss temperature, J_1 refers to the nearest neighbour exchange coupling constant extracted with Equation 2.73, and T_N refers to the Néel temperature. Theoretical spin-only values for the MgMn_2O_4 compositions determined by phase fractions and occupancy refinements are also shown.	72
3.4	Rietveld refined parameters from the PXRD data of MgCr_2O_4	74
3.5	Rietveld refined parameters from the PXRD data of MgV_2O_4 prepared <i>via</i> a solid-state method (SS- MgV_2O_4).	76
3.6	Rietveld refined parameters from the PXRD data of MgMn_2O_4	78
3.7	<i>Ab-initio</i> calculated and experimentally fitted paramagnetic NMR parameters of Mg_6MnO_8 , MgCr_2O_4 , MgV_2O_4 , and MgMn_2O_4 . Hyb20 and Hyb35 refer to the degree of Hartree-Fock exchange energy (see methods). Values marked with asterisks (*) were fixed in the fitting. For MgV_2O_4 , the experimental Weiss constant was obtained from literature.[164] EFG tensor eigenvalues and anisotropic hyperfine tensor components are near zero for MgV_2O_4 and MgCr_2O_4 and Euler angles are not reported for these systems. Detailed magnetic characterisation data are reported in Table 3.3.	89
3.8	Mulliken spin population analysis of transition metal <i>d</i> orbitals in selected spinel compounds.	93
4.1	Rietveld refined parameters from the PXRD data of MgV_2O_5 as prepared by the CTR method.	117

4.2	Magnetic parameters of MgV_2O_5 determined by experiment and DFT calculations. Experimental parameters were determined by SQUID magnetometer (Figure 4.17); J-couplings are as denoted on Figure 4.18a.	126
4.3	NMR parameters of MgV_2O_5 determined by experiment and DFT calculations. Experimental parameters are fitted from the spectrum in Figure 4.11a (anisotropies could not be determined from the spectrum). Herzfeld-Berger convention is used for the shift anisotropy.	130
4.4	Rietveld refined parameters from the PXRD data of MgV_2O_4 prepared <i>via</i> a carbothermal method (CTR- MgV_2O_4).	132
4.5	Estimated hyperfine shifts and the intensity ratio for the Mg ions in the MgV_2O_4 spinel structure neighbouring V^{3+} and V^{4+} ions. The shifts ‘referenced’ from the 1845 ppm (SS- MgV_2O_4) or 1861 ppm (CTR- MgV_2O_4) are shown. Integrated relative intensities are shown for the experimental spectrum and also calculated assuming a random distribution of the V^{4+} ions.	135
5.1	DFT-predicted cell parameters of Mg_3Bi_2 using the PBE and HSE06 exchange-correlation functionals using CASTEP and VASP. NR, SR and FR refer to nonrelativistic, scalar relativistic, and full relativistic (i.e. explicit spin-orbit coupling) calculations, respectively. ZORA method was used for SR calculation on CASTEP. Experimental lattice constants are from Lazarev <i>et al.</i> [224]	148
5.2	Scalar relativistic (SR) and full relativistic (FR) Bader charge analysis of Mg_3Bi_2 using the Perdew-Burke-Ernzerhof (PBE) and Heyd-Scuseria-Ernzerhof (HSE06) exchange-correlation functionals. Only the valence charge is calculated.	149
5.3	Calculated NMR parameters of the two Mg sites (octahedral and tetrahedral) in Mg_3Bi_2 using the GIPAW method. Core electrons are treated with two levels of theory: scalar relativistic (SR) ZORA and nonrelativistic (NR) Schrödinger. δ_{iso} , Ω , and η refer to the chemical shift tensor expressed in the Herzfeld-Berger convention. C_Q and η refer to the quadrupolar coupling parameter and asymmetry, respectively.	153

5.4	Scalar relativistic (SR) and full relativistic (FR) <i>ab initio</i> formation energies ΔE_f of various stoichiometric and non-stoichiometric defects in Mg_3Bi_2 using the PBE functional. Defect notations follow the convention of Kroger and Vink with neutral sign omitted for clarity.[218] All calculations assumed non-charged defects (see text) with cell dimensions fixed to simulate a dilute limit. Vacancy defect energies are referenced to the respective metals. For Frenkel defects, two scenarios where the Mg sits on a nearby (nn) or far interstitial sites were considered. Asterisks(*) indicate that the resulting structure was unstable and reverted back to the starting structure. All values are quoted in electron-volts. Only some of the calculations were performed under the 120-atom supercell condition after an initial screening with the 40-atom supercell.	157
5.5	Effective migration barriers E_a^{eff} estimated through DFT and VT NMR techniques. VT NMR data are taken from Liu <i>et al.</i> [40] For the NMR measurements, Mg_3Bi_2 prepared through electrochemical insertion and mechanical milling were considered. SR and FR refer to scalar relativistic and full relativistic calculations, as described in the text.	161

Chapter 1

Introduction

1.1 Introduction to Mg-ion Batteries

1.1.1 The Working Principles of Rechargeable Batteries

The rapid increase in global energy demand requires more renewable energy sources and subsequently novel energy storage solutions, both on a grid and a portable scale. Indeed, the rapid development of current portable electronics such as smartphones is heavily indebted to rechargeable Li-ion batteries (LIBs). The key to the commercial and technological success of LIBs lies in the light weight and high oxidation potential of lithium, which is ideal for portable devices where high energy density is the most important factor. However, the perennial demand for higher capacity and faster charging/discharging capability has driven the research in building ‘better batteries’.

To this end, understanding the working principles of a battery is essential. This is schematically illustrated in Figure 1.1. Most simply put, any battery is formed of an anode, a cathode, and an electrolyte. Energy stored on the electrodes in the form of free energy G could be released upon redox processes of the electrode materials, resulting in electric potentials \mathcal{E} according to Equation 1.1:

$$\Delta G = -nF\mathcal{E} \quad (1.1)$$

where n and F refer to the electron count and Faraday constant, respectively.

Here we discuss rechargeable batteries relying on an intercalation mechanism. Upon charging, the charge carrying ions move out of the cathode and migrate towards the anode, resulting in the net energy being stored in the system. The opposite happens in a discharge:

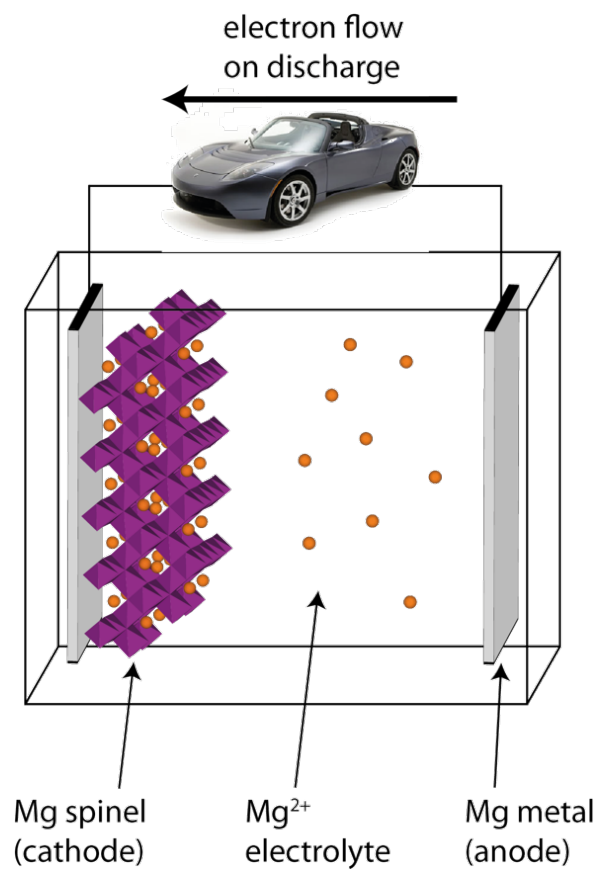


Fig. 1.1 A schematic illustration of a MIB system under work.

ions migrate from the anode towards the cathode, resulting in an energy release. Separation of the redox centres on the two electrodes by means of an ion-conducting but electrically insulating electrolyte ensures the generated electric energy could be passed through an external circuit to do useful work. This poses several requirements for the materials involved in the electrochemistry:[1]

- The intercalation must be reversible; *i.e.* the host structure must not be destroyed during the insertion/de-insertion of guest ions.
- As both charging/discharging processes involve the guest ions moving in a host structure, the diffusion must be rapid in order to extract currents at a useful rate. This is commonly called the cycling rate C, where 1 C denotes a current density to charge/discharge the cell in 1 hour.
- The difference in redox potentials between the anode and the cathode preferably should be large to allow the flow of current at higher potentials, resulting in larger energy densities.

Combination of a graphite anode with a LiCoO_2 cathode satisfies all three requirements; this is the concept of the famous ‘rocking-chair’ battery.

1.1.2 Motivation for Secondary Mg-ion Batteries

Despite the immediate success of LIBs in portable electronics and electric vehicles applications, currently several problems are faced in using lithium in a large-scale energy storage, or even in extending the electric vehicles applications:

- High cost of lithium. Li only takes up 0.002 % of the Earth’s crust by mass,[2] and is generally sourced from salt mines, or extracted from seawater.
- Geopolitical constraints. Li is mainly produced in certain parts of the world (Australia, China, and South America); the production is vulnerable to geopolitics which is also linked to the growing prices of lithium.[3]
- Dendrites and safety issues. Currently, Li metal (which gives the largest cell potential possible) cannot be used in LIBs due to problems with dendrite growths and eventual short-circuiting of the cell.[4, 5] This leads to safety concerns on thermal runaways ultimately leading to battery explosions.

- Low volumetric capacity. As lithium forms a monovalent cation, higher volumetric capacity could be attained by using a higher valent cation instead.

Despite the continuing political and technological efforts in solving these problems, batteries based on alternative chemistries other than Li have been investigated over the years. These include those using different alkali/alkaline-Earth metals (Na-ion, K-ion, Mg-ion, K-ion) or relying on a chemistry different to a simple intercalation mechanism (metal-sulphur, metal-air).[6, 7, 8, 9] Of these, Mg-ion batteries (MIBs) are particularly promising due to the following factors:

- Low cost due to the high natural abundance of Mg in the Earth's crust (2.8 %).[2]
- Distribution of Mg is less uneven, with many of the minerals contain Mg as a component. Also, Mg could be extracted from MgCl_2 (obtained from brines) by electrolysis.
- Mg metals are commonly known not to suffer from dendritic growth.[10] This is due to the self-diffusion of Mg atoms being faster than Li or Na on a surface[11], although under certain conditions dendrite growth could be possible (see [12, 13, 14] for reports)
- Mg forms a divalent cation, thus resulting in a significantly higher volumetric capacity compared to Li metals (3833 mAh/cm^{-3} for Mg *versus* 2046 mAh/cm^{-3} for Li).
- Unlike metal-air batteries, many technologies for LIBs can be extended to MIBs to aid faster commercialisation.[15]

1.1.3 Challenges of Developing MIB Systems

Hence, since the 1990s many attempts were made to develop a working MIB system.[10] The first system to show more than 2000 reversible charge-discharge cycles was reported in 2000 using $\text{Mg}_x\text{Mo}_6\text{S}_8$ Chevrel-type cathodes,[16] but their low redox potential (1.1 V *versus* Mg/Mg^{2+}) and low specific capacity (110 mAhg^{-1}) seriously limit the commercial applications to replace LIBs (3.6 V and 200 mAhg^{-1} using LiCoO_2 cathodes). Furthermore, nonaqueous magnesium electrochemistry is still relatively poorly understood and the development of reliable electrolytes with wide potential windows is still an active area of research.[17]

The challenge could be largely divided into two sub-problems: electrode and electrolyte.

Electrodes

Mg^{2+} has a similar size to Li^+ (0.72 versus 0.76 Å for 6-fold coordinated environments).[18] This means that the significant electrostatic interaction between the Mg^{2+} and O^{2-} ions in the structure hampers the mobility of Mg ions. This is clearly different from the Na case, where the same monovalent nature of Na^+ enables many of the LIB materials to be used without problems in diffusion. This means that the typical high-voltage transition metal (TM) oxides performs poorly in MIBs.

To circumvent this issue, many previous reports have tried using chalcogenides (sulphides or selenides) to reduce the charge density on the anionic sublattice and weaken the electrostatic interaction. However, this inevitably results in a lower redox potential of the cathodes compared to the oxides, as the strongly polarising oxygen ligand contributes to the redox reactions happening at higher potentials.

Electrolytes

Currently there is no reliable Mg electrolyte that can (i) electrochemically remove and deposit (*i.e.* strip and plate) Mg reversibly on metallic surfaces, (ii) stable at high potentials to allow use of high-voltage cathodes, and (iii) stable at high potentials (>4 V) against commonly used current collectors (stainless steel, copper, aluminium). This makes testing of the potential high-voltage cathodes problematic and often parasitic reactions are the dominant source of observed capacity. While significant advances have been made in this area of research for the past decades, the absence of a reliable electrolyte makes it difficult to test especially high-voltage cathode materials. To this end, initial charging (de-magnesiumation) is often tested in Li-ion half cells (against Li metal as the counterelectrode) to assess the charging capacity. For more accounts on electrolyte development the reader is referred to some recent reviews in this aspect;[17, 10, 19] also, works on *solid-state* Mg-ion electrolytes using sulphide spinels (thiospinels) have been recently reported.[20, 21]

1.2 ^{25}Mg NMR Spectroscopy Applied to MIBs

1.2.1 Motivation and Challenges for Using ^{25}Mg NMR for Studying MIBs

Nuclear Magnetic Resonance (NMR) is a valuable method to study battery materials as the characteristic NMR shift, quadrupolar coupling, lineshape, and relaxation behaviour can

give important information on the *local* structure and dynamics.[22, 23] This allows us to characterise the individual local environments in disordered systems, which are difficult to analyse with diffraction methods that probe long range order. In particular, solid-state magic-angle spinning (MAS) NMR is particularly useful as electrode materials can be studied.

NMR techniques have been successfully used in studying many battery systems including Li-ion, Na-ion, Li-air, and Li-S.[22] Applying the same experimental approach to MIBs, however, is challenging because of the low gyromagnetic ratio (approximately 1/20 of ^1H) and natural abundance (10 %) of ^{25}Mg , the only NMR active nucleus. In addition, significant quadrupolar interactions ($^{25}\text{Mg } I = 5/2$; quadrupole moment $Q = 0.2$ barns) can lead to a broadening of the signal and poor resolution.

Despite the prevalence of Mg in many important minerals and bioinorganic complexes, the challenging nature of ^{25}Mg has prevented serious solid-state NMR studies of such compounds for many years.[24] The first ^{25}Mg MAS spectrum was recorded in 1988.[25] Since then, the development of high-field magnets made the sufficient resolution possible by larger splitting of the Zeeman levels and by suppressing the quadrupolar effects relative to the Zeeman effects.[26] Also, developments of novel pulse sequences such as qCPMG[27] have allowed broad spectra to be recorded for local structure analysis of a number of different diamagnetic compounds.[28, 29]

These difficulties are made more problematic when studying cycled battery cathodes, since the samples are inherently diluted (mixing with conductive carbon, binders, *etc.*) and less crystalline (many electrode formulations use nanocrystalline materials for better cycling performances). Thus, only a few reports have been published which have used solid-state ^{25}Mg NMR in a context of MIBs. In the following sections, we briefly discuss the prior results and set where this thesis stands in terms of the literature.

1.2.2 Previous Reports on ^{25}Mg NMR Spectroscopy for MIB Materials

To date, there only exists a scarce (<20) literature on solid-state ^{25}Mg NMR spectroscopy applied to MIB materials. These can be broadly divided according to their compositions: oxides, other chalcogenides, and intermetallics.

Oxides

Perhaps the most obvious place to start, various Mg TM oxides have been investigated as potential cathode materials for MIBs. The first observation of reversible Mg intercalation into

such oxides was observed for MgMn_2O_4 , where a combined ^{25}Mg qCPMG NMR and X-ray spectroscopic approach was used to confirm the reversible Mg chemistry into this spinel type cathode.[30] However, the system was cycled in an aqueous electrolyte, which limits the application to low-voltage cells; absence of high-voltage electrolytes have not seen reports to cycle this material under nonaqueous conditions. This could also be related to water co-insertion aiding the Mg diffusion, as was shown for V_2O_5 xerogels and birnessite-type MnO_2 structures.[31, 32, 33, 34]

V_2O_5 -type cathode materials were also investigated using ^{25}Mg NMR spectroscopy, confirming the reversible insertion and elucidating the local structure of Mg ions upon intercalation. Sa *et al.* have reported the presence of two local environments with 24.7 and 1840 ppm shifts, the second of which was attributed to the MgV_2O_5 phase.[34] Absence of MgO in the pair distribution function analysis denoted the 24.7 ppm environment to be present inside the V_2O_5 xerogel host, which was identified as hydrated Mg ions octahedrally coordinated inside the V_2O_5 layers.

A study of ^{25}Mg NMR in chemically magnesiated oxide structures was performed by Wang *et al.*[35] It was shown that MgO is formed as a by-product in many chemically magnesiated oxides (resonance of 26 ppm), including Mg_xTiO_2 , $\alpha\text{-V}_2\text{O}_5$, and TiO_2 , questioning the previously observed ‘reversible’ electrochemistry in these materials. As expected, magnesiation of MnO_2 have resulted in resonances around 1800 ppm, which is characteristic of large hyperfine-type shifts typically observed in TM oxides. Thus, ^{25}Mg NMR spectroscopy could be used to observe the intercalation and identify any amorphous side products difficult to detect with diffraction techniques.

Finally, ^{25}Mg NMR was also used to study a molybdenum oxyfluoride cathode material $\text{Mg}_x\text{MoO}_{2.8}\text{F}_{0.2}$.[36] Broad resonances around -60 ppm was observed in this case, which was attributed to disordered Mg intercalation in these structures. No in-depth NMR characterisation was performed apart from observing the signal in this case.

Other Chalcogenides

As discussed above, using chalcogenides (S, Se) as the anion to facilitate diffusion is a commonly adopted strategy to devise novel electrode materials for MIBs. In the context of ^{25}Mg NMR, the fast dynamics afforded by such approach could be directly observed. A recent report have demonstrated that fast Mg motion is present in thiospinels MgX_2Z_4 ($\text{X}=(\text{In}, \text{Y}, \text{Sc})$ and $\text{Z}=(\text{S}, \text{Se})$) with a measured activation barrier of 320 to 360 meV, which are comparable to fast Li-ion conductor garnets.[20] More importantly, variable temperature spin-lattice (T_1) relaxation rates were conducted on the sample MgSc_2Se_4 to determine the

activation barrier of 370 meV, which is a first demonstration of using T_1 relaxation rates to investigate fast Mg-ion dynamics. These class of materials are potentially interesting for solid-state electrolyte applications.

Other thiospinel cathodes were also investigated in this aspect. Wustrow *et al.* have synthesised MgCr_2S_4 thiospinel structure and reported the ^{25}Mg NMR resonance at 11220 ppm.[37] This is clearly a large downfield shift from 2862 ppm resonance of MgCr_2O_4 ,[38] which clearly displays the more covalent nature of Cr–S–Mg bonding compared to Cr–O–Mg, which results in a larger hyperfine shift. Attempted electrochemical cycling, however, has resulted in structural degradation and no reversible capacity was observed. This may be a common problem for structures containing sulphur in general, as the electrostatic forces holding the structure intact is much smaller and degradation is more likely than the corresponding oxides.

Chevrel cathodes $\text{Mg}_x\text{Mo}_6\text{X}_8$ (X=S, Se), despite being the besting working cathode so far, have not been investigated systematically with ^{25}Mg NMR. One ^{25}Mg spectrum of a chemically magnesiated Chevrel cathode $\text{Mg}_x\text{Mo}_6\text{S}_8$ is reported with a broad resonance spanning 0 to -500 ppm, which may be attributed to the fast Mg dynamics and the asymmetric nature of Mg sites present in the structure.[35] Negative shifts indicate that polarisation-type hyperfine shift is predominantly present in this material. In contrast, ^{23}Na spectra for Chevrels cycled in Mg aluminate electrolytes $\text{Mg}(\text{THF})_n[\text{Al}(\text{OR})_4]_2$ contaminated with Na ions clearly show positive values of hyperfine shifts (344.8 and 783.1 ppm).[39] This is attributed to a co-insertion of Na into the Chevrel structure (accounting for around 22 % of the capacity) in this contaminated electrolyte. More work is needed to fully understand the extent of NMR shift mechanisms in these materials.

Intermetallics

These class of materials which formally ‘alloys’ with Mg to form intermetallic phases are normally used for anode materials due to their low redox potentials. In this regard, Liu *et al.* have investigated bismuth anodes for MIBs, which accepts Mg to form a phase Mg_3Bi_2 . [40] Mg_3Bi_2 adopts a hexagonal lattice with two available Mg sites: octahedral and tetrahedral (Chapter 5); two ^{25}Mg resonances corresponding to each Mg was observed experimentally at -6 (octahedral) and -306 (tetrahedral) ppm. An interesting aspect of this material is that it shows fast Mg (de)-insertion kinetics: rates of up to 5 C were observed in real cells. By use of a variable-temperature ^{25}Mg NMR and lineshape fitting, Mg exchange rates and the activation barrier were calculated, which shows a very small activation barrier (0.2 eV)

comparable to Li-ion battery electrodes (<0.3 eV). This observation forms the motivation of Chapter 5, where this result is validated computationally by use of *ab initio* methods.

As Sb belongs to the same group as Bi, investigations have been performed on the alloy Mg_3Sb_2 and the mixed-composition electrodes $\text{Mg}_3\text{Sb}_{2-x}\text{Bi}_x$. [41] Mg_3Sb_2 is isostructural with Mg_3Bi_2 and the resulting NMR spectrum also showed two resonances at 50 and -106 ppm, where the downfield shifts could be attributed to the larger electronegativity of Sb compared to Bi. Motional averaging by Mg dynamics was not observed in this material, which could be explained by an increased crystallinity in the sample compared to the above results by Liu *et al.* It was also found that Sb is also electrochemically active in this alloy, thus reaching a complete magnesiation up to $\text{Mg}_3\text{Sb}_{2-x}\text{Bi}_x$ regardless of the Sb content.

Finally, reports on ^{25}Mg spectra in other intermetallics also have been published (not in the context of MIBs). They may find importance as potential candidate anode materials, or investigating Mg alloying into current collectors: Mg_2Sn , MgZn_2 , Mg_2Si , Cu_2Mg , CuMg_2 , and Al_2CuMg . [42, 25, 43, 44]

1.3 Investigated Oxide Structures

Despite the apparent success, chalcogenide systems such as Chevrels have a major drawback in terms of the energy density of a battery: the reduced electrostatic attraction backfires to give low redox potentials. In addition, the gravimetric capacity is also reduced due to the use of heavier sulphur and selenium compared to oxygen. As the energy density depends on both the potential difference between the operating electrodes and their capacities, this results in a lower energy density compared to other systems such as Na-ion batteries. Hence, the seemingly contradictory goal of finding TM oxide cathodes which display low barrier of Mg-ion diffusion need to be achieved to allow high energy density Mg-ion batteries.

Fortunately, the solution to this seemingly contradictory goal could be approached from a structural point of view. Solid-state ionic diffusion should occur via a saddle point (energy maxima along the diffusion pathway), commonly denoted as transition states. Local structural similarities between the local minima and saddle point can reduce the energy differences, thus effectively reducing the activation barrier required for diffusion. [45, 46] In light of this argument, systems with Mg-ions sitting in a high-energy coordination environment are expected to show low diffusion barriers and good Mg-ion mobilities.

This is also interesting from a ^{25}Mg NMR point of view, as the high degree of structural distortion is likely to result in a strong quadrupolar coupling and hence broad spectra. Developing experimental NMR techniques aided by computational predictions is thus likely

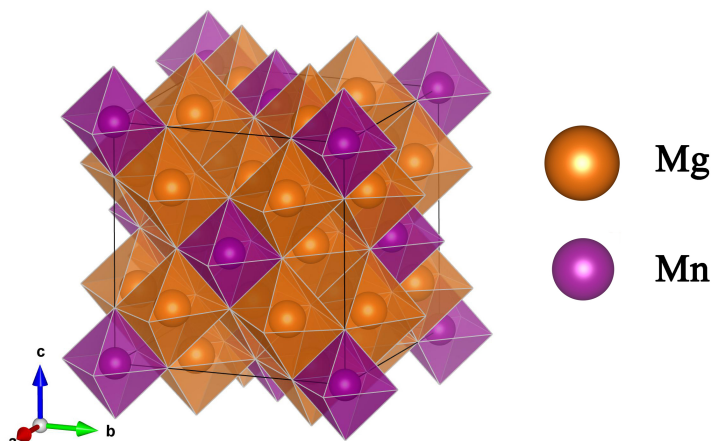
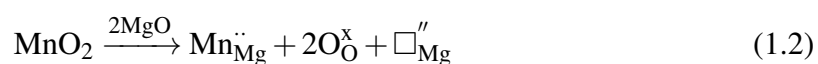


Fig. 1.2 Structure of Mg_6MnO_8 , shown with oxygen polyhedra around the metal ions.

to be valuable to investigating such compounds. Here, we briefly discuss the structural aspects of the oxide materials under study in this thesis.

1.3.1 Mg_6MnO_8

First reported in 1954 by Kasper *et al.*,^[47] Mg_6MnO_8 shows a defect rocksalt structure with both Mg/Mn ordering and defect ordering: $[\text{Mg}_{6/8}^{2+}\text{Mn}_{1/8}^{4+}\square_{1/8}]\text{O}^{2-}$ with the $Fm\bar{3}m$ space group symmetry. A family of oxide and halides, such as Ni_6MnO_8 and Na_6CdCl_8 , adopts this structure, commonly called Murdochite or Suzuki-like phases; a high pressure polymorph of Cu_6PbO_8 is also expected to adopt this structure.^[48] This compound has an interesting structure with ordered vacancies, where a vacancy is formed according to the following defect reaction written in Kröger-Vink notation:



In addition, the oxygen sublattice is slightly distorted (Figure 1.2) from the ideal rocksalt structure due to the smaller ionic radius of Mn^{4+} (0.53 Å) compared to Mg^{2+} (0.72 Å).^[49] This should give a nonvanishing quadrupolar coupling constant for Mg, as the local environment is no longer spherically symmetric. Mg site in this structure shows a $m.mm$ site symmetry, reflecting the distorted octahedra as opposed to the Mg in the MgO structure. Although this material is not expected to display any electrochemical activity, these structural properties make Mg_6MnO_8 a good reference material for performing ^{25}Mg paramagnetic solid-state NMR (Chapter 3).

1.3.2 Spinel Structures

Spinel is a group of metal oxide minerals with chemical formula AB_2O_4 where A and B are metal ions. Various spinel-type TM oxides have also been investigated as cathode materials for LIBs,[50] which makes it a natural extension to apply them for MIBs.

Spinel generally displays a cubic $Fd\bar{3}m$ space group symmetry with the 32 oxygen atoms occupying the $32e$ Wyckoff positions, forming an approximate cubic close-packed (ccp) arrangement. Distortions from the ccp structure towards the $[111]$ direction can be described in terms of an oxygen parameter u ($u = 0.25$ for perfect ccp). As u increases, the $8a$ tetrahedral sites are enlarged at the expense of $16d$ octahedral sites.[51] In addition, there exist empty octahedral $16c$ sites, which are important for cationic diffusion (*vide infra*).

A^{2+} and B^{3+} cations can occupy the $8a$ or $16d$ positions in the ccp lattice. If all $8A^{2+}$ ions occupy the $8a$ site, the structure is perfectly ordered and called a normal spinel. At the other end we have $8A^{2+}$ ions occupying half of the $16d$ sites and $16B^{3+}$ ions distributed equally among the $8a$ and $16d$ sites, called an inverse spinel. Most real spinels are somewhere between the completely normal and inverse spinels, having some degree of disorder. This is quantified in terms of the inversion parameter x : $[A_{1-x}B_x]_{tet} [A_xB_{2-x}]_{oct} O_4$. [52]

Thermodynamics of cation distribution in spinels

The free energy of any spinel can be expressed as a function of x : [52, 51]

$$\begin{aligned} G(x) &= H - TS \\ &= U - TS + PV \\ &= U_{elec} + U_{CFSE} - T(S_{int} + S_{config}) \end{aligned} \quad (1.3)$$

Here we have assumed purely electrostatic interactions between the ions and ignored any vibrational and volumetric contributions to the free energy. The remaining terms are determined by electrostatic interactions (U_{elec}), crystal field stabilisation energy (U_{CFSE}), and internal (electronic) degree of freedom (TS_{int}). [53] Configurational entropy (S_{config}) is maximised in the completely random distribution and is expressed as [52]

$$S_{config} = -k_B \left[x \ln(x) + (1-x) \ln(1-x) + x \ln\left(\frac{x}{2}\right) + (2-x) \ln\left(1 - \frac{x}{2}\right) + C \right] \quad (1.4)$$

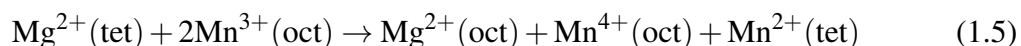
where C is a constant.* Electrostatic interactions are primarily determined by the cationic radii r and charges. Here a balance between two factors exists: trivalent ions are better stabilised in 6-coordinate octahedral sites by electrostatics,[54] but they cannot fully fill the large octahedral site. The structure distorts along the $[111]$ direction, changing the u parameter:[51] small r_B/r_A results in $u > 0.25$, favouring the B^{3+} ions in octahedral sites and the A^{2+} ions in the tetrahedral sites.

CFSE is important for TM ions with d^n electronic configurations.[55] As the O^{2-} ion is a low-field ligand, almost all TM ions adopt the high-spin configuration;[53] the CFSE can then be obtained from the tetrahedral and octahedral crystal field splitting Δ_{oct} and $\Delta_{\text{tet}} \sim \frac{4}{9}\Delta_{\text{oct}}$. [56] The CFSE effect is especially dominant for the Cr^{3+} ion, where d^3 spin configuration produces large CFSE and all known ACr_2O_4 spinels are normal.[57, 58]

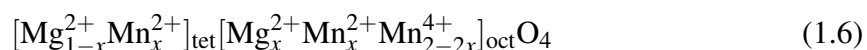
The electronic degree of freedom, although small in magnitude, can be important in some structures, *e.g.* MgV_2O_4 . Here the V^{3+} (d^2) ions can have orbital degrees of freedom only in an octahedral configuration. This reinforces the small CFSE effect of V^{3+} ions, making MgV_2O_4 a normal spinel.[53]

MgMn₂O₄

$MgMn_2O_4$, which shows a spinel structure with $I4_1/amd$ symmetry, is different from the above two compounds since the two Mn^{3+} (d^4) ions in octahedral environments cause a Jahn-Teller distortion of the original cubic spinel structure, resulting in a tetragonal spinel (as evident from the space group symbol). This d^4 electronic configuration is also important for structural changes at high temperatures, combined with the inversion of the Mg and Mn cations:



This charge disproportionation is favourable because of the smaller CFSE of tetrahedral sites, resulting in a $t_{2g}^3 e_g^2$ configuration of the inverted tetrahedral Mn atom, whereas a nearby octahedral Mn atom tends to get oxidised to t_{2g}^3 state. This inversion behaviour is known to occur around 800 °C,[59, 60] resulting in the following cation distribution:



*As only the change in entropy as a function of x is relevant, the exact value of C is unimportant.

This disproportionation was studied with resistance measurements[59] and Mn X-ray absorption studies.[30] As the Mn^{2+} , Mg^{2+} , and Mn^{4+} cations are all non Jahn-Teller active in their respective coordination environments, increasing the temperature results in a removal of the Jahn-Teller distortion. The sample undergoes a tetragonal to cubic transformation above 1200 °C.[61]

Ab initio studies on the impact of this cation inversion on the Mg-ion mobility in MgMn_2O_4 was also reported.[62] It was found that the tetrahedral (8a) Mg hopping via a tet(8a)–oct(16c)–tet(8a) pathway could be considered as ‘open’ (<750 meV barrier) when perfectly normal spinels are considered with no degree of cation inversion ($x = 0$). Barrier heights of 475 meV and 717 meV were observed with dilute Mg and vacancy limits, respectively. Upon increasing the degree of inversion, the barrier initially shows a decrease then again increases to >1000 meV under a full degree of inversion ($x = 1$). In addition, the octahedral (16d) Mg, if present, shows low migration barrier only if a nearby tetrahedral (8a) site is either empty or occupied by a Mg. In this study, therefore, we restrict ourselves to study only the perfectly normal spinel with ^{25}Mg NMR.

MgV₂O₅

As discussed above, one way of achieving low migration barrier of Mg in oxides likely requires unusual high-energy Mg coordination environments. This, in turn, calls the necessity for structural flexibilities in designing the candidate host materials if one would like to systematically investigate a particular TM ion.

Vanadium oxides are especially interesting in this regard due to the versatile structures with different vanadium oxidation states, spanning from V^{2+} to V^{5+} . Phase diagram of the Mg–V–O system (Figure 1.3) shows the presence of numerous stable vanadium oxide structures (at 0 K) with different averaged oxidation states; many other metastable states are also reported in the literature. These include V_2O_5 , V_6O_{13} , VO_2 , V_5O_9 , V_3O_7 , V_4O_7 , V_3O_5 , V_2O_3 , and substoichiometric $\text{VO}_{1-\delta}$, where incorporation of metal atoms (Li, Na, Mg...) gives rise to further structural versatility.[2, 63] Many of these vanadium oxides have been studied as Li- and Na-ion battery cathodes, where the multiple possible oxidation states were exploited to give good Li- and Na-ion storage capacity.[64]

Recently, two computational works were reported on a magnesium vanadate material MgV_2O_5 which adopts a layered structure with potential 1-dimensional diffusion channels.[67, 68] This material is a natural extension from $\alpha\text{-V}_2\text{O}_5$, which previously showed reversible Mg insertion up to $\text{Mg}_{0.5}\text{V}_2\text{O}_5$ at a potential of 2.3 V vs Mg/Mg^{2+} . A full cycling of Mg ions would be expected to yield 260 mAh/g capacity.

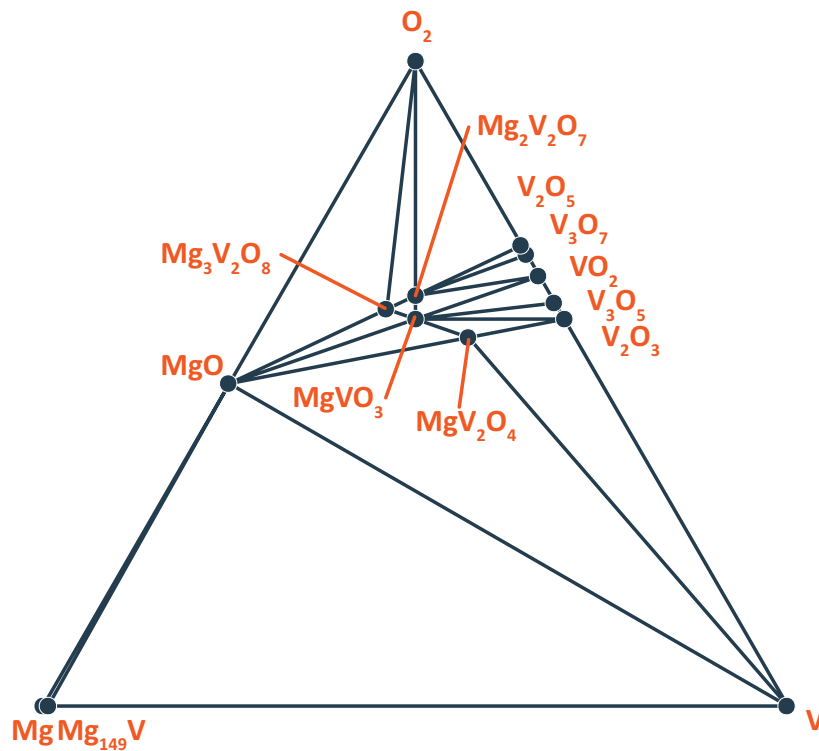


Fig. 1.3 Compositional phase diagram (at 0 K) of the Mg–V–O system, calculated using the Materials Project.[65, 66]. PBE+U functional was used with $U = 3.25$ eV for V. Stable phases at 0 K are also labelled on the diagram. MgV_2O_5 exists at only 0.026 eV above the hull.

α -V₂O₅ exhibits an AA-type stacking of the V₂O₅ layers. Introduction of a stacking fault by translation of every other layer by $a/2$ results in a new polymorph, δ -V₂O₅, with an AB-type stacking and additional puckering of the V₂O₅ layers (Figure 1.4). It was shown that the V₂O₅ layers in the MgV₂O₅ structure adopt the δ -V₂O₅ motif,[69] which has Mg activation barriers substantially lower than those predicted in α -V₂O₅ (0.6–0.8 eV compared to 1–1.2 eV).[67] In the same paper, the intercalation phase diagram of δ -V₂O₅ was generated through a cluster expansion technique; it was also suggested that the V₂O₅ layer stacking is likely to remain metastable over a range of Mg stoichiometries, allowing reversible cycling of this phase. However, direct electrochemical cycling and detailed NMR characterisation of this compound has not been reported to date, despite several observations on the ²⁵Mg NMR of this material (without a detailed characterisation).[35, 34] This is likely to be due to difficulties in preparing this material pure-phase, alongside the aforementioned challenges in cycling this high-voltage cathode candidate.

Finally, we note that many of these compounds show interesting physical phenomena due to the relatively diffuse nature of vanadium *d*-orbitals compared to the late TMs: VO₂ shows a metal-insulator transition at 340 K, MgV₂O₅ is a compound with competing magnetic interactions in a spin-ladder structure, and LiV₂O₄ is an example of a ‘heavy fermion’ compound with the effective electron mass much greater than that of a free electron. Hence, reliable ways for preparing these compounds and characterising the local structures would be valuable, as it is in general difficult to control the precise oxidation states of these compounds.[63]

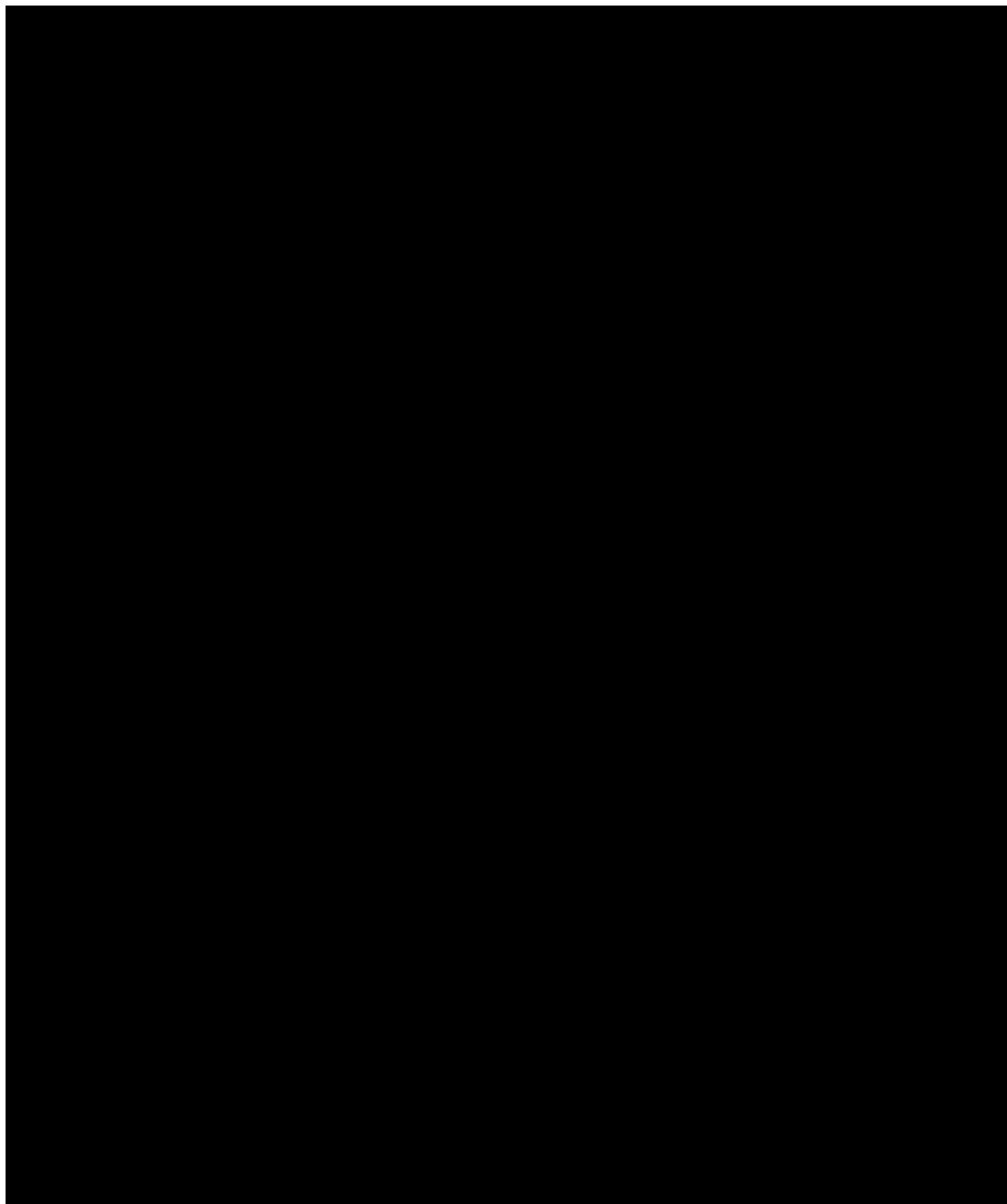


Fig. 1.4 Structures of the α -, δ -, and metastable ε -polymorphs of MgV_2O_5 . Reproduced from Sai Gautam *et al.*[67]

1.4 Outlook and Structure of This Thesis

Despite several reports on observing ^{25}Mg NMR spectra in MIB electrode materials being presented before, no detailed systematic investigations on the NMR spectra have been performed in many cases. For more complicated electrodes, it is likely that one will face a challenge in obtaining good spectra and assigning the resonances. *Ab initio* methods, combined with advanced NMR techniques, are thus needed to facilitate the understanding and development of novel electrode materials.

Based on the motivations above, this thesis attempts to develop a combined computational and experimental methodology in utilising ^{25}Mg NMR in MIB research. In Chapter 2, we first start by outlining the experimental and computational approaches used in this thesis. In the following Chapter 3, various Mg TM oxides are investigated experimentally with ^{25}Mg NMR, aided by computational predictions on the spectral parameters. As many of the potential cathode materials contain paramagnetic TM ions, a systematic investigation on paramagnetic ^{25}Mg NMR parameters is shown, alongside the detailed report on the structural and magnetic aspects on these samples. Application of advanced NMR pulse sequences to enhance the sensitivity and resolution is also validated.

Following this, we turn our attention to MgV_2O_5 , a promising candidate MIB cathode material. Here the focus is on (i) developing synthetic approaches to this sample using *ab initio* thermodynamic parameters, (ii) structural and magnetic characterisation of the compound, (iii) validation of the ^{25}Mg NMR techniques as developed in Chapter 3, and finally (iv) attempts in cycling this compound in an electrochemical cell. A brief discussion on the NMR and magnetic characterisation of MgV_2O_4 prepared through the same synthetic approach is presented in the end.

In the final chapter, the focus is shifted towards an anode material Mg_3Bi_2 . This compound has been shown to display fast Mg kinetics *via* ^{25}Mg NMR spectroscopy with electrochemical cycling; by application of *ab initio* transition state searching and defect energy calculations, we attempt to confirm the fast Mg dynamics. Investigations on the electronic and structural aspects behind this fast ionic conduction are also presented. The thesis concludes with the major achievements and implications for future researches in this direction.

Chapter 2

Background Theory

In this chapter, the physical grounds of the computational and experimental techniques used in this thesis are reviewed, in three broad sections.

This chapter starts by introducing the *ab initio* computational techniques, including the Density Functional Theory (DFT) and the relativistic corrections that can be applied to the standard DFT methods. Transition state searching approaches using *ab initio* methods are then discussed.

This is followed by an introduction to the Nuclear Magnetic Resonance (NMR) spectroscopy, with particular focus on the solid-state and quadrupolar NMR techniques. A separate section on the electron magnetism and the paramagnetic NMR theory is presented.

This chapter concludes with the thermodynamics behind the idea of carbothermal synthesis central in Chapter 4, with a brief discussion on the X-ray diffraction as a characterisation technique in crystalline materials.

2.1 Density Functional Theory

2.1.1 The Hartree-Fock Approximation

In principle, many of the physico-chemical behaviour of any quantum system can be described exactly with the (time-independent) Schrödinger equation:

$$\hat{H}\Psi = E\Psi \tag{2.1}$$

where \hat{H} is the Hamiltonian operator of the system, Ψ is the wavefunction, and E is the energy corresponding to Ψ . By taking the modulus $|\Psi|^2$ of this (complex) wavefunction, one can extract the electron distribution and hence the related properties.

The Hamiltonian \hat{H} describes all the possible interactions present in this system. In a system containing N -electrons and M -atoms such as a molecule, however, the many-body interactions in general cannot be solved exactly and approximations must be taken. For an atom, the nucleus is much heavier than the electrons by a factor of 1820 (at least) and we can consider them to be stationary in the frame of electrons (the Born-Oppenheimer approximation) and subsequently the Hamiltonian can be written as (in atomic units)[70]

$$\hat{H} = -\sum_i^N \frac{1}{2} \nabla_i^2 - \sum_i^N \sum_A^M \frac{Z_A}{r_{iA}} + \sum_i^N \sum_j^N \frac{1}{r_{ij}} \quad (2.2)$$

where the individual terms refer to the electron kinetic energy, electron-nuclear electrostatic attraction for nuclei of charge Z_A , and electron-electron repulsion. As the last many-body term depends on the positions of other electrons, there are no exact solutions to this equation and numerical methods are necessary. One such approach is to exploit the Fermionic nature of electrons to variationally minimise the ground state wavefunction Ψ_0 ; here the degree of freedom lies in the choice of spin-orbitals. Such procedure yields the Hartree-Fock (HF) equation in a form of

$$f(i)\chi(\mathbf{x}_i) = \varepsilon\chi(\mathbf{x}_i) \quad (2.3)$$

$$f(i) = -\frac{1}{2}\nabla_i^2 - \sum_A^M \frac{Z_A}{r_{iA}} + v^{\text{HF}}(i) \quad (2.4)$$

where $V^{\text{HF}}(i)$ describes the effective ‘averaged’ potential of all other electrons on the i -th electron, similar to the idea of molecular field used in magnetism (Section 2.5.1). As this equation is nonlinear, it should be solved self-consistently: the energy is minimised by feeding in the resultant v^{HF} into the new equation to solve the spin-orbitals χ until the energy change falls below a set limit. This method of self-consistent field (SCF) is central to quantum chemical calculations.

However, it needs to be stressed that the HF method does not take (Coulombic) electron correlation into account by virtue of the fact that only an averaged potential v^{HF} is used in the calculation; it ignores the ‘hole’ around a single electron where the other electrons are unlikely to be present due to the repulsive Coulomb interactions (but does take the Fermi correlation into account). Thus, considering also the variational nature of minimisation involved, HF energies are always higher than the ‘exact’ energies.

2.1.2 The Hohenberg-Kohn-Sham Approach

One downside of the HF method is its associated computational cost and unfavourable scaling. As the electron density could be directly obtained from the wavefunction and is physically observable, methods using this 3-variable electron density $n(\mathbf{r})$ instead of the full $3N$ -variable wavefunction have been investigated over years for a cheaper solution to the Schrödinger equation.

$n(\mathbf{r})$ already contains information about the total number of electrons and nuclear positions with charge Z_A : [71]

$$\int n(\mathbf{r}) d\mathbf{r} = N \quad (2.5)$$

$$\lim_{r_{iA} \rightarrow 0} \frac{\partial}{\partial r} n(\mathbf{r}) = -2Z_A n(0) \quad (2.6)$$

The relationship of energy to the electron density is formulated by the famous Hohenberg-Kohn theorems. [72]

- In a system with the full Hamiltonian $\hat{H} = \hat{T} + \hat{V}_{ee} + \hat{V}_{\text{ext}}$ where T is the electronic kinetic energy, V_{ee} is the Coulombic repulsion, and V_{ext} is the potential energy due to an external field, V_{ext} and hence the ground-state energy $E_0[n]$ is a unique functional of $n(\mathbf{r})$.
- The energy functional $E[n]$ is minimised if and only if $n(\mathbf{r})$ is the true ground-state electron density.

The Hohenberg-Kohn energy functional can be expressed as

$$E[n] = \int V_N e n(\mathbf{r}) d\mathbf{r} + \frac{1}{2} \iint \frac{n(\mathbf{r}_1) n(\mathbf{r}_2)}{r_{12}} d\mathbf{r}_1 d\mathbf{r}_2 + T[n] + E_{\text{ncl}}[n] \quad (2.7)$$

The idea of Kohn and Sham was to do exact calculations on the kinetic energy and nonclassical energy functionals $T[n]$ and $E_{\text{ncl}}[n]$ as far as possible, and then put the rest under a collective ‘unknown’ functional called the exchange-correlation functional. [73] By use of a similar variational approach to the HF method, the Kohn-Sham equations could be obtained as:

$$\hat{f}_{\text{KS}} \varphi_i = \varepsilon_i \varphi_i \quad (2.8)$$

$$\hat{f}_{\text{KS}} = -\frac{1}{2} \nabla^2 + V_{\text{eff}}(\mathbf{r}) \quad (2.9)$$

where φ_i are called the Kohn-Sham (KS) orbitals. From this we can extract the exact kinetic energy of non-interacting electrons and re-write $E[n]$ as

$$E[n] = \int V_{Ne} n(\mathbf{r}) d\mathbf{r} - \frac{1}{2} \sum_i^N \langle \varphi_i | \nabla^2 | \varphi_i \rangle + \frac{1}{2} \iint \frac{n(\mathbf{r}_1)n(\mathbf{r}_2)}{r_{12}} d\mathbf{r}_1 d\mathbf{r}_2 + E_{xc}[n] \quad (2.10)$$

where the exchange-correlation functional $E_{xc}[n]$ accounts for all the unknowns in the Hamiltonian. It is independent of the system, and hence finding approximate functional forms of $E_{xc}[n]$ is one of the major goals of DFT.

The most basic functional of these exchange-correlation functionals is the local density approximation (LDA) functional, where the functional only depends on the electron density n at any given point

$$E_{xc}^{\text{LDA}}[n] = \int n(\mathbf{r}) \varepsilon_{xc}(n) d\mathbf{r} \quad (2.11)$$

where $\varepsilon_{xc}(n) = \varepsilon_x(n) + \varepsilon_c(n)$ is the exchange-correlation energy of a single particle, calculated for a homogenous electron gas of density n . Analytical expression for the exchange part $\varepsilon_x(n)$ is known, but further approximations must be employed for $\varepsilon_c(n)$. This LDA functional and its spin-polarised variant LSDA functional can accurately describe systems with a homogeneous electron distribution such as metals. Extension of this method to include higher order gradients in the density have resulted in generalised gradient approximation (GGA) functionals which include a $\nabla n(\mathbf{r})$ term and meta-GGA functionals which also include a $\nabla^2 n(\mathbf{r})$ term.[74]

However, all DFT methods suffer from what is called a self-interaction error (SIE); this arises due to the electrons ‘interacting’ with the mean field created by itself in the DFT framework, thus resulting in an excessive delocalisation of the density compared to the true density. For TM oxides where the d -electron correlation makes the system insulating (Mott insulator), DFT methods often (incorrectly) predict a metallic groundstate. In the following sections, we will look at two different ways of treating this error: Hubbard- U and hybrid functionals.

2.1.3 The Hubbard- U Method

The LDA+ U formalism was introduced to resolve this problem of strong correlation.[75] In this model, the correlated electronic states (*e.g.* localised d -orbitals), are treated with a Hubbard model where the electron hopping and on-site Coulombic interactions are taken into account by two parameters t and U . [76] In the limit of $U \ll t$, the electrons are more favourable to ‘hop’ or delocalise and the DFT methods would correctly predict a metallic

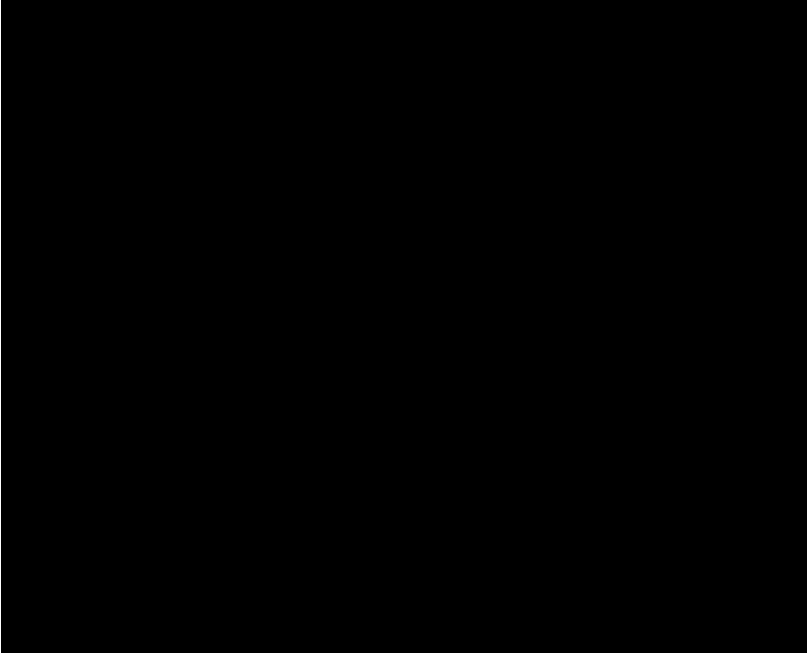


Fig. 2.1 Total energy as a function of electron count in the system. Black line gives the analytical DFT energy, red line gives the exact energy, and the blue line gives the parabolic energy difference given by the U -correction. Figure adopted from [81].

state. On the other hand, DFT performs poorly when $t \ll U$, as the strong on-site Coulombic repulsion forces dictate that an electron ‘hop’ at the cost of U would be unfavourable; a localised, insulating state then results.[77]

In the fully localised limit (FLL) formulation of this approach, the energy consists of three components $E_{\text{DFT}+U} = E_{\text{DFT}} + E_{\text{Hub}} + E_{\text{dc}}$. Here the Hubbard correction E_{Hub} and the ‘double-counting’ term E_{dc} (to compensate for the interactions already counted in the DFT energy) are applied to the normal DFT energy E_{DFT} . Different implementations of this formulation exist;[78, 79] here we have used the rotationally invariant formulation of Dudarev *et al.*[80] where only one parameter $U_{\text{eff}} = U - J$ is used:

$$E_{\text{DFT}+U} = E_{\text{DFT}} + \sum_l \frac{U_{\text{eff}}^l}{2} \left[(n^l)^2 - \sum_{\sigma} \text{Tr} \left[(\mathbf{n}^{l\sigma})^2 \right] \right] - \sum_l \frac{U_{\text{eff}}^l}{2} n^l (n^l - 1) \quad (2.12)$$

where $n^{l\sigma}$ are the occupation numbers of each local orbitals labelled by atomic site l and spin σ . This formulation essentially ignores the dependence of U on the magnetic quantum number (*i.e.* the orbital orientation).

An intuitive picture of this U correction could be envisaged by looking at the energy change of a system as a function of electron counts (Figure 2.1). Exact wavefunction solutions

should result in kinks at integer occupations due to the changes in electron count changing the effective band gap. DFT wavefunctions, however, are analytic: discontinuities in the derivatives are less well represented in this case. This spurious curvature of the DFT energy profile is the main reason for the underestimation of the band gap (or excessive electron delocalisation). The U correction in this case attempts to restore the discontinuities by adding a parabolic energy term to the DFT energy.[75]

Now the values of U could be computed simply as the spurious curvature of the energy differences (blue line in Figure 2.1) as a second derivative term d^2E/dn^2 using a linear-response theory.[82] Since it is not possible in general to control the site occupation in plane-wave DFT implementations, the diagonal component of the response matrix χ can be evaluated as a variation in n^l due to α^l , the perturbing potential on site l .

$$\chi_{ll} = \frac{dn^l}{d\alpha^l} \quad (2.13)$$

Then, it can be shown that $d^2E/dn^2 = -d\alpha/dn$. Extracting the ‘noninteracting’ variation in occupation χ_0 arising from the rehybridisation of orbitals (obtained by fixing the charge density), the U can now be calculated as

$$U = (\chi_0^{-1} - \chi^{-1}) \quad (2.14)$$

which is used in Chapter 4.

2.1.4 Hybrid Functionals

In contrast to the DFT approach, the SIE is explicitly cancelled out in the HF approach by the exchange contribution to the energy. As LDA functional shows self-interaction error whereas the HF exchange energy does not, incorporating a degree of HF exchange energy into LDA functionals could cancel this error.[83] Several such ‘hybrid’ functionals were developed, such as the B3LYP[84], PBE0,[85] and HSE[86] functionals. The most popular of these ‘hybrid’ functionals is the B3LYP functional which has the form

$$E_{xc}^{B3LYP} = (1 - a)E_x^{LSD} + aE_x^{HF} + bE_x^B + cE_c^{LYP} + (1 - c)E_c^{LSD} \quad (2.15)$$

where E_x^B is Becke’s exchange functional[87] and E_c^{LYP} is the Lee-Yang-Parr (LYP) correlation functional.[88] B3LYP functional has been shown to give good results in many systems.[89] In the ‘pure’ B3LYP functional $a = 0.20$, $b = 0.72$, and $c = 0.81$; however,

recent results indicate that for solid-state magnetic calculations, $a = 0.35$ gives better results.[90, 91] Previous work on ${}^6/7\text{Li}$ and ${}^{23}\text{Na}$ hyperfine calculations indicate that the experimental value lies between $a = 0.20$ and $a = 0.35$.[92, 93, 94] Hence in this study both cases are considered.

2.1.5 Basis Sets in DFT Calculations

In general, the Hartree-Fock or Kohn-Sham equations cannot be solved directly to yield a close-form analytical solution. Instead, the corresponding wavefunctions are usually expressed as a linear combination of some basis functions $\{\eta_\mu\}$:

$$\varphi_i = \sum_{\mu} c_{\mu} \eta_{\mu} \quad (2.16)$$

This allows us to express the KS/HF equation in a matrix form, which is easily solvable using numerical linear algebra algorithms. Two families of basis sets are widely used in DFT programs: Gaussian-type orbitals (GTOs) and plane-waves.

GTOs have form[95]

$$\eta^{GTO} = N x^l y^m z^n e^{-\alpha r^2} \quad (2.17)$$

where $x^l y^m z^n$ describes the rotational symmetry and $e^{-\alpha r^2}$ describes the radial part. In this approach, the basis functions are localised to a particular atom which makes it convenient to think of them as ‘atomic orbitals’, and the overall wavefunction is expressed as a linear combination of these basis functions: hence the name Linear Combination of Atomic Orbitals (LCAO) method.

Another choice of basis sets is plane-waves $\eta^{PW} = e^{i\mathbf{k}\cdot\mathbf{r}}$. In solid-state calculations plane-waves are desirable as they explicitly contain the periodic boundary condition and reciprocal space representations. The number of plane-waves used in the calculation is often set by the cutoff energy where we set the energy of plane-wave $\varepsilon = \frac{\hbar^2}{2m_e} |\mathbf{k} + \mathbf{G}|^2$ where \mathbf{G} is a reciprocal lattice vector .[96]

In paramagnetic NMR we are interested in the spin density at nuclear positions. This is problematic as neither of the two bases can accurately represent the cusp condition at the nucleus. This can be approximated in GTO bases by adding functions with large α . If we wish to use plane-wave bases, pseudopotentials are normally used to represent the core states and a more sophisticated scheme such as gauge-including projector augmented wave (GIPAW) method is necessary to describe the core behaviour.[97]

In this study, GTO-type basis sets were used to accurately describe the core electronic states using the CRYSTAL code (see below).

2.1.6 Solid-state DFT

In a periodic lattice we have an infinite array of primitive cells with a general lattice vector given as $\mathbf{g} = n_1\mathbf{a}_1 + n_2\mathbf{a}_2 + n_3\mathbf{a}_3$. Since the system is periodic, any wavefunction of the system with basis set $\{\mu\}$ should satisfy the Bloch's theorem[98]

$$\phi_\mu(\mathbf{r} + \mathbf{g}; \mathbf{k}) = e^{i\mathbf{k}\cdot\mathbf{g}}\phi_\mu(\mathbf{r}; \mathbf{k}) \quad (2.18)$$

Functions satisfying the Bloch's theorem can be expressed as the Bloch functions

$$\phi_\mu(\mathbf{r}; \mathbf{k}) = \frac{1}{\sqrt{N}} \sum_{\mathbf{g}} e^{i\mathbf{k}\cdot\mathbf{g}} \eta_\mu^{\mathbf{g}}(\mathbf{r} - \mathbf{R}_\mu) \quad (2.19)$$

Such functions have translational symmetry in the \mathbf{k} -space, hence we only need to evaluate a number of sampled \mathbf{k} -points in the irreducible Brillouin zone and then interpolate between the \mathbf{k} -points. Using the Bloch function we can represent the crystalline orbitals as a linear combination

$$\psi_n(\mathbf{r}; \mathbf{k}) = \sum_{\mu} c_{\mu n}(\mathbf{k}) \phi_\mu(\mathbf{r}; \mathbf{k}) \quad (2.20)$$

which satisfies the Schrödinger equation labelled with \mathbf{k} , evaluated in the real space. This problem is analogous to the basis set expansion in the Kohn-Sham equation with an infinitely large matrix. For details on approximate evaluation methods in this study using the CRYSTAL code see [99].

2.2 Relativistic Quantum Chemistry: a Brief Introduction

2.2.1 Relativity and the Dirac Equation

Many important systems relevant to battery chemistries, such as Bi, Sn, and Pb for instance, involve 'heavy' elements, *i.e.* elements with large proton number Z . For instance, Bi, which is important as a high-rate MIB anode material (Chapter 5) has $Z = 83$; Pb, which finds use in lead-acid batteries, has $Z = 82$; Sn, which is being widely investigated as secondary battery anodes, has $Z = 50$. As Z is increased, the core electrons experience a significantly

enhanced electrostatic attraction to the nucleus, which is exhibited as a decrease in potential energy and an increase in kinetic energy.

What this means in practice is that the electron kinetic energy E_k , and subsequently the momentum p , ultimately reaches a level where the electron ‘velocity’ is a significant fraction of the light velocity c . Under such conditions, the assumptions of classical electrodynamics (Newtonian and Maxwellian) do not hold and the particles should be treated within the framework of *relativistic* quantum theory. Subsequently, the Schrödinger equation should now be extended to include the theory of relativity; this yields the Dirac equation[100]

$$\left(\beta m_0 c^2 + c \left(\sum_{n=1}^3 \alpha_n p_n \right) \right) \psi(\mathbf{x}, t) = i\hbar \frac{\partial \psi(\mathbf{x}, t)}{\partial t} \quad (2.21)$$

where the ψ is the electron wavefunction with the rest mass m_0 , c is the light velocity, p_n are the x, y, z components of the momentum. Solutions to this equation can correctly describe the relativistic motion of the electrons. By introducing spin into the equation by means of Pauli matrices α_n and β , solutions to this equation could be obtained as a four-component wavefunction

$$\psi = \begin{pmatrix} \psi_1 \\ \psi_2 \\ \psi_3 \\ \psi_4 \end{pmatrix} \quad (2.22)$$

(*i.e.* superposition of four different components), which can describe the full behaviour of a relativistic electron in terms of spin up/down electron and spin up/down positron (antiparticle of electron).

In theory this equation could be solved for all particles, regardless of their relativistic nature, to yield the correct wavefunctions and their energies. From the solid-state chemistry point of view, however, this problem is unwieldy; often, simple nonrelativistic calculations are performed with the relativistic ‘correction’ terms applied to the energy, which will be discussed below.

2.2.2 Relativistic Corrections: the Mass-velocity and Darwin Terms

Most of the quantum chemical calculations have the aim of looking at ‘valence’ states, *i.e.* states that participate the most in bonding interactions. As the elements for which the relativistic corrections are meaningful have a lot of ‘core’ states that do not directly participate in bonding, this calls for parametrising the core states. This is most often done

with pseudopotentials, as the core could safely be frozen. As generation of pseudopotentials require a calculation of the atomic wavefunctions, different levels of corrections could be applied while generating the wavefunctions (and subsequently the pseudopotential).

To see how this could work, let us consider the nonrelativistic expression for the electron energy E_{NR} : [101]

$$E_{NR} = E_k + E_V = \frac{p^2}{2m} + V \quad (2.23)$$

where p and m represent the electron momentum and mass, and V the potential energy. Under relativistic conditions, the increase in electron ‘velocity’ means the kinetic energy E_k should follow the relation $E_k^2 = m_0^2 c^4 + p^2 c^2$ instead. Excluding the rest mass contribution $m_0 c^2$, the relativistic energy expression is shown as:

$$E_R = \sqrt{m_0^2 c^4 + p^2 c^2} - m_0 c^2 + V \quad (2.24)$$

$$= m_0 c^2 \sqrt{\left(1 + \left(\frac{p}{m_0 c}\right)^2\right)} - m_0 c^2 + V \quad (2.25)$$

Under the condition $(p/m_0 c) \ll 1$, by means of Binomial expansion the square root term approximates to

$$\sqrt{\left(1 + \left(\frac{p}{m_0 c}\right)^2\right)} = 1 + \frac{1}{2} \left(\frac{p}{m_0 c}\right)^2 - \frac{1}{8} \left(\frac{p}{m_0 c}\right)^4 + \dots \quad (2.26)$$

which then gives the final energy expression (to a second order)

$$E_R = \frac{p^2}{2m_0} - \frac{1}{8} \frac{p^4}{m_0^3 c^2} \quad (2.27)$$

From this we can see that the correction term for the Hamiltonian should be

$$\hat{H}'_{mv} = \frac{\hat{\mathbf{p}}^4}{8m_0^3 c^2} \quad (2.28)$$

which has the physical meaning of change in electron mass with the momentum, and is accordingly called the mass-velocity term. Applying this as a first-order perturbation to a

hydrogen-like wavefunction ψ_n with an energy of E_n^0 gives[101]

$$\Delta E'_{mv} = \langle \psi_n | \hat{H}'_1 | \psi_n \rangle \quad (2.29)$$

$$= -E_n^0 \frac{Z\alpha^2}{n^2} \left(\frac{3}{4} - \frac{n}{l+1/2} \right) \quad (2.30)$$

with α being the fine-structure constant, which now shows the dependence of energy on l . For a given n , the effect would be the greatest for $l = 0$, *i.e.* the s -orbital, as they ‘approach’ the nucleus closer than any other orbitals.

The above mass-velocity correction arises from a purely relativistic point of view assuming a point mass/charge. From a microscopic point of view, however, electrons are represented by a positional uncertainty on the order of its Compton wavelength $\lambda_c = h/m_0c$, which then gives a variation of potential inside the electron when placed under the nuclear field.

The magnitude of this interaction can be evaluated by averaging the potential over a sphere of λ_c , which yields:[101]

$$\Delta \hat{H}'_d = \frac{Ze^2}{4\pi\epsilon_0} \frac{\pi\hbar^2}{2m^2c^2} \delta(\mathbf{x}) \quad (2.31)$$

and we can clearly see that this effect is nonzero only for the s -orbitals of $l = 0$ due to the Dirac delta function. Evaluation of this as a perturbation for a hydrogen-like wavefunction again yields an energy correction which is n -dependent in this case:

$$\Delta E'_d = -E_n^0 \frac{(Z\alpha)^2}{n} \quad (2.32)$$

This term, which can be thought of as an energy correction due to the positional uncertainty of the electron at the nucleus, is again only significant for the s -orbital; this term is commonly called the Darwin term. Combined together, the mass-velocity and Darwin terms represent the relativistic interaction which happens to be strongest at the nucleus. Both effects are most pronounced for the s -orbitals and have a quadratic dependence on the nuclear charge Z ; thus, these effects become stronger for the heavy atoms with large Z . As the correction for these two effects are significant and also computationally inexpensive, most pseudopotentials/basis sets take them into account when built. As these corrections do not involve explicit spin vector components, they are termed ‘scalar relativistic’ corrections.

2.2.3 Relativistic Corrections at the Core and Valence: Spin-orbit Coupling

As the Dirac equation is fundamentally about the spins and their behaviours under relativistic conditions, this gives rise to a phenomenon called spin-orbit coupling (SOC). The classical picture of an atom involves electrons circling around the nucleus which poses an electric field $\mathbf{E} = -(\mathbf{x}/r)d\phi/dr$. Under this picture, the electrons experience a magnetic field $\mathbf{B} = -\mathbf{v} \times \mathbf{E}/c$ generated by the nucleus: in the stationary frame of the electron, the positively charged nucleus is seen to circle around it, and this accelerating charge creates a magnetic field. This magnetic field is responsible for the angular momentum $\hat{\mathbf{L}}$ coupled to the spin momentum $\hat{\mathbf{S}}$, which can be expressed as a coupling of $\hat{\mathbf{S}}$ and \mathbf{B} : [101]

$$H'_{so} = -\frac{e}{mc} \hat{\mathbf{S}} \cdot \mathbf{B} = -\frac{e}{mc^2} \mathbf{S} \cdot (\mathbf{v} \times \mathbf{x}) \frac{1}{r} \frac{d\phi}{dr} \quad (2.33)$$

$$= -\frac{e}{mc^2} \hat{\mathbf{S}} \cdot \hat{\mathbf{L}} \frac{1}{r} \frac{d\phi}{dr} \quad (2.34)$$

For a hydrogen-like atom, the electric potential ϕ varies as $Ze^2/(4\pi\epsilon_0 r)$, which then gives the expected Z -dependence of Z^4 . Under this condition, the spin and angular momenta are expected to be coupled to each other, thus giving the name spin-orbit coupling. Here the quantum number $\mathbf{J} = \mathbf{L} + \mathbf{S}$ decides the energy, which results in an energy splitting between states of same l . However, this term by definition vanishes with $l = 0$; other higher l -states such as p , d , and f are significantly affected by this, resulting in a ‘fine structure’. For heavy atoms, relativistic SOC often significantly influences the electronic structure and subsequently their properties. However, treatment of this requires an explicit SOC Hamiltonian 2.34 which is computationally demanding; this treatment gives the ‘fully relativistic’ solution.

2.2.4 The Zeroth-Order Regular Approximation

As seen from the derivation, validity of the mass-velocity term (Equation 2.28) entirely relies on the approximation 2.26 holding true. It was, however, not explicitly justified why the condition $(p/m_0c) \ll 1$ should hold true, or even whether it does. Indeed, it was first pointed out by Farazdel and Smith [102] that this condition may not hold true in presence of a strong Coulomb potential $V \propto -Ze/r$ in the vicinity of the nucleus, as the kinetic energy E_k and subsequently momentum p will increase as far as the relativistic limit permits. Whereas this normally has a small effect for valence properties such as bonding, it is largely problematic for computing core properties such as chemical shielding and EFG tensors: the ‘perturbation’

applied by the mass-velocity term \hat{H}'_{mv} may not be a small one. Subsequently, the computed core states will be unreliable and so are the properties that rely on them.[103]

In this regard, a slightly better approximation to Equation 2.24 could be found by a different kind of expansion:[104, 105]

$$E_R = \sqrt{m_0^2 c^4 + p^2 c^2} - m_0 c^2 + V \quad (2.35)$$

$$= \frac{p^2 c^2}{m_0 c^2 + \sqrt{m_0^2 c^4 + p^2 c^2}} + V \quad (2.36)$$

$$= \frac{p^2 c^2}{(2m_0 c^2 - V) \left(1 + \frac{E_R}{2m_0 c^2 - V}\right)} + V \quad (2.37)$$

$$= \frac{p^2 c^2}{(2m_0 c^2 - V) \left(1 + \frac{E_R}{2m_0 c^2 - V}\right)^{-1}} + V \quad (2.38)$$

$$\approx \frac{p^2 c^2}{2m_0 c^2 - V} + V \quad (2.39)$$

where the last approximation have used a *zeroth-order* expansion in $E_R/(2m_0 c^2 - V)$ term. Under most chemical conditions, $E \ll m_0 c^2$ (orbital energies are hundreds of eV compared to rest mass energy 0.511 MeV); so this approximation is physically justified, unlike the $(p/m_0 c) \ll 1$ used in the derivation for the mass-velocity term. This method is hence called the Zeroth-Order Regular Approximation (ZORA) as the correction is ‘regular’ even for the states close to the nucleus. The corresponding ZORA Hamiltonian can be thus written as[106]

$$\hat{H}_{ZORA} = \frac{\hat{\mathbf{p}}^2 c^2}{(2c^2 - V)} + \frac{c^2}{(2c^2 - V)^2} \hat{\mathbf{S}} \cdot \nabla V \times \hat{\mathbf{p}} \quad (2.40)$$

where the scalar relativistic and the SOC terms are both included. This scalar relativistic version of ZORA was first used to calculate the chemical shielding in ^{77}Se and ^{125}Te -containing systems;[107] since then, it has been applied on various systems containing heavy atoms such as ^{127}I and ^{209}Bi . [108, 109]

2.2.5 Handling of Relativistic Corrections: VASP *versus* CASTEP

At this point, a brief comparison between the two plane-wave codes used in this study, VASP and CASTEP, is needed. While both codes utilise pseudopotentials to treat the core electrons, VASP is provided with pre-generated pseudopotentials by the developers, which accounts for the scalar relativistic mass-velocity and Darwin terms (Equations 2.28 and 2.31).[110, 111]

CASTEP, on the other hand, gives an option for the on-the-fly generation of pseudopotentials, with different Hamiltonians available for the reference atomic calculations: Schrödinger, Koelling-Harmon, or ZORA (only scalar relativistic). Such flexibility in pseudopotential generation is not available in VASP; hence both CASTEP and VASP are tried for the electronic structure calculations, especially to evaluate the effects of the relativistic corrections. Both codes do not include spin-orbit coupling by default: this interaction needs to be switched on in each code.

2.3 Transition State Searching: The HEF Method

2.3.1 Transition States: Definition and the Motivation for Searching Them

A chemical reaction, whether it being an actual transformation or simply an ion hopping inside a lattice, can be represented by a $3N$ -dimensional potential energy space (PES) where the 3-dimensional coordinates of N atoms can change freely. Obviously, some of the atomic arrangements are bound to be more stable than others, thus creating energy minima; multiple local minima can be present alongside the one global minimum. For a single Mg atom moving through an empty Mg sublattice in intercalation-type electrodes, for instance, all the available Mg positions represent a possible local minimum, with the corresponding transition pathways connecting these local minima.

For most of the time, the system sits in one of its minima since it is kept inside a stable potential well. However, extra energies made available to the system (by means of thermal energy or external potential, such as charging a cathode) can drive the system to walk an uphill path in energy and ultimately make transformations happen from one state to another. This pathway could be illustrated mathematically as a saddle point (Figure 2.2) connecting the two minima, as the system must follow a path along an energy minimum perpendicular to the reaction vector but ultimately go through an energy maximum (the energy barrier), commonly referred to as the transition state (TS). Locating the transition state in any reaction is important for (a) understanding the mechanism of reactions, as the local structure of TS can give hints on why this particular path is chosen; and (b) calculation of activation barriers in the reaction under concern, which is a key factor in determining the reaction rate.

Despite the importances, finding the TS in any reaction is known to be difficult since there is no *a priori* knowledge of the $3N$ -dimensional energy landscape available to the system. Since we already have a good knowledge of at least one local minimum involved in

the reaction (again, stable Mg lattice positions for example) but not necessarily the pathway connecting it to the another nearby local minimum, locating the TS and its energy then reduces to a problem of finding the TS starting from a nearby energy minimum, down the saddle point. Once the TS has been identified, both local minima could simply be identified by walking the positive and negative downhills along the reaction path. Hence this problem is called a ‘single-ended’ transition state searching, since both the endpoints are not fixed; alternatively, one can look for the TS and the related pathway with fixing the both minima, which is called a ‘double-ended’ TS searching. The idea of hybrid eigenvector-following approach discussed here is a single-ended method; other popular techniques such as a nudged elastic band (NEB) method are typically double-ended.[112]

2.3.2 The Hybrid Eigenvector-following Method

As discussed above, the problem of finding the TS starting from a local minimum requires essentially finding an uphill path to the saddle point in one degree of freedom (maximising the energy) while keeping the minimum energy in all other degrees of freedom. To achieve this, knowledge of the full Hessian at any given point on the PES is typically required, as it gives information on the local curvature around that point. However, the computational cost associated with this approach when combined with *ab initio* methods is prohibitively expensive; thus a different approach needs to be developed.

The method of hybrid eigenvector-following (HEF) TS search[113, 114] circumvents this problem by exploiting the fact that one can often approximate the local PES to be quadratic in nature, thus requiring only the first- and second-order derivatives. Then a variational approach is taken to obtain the minimum eigenvalue of Hessian \mathbf{H} without calculating the full \mathbf{H} and subsequently the reaction vector.

To see how this could work, let us assume an arbitrary reaction vector \mathbf{y} at nuclear coordinates \mathbf{x}_0 on the PES. We can define the Rayleigh-Ritz ratio, or the ‘expectation value’ for the eigenvalue λ corresponding to \mathbf{y} as

$$\lambda(\mathbf{y}) = \frac{\mathbf{y}^T \mathbf{H} \mathbf{y}}{\mathbf{y}^T \mathbf{y}} \quad (2.41)$$

where \mathbf{y}^T refers to the transpose of \mathbf{y} . Minimising this ratio variationally to find a negative value of λ equals finding the uphill path on the PES to yield the initial search direction. Since calculation of the full Hessian is undesirable on an *ab initio* level, a quadratic approximation

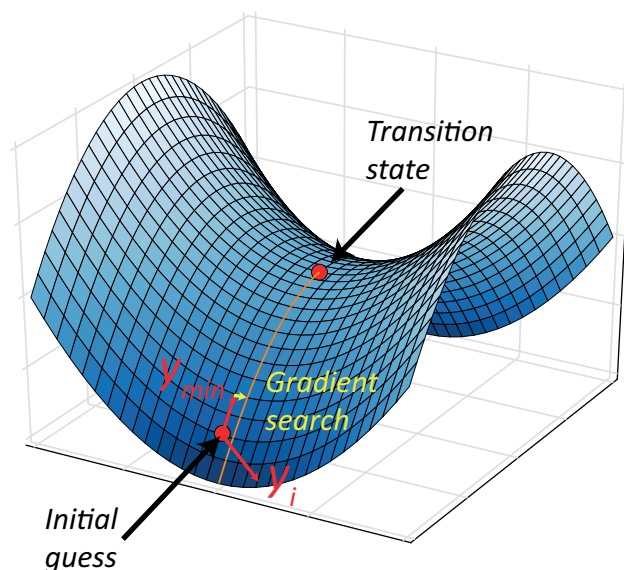


Fig. 2.2 Schematic illustration of the HEF method for TS searching. Detailed explanations are presented in the main text. Saddle point figure was adopted from Wikipedia under a CC-BY 3.0 license.

to the local PES is applied to compute this expectation value:

$$\lambda(\mathbf{y}) \approx \frac{E(\mathbf{x}_0 + \xi \mathbf{y}) + E(\mathbf{x}_0 - \xi \mathbf{y}) - 2E(\mathbf{x}_0)}{(\xi \mathbf{y})^2} \quad (2.42)$$

where $E(\mathbf{x}_0)$ is the energy corresponding to \mathbf{x}_0 and $\xi \ll 1$. Then a conjugate gradient minimisation could be performed using a numerical derivative as defined below:

$$\frac{\partial \lambda}{\partial \mathbf{y}} = \frac{\nabla E(\mathbf{x}_0 + \xi \mathbf{y}) - \nabla E(\mathbf{x}_0 - \xi \mathbf{y})}{\xi} \quad (2.43)$$

The result of this is the smallest eigenvalue λ and the corresponding eigenvector \mathbf{y} at \mathbf{x}_0 . This gives the uphill path on the point \mathbf{x}_0 ; once a step in this direction is taken, the system is then minimised along the tangential direction using a gradient-based algorithm to find the reaction path. This process, illustrated schematically in Figure 2.2, is repeated until the gradient and the path both converge under a given limit, and the TS and reaction vector are found as \mathbf{x}_0 and \mathbf{y} .

2.4 Nuclear Magnetic Resonance

The macroscopic properties and the physico-chemical behaviour of any material is closely related to its microscopic structure at the atomic level. This requires understanding of the *local* structures around the atom of interest, which can often be different from the long-range ordered structure commonly probed by diffraction techniques. Local disorder, arising from many different origins such as stacking faults, point defects, and ionic motions, to name a few, significantly influences the battery performance; hence, experimental techniques to look at atomic structures on a local level are valuable.

Nuclear Magnetic Resonance (NMR) is a very powerful technique to look at such local structures. As we will see in the following sections, the physical origin of the various NMR-related interactions make it suitable for observing the structure and dynamics of ions at a local level, which is often difficult by conventional diffraction methods. Here we briefly present the physical basis of NMR experiments, followed by more specific pulse sequences utilised in this study.

2.4.1 Physical Basis of NMR Interactions

Here we briefly discuss the physical basis of relevant NMR interactions. Electron-nuclear interactions are discussed in a separate section (Section 2.5) alongside the electron magnetism.

The Zeeman interaction

Nuclei possessing spin \mathbf{I} can interact with an external static magnetic field \mathbf{B}_0 pointing along the z -direction, resulting in the nuclear Zeeman interaction. Classically this can be thought of as a spin magnetic moment precessing around the \mathbf{B}_0 direction with the Larmor frequency $\nu_0 = \omega_0/2\pi = -\gamma B_0/2\pi$. The relevant nuclear Zeeman Hamiltonian for this interaction can be expressed as[115]

$$\hat{H}_0 = -\gamma\hbar B_0 \hat{I}_z = h\nu_0 \hat{I}_z \quad (2.44)$$

where γ is the gyromagnetic ratio of the nucleus (in $\text{rad s}^{-1} \text{T}^{-1}$). For a system of spin-1/2 nuclei, this gives only two possible quantisation of the spins: $|+1/2\rangle$ or $|-1/2\rangle$ (relative to the \mathbf{B}_0 field), with an energy separation $\Delta E = h\nu_0$. Under a thermal equilibrium, the spins inside any sample on average occupy the two states according to the Boltzmann distribution, which results in a net magnetisation along the z -direction.

Upon application of a radiofrequency (rf) pulse of amplitude $\nu_1 = \omega_1/2\pi = \gamma B_1/2\pi$ on the xy -plane which resonates with ΔE , the system can undergo a time-dependent deviation

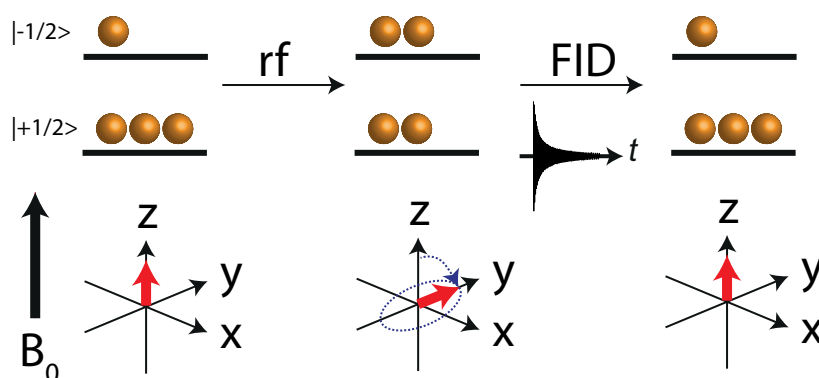


Fig. 2.3 Schematic illustration of the pulse-acquire experiment on a 2-level system. Both spin state and vector formalisms are shown.

from the equilibrium, which is expressed as a superposition/linear combination of the two allowed states $|\pm 1/2\rangle$. This results in a nonequilibrium state which evolves during the length of rf pulse. If the pulse length t_p is such that $\omega_1 t_p = \pi/2$, the two states are equally populated after the pulse; thus this represents a 90° pulse from the vector model of NMR. Analogously, a pulse with a length of $2 \times t_p$ results in a population inversion between the $|\pm 1/2\rangle$ levels. Thus, the spins undergo a forced oscillation from the \mathbf{B}_1 field, a phenomenon observed in nutation experiments.

After the application of a pulse to perturb the population difference, the system relaxes back to its equilibrium *via* a nutational motion along the field axis. This process involves a dissipation of the energy difference as electromagnetic radiation (for the \mathbf{B}_0 fields pertinent to NMR spectroscopy, in the rf-region) of the same frequency ν_0 , convoluted with a decay function. This time-domain free-induction decay (FID) signal is recorded and Fourier transformed to yield a frequency-domain spectrum, which shows the dispersion of signals with respect to their frequencies. This forms the basis of a simple pulse-acquire (zg) experiment in NMR spectroscopy, which is illustrated schematically in Figure 2.3.

Chemical shielding interaction

The Zeeman interaction above tells us that each isotope should exhibit a distinct Larmor frequency ν_0 in the presence of a field. Were this the only interaction, NMR could only be used to differentiate between different isotopes which resonate at characteristic frequencies; in order to gain insights on the different local arrangements of the same nucleus, a mechanism which gives dispersion according to the local electronic arrangements is needed. The chemical

shielding interaction, which is present in all systems (paramagnetic or diamagnetic) is the first important interaction relevant to gaining chemical insights from NMR.

When placed under an external field \mathbf{B}_0 , diamagnetic, or spin-paired, electrons by definition generates a local magnetic field which opposes the applied field.* This means that the effective field \mathbf{B}_{loc} at the nuclear position becomes marginally different from the applied field. This in effect changes the Larmor frequency of the nucleus, where an increased electron density should result in an enhanced ‘shielding’ of the nuclear spin from \mathbf{B}_0 , and subsequently a reduction in the effective Larmor frequency. This mechanism is commonly called the ‘chemical shielding’ interaction, and is the dominant mechanism for the NMR shifts for diamagnetic systems.

The local field could be expressed in terms of the shielding tensor σ as:

$$\mathbf{B}_{\text{loc}} = \sigma \cdot \mathbf{B}_0 \quad (2.45)$$

which includes the effect of the local magnetic fields produced by electrons in the applied field. Hence, the chemical shielding Hamiltonian can be written as

$$\hat{H}_{\text{CS}} = -\gamma \hbar \hat{\mathbf{I}} \cdot \sigma \cdot \mathbf{B}_0 \quad (2.46)$$

The chemical shielding tensor can be separated into the symmetric and antisymmetric components, and the symmetric part of the tensor is transformed into the principal axis frame (PAF) where σ is diagonal to obtain the anisotropy parameters.[116] However, in NMR experiments, the formalism of chemical shielding is inconvenient since it is referenced to a fictitious nucleus of zero electron density (*i.e.* completely deshielded). Moreover, the full shielding tensor components are difficult to obtain (unless a single crystal experiment with goniometer is performed) and only the principal values could be measured; hence the more convenient formalism of chemical shift is used, where the values of the shift tensor are referenced to the isotropic shielding of a reference compound σ_{ref} :[117]

$$\delta_{ii} = \frac{\sigma_{\text{ref}} - \sigma_{ii}}{1 - \sigma_{ii}} \quad (2.47)$$

*For elements heavier than ^1H , the ‘paramagnetic’ contribution to the chemical shielding is also significant; this arises from the electron excitation from the ground state into the high-lying orbitals. This contribution often has the same sign as the diamagnetic term.

Under this formalism, we have a sequence of the principal values as $\delta_{11} \geq \delta_{22} \geq \delta_{33}$; the anisotropy of chemical shielding can now be represented as[118]

$$\delta_{\text{iso}} = \frac{\delta_{11} + \delta_{22} + \delta_{33}}{3} \quad (2.48)$$

$$\Omega = \delta_{11} - \delta_{33} \quad (2.49)$$

$$\kappa = \frac{3(\delta_{22} - \delta_{\text{iso}})}{\Omega} \quad (2.50)$$

in the Herzfeld-Berger convention. δ_{iso} gives the isotropic chemical shielding, Ω gives the span of anisotropy ($\Omega \geq 0$), and κ gives the skewness (*i.e.* axial symmetry; $-1 \leq \kappa \leq +1$). Axially symmetric shift tensor gives either $\kappa = \pm 1$ depending on the value of δ_{22} relative to δ_{iso} . The anisotropy can also be expressed in the more common Haeberlen convention, which orders the principal values by their separation from δ_{iso} : $|\delta_{zz} - \delta_{\text{iso}}| \geq |\delta_{xx} - \delta_{\text{iso}}| \geq |\delta_{yy} - \delta_{\text{iso}}|$. Using this convention, the anisotropies can be represented as[119]

$$\delta_{\text{iso}} = \frac{\delta_{xx} + \delta_{yy} + \delta_{zz}}{3} \quad (2.51)$$

$$\Delta = \delta_{zz} - \delta_{\text{iso}} \quad (2.52)$$

$$\eta = \frac{(\delta_{yy} - \delta_{xx})}{\Delta} \quad (2.53)$$

which is often more convenient for calculating the tensor components under spinning.

Quadrupolar interaction

Non spin-1/2 nuclei possess nonspherical nuclear charge distributions. Such quadrupolar nuclei can interact with the traceless electric field gradient (EFG) tensor \mathbf{V} at the nuclear position according to

$$\hat{H}_Q = \frac{eQ}{6hI(2I-1)} \hat{\mathbf{I}} \cdot \mathbf{V} \cdot \hat{\mathbf{I}} \quad (2.54)$$

where Q is the nuclear quadrupole moment and e is the unit charge. In the PAF where \mathbf{V} is diagonal, it is conventional to define η_Q , the EFG asymmetry parameter in the PAF and C_Q ,

the quadrupole coupling constant (usually defined in Hz).[117]

$$eq = V_{zz} \quad (2.55)$$

$$\eta_Q = \frac{V_{xx} - V_{yy}}{V_{zz}} \quad (2.56)$$

$$C_Q = \frac{e^2 q Q}{h} \quad (2.57)$$

From the structural point of view, C_Q is a parameter which gives the degree of non-spherical electron distribution; a large C_Q represents a highly non-spherical distribution. η , on the other hand, represents the degree of axial symmetry present in the electron distribution. For instance, a perfectly octahedral/tetrahedral environment should give a vanishing C_Q and η . Typical observed values of C_Q for ^{25}Mg lie between hundreds of kHz and several MHz.

When purely quadrupolar transitions are considered, *e.g.* in a nuclear quadrupole resonance experiment in absence of any external field, this treatment of quadrupolar coupling is sufficient on its own. In NMR experiments, however, usually the nuclear Zeeman interaction is the dominant interaction and we must treat the quadrupole as a perturbation to the nuclear Zeeman Hamiltonian (Equation 2.44). Usually a perturbation treatment up to second order is sufficient; however, in nuclei with large quadrupole moment Q such as $^{185/187}\text{Re}$, higher order effects are observed[120] and a solution considering the combined Zeeman and quadrupolar Hamiltonian by means of numerical techniques is necessary.[121] Here, the experiment is conducted in the laboratory frame and the sample is placed inside a static field \mathbf{B}_0 . This means that we need to consider the relative orientation between the \mathbf{B}_0 field direction and the anisotropy tensor of interest. As the field is axially symmetric, only two angles are necessary to express this orientation: the resonance frequency can be parametrised as $\nu(\theta, \phi)$.

We now define the quadrupolar frequency ν_Q and the orientation-dependent quadrupolar frequency ν'_Q :

$$\nu_Q = \frac{3C_Q}{2I(2I-1)} \quad (2.58)$$

$$\nu'_Q = \nu_Q \left(\frac{3 \cos^2 \theta - 1}{2} + \frac{\eta_Q}{2} \sin^2 \theta \cos 2\phi \right) \quad (2.59)$$

Applying the quadrupolar Hamiltonian as a perturbation to the dominant Zeeman interaction gives the first- and second-order energy changes to the transition frequencies $\nu_{m,m+1}$ from $m+1 \rightarrow m$:

$$\nu_{m,m+1}^{(1)} - \nu_0 = \nu'_Q \left(m + \frac{1}{2} \right) \quad (2.60)$$

$$\nu_{m,m+1}^{(2)} - \nu_0 = -\frac{\nu_Q^2}{18\nu_0} \{ [24m(m+1) - 4I(I+1) + 9] V_{+1}V_{-1} + [6m(m+1) - 2I(I+1) + 3] V_{+2}V_{-2} \} \quad (2.61)$$

where V are expressed in terms of spherical tensors (in the laboratory frame)[122]

$$V_{\pm 1} = \mp(V_{zx} \pm iV_{zy}) \quad (2.62)$$

$$V_{\pm 2} = \frac{1}{2}(V_{xx} - V_{yy} \pm iV_{xy}) \quad (2.63)$$

The resulting first- and second-order energy shifts are complex, and are described for the $I = 5/2$ systems in Figure 2.4 for an oriented single crystal ($\theta = 0$ and $\eta_Q = 0$ for illustration). A few insights from the first- and second-order energy corrections are discussed below:

- The central transition (CT; $m = -1/2$ to $+1/2$) frequency for any half-integer I is not affected by the first-order quadrupolar coupling (Figure 2.4).
- The second-order energy correction varies as $1/\nu_0$, meaning that the second order quadrupolar effect is reduced as the magnetic field gets stronger.
- There exists an isotropic term in the second-order energy correction, meaning that the observed shift is the sum of chemical and quadrupolar shifts, even under MAS (Section 2.4.2). Because of this, methods such as lineshape fitting or more advanced pulse sequences are necessary to extract the isotropic chemical shift.

Nutation effects for the quadrupolar interaction

We have seen in Section 2.4.1 that rf pulses with amplitudes ν_1 induce a time-dependent perturbation to the spin system, resulting in a fluctuation of the spin populations which exhibits itself as a nutation of the net magnetisation. Of course, this ‘perturbation’ needs to be small relative to the main interaction in order for this approximation to hold true. For the Zeeman interactions, this is always the case since nuclear Larmor frequencies are on the order of $\nu_0 \approx 100$ -1000 MHz whereas the available rf field is typically $\nu_1 \approx 10$ -100 kHz. Thus $\nu_1 \ll \nu_0$ and the perturbative approach is justified.

For quadrupolar interactions, however, this is not always the case: for ^{25}Mg which has a C_Q range of 1-10 MHz, the quadrupolar frequency $\nu_Q = 0$ -1.5 MHz. Unlike the Zeeman

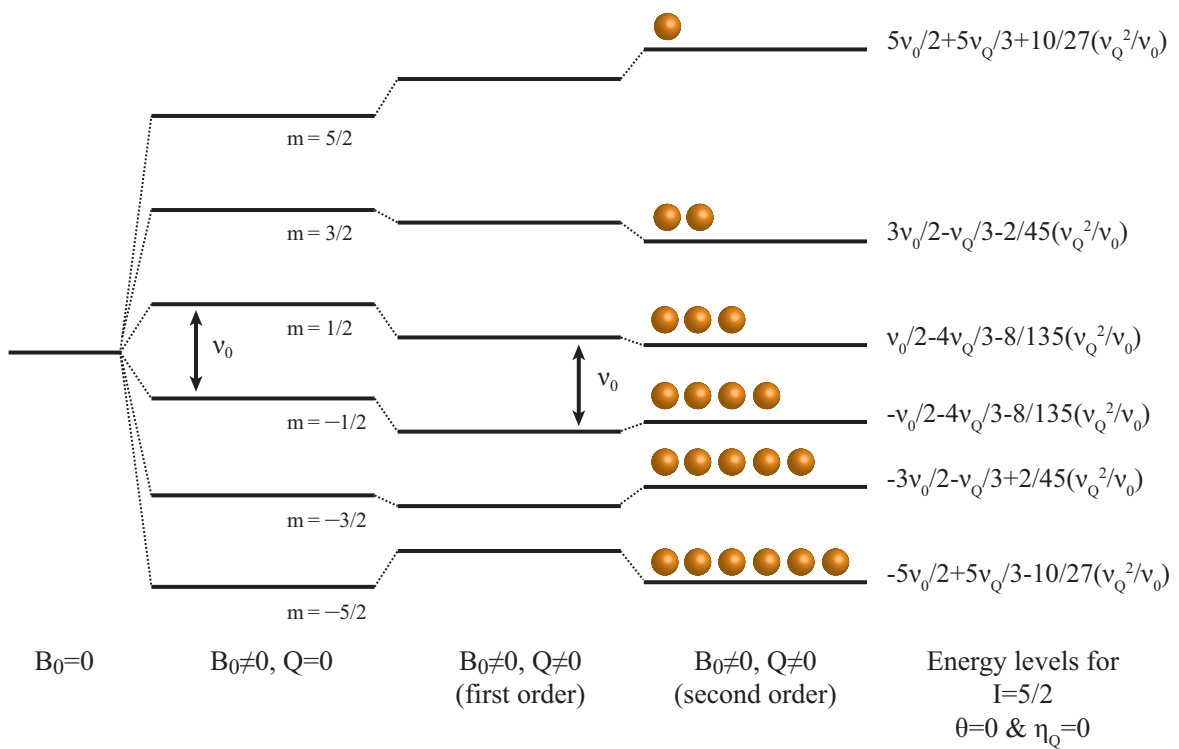


Fig. 2.4 Schematic energy levels (not drawn to scale) in the presence of quadrupolar coupling, illustrated for $\gamma < 0$ and $I = 5/2$ (the case for ^{25}Mg).

interaction, the magnitude of this interaction could be comparable to the available ν_1 field. Two extremes could then be identified:[123]

- $\nu_Q \ll \nu_1$ (small C_Q), where the pulse is strong enough to excite the whole spectrum evenly. In such cases, the pulse is said to be ‘hard’, *i.e.* it excites the CT and STs nonselectively. The system behaves in the limit of no quadrupolar interaction with the same nutation behaviour.
- $\nu_Q \gg \nu_1$ (large C_Q), where the pulse on resonance with the CT is unable to excite the whole transition uniformly. Here, it is observed that the CT nutates faster than the nonquadrupolar case by a factor of $I + 1/2$. Selective excitation of the CT is possible by means of a low-power pulse. The pulse in this case is said to be ‘soft’.

2.4.2 Solid-state NMR and Magic Angle Spinning

MAS for averaging anisotropic interactions in solids

In solution state NMR, rapid isotropic tumbling of molecules inside the liquid faster than the NMR timescale, results an averaging of all anisotropic interactions (chemical shift, dipolar, and quadrupolar); only scalar (J -)coupling and the isotropic shift (δ_{iso}) are observed in such cases. In solid-state NMR, however, the system is stationary (in the absence of atomic motion) on the NMR timescale. This means that the anisotropy averaged out in the solution-state remains present.

Recall in Section 2.4.1 that we can represent the orientation of any anisotropic tensor in a static field with two polar angles (θ, ϕ). In well-ground powder samples, all possible combination of the angles (θ, ϕ) are randomly present; spectra in such cases exhibit a ‘static’ powder pattern which is a superposition of the individual resonances for each crystallite in the system. Such spectra are influenced by any anisotropic interactions present in the system (chemical shift, dipolar, and quadrupolar). Typically, this is undesirable since the resulting broad spectra give poor resolution and sensitivity.

A solution to rectify this problem is to exploit the fact that the applied field is axially symmetric; under rapid averaging about an the axis at an angle β to \mathbf{B}_0 , the anisotropic component of any perturbation depends on the n -th order Legendre polynomials $P_n(\cos \beta)$:[124]

$$P_0(\cos \beta) = 1 \quad (2.64)$$

$$P_2(\cos \beta) = (3 \cos^2 \beta - 1) \quad (2.65)$$

$$P_4(\cos \beta) = (35 \cos^4 \beta - 30 \cos^2 \beta + 3) \quad (2.66)$$

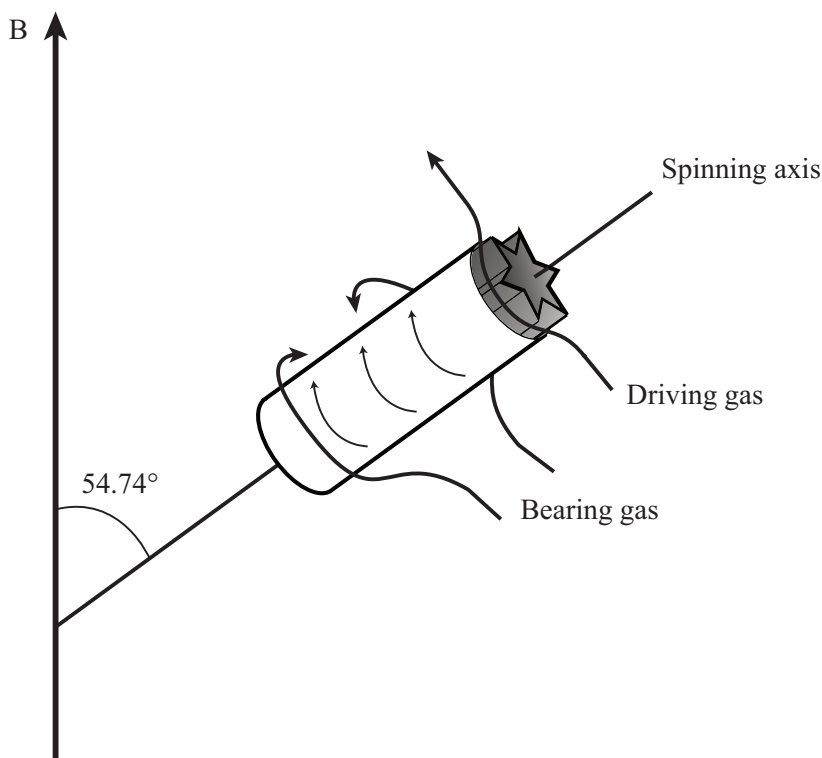


Fig. 2.5 Schematic illustration of MAS experiments.

For the chemical shift and dipolar coupling Hamiltonians, a first-order perturbation suffices as their magnitudes are small compared to the Zeeman Hamiltonian. This means that the anisotropic interaction depends solely on the second-order Legendre polynomial $P_2(\cos \beta)$. Therefore, a choice of the angle β which removes this term should result in effective averaging of the shift anisotropy. Such an angle $\beta = \arccos(\sqrt{1/3}) = 54.74^\circ$ to the B_0 axis is called the ‘magic angle’; [125] rapid sample rotation about this axis removes the anisotropy for a first order interaction. Mechanically, this is achieved by two types of gases: the ‘bearing’ gas keeps the rotor afloat and the ‘drive’ gas rotates the turbine fins on the rotor. This technique of Magic Angle Spinning (MAS) is essential to solid-state NMR spectroscopy to obtain high-resolution spectra.

Typically, spinning frequencies ν_r on the order of 4 times the magnitude of the anisotropic interaction is needed for complete averaging. [126] This represents different requirements for ν_r depending on the sample. For instance, ^{13}C typically has $\Omega \simeq 200$ ppm (35 kHz at 16.4 T), whereas typical MAS rotors are capable of 5-60 kHz spinning depending on the size; incomplete averaging of the anisotropic chemical shift interaction under slow MAS results in spinning ‘sidebands’ which occur at multiples of ν_r from the centreband. The envelope of these sidebands follow that of the original anisotropic interaction, from which

the anisotropic tensor components can be extracted to give extra information on the local structure and dynamics.

The case of quadrupolar interactions: incomplete averaging by MAS

The case is more complicated for the quadrupolar coupling Hamiltonian \hat{H}_Q , as both the first- and second-order perturbations need to be taken into account. The first-order perturbation, as in the case of chemical shift, has a $P_2(\cos\beta)$ -dependence and is averaged out by sufficiently fast MAS. Of course this is irrelevant to the CT as we have seen that the CT frequency is not affected by quadrupolar coupling to first order; however, the STs undergo a significant line-narrowing under MAS as the first-order broadening is now removed.

On the other hand, the second-order perturbation depends on both $P_2(\cos\beta)$ and $P_4(\cos\beta)$, and the latter is incompletely averaged by MAS. This results in a second-order quadrupolar interaction which gives rise to an isotropic shift according to the following equation:

$$\delta_Q = -\frac{\nu_Q^2}{30\nu_0} \left[I(I+1) - \frac{3}{4} \right] \left(1 + \frac{\eta_Q^2}{3} \right) \quad (2.67)$$

However, it needs to be stressed that MAS is still beneficial in this case as the P_2 term is still removed from the second-order perturbation; nonetheless, suppression of this second-order effect has been an active area of research in solid-state NMR:

- As the second-order Hamiltonian depends on $1/\nu_0$ (Equation 2.62), higher magnetic fields can be used to suppress this second-order broadening. This is the most obvious and straightforward method to obtain high-resolution spectra; however, design and construction of strong superconducting magnet >20 T is very challenging. Higher fields have been achieved by means of superconducting-resistive hybrid magnets (40 T), [127] or pulsed magnets (>100 T). [128]
- Examination of P_4 reveals that two solutions are possible at $\beta_1 = 30.56^\circ$ and $\beta_2 = 70.12^\circ$. Thus, spinning at either of the angles can remove this second-order interaction. Technologically this is achieved by two ways: Double-rotation (DOR) or Dynamic-Angle Spinning (DAS). [129, 130] Both require specialised probes which can either spin rotors at two different angles (DOR) or change the spinning axis while keeping the sample rotating (DAS).
- As the above two methods require specialised hardware, pulse sequences that attempt to correlate the other quadrupolar transitions to the CT under MAS have been developed.

Two such examples are Multiple-Quantum Magic Angle Spinning (MQMAS), which correlates the multiple-quantum transition to the CT, and Satellite-Transition Magic Angle Spinning (STMAS), which correlates the satellite transitions to the CT.[131, 132] Despite the fact that both the CT and the ST are broadened by the second-order effect, the STs have a lineshape that is narrowed by a constant factor compared to the CT. Hence, the correlation between the CT and the ST could be determined by a 2-dimensional experiment, where the narrower STs can be correlated to the broad CTs. However, MQMAS requires a rather strong rf pulse for effective excitations of the MQ coherence; STMAS requires a very stringent setting of the magic angle.

2.4.3 Pulse Sequences

The pulse-acquire experiment introduced in Section 2.4.1 forms the basis of all NMR pulse sequences. The idea of manipulating spin populations by means of rf pulses has led to the application of a sequence of rf pulses to achieve a particular aim (*e.g.* enhanced resolution, sensitivity...). In this regard, four types of pulse sequences were used in this work:

Hahn-echo

While the pulse-acquire experiment gives in general the best sensitivity for 1-dimensional spectra, it suffers from a practical problem: the FID acquisition cannot start immediately after the initial $\pi/2$ -pulse due to probe ringdown and delays in transmitter gating. Typically, delays of several μs are inserted to allow the pulse to decay leading to a loss in intensity; even so the residual ringdown may still be present in the FID resulting in a rolling background and difficulty in phasing the spectra. The Hahn-echo[133] experiment (Figure 2.6a) uses a π -pulse as the refocusing pulse after the initial $\pi/2$ -pulse in a $\pi/2 - \tau - \pi - \tau$ sequence. FID acquisition starts immediately after the second τ delay in the half-echo acquisition; alternatively, the full echo can also be acquired. In solid-state MAS NMR, the delay τ is typically rotor synchronised to an integer multiple of the rotor period t_r .

The working principle of Hahn-echo experiments is best illustrated with the vector model following the scenario in Section 2.4.1. After the initial $\pi/2$ -pulse which rotates the net magnetisation to the xy -plane, the magnetisation vectors undergo a dephasing about the field axis with different offsets in the Larmor frequency (arising from various isotropic and anisotropic interactions present). After a fixed delay τ , a π -pulse is then applied; this results in magnetisation being refocused at the end of the second τ delay irrespective of the offset frequency. The system is now in the exact same condition as following a simple $\pi/2$ -pulse

minus any T_1 and T_2 -relaxations that have occurred during 2τ . Acquisition of the FID can then start at the echo top.

This technique of spin-echo is indispensable for low- γ ^{25}Mg NMR, since the issues with probe ringing and background at this low frequency (42.8 MHz at 16.4 T) could largely be removed with spin-echo experiments.

Rotor Assisted Population Transfer

In this section and the following, CT signal enhancement techniques in quadrupolar NMR are briefly discussed; for more detailed discussion the reader is referred to a recent review paper.[134]

The RAPT pulse sequence (Figure 2.6b)[135] allows enhancements of the CT signal for quadrupolar nuclei. The idea behind this pulse sequence is that under thermal equilibrium, the spin levels arising due to quadrupolar interactions (Figure 2.4) are populated according to the Boltzmann distribution, but the STs are not usually observed (unless we are specifically probing them, as in STMAS experiments). Hence, irradiation of the spins with rf pulses that can saturate, or invert, these satellite levels can result in a larger population difference for the CT.

To understand how this is feasible, let us look at the case of a single crystal in a \mathbf{B}_0 field. As the EFG tensor in single crystals can only have one possible orientation with respect to this field, the transition frequencies determined by Equations 2.60 and 2.62 are fixed at multiples of ν_Q (illustrated in Figure 2.4). Hence, the STs could be saturated by a train of rf pulses at the offset frequencies equal to the STs, thus allowing an enhanced population difference for the CTs. Maximum CT enhancements of up to $I + 1/2$ could be achieved this way.[135]

However, most of the solid-state samples of interest are in powder forms, thus having all possible EFG orientations. This means that a dispersion of the resonances is present and rf pulses at a fixed offset are not able to uniformly excite the resulting powder spectra under static conditions. However, under MAS the individual ST isochromats are modulated in frequencies by the rotational motion of the sample; thus the ST frequencies can effectively ‘sweep’ through a fixed offset multiple times. From Equations 2.58 and 2.59, we can see that the outermost ‘edge’ of any given (static) ST powder pattern should occur at $\pm\nu_{\text{edge}}$ away from the centreband:

$$\nu_{\text{edge}} = \nu_Q = \frac{3C_Q}{2I(2I-1)} \quad (2.68)$$

and an excitation with a frequency of ν_{\max} , which is roughly half of ν_{edge} , is expected to give a maximum saturation of the STs:

$$\nu_{\max} = \frac{\nu_Q}{2} = \frac{3C_Q}{4I(2I-1)} \quad (2.69)$$

which was first experimentally demonstrated by Yao *et al.*[135] The first generation of the RAPT pulse sequence used in their study employed a train of fast amplitude modulated (FAM) pulses alternating in phase $X-\bar{X}$, which were applied at the same offset as the CT frequency. Manipulation of the satellite level populations was achieved by tuning the pulse lengths t_p which results in an effective RAPT modulation frequency $\nu_m = 1/2t_p$. In the Fourier transformed frequency dimension, this equals harmonics in odd multiples of ν_m ; these harmonics can then be used to selectively saturate the satellite populations by setting $\nu_m = \nu_{\max}$. It was successfully demonstrated that under sufficiently slow MAS and with a large number of pulses, this ST saturation could yield enhancements in the CT population differences, yet still short of the expected maximum; for instance, an enhancement factor of 2 was reported for the ^{27}Al ($I = 5/2$) spectrum in diamagnetic polycrystalline albite $\text{NaAlSi}_3\text{O}_8$. [135, 136]

While the RAPT pulse sequence can be used to enhance the CT sensitivity, another interesting application of the RAPT pulse sequence is measurement of the quadrupolar coupling parameters C_Q and η_Q . [137] By varying ν_m , an enhancement profile can be generated which exhibits a maximum when ν_Q matches ν_{\max} . Since the first-order quadrupolar lineshapes of the STs have widths that only depend on the C_Q and not on η , the enhancement returns to unity at ν_{edge} . Additionally, the enhancement edges can be used to find out qualitative information on η_Q as steep edges correspond to a large η_Q .

However, the range of ν_m that can be explored in this manner is principally limited by the lower limit of pulse length the spectrometer can generate (only pulses longer than 0.5-1 μs can reliably be generated from modern day spectrometers). Also, an important consideration when saturating the satellite levels is that the pulses should be selective to the STs without affecting the CT, or the generated population difference would be destroyed. In this regard, Gaussian pulses at given offsets ν_{off} could also be used for selective ST saturation; this second generation of the RAPT pulse sequence is called Frequency Switched Gaussian RAPT, or FSG-RAPT. [136, 137] As the probe bandwidth is proportional to the resonance frequency, however, the available bandwidth at ^{25}Mg frequencies is quite narrow and often large values of ν_{off} cannot be applied. This means that the enhancement maximum, rather

than the enhancement edge, is more straightforward to observe experimentally with smaller values of C_Q , which we investigate in Chapter 5 for MgV_2O_5 .

For the paramagnetic samples under consideration, fast relaxation effects by the paramagnetic electrons also need to be taken into account; as Gaussian pulses are typically longer than normal square pulses (10-20 μs versus 2-5 μs), the additional relaxation that takes place during this period is expected to make the RAPT enhancement less efficient when Gaussian pulses are used for these samples.

Double Frequency Sweep

Another way of enhancing the CT population difference is to invert the STs instead of saturating them.[138] This method is expected to yield even higher enhancements ($2I$ if all the satellite populations could be inverted), but comes at a cost of longer, more complex shaped pulses to invert the magnetisation. Normal hard pulses will saturate the STs instead of inverting them, as we have seen earlier for RAPT.

The solution is to apply a small rf field and then slowly ‘sweep’ it from off resonance to the desired transition. Under sufficiently slow sweep conditions, the magnetisation vector is in equilibrium with the applied rf field at all times (adiabaticity condition) and slowly nutate from the initial equilibrium along the $+z$ direction (off resonance), to the xy -plane (on resonance), and to the final inverted state along the $-z$ -direction (off resonance). This condition is achieved by a linear frequency sweep from both high and low frequencies towards the desired STs, hence the title Double Frequency Sweep (DFS). This typically requires a very long low-power pulse (on the order of several ms) to meet the adiabaticity condition; significant paramagnetic relaxation during the sweep period makes DFS less useful than RAPT methods, as we will see later (Chapter 3).

Quadrupolar Magic Angle Turning

The QMAT experiment by Hung and Gan[139] is designed to identify the isotropic shift from a series of spinning sidebands, as frequently seen in MAS experiments. The QMAT pulse sequence, shown in Figure 2.6c, consists of nine π -pulses where the even-numbered π -pulses remain fixed, but the odd-numbered π -pulses are delayed by incrementing t_1 . When the MAT condition is satisfied, the net evolution of the sideband modulations sums to zero and the centreband frequency (including the chemical shift and quadrupolar shift) evolves as $\nu_0 t_1$, resulting in a resonance in the F_2 dimension. This enables us to extract the isotropic shift, ν_0 .

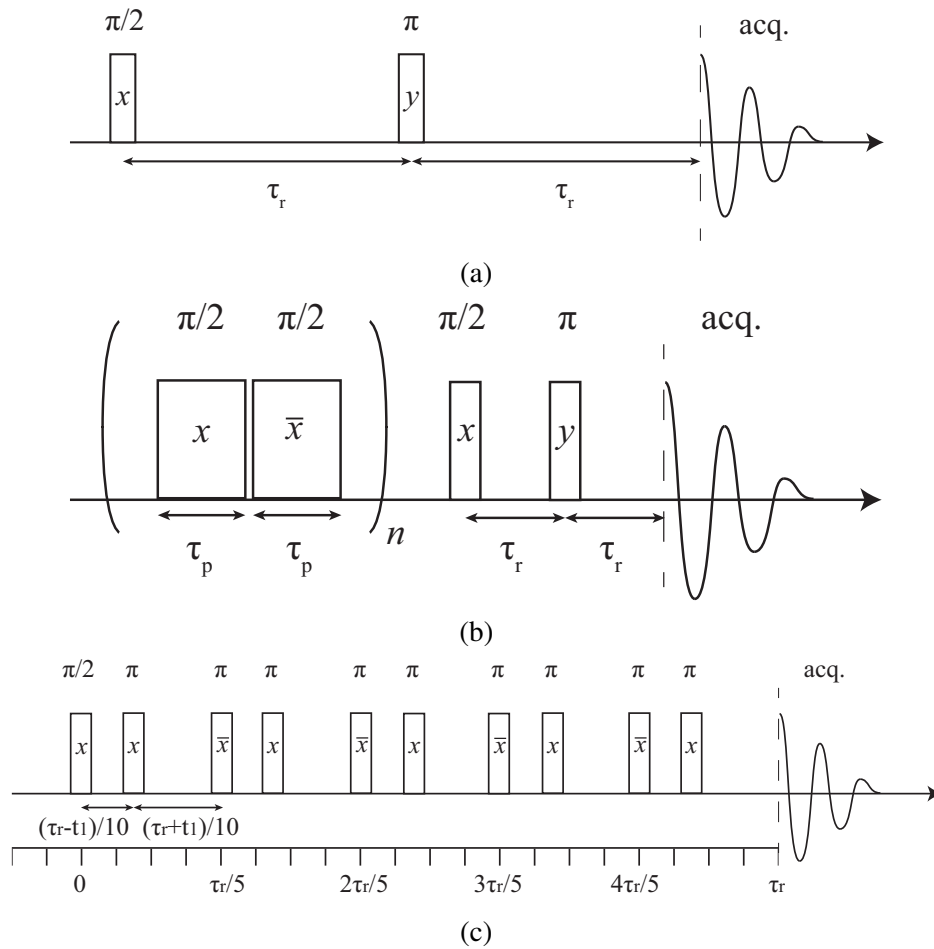


Fig. 2.6 (a) Hahn-echo pulse sequence. (b) RAPT-echo pulse sequence. (c) QMAT pulse sequence.

2.5 Magnetism and the Paramagnetic NMR Shifts

The above description of chemical shielding holds principally for diamagnetic samples, where the paired electron density near the nucleus shields the external magnetic field. In materials with localised unpaired electrons with spin S , however, the electron spin also possesses a magnetic moment[140]

$$\mu_e = -\mu_B g_e S \quad (2.70)$$

where the Bohr magneton is defined as $\mu_B = e\hbar/2m_e$ and $g_e = 2.0023$ is the free electron g -factor. Inside an applied magnetic field \mathbf{B}_0 , these $(2S + 1)$ -fold degenerate spin states split in energy by means of the electron Zeeman interaction, analogous to the nuclear spins described above:

$$E(m_s) = m_s \mu_B g_e B_0 \quad (2.71)$$

Transitions between these levels form the physical basis of Electron Paramagnetic Resonance (EPR) spectroscopy. As this electron magnetism is essential to understanding the calculations of the paramagnetic shifts central to this work, a brief discussion on the principles of electron magnetism is presented below. Using these ideas, methods to calculate the paramagnetic (Fermi-contact) NMR shifts are discussed in Section 2.5.5.

2.5.1 The Basics of Electron Magnetism

For a coupled n -electron spin system with spin quantum number S , the combined Zeeman and magnetic Hamiltonian can be expressed as

$$\hat{H} = -\sum_J \sum_{(i,j)} J s_i s_j + g_e \mu_B \sum_j B_0 s_j \quad (2.72)$$

where s_i and s_j denote the spin quantum numbers on each site. The sum over spin pairs (s_i, s_j) with magnetic interactions ($J < 0$ denotes antiferromagnetically coupled spins) is included to express the effect of coupled electron spins. The idea of Weiss to solve this equation to obtain the energy states is to approximate the effect of neighbouring spins as an effective molecular field B_{mf} , which is proportional to the expectation value of the total magnetisation $M = n g_e \mu_B \langle m_s \rangle$. [140] Solutions to this system feature several important observations under a low-field approximation (molecular fields are typically much stronger than the applied magnetic field under NMR conditions) and counting only the nearest-neighbouring interactions (z is the number of nearest neighbouring spins):

- There exists a critical temperature

$$T^* = \frac{2zS(S+1)J}{3k_B} \quad (2.73)$$

above which the system loses spontaneous ordered magnetisation; the thermal energy is large enough to arrange the electrons in a random orientation. The system is then called ‘paramagnetic’. For $J < 0$ (antiferromagnetic), this temperature is called the Néel temperature T_N .

- Above T^* , the magnetic susceptibility $\chi = M/B_0$ can be expressed as

$$\chi = \frac{C}{T - \Theta} \quad (2.74)$$

where

$$C = \frac{ng_e^2\mu_B^2S(S+1)}{3k_B} \quad (2.75)$$

is called the Curie constant, which depends on the magnitude of electronic spins present in the system (S) and Θ is the Curie-Weiss constant, which gives the strength of interaction. For frustrated magnets, typically $|T_N| \leq |\Theta|$, as it is more difficult for the spins to order themselves.

- The scaled magnetisation Φ , which gives the fraction of magnetisation M to the maximum possible saturated M_{sat} , is given as

$$\Phi = \frac{M}{M_{\text{sat}}} = \frac{B_0\mu_{\text{eff}}^2}{3k_B\mu_B S(T - \Theta)} \quad (2.76)$$

where we have substituted the spin-only moment $\mu_{\text{eff}} = g_e\sqrt{S(S+1)}\mu_B$.

2.5.2 Magnetic Measurements with a SQUID Magnetometer

As paramagnetic NMR fundamentally depends on the response of paramagnetic electrons inside the NMR magnet, its room temperature magnetism must be studied to allow the link between calculation and experiment. Although various experimental methods exist to measure the magnetic behaviour of materials, the instrument most widely used today is the superconducting quantum interference device, or SQUID.

The working physical principle of SQUID is the Josephson effect, where a supercurrent flow is observed across an insulator staged between two superconductors. Two identical

Josephson junctions are used; originally, current I flows through the two junctions equally. Upon application of external magnetic flux, an extra current is induced through the coil, resulting in a voltage difference across the two junctions. The induced field (and hence induced voltage) oscillates as the external magnetic flux is increased, because the flux inside the coil must be an integer multiple of the magnetic flux quantum Φ_0 . This allows a very sensitive measurement of the magnetic flux.

2.5.3 Electron-Nucleus Interactions in Paramagnetic Systems

Intuitively speaking, electronic spin momentum could be understood as a small magnet which generates a magnetic field of its own. When present close to a nuclear spin momentum, the two spins can then couple to each other to cause a split in both energy levels, called the hyperfine interaction.

It is important to stress that the individual electron spins fluctuate very rapidly in paramagnetic systems to which most battery cathode materials belong. EPR experiments indicate that this fluctuation is on the order of nanoseconds to femtoseconds,[141] which is much faster than the typical correlation time of nuclear spins (100s of seconds to microseconds for the NMR timescale); thus, the nuclear spin can be treated as fully decoupled from the electronic spin transitions m_s and only ‘sees’ a time-averaged state of $\langle m_s \rangle$, which is of course non-zero under an applied \mathbf{B}_0 field. This net electronic magnetic moment $\langle m_s \rangle$ is expressed as the population difference between the parallel and antiparallel moments to the field.

The magnitude and orientation of this interaction can be expressed in terms of a hyperfine coupling tensor \mathbf{A} with the relevant hyperfine coupling Hamiltonian defined as

$$\hat{H}_{hf} = \hat{\mathbf{S}} \cdot \mathbf{A} \cdot \hat{\mathbf{I}} \quad (2.77)$$

where $\hat{\mathbf{S}}$ and $\hat{\mathbf{I}}$ refer to the electron and nuclear spins. \mathbf{A} can be further divided into the isotropic and anisotropic components.[142] Under high fields, there exists four different coupling mechanisms:

$$\mathbf{A} = (A_{iso,FC}^{NR} + A_{iso,FC}^{SO}) \cdot \mathbf{1} + (\mathbf{A}_{dip}^{NR} + \mathbf{A}_{dip}^{SO}) \quad (2.78)$$

- $A_{iso,FC}^{NR}$: Nonrelativistic, isotropic through-bond (Fermi contact) shift, in which the localised unpaired spin density can delocalise through a chemical bond pathway to the observed nucleus

- A_{dip}^{NR} : Nonrelativistic, anisotropic through-space (electron-nuclear dipolar) shift, in which the electronic spin moment is coupled to the nuclear spin moment through dipolar coupling
- $A_{iso,FC}^{SO}$: Relativistic, isotropic pseudocontact shift, where the spin and orbital angular momenta (if present) both contribute to the electron magnetic moment and ultimately couple to the nuclear spin
- A_{dip}^{SO} : Relativistic, anisotropic dipolar contact shift, which happens *via* a through-space dipolar coupling between the orbital angular momentum and the nuclear spin momentum

Pseudocontact shift may have an effect in the shifts of MgV_2O_4 ($S = 1$ in an octahedral crystal field) where an orbital degree of freedom is present; but previous reports have shown that the magnitude of such pseudocontact interactions is an order of magnitude smaller than the main Fermi contact interaction[143] and they are not considered further. This leaves us with the Fermi contact and electron-nuclear dipolar interactions, which we will discuss in detail below.

The Fermi contact interaction

In chemical bonding, all bonds are covalent to some extent. Even in metal oxides where one naïvely expects an ionic bonding, some degree of covalency exists; hence, an electronic spin can delocalise through chemical bonding (similar to the mechanism of spin-spin coupling often observed in solution NMR), resulting in a finite unpaired spin density on nuclear positions. This causes a small change in the local magnetic field at the nucleus, resulting in coupling to the electronic spins. This interaction is isotropic and commonly called the Fermi contact (FC) interaction.

As the FC interaction is a through-bond interaction, the net spin transfer depends on the nature of the orbitals involved in bonding; in particular the symmetry of the orbitals is the most important factor in determining the sign and magnitude of coupling. In TMs, unpaired spins occupy the d orbitals; for the observed nucleus, however, only the s orbital is important since it has a finite value of the wavefunction value at the nuclear position. Selected cases of resulting spin density for the 90° and 180° bond angles are shown in Figure 2.7.

A further important point about the FC interaction is its additive property; *i.e.* the observed A_{iso} can be expressed as a sum of different bond pathways connecting the observed atom to the electronic spin. This leads to a rational way of explaining the FC shifts by looking

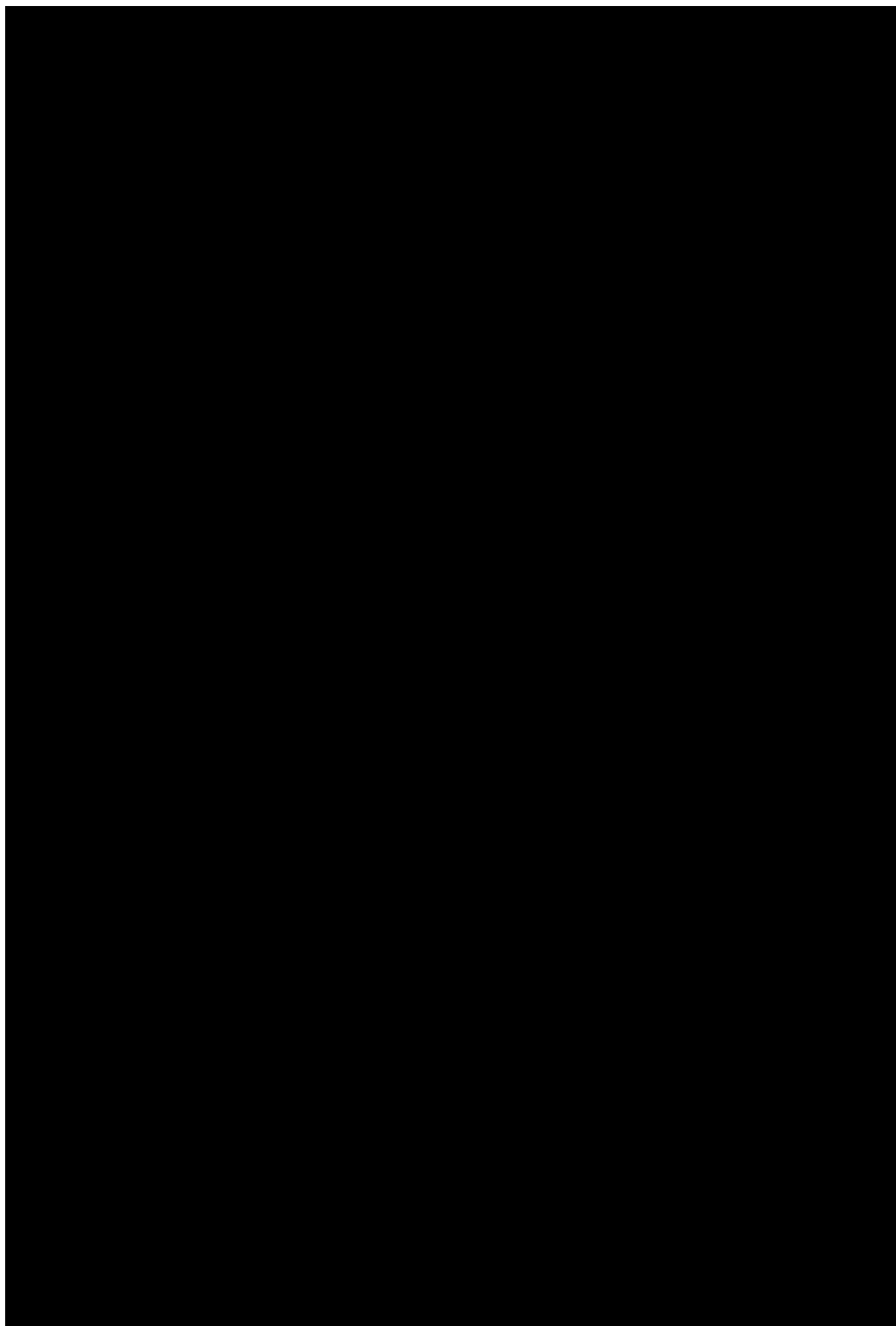


Fig. 2.7 Illustration of different spin density transfer mechanisms in TM – O – Li bonds, with 90° and 180° bond angles. Figure reproduced from Carlier et al. [144]

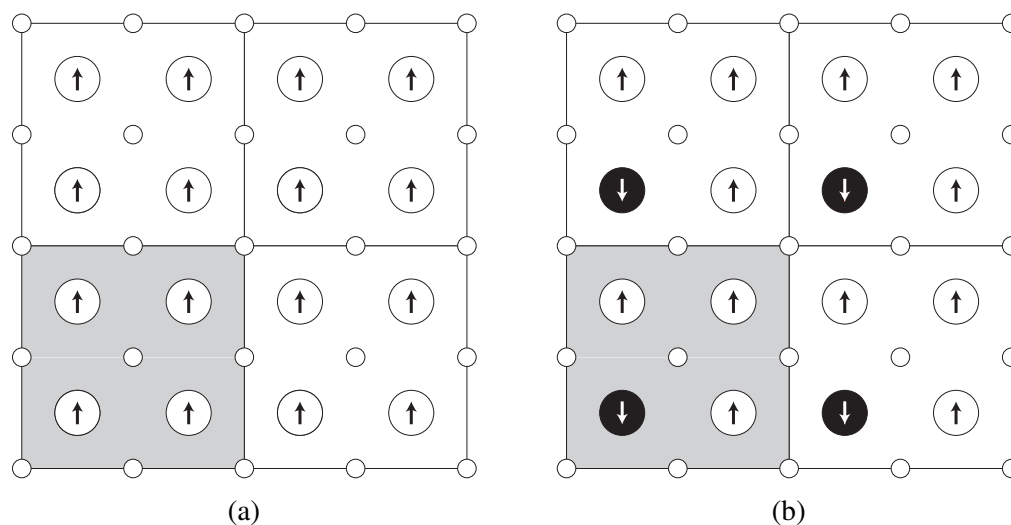


Fig. 2.8 Illustration of calculating J by a broken symmetry supercell approach. In (a), the total energy equals $E_a = E_0 + 8J_1$. In (b), the total energy equals $E_b = E_0$. Subtracting the energies yields $J_1 = (E_a - E_b)/8$.

at the bond geometry and the spin distribution, and can be used for estimating different bond contributions to the observed shift, as explored extensively in Chapter 3.

The Electron-nuclear dipolar interaction

This interaction does not require a chemical bonding to be present between the two atoms; rather, it describes the through-space dipolar coupling of spins *via* the magnetic field generated by electron spins.

The dipolar interaction varies as $1/r^3$, where r is the distance between the spins. As this interaction depends on the relative orientation between the two spins, it is anisotropic and also contributes to the observed anisotropy of the resulting NMR spectrum. Hence, the same argument of chemical shielding anisotropy could be applied to this dipolar interaction with the same convention on the tensor anisotropy (Section 2.4.1).

2.5.4 *Ab initio* Calculation of the Magnetic Coupling Parameter J

Often, one wishes to know the size of magnetic coupling J present in the system. For instance, complete *ab initio* calculation of the Fermi contact shift (see Section 2.5.5) requires precise knowledge of the magnetism at finite temperatures; this can be done either *ab initio* or by experiment using a SQUID magnetometry (Section 2.5.2).

The Hamiltonian 2.72 can be rewritten, in an absence of external magnetic fields, as

$$\hat{H} = - \sum_J \sum_{(i,j)} J_{S_i S_j} \quad (2.79)$$

Using this Hamiltonian, one can determine the J 's by a broken symmetry approach in a supercell by calculating the DFT energies of various ferromagnetic, ferrimagnetic, and antiferromagnetic spin configurations (Figure 2.8). Then a multivariate linear regression can be performed to yield the interaction parameters J_n . In this definition of \hat{H} , positive J corresponds to a ferromagnetic interaction, and negative J corresponds to an antiferromagnetic interaction. Using this value of J , the Brillouin function for magnetisation is solved self-consistently at various temperatures to yield the susceptibility $\chi(T)$ as a function of temperature.[140] A Curie-Weiss fit is then performed to obtain the Weiss constant Θ .

2.5.5 *Ab initio* Calculation of Paramagnetic NMR Parameters from the Curie-Weiss Law

Hyperfine shift parameters

Paramagnetic NMR parameters can be calculated *ab initio* using the scaling approach of Kim *et al.*[92] assuming the FC as the dominant shift mechanism. This method takes A_{iso} and A_{aniso} from a DFT calculation using a ferromagnetic spin configuration (performed at 0 K). As the samples are in a paramagnetic regime in the temperature range of NMR experiments, the electron magnetic moment needs to be 'scaled' from the (maximum) ferromagnetic value to values at finite temperatures. This is performed by scaling the ferromagnetic moment by a Curie-Weiss type factor Φ as defined in Equation 2.76. From this, the FC shift δ_{iso} could be obtained as

$$\delta_{\text{FC}} = \frac{10^6 A_{\text{iso}}}{2h\nu_0} \Phi \quad (2.80)$$

$$A_{\text{iso}} = \frac{2}{3} \mu_0 \mu_B \mu_N g_e g_I |\Psi_N^{\alpha-\beta}|^2 \quad (2.81)$$

where h is the Planck constant, ν_0 is the nuclear Larmor frequency in Hz, g_e is the free electron g -factor, g_I is the nuclear g -factor, μ_B is the Bohr magneton, and μ_N is the nuclear magneton. Most importantly, $|\Psi_N^{\alpha-\beta}|^2$ refers to the spin density at the nuclear position N which, assuming a point nucleus model, can only be nonzero for orbitals with s -symmetry.

In the above formalism, shift anisotropy can also be computed from the electron-nuclear dipolar interaction tensor T_{ij} and scaled in the same way to obtain the anisotropic components of the shift tensor δ_{ij} :

$$\delta_{ij} = \frac{10^6 A_{ij}^{\text{dip}} \Phi}{2h\nu_0} \quad (2.82)$$

$$A_{ij}^{\text{dip}} = \frac{T_{ij}}{4\pi} \mu_0 \mu_B \mu_N g_e g_I \quad (2.83)$$

After this δ_{ij} can be diagonalised to obtain the principal components δ_{ii} which can be used to calculate the shift anisotropy as detailed in Section 2.4.1.

Euler angles: relative orientation of the shift and EFG tensors

For systems with a large shift anisotropy tensor and EFG tensor (such as Mg_6MnO_8 in Chapter 3), the relative orientation of the two tensors is also important for accurate fitting of the spinning sideband manifolds. This can be represented by a combination of three Euler angles α , β , and γ , where the angles represent rotations of the electric field gradient principal axes to match the A_{ii}^{aniso} principal axes. Hyperfine and electric field gradient tensor principal axes are ordered such that $|A_{yy}| \leq |A_{xx}| \leq |A_{zz}|$ and $|V_{22}| \leq |V_{11}| \leq |V_{33}|$ (*i.e.* the Haeberlen convention with setting $A_{\text{iso}} = 0$). The ZYZ convention and counterclockwise (positive) rotation are assumed. The full rotation matrix is shown in Equation 2.84.

$$\begin{bmatrix} x' \\ y' \\ z' \end{bmatrix} = \begin{bmatrix} \cos \alpha \cos \beta \cos \gamma - \sin \alpha \sin \gamma & \sin \alpha \cos \beta \cos \gamma + \cos \alpha \sin \gamma & -\sin \beta \cos \gamma \\ -\cos \alpha \cos \beta \sin \gamma - \sin \alpha \cos \gamma & -\sin \alpha \cos \beta \sin \gamma + \cos \alpha \cos \gamma & \sin \beta \sin \gamma \\ \cos \alpha \sin \beta & \sin \alpha \sin \beta & \cos \beta \end{bmatrix} \begin{bmatrix} x \\ y \\ z \end{bmatrix} \quad (2.84)$$

2.6 Carbothermal Reaction: Thermodynamics

2.6.1 Using Carbon as a Reducing Agent

Setting fire to carbon results in a combustion reaction with atmospheric O_2 , producing a mixture of CO and CO_2 . If, however, the carbon is mixed with a metal oxide and heated under an anaerobic condition, the carbon can remove oxygen from the metal oxide to effectively reduce the metal oxide to a metal. This principle, of course, has been exploited in smelting furnaces for several centuries to extract metals from their ores, where a cheap source of carbon such as coke is used.

Let us assume that V_2O_3 is to be reduced to V using this method. The corresponding reduction reaction would read:



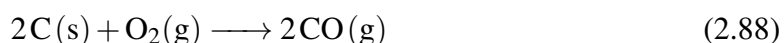
where the equation is normalised to 1 mol of oxygen. The spontaneity of this reaction then could be expressed in terms of the free energy change. Under constant pressure conditions, the change in Gibbs free energy, ΔG , is the relevant quantity where a negative ΔG would give a spontaneous reaction.

The overall Gibbs free energy change could be separated into the enthalpic and entropic components

$$\Delta G = \Delta H - T\Delta S \quad (2.86)$$

where ΔH is the enthalpy change, ΔS is the entropy change, and T is the temperature. As this reaction involves only solids on the reactant side and releases O_2 as a product, ΔS must be positive, indicating the reaction becomes more spontaneous as the temperature increases.

Of course, chemical intuition tells that reduction of metals just by heating would require a very high temperature, as the strong metal-oxygen bond dictates a very large enthalpic penalty to this reaction. Hence, to reduce this energy penalty, carbon is added to the oxides and heated to drive off CO and CO_2 ; thus this method is named carbothermal reduction (CTR). This produces nominally triple bonded CO and two double bonded CO_2 upon oxidation:



As the first reaction involves the same number of gaseous species on both sides of the equation, a flat line is anticipated for the $\Delta G - T$ plot since the $T\Delta S$ contribution to ΔG is expected to be small. Conversely, a downward sloping curve is expected for the second reaction since $\Delta S > 0$; both lines follow the expected trend.

More importantly, the two lines cross at a temperature around $T = 973 \text{ K}$ ($700 \text{ }^\circ\text{C}$): at lower temperatures, the CO_2 -reduction is thermodynamically more favoured, whereas the CO-reduction would be more favoured at elevated temperatures. This implies that the CTR treatment temperature has to be kept below 973 K to generate *stoichiometrically* reduced products, as the required ratio of carbon to oxygen increases from 1:2 to 1:1 above this temperature.

For the possible redox reactions, a convenient way of representing the temperature dependence of ΔG is the Free energy-temperature diagram, or the Ellingham diagram. In this diagram, ΔG is plotted as a function of T , where all the energies are normalised to 1 mol of O_2 to allow direct calculation of ΔG for the full reaction. A sample Ellingham diagram is shown in Figure 2.9.

For transition metals with several possible oxidation states, thermodynamic considerations could reveal conditions for a partial reduction, based on the ΔG of the reactions involved. This idea lies at the heart of the CTR method used in this work.

2.6.2 *Ab initio* Computation of G for Solids

Determining the appropriate CTR reaction conditions require knowledge of G , or equally, H and S . For many binary oxides, experimental values for the H and S are well known and often available in tabulated forms. Many of the complex oxides, however, lack such data, and it would normally require calorimetric measurements to determine the values of H and S .

Fortunately, the development of classical pair potential methods and the advent of quantum chemical methodologies allows a reasonable estimate for these thermodynamic parameters.

G for any compound can be further expanded into

$$G = H - TS = U + PV - TS \quad (2.89)$$

where the internal energy U , thermal expansion (work against external pressure) PV , and lattice vibration (entropy) TS terms are included. In theory, all three terms could be obtained from any classical or *ab initio* calculations: U could be equated to the zero-temperature cohesive energy of a system from a given reference point; PV could be estimated from the volume-energy relationship by varying the external pressure, commonly called the equation of state (EOS); TS could be obtained from the energies of lattice phonon modes at finite temperatures (in absence of other compositional or defect-related disorders). However, in many solids the latter two terms are often negligible compared to the U , since (i) solids have small compressibility due to their close packed nature and (ii) phonons only represent a small displacement of atoms from their equilibrium positions, limiting the level of disorder present in solids. Thus the PV and TS terms could be safely neglected from the calculation to yield the approximation $G \approx U$. This approximation allows us to avoid calculating the EOS and phonon energies, which are computationally expensive especially at an *ab initio* level.

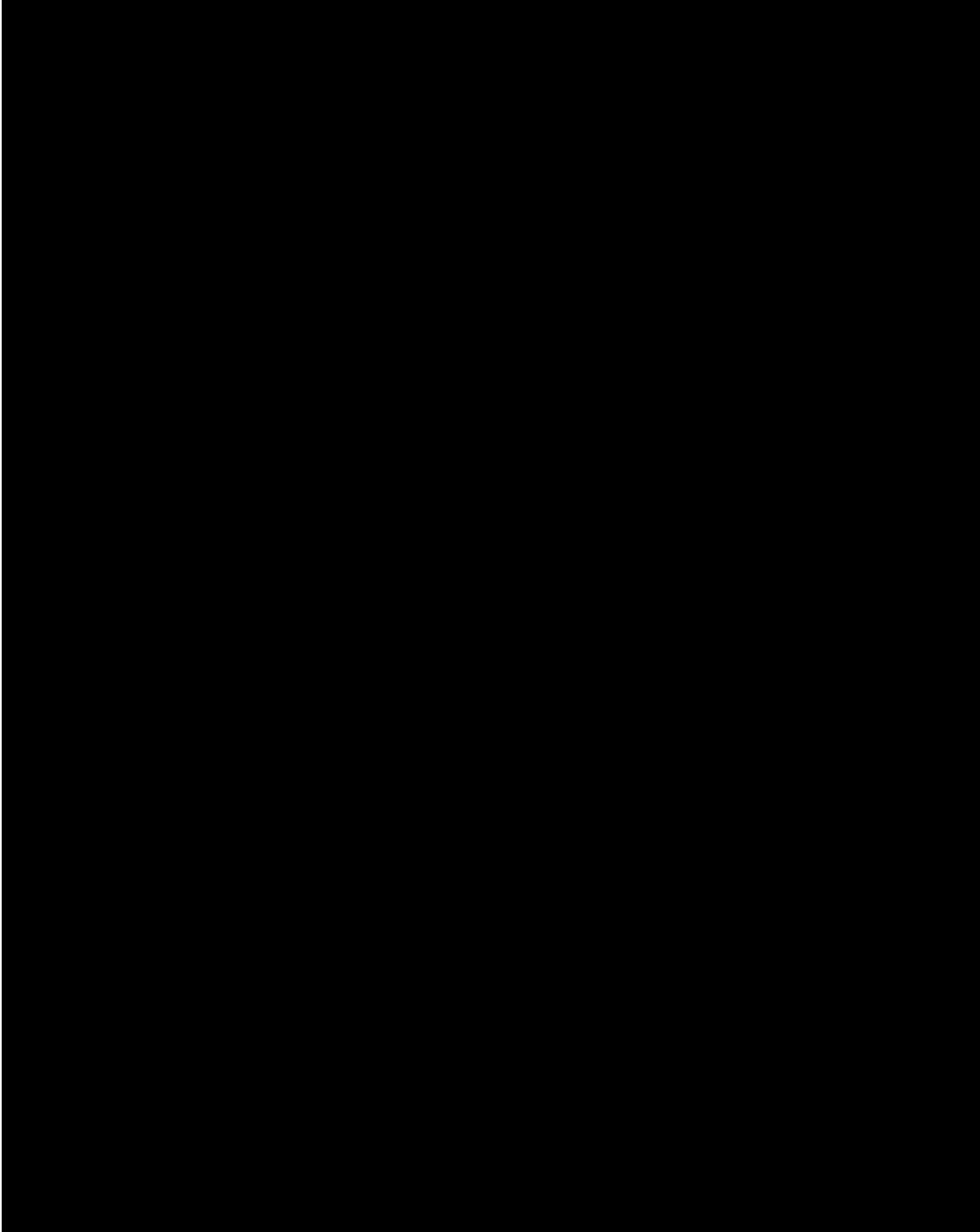


Fig. 2.9 Ellingham diagram, reproduced from the original construction by Ellingham.[145]

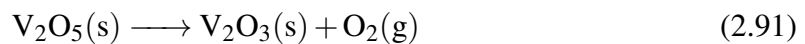
However, calculation of U with *ab initio* approaches require a further consideration of the functional used. As the ΔG we are interested in represents a change in oxidation states of the system (*e.g.* $\text{MgV}_2\text{O}_6 + \text{C} \longrightarrow \text{MgV}_2\text{O}_5 + \text{CO}$), methods are needed to accurately treat the localised electrons in these Mott insulators. Hubbard- U corrections, although computationally inexpensive, are sensitive to the oxidation states and even the local environment in which the metal ions reside; it have been shown to produce large errors in energies for reactions involving a change in oxidation states.[66, 75, 146] Thus, the more computationally expensive hybrid functionals are necessary not only to obtain the correct insulating electronic states, but also to account for the changes in transition metal valences. In this regard, CRYSTAL, a code which allows a more efficient use of hybrid functionals especially with lattice symmetry, was used in combination with the B3LYP functional to calculate U .

G for gases: dependence on partial pressure

G for gaseous species such as CO and CO₂ needs further consideration as their partial pressures also influence the values of G . The dependence of chemical potential μ on the partial pressure can be expressed as

$$\mu = \mu^\circ + RT \ln \left(\frac{\rho}{\rho^\circ} \right) \quad (2.90)$$

where μ° is the chemical potential under standard conditions, R is the gas constant, and ρ° is the standard pressure (1 atm). As ΔG represents a change in chemical potentials between the reactants and products, this equation could be used to calculate the dependence of ΔG on ρ at a given temperature. For instance, assuming that the reaction



has a standard free energy change ΔG° , the change due to oxygen partial pressure ρ_{O_2} could be expressed as

$$\Delta G = \Delta G^\circ + RT \ln \left(\frac{\rho_{\text{O}_2}}{\rho^\circ} \right) \quad (2.92)$$

Under $\rho_{\text{O}_2} < 1$ atm, the second term becomes negative, resulting in a change in ΔG towards negative direction, *i.e.* making it more spontaneous (which corresponds with the Le Châtelier principle).

2.7 X-ray Diffraction Techniques

2.7.1 Powder Diffraction

The majority of technologically important materials are in solid form, and many of them are periodic crystals with repeating lattices. Upon irradiation of a wave (X-rays, electrons, or neutrons), components of the repeating lattice can reflect the incident wave by scattering. X-ray and electrons are scattered by the electron densities, whereas neutrons are scattered by the nuclei or magnetic fields from unpaired electrons. The reflected waves can either constructively or destructively interfere with each other, where the Bragg's law gives the criterion for constructive interferences

$$n\lambda = 2d \sin \theta \quad (2.93)$$

where n is an integer, λ is the incident wavelength, d is the lattice spacing, and θ is the scattering angle. In laboratory powder diffraction, usually the Bragg-Brentano $\theta - \theta$ configuration is used. In this setup the X-ray source and detector are rotated around a fixed flat sample with random crystallite orientations by the same angle θ . As the angle is changed, only the crystallites which satisfy the Bragg condition at the given angle will show a constructive interference. The resulting diffraction intensities are usually plotted against the angle 2θ , which is equivalent to projecting the 3-dimensional reciprocal space to a 1-dimensional line.

2.7.2 Rietveld Refinement

Rietveld refinement [147] is a whole-profile method to extract structural information from the powder diffraction data. This method is essentially a least-squared fitting process where the sum of squared differential between the observed and calculated intensities $y(obs)$ and $y(calc)$ is minimised over the observed data points i in the 2θ domain

$$M = \sum_i W_i \left[y_i(obs) - \frac{1}{c} y_i(calc) \right]^2 \quad (2.94)$$

where W_i is the weighting factor and c is the scaling factor. Starting from an initial structural model, a least-squares minimisation is performed to yield a refined model that best fits the diffraction data.

Chapter 3

A Systematic Study of ^{25}Mg NMR in Paramagnetic Transition Metal Oxides

3.1 Introduction

Mg transition metal (TM) compounds are an important class of materials for uses as Mg-ion battery cathode systems.[148] With the high redox potential and capacity afforded by the often paramagnetic TM, such systems are promising candidates for advanced Mg-ion batteries for *e.g.* automotive applications.[149, 15] In addition, they can, for example, be potentially used as carbon capture materials[150] and electrochemical catalysts for water oxidation.[151] Therefore, elucidating the Mg local environment is crucial for understanding and evaluating the working principles of this important class of materials.

In light of this, the current chapter presents a baseline for a combined experimental and theoretical approach for performing ^{25}Mg solid-state NMR experiments in paramagnetic TM oxides. Four Mg TM oxides which have different crystal structures are considered: Mg_6MnO_8 (defect rocksalt), MgCr_2O_4 , MgV_2O_4 (cubic normal spinel), and MgMn_2O_4 (tetragonal normal spinel). First, we report the results of their structural and magnetic characterisation, which is followed by ^{25}Mg NMR experiments. Then *ab initio* calculations for magnetic data and paramagnetic ^{25}Mg NMR shifts are presented. First principles results are compared to experimental spectra to aid their interpretation. Finally, we discuss the observed NMR shifts in terms of the Fermi contact interaction and decompose the value of shifts in terms of the individual TM–O–Mg spin transfer pathways.

Sample	Thermal profile	Atmosphere
MgV_2O_4	1273 K 24h	5% H_2 in Ar
MgCr_2O_4	1073 K 12h - 1473 K 24h	Air
Mg_6MnO_8	1173 K 12h	Air
MgMn_2O_4	453 K 12h - 773 K 36h	Air

Table 3.1 Synthesis conditions of samples.

3.2 Experimental

3.2.1 Sample Preparation

Mg_6MnO_8 , MgCr_2O_4 , and MgV_2O_4 samples were prepared *via* solid state (SS) synthesis from stoichiometric amounts of MgO (Sigma-Aldrich, 99.99 %), V_2O_3 (Sigma-Aldrich, 99.7 %), Cr_2O_3 (Sigma-Aldrich, 99.99 %), and MnO_2 (Sigma-Aldrich, 99.99 %).^{*} Mixtures were ball milled using ZrO_2 jar and balls (SPEX M8000 high energy ball mill) for 30 minutes, pressed into pellets, and calcined according to Table 3.1. The MgMn_2O_4 sample was synthesised from anhydrous citric acid (Breckland Scientific, 99 %), $\text{Mg}(\text{NO}_3)_2 \cdot 6\text{H}_2\text{O}$ (Sigma-Aldrich, 99 %), and $\text{Mn}(\text{NO}_3)_2 \cdot 4\text{H}_2\text{O}$ (Sigma-Aldrich, 97 %) through a citrate sol-gel method.[152] The organic matter was burned off at 453 K and final calcination was performed at 773 K with one intermediate grinding. Synthesised samples were checked using a PANalytical Empyrean powder X-ray diffractometer ($\text{Cu } K_\alpha = 1.5406 \text{ \AA}$) and the structures were refined from their diffraction patterns by using the Rietveld method[147] as implemented in the X'pert Highscore Plus software.

3.2.2 Magnetic Measurements

Magnetisation measurements were performed on a Quantum Design Magnetic Property Measurement System (MPMS) with a SQUID magnetometer. Magnetic moments of zero field-cooled samples were measured at temperatures from 2 K up to 301 K in a field of 1000 Oe to obtain the dependence of magnetic susceptibility $\chi(T) = dM/dH \approx M/H$ (low-field approximation) on temperature. The Weiss constant Θ was extracted by fitting the Curie-Weiss law $\chi = C/(T - \Theta)$, where C is the Curie constant at high temperatures. The effective electron magnetic moment μ_{eff} was extracted from C by the relation $\mu_{\text{eff}} = \sqrt{3k_B C/N_A}$ (Equation 2.75) where k_B is the Boltzmann constant and N_A is the Avogadro constant. The

^{*} MgCr_2O_4 and SS- MgV_2O_4 samples were prepared during the previous Part III research project carried out by the author.

magnetic exchange coupling constant J_1 between the nearest neighbouring spins (S) was calculated from Θ by the mean-field relation (Section 2.5.1, Equation 2.73).

3.2.3 ^{25}Mg NMR

All NMR spectra were acquired on a 16.4 T Bruker Avance III spectrometer operating at a Larmor frequency of 42.9 MHz for ^{25}Mg with conventional Bruker 4 mm and 3.2 mm triple resonance MAS low- γ probes. $\pi/2$ -pulse amplitudes were calibrated on solid MgO, giving 90° pulse amplitudes of 30 kHz and 36 kHz for the 4 mm and 3.2 mm probes, respectively. For quadrupolar samples, CT-selective $\pi/6$ -pulses were used. All shifts were referenced to MgO at 26 ppm.[153] Recycle delays of 0.1 s were used for all acquisitions unless otherwise indicated. Spectra were acquired with rotor-synchronised spin echo,[133] magic angle turning (MAT),[139] and rotor assisted population transfer (RAPT)[135] pulse sequences as shown in Chapter 2. A FAM-type \bar{X} -X pulse train was used to saturate the satellite levels. The RAPT modulation frequency ν_m was calculated from DFT values of C_Q . Values of $\nu_m = 270$ kHz ($C_Q = 3.6$ MHz) and 240 kHz ($C_Q = 3.2$ MHz) were used for Mg_6MnO_8 and MgMn_2O_4 , respectively. Experimental signal enhancement was measured for varying saturation frequencies for Mg_6MnO_8 . Fitting of the spectra was performed assuming a central transition lineshape using the Bruker Topspin 3.0 software.

3.2.4 *Ab Initio* Calculations

DFT calculations

All calculations were performed in CRYSTAL09, a solid-state DFT code using a Gaussian-type basis set to describe core states accurately. CRYSTAL has been used successfully in calculation of ^{67}Li -, ^{23}Na -, and ^{31}P -paramagnetic shifts.[92, 94, 93] Given that the calculation of paramagnetic shifts depends substantially on the quality of Gaussian basis sets, two types of basis sets were utilised: a smaller basis set (termed BS-I) for geometry optimisations, and a more extended basis set (BS-II) for hyperfine and magnetic single-point calculations. This dual basis set scheme was first reported by Kim *et al.*[92] for paramagnetic shift calculations in periodic systems and is known to work well for ^{67}Li -, ^{23}Na -, and ^{31}P -paramagnetic shifts.[94, 93] BS-I sets were taken from solid-state studies of Catti *et al.*[154, 155, 156] and were used unchanged. BS-II sets for metal ions were taken from the Ahlrichs set, with TZDP-derived basis for Mg and DZP-derived sets for Cr and V. Modified IGLO-III

sets[157] are adopted for O. The choice of BS-II is similar to the previous works on Li transition metal oxides.[92, 94, 93]

All calculations were performed using the spin-polarised B3LYP functional[83, 158]. Recent results indicate that using 35% of HF exchange gives better results for solid-state magnetic calculations.[90, 91] Previous *ab initio* studies on ^7Li , ^{23}Na , and ^{31}P paramagnetic shifts show that values obtained using 20% and 35% provide the upper and lower bounds for the experimental shifts.[92, 94, 93] Hence the original B3LYP (termed ‘Hyb20’) and a modified B3LYP with 35% of HF exchange (termed ‘Hyb35’) were both used in calculations.

Convergence of energy and spin density was checked with the number of sampled points in the reciprocal space, and a $4 \times 4 \times 4$ Monkhorst-Pack[159] sampling scheme was used for all systems. Self-consistent field (SCF) cycles were converged to an energy difference of 10^{-7} Hartree limit.

Experimental cell geometries were expanded into supercells and were optimised in CRYSTAL09 with all cell symmetries removed, except for the MgV_2O_4 case where the cubic cell was used with the available space group symmetry due to instabilities in the self-consistent field cycles. All geometry optimisations were performed under the CRYSTAL default convergence criteria. Results from DFT calculations are reported in Table 3.7 and are also discussed in detail in the Results section.

Magnetic parameters

Values of Θ were obtained through *ab initio* DFT methods and also from SQUID magnetometer measurements. As determination of the magnetism is crucial to calculating paramagnetic shifts, magnetic exchange coupling constants J were obtained from DFT calculations as detailed in Section 2.5.4.

NMR parameters

Ab initio calculation of the total NMR shift tensor requires consideration of two contributions: the diamagnetic orbital contribution and the paramagnetic (FC) contribution due to unpaired electrons. Diamagnetic ^{25}Mg shifts in inorganic solids are known to be around tens of ppm (e.g. MgAl_2O_4 $\delta_{iso} = 48$ ppm).[160] As the diamagnetic contribution (positive or negative relative to the reference) is much smaller than the paramagnetic contribution, we have ignored the former in the calculation of shifts.

The paramagnetic contribution to the shift tensor originates from the isotropic A_{iso} and anisotropic A_{aniso} components of the electron-nuclear hyperfine coupling tensor. Here

the isotropic component is ascribed solely to the Fermi contact (FC) mechanism, which contributes to the isotropic shift. The anisotropic (dipolar) component contributes to the shift anisotropy. Detailed discussion on the formalism behind the hyperfine shift calculation could be found in Section 2.5.3.

Following the approach of Middlemiss *et al.*, the contributions of each Fermi contact pathway to the total spin density $\Delta|\Psi_N^{\alpha-\beta}|^2$ were also calculated by reversing the direction of electronic spins on each TM site in turn.[94] In addition, the total spin density $|\Psi_N^{\alpha-\beta}|^2$ was calculated from experimental shift by Equations 2.81 and 2.82.

As ^{25}Mg is a quadrupolar nucleus ($I = 5/2$), the overall observed isotropic shift δ_{iso} under MAS conditions can be expressed as a sum of Fermi contact component δ_{FC} and second-order quadrupolar component δ_Q (as defined in Equation 2.67). Hence, both contributions to the observed shift are separately considered in this work.

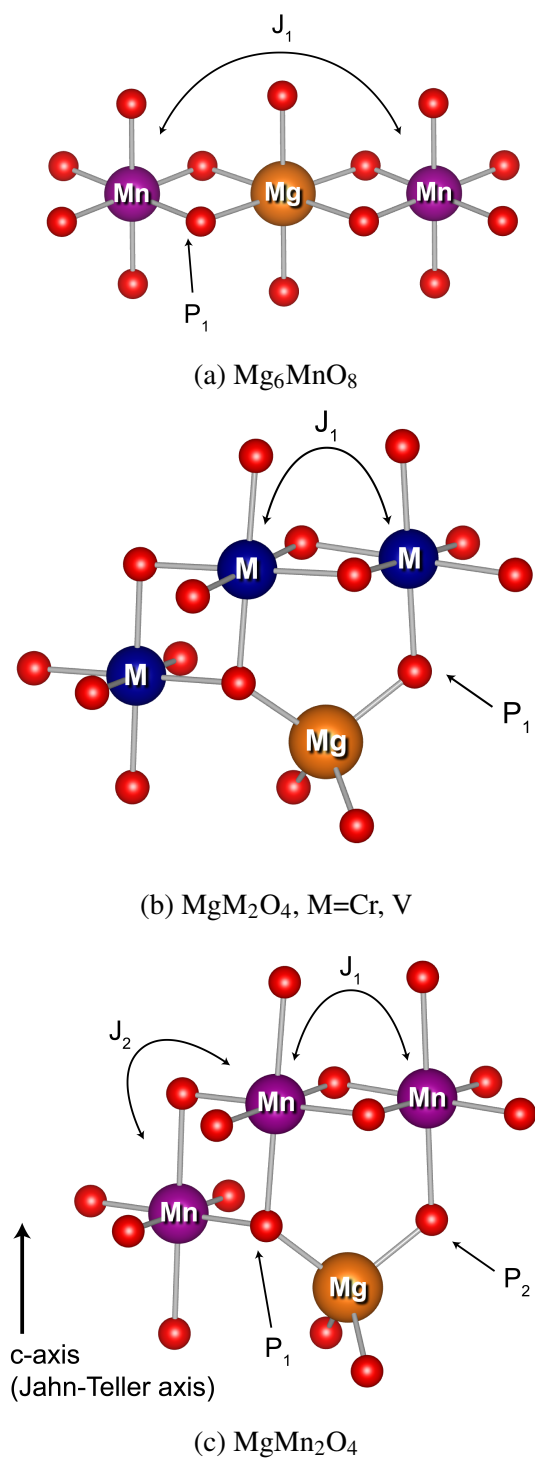


Fig. 3.1 ^{25}Mg bond pathway (P) contributions and TM–TM J couplings.

3.3 Results and Discussion

3.3.1 Diffraction and Magnetic characterisation

Defect rocksalt Mg_6MnO_8

As introduced in Chapter 1, Mg_6MnO_8 has an ordered defect rocksalt structure $[\text{Mg}_{6/8}^{2+}\text{Mn}_{1/8}^{4+}\square_{1/8}]\text{O}^{2-}$ with a $Fm\bar{3}m$ space group symmetry. The oxygen sublattice is also slightly distorted from the ideal cubic rocksalt structure due to the smaller ionic radius of Mn^{4+} (0.53 Å) compared to Mg^{2+} (0.72 Å).[49] The Mg site in this structure shows $m.mm$ site symmetry, reflecting the distorted octahedra as opposed to the undistorted octahedra in the parent MgO structure. This should give a nonvanishing quadrupolar coupling constant, C_Q , and quadrupolar asymmetry parameter, η , for ^{25}Mg .

The powder X-ray diffraction pattern of Mg_6MnO_8 and the Rietveld refinement result are shown in Figure 3.2 and Table 3.2. The product is single phase with a diffraction pattern that matches to the previously reported result of Mg_6MnO_8 , showing a cubic $Fm\bar{3}m$ symmetry.[47]

Transition metal (TM) sites in Mg_6MnO_8 are separated by Mn–O–Mg–O–Mn bond pathways, resulting in an extended superexchange interaction between the unpaired electronic spins of Mn^{4+} (Figure 3.1a). The nature (ferromagnetic or antiferromagnetic) and magnitude of this interaction can be represented by an exchange coupling parameter J_1 , where we are only considering the nearest neighbouring interactions (12 for each Mn^{4+}). At temperatures $T > 20$ K, the magnetic susceptibility data of Mg_6MnO_8 (Figure 3.3) show the weak Curie-Weiss paramagnetism, with an antiferromagnetic ordering transition at the Néel temperature of $T_N = 5$ K. Fitting to the Curie-Weiss law, $35 < T < 300$ K, yielded the Weiss constant $\Theta = -21.9 \pm 0.4$ K and $J_1 = -0.73 \pm 0.01$ K. Due to the long Mn – Mn distance (6 Å), weak exchange coupling is expected; in this case, the coupling is antiferromagnetic ($J < 0$) as expected for the extended superexchange interactions.[161] The obtained Weiss constant is in excellent agreement with the published experimental result of -20 ± 5 K.[162] In addition, the effective electron magnetic moment $\mu_{\text{eff}} = 3.99 \pm 0.01 \mu_B$ obtained from the Curie constant shows good agreement with the spin-only value of $3.87 \mu_B$.

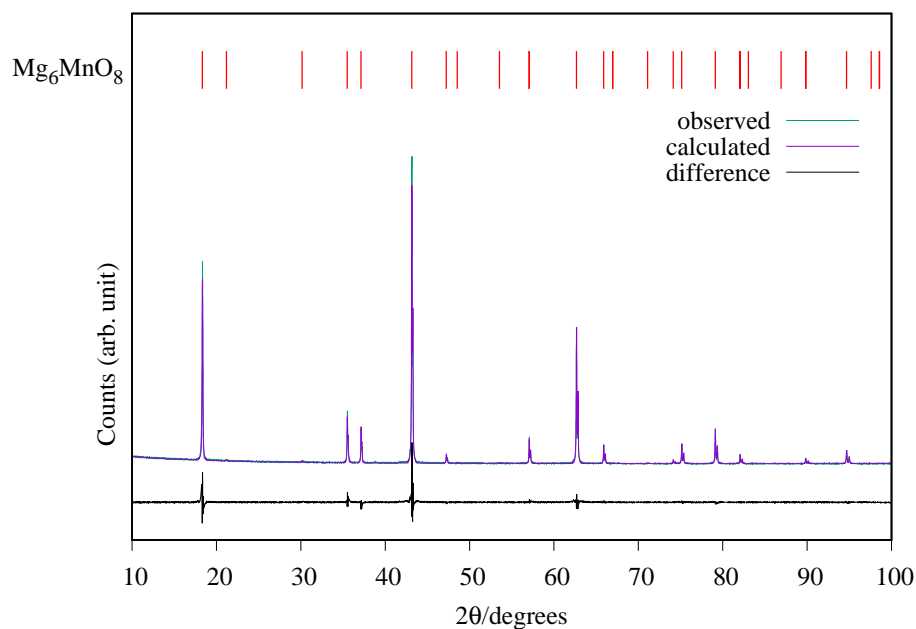


Fig. 3.2 X-ray powder diffraction pattern and Rietveld refinement data for Mg_6MnO_8 . The positions of allowed reflections are indicated by the tick marks.

Mg_6MnO_8 100 wt %		$Fm\bar{3}m$ space group	
$a / \text{\AA}$	8.38008(6)	$\alpha / ^\circ$	90
$b / \text{\AA}$	8.38008(6)	$\beta / ^\circ$	90
$c / \text{\AA}$	8.38008(6)	$\gamma / ^\circ$	90
Atom	x	y	z
Mg1 (24d)	0	0.25	0.25
Mn1 (4a)	0	0	0
O1 (8c)	0.25	0.25	0.25
O2 (24e)	0.229(3)	0	0
	R_{exp}	2.41	
	R_{wp}	14.21	
	χ^2	5.60	

Table 3.2 Rietveld refined parameters from the PXRD data of Mg_6MnO_8 .

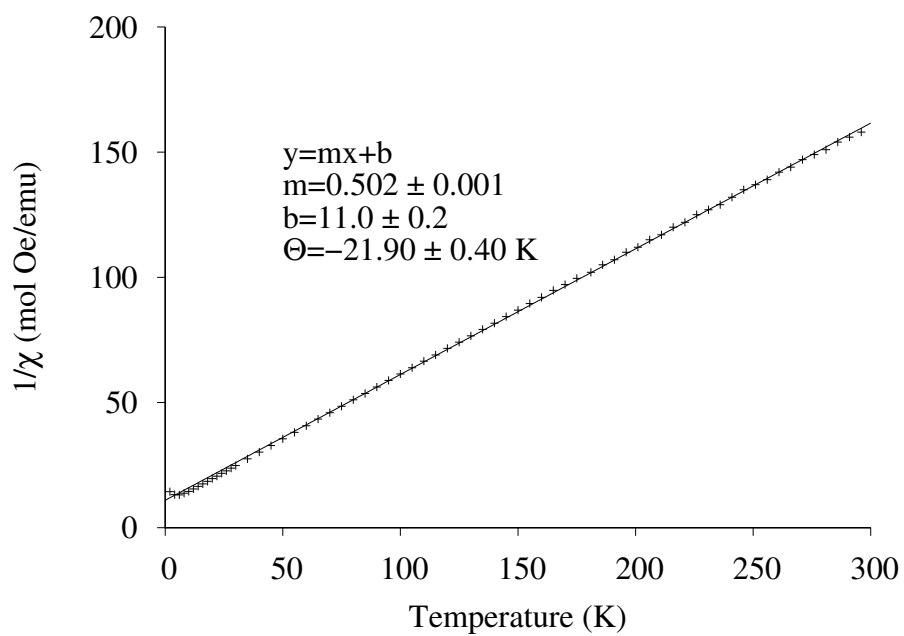


Fig. 3.3 Inverse magnetic susceptibility per mol Mn, $1/\chi$, as a function of temperature for Mg_6MnO_8 .

	$\mu_{\text{eff}}(\text{SO}) / \mu_B$	$\mu_{\text{eff}}(\text{expt}) / \mu_B$	Θ / K	J_1 / K	T_N / K	Fitted range / K
Mg_6MnO_8	3.87	3.99 ± 0.01	-21.9 ± 0.4	-0.73 ± 0.01	5	35–301
MgCr_2O_4	3.87	4.25 ± 0.03	-457 ± 3	-30.4 ± 0.2	13	100–301
MgMn_2O_4	4.90	5.93 ± 0.06	-453 ± 5	–	–	200–301
$(\text{Mg}_{0.81}^{2+}\text{Mn}_{0.19}^{2+})\text{Mn}_2^{3+}\text{O}_4$	5.00					
$(\text{Mg}_{0.91}^{2+}\text{Mn}_{0.09}^{2+})\text{Mn}_2^{3+}\text{O}_4$	4.95					

Table 3.3 Magnetic characterisation data of compounds studied. μ_{eff} refers to the effective magnetic moment in Bohr magneton (μ_B) per TM ion, Θ refers to the Weiss temperature, J_1 refers to the nearest neighbour exchange coupling constant extracted with Equation 2.73, and T_N refers to the Néel temperature. Theoretical spin-only values for the MgMn_2O_4 compositions determined by phase fractions and occupancy refinements are also shown.

Cubic spinel MgCr₂O₄

MgCr₂O₄ adopts the normal spinel structure with cubic $Fd\bar{3}m$ space group symmetry and Mg²⁺ ions in the tetrahedral (8a) sites, the Cr³⁺ occupying the octahedral (16d) metal sites. The thermodynamic factors controlling normal versus inverse spinel formation are previously described in the Introduction (Section 1.3.2). In MgCr₂O₄ and MgV₂O₄ (described later in the text), the crystal field stabilisation energy (CFSE) of the TM ions are responsible for their preference for occupancy of the 16d site.

The powder X-ray diffraction pattern of prepared MgCr₂O₄ is shown in Figure 3.4. As expected from the structural discussion above, Rietveld refinement of the pattern shows a cubic $Fd\bar{3}m$ symmetry and is a normal spinel. No impurity phase is detected in the MgCr₂O₄ sample.

The TM sites in cubic spinels have six nearest neighbouring TM sites connected through 90° TM–O–TM bonds, resulting in magnetic exchange which can be represented with J_1 (Figure 3.1b). For the MgCr₂O₄ sample under consideration, SQUID magnetometry measurements were performed. From the Curie-Weiss fit ($100 < T < 301$ K) to the experimental magnetic susceptibility data (Figure 3.5), Néel temperature of $T_N = 13$ K and Weiss constant of $\Theta = -457 \pm 3$ K are obtained. By use of the relation 2.73, $J_1 = -30.4 \pm 0.2$ K could be calculated from Θ . The effective electron magnetic moment $\mu_{\text{eff}} = 4.25 \pm 0.03 \mu_B$ obtained from the Curie constant is slightly larger than the spin-only value of $3.87 \mu_B$, which originates from the fact that there are still significant short-range fluctuations over the temperature range of fitting ($\Theta > 300$ K). The observed Weiss constant is in good agreement to the previously reported value of -433 K.[163]

Cubic spinel MgV₂O₄

MgV₂O₄, similar to MgCr₂O₄, adopts the normal spinel structure with the Mg²⁺ ions in the tetrahedral (8a) sites, the V occupying the octahedral (16d) metal sites. On top of the CFSE effect, it is known that the orbital degree of freedom in the $S = 1$ V³⁺ ion also favours the normal spinel structure.[53]

The powder X-ray diffraction pattern of MgV₂O₄ prepared *via* a conventional solid-state reaction (denoted SS-MgV₂O₄ to differentiate from the sample prepared and analysed in Chapter 4) is shown in Figure 3.6 and Table 3.5. Rietveld refinement indicates a normal spinel with $Fd\bar{3}m$ symmetry as expected. 15.4 ± 0.4 % by weight of unreacted V₂O₃ is also seen in the diffraction pattern, also demonstrated by previous reports of SS-MgV₂O₄. [164] This behaviour is known to occur due to a reduction of MgO and sublimation of Mg metal

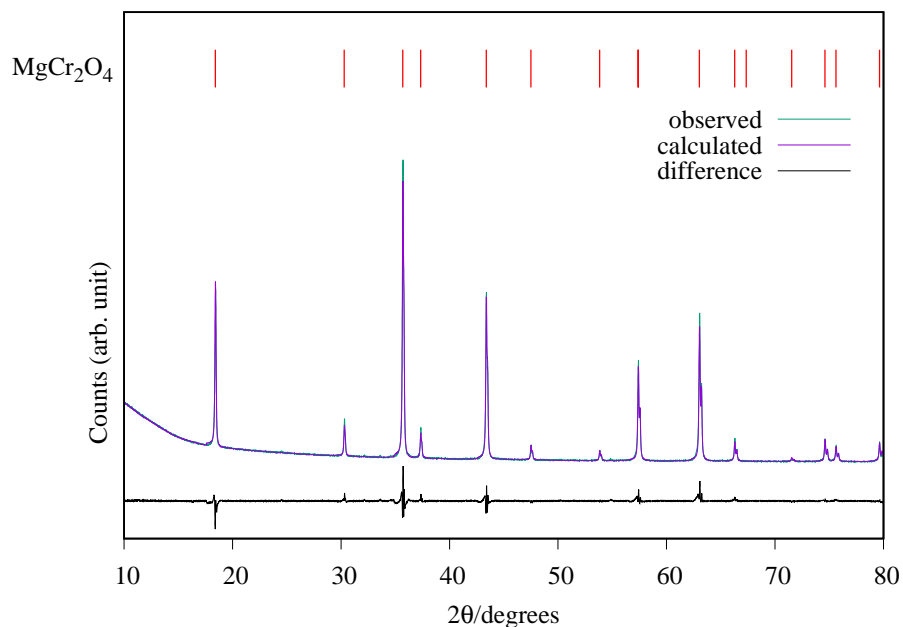


Fig. 3.4 X-ray powder diffraction pattern and Rietveld refinement data for MgCr_2O_4 . The positions of allowed reflections are indicated by the tick marks.

MgCr_2O_4 100 wt %		$Fd\bar{3}m$ space group	
$a / \text{Å}$	8.33242(9)	$\alpha / ^\circ$	90
$b / \text{Å}$	8.33242(9)	$\alpha / ^\circ$	90
$c / \text{Å}$	8.33242(9)	$\alpha / ^\circ$	90
Atom	x	y	z
Mg1 (8b)	0.375	0.375	0.375
Cr1 (16d)	0	0	0
O1 (32e)	0.2423(2)	0.2423(2)	0.2423(2)
	R_{exp}	2.19	
	R_{wp}	9.76	
	χ^2	4.46	

Table 3.4 Rietveld refined parameters from the PXRD data of MgCr_2O_4 .

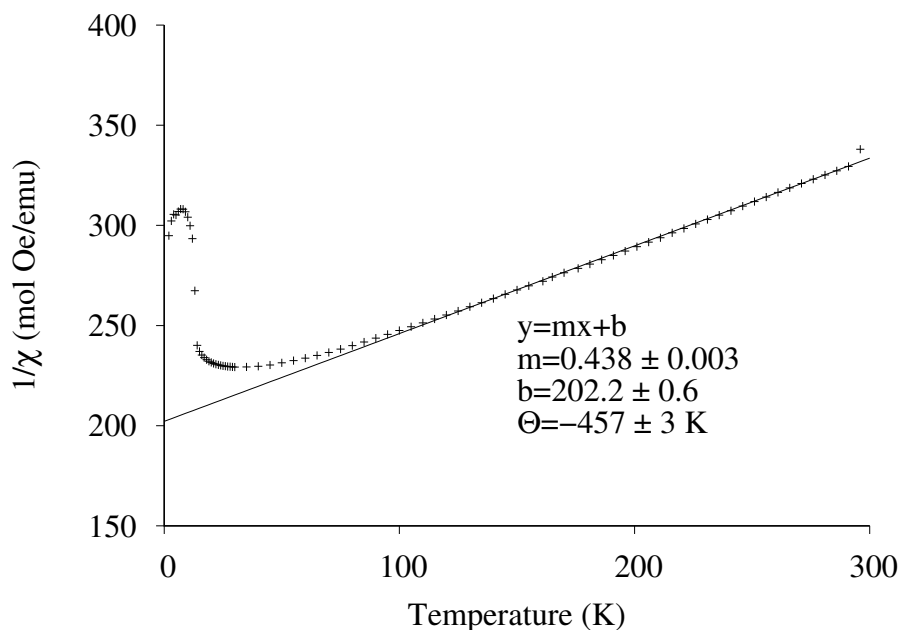


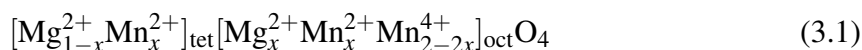
Fig. 3.5 Inverse magnetic susceptibility per mol Cr, $1/\chi$, as a function of temperature for MgCr_2O_4 .

at high temperatures under a reducing atmosphere of H_2 ; however, it is known that H_2 gas flow is essential to keep the vanadium oxidation state of 3+.[165] Previous syntheses, therefore, resorted to adding excess MgO in the starting material to compensate for this evaporation.[165, 166]

However, in the case of the solid-state prepared $\text{SS-MgV}_2\text{O}_4$, an experimental measurement of magnetic susceptibility was not performed due to the presence of the V_2O_3 secondary phase. More discussion on the MgV_2O_4 sample prepared through a different synthesis method to eliminate this secondary phase is presented in Chapter 4, Section 4.3.6.

Tetragonal spinel MgMn_2O_4

As introduced in Chapter 1, MgMn_2O_4 shows a spinel structure with $I4_1/amd$ symmetry, which is different from the above two compounds. Since the octahedral Mn^{3+} (d^4) ions cause a Jahn-Teller distortion of the original cubic spinel structure, a tetragonal spinel is obtained. Mn^{3+} ion disproportionates at high temperatures, resulting in an antisite defect between the Mn and Mg ions. This inversion behaviour is known to occur around 1073 K,[59, 60] resulting in the following cation distribution:



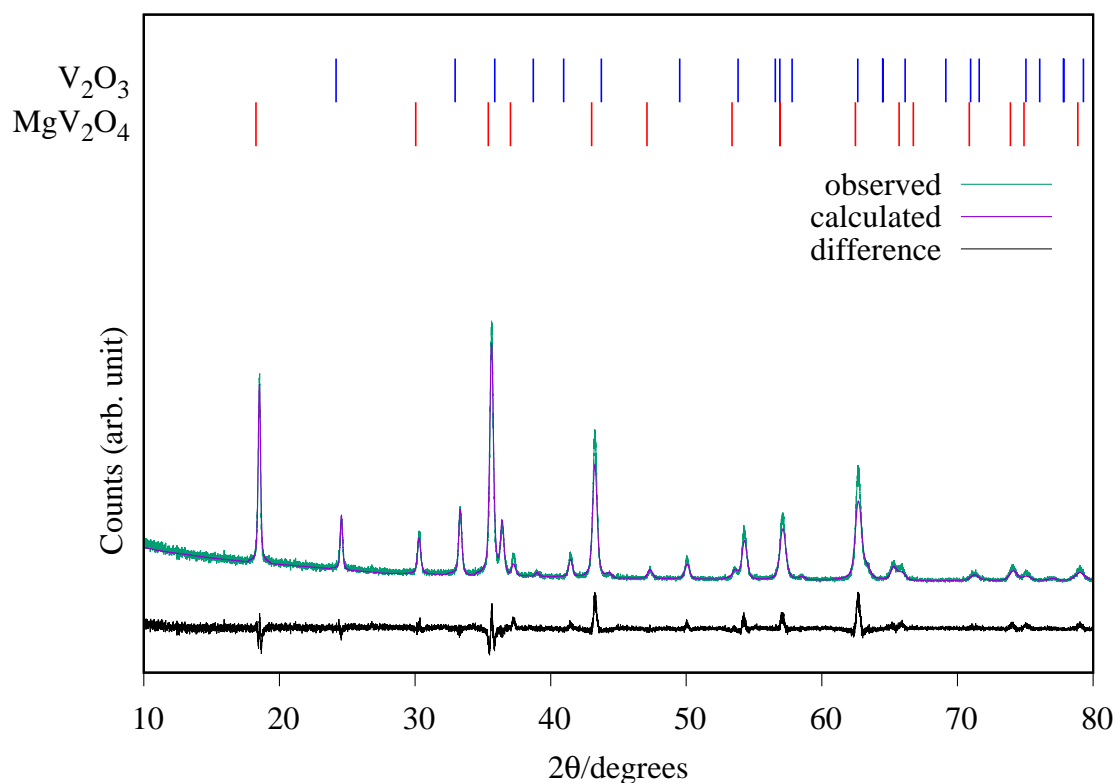


Fig. 3.6 X-ray powder diffraction pattern for the SS- MgV_2O_4 . The positions of allowed reflections are indicated by the tick marks.

MgV_2O_4 84.6(4) wt %		$Fd\bar{3}m$ space group	
$a / \text{Å}$	8.4131(1)	$\alpha / ^\circ$	90
$b / \text{Å}$	8.4131(1)	$\alpha / ^\circ$	90
$c / \text{Å}$	8.4131(1)	$\alpha / ^\circ$	90
Atom	x	y	z
Mg1 (8b)	0.375	0.375	0.375
V1 (16d)	0	0	0
O1 (32e)	0.2442(2)	0.2442(2)	0.2442(2)
	R_{exp}	11.69	
	R_{wp}	16.33	
	χ^2	1.40	

Table 3.5 Rietveld refined parameters from the PXRD data of MgV_2O_4 prepared *via* a solid-state method (SS- MgV_2O_4).

It is known experimentally that low-temperature synthesis of this material through a coprecipitation or sol-gel method suppresses this inversion, resulting in an ordered normal spinel.[152, 167] We also note that this material has been previously shown to be a promising Mg-ion battery cathode material, being able to reversibly de-insert ^{25}Mg ions in an aqueous electrolyte system.[30]

As discussed above, we have attempted the synthesis of an ordered, normal MgMn_2O_4 spinel through a citrate sol-gel method at a relatively low temperature of 773 K. The X-ray diffraction pattern of this sample is shown in Figure 3.7, alongside the results from the Rietveld refinement. Refinement of the sample shows a tetragonal spinel, with 7.9 ± 0.3 % of Mg_6MnO_8 secondary phase by weight. This impurity phase could not be eliminated despite attempts to make a homogeneous mixture of Mg and Mn in the gel, and repeated calcination attempts with intermediate grinding. Previous syntheses of MgMn_2O_4 through sol-gel and solid-state methods have also reported the presence of this secondary phase.[152, 168, 30] This suggests that excess Mn is present in the tetrahedral ($4a$) site of the spinel structure in a divalent form, Mn^{2+} . From the starting Mg to Mn ratio of 1:2, the stoichiometry of this sample is calculated as $(\text{Mg}_{0.81}^{2+}\text{Mn}_{0.19}^{2+})\text{Mn}_2^{3+}\text{O}_4$. However, refinement of the site occupancies shows a composition of $(\text{Mg}_{0.91 \pm 0.01}^{2+}\text{Mn}_{0.09 \pm 0.01}^{2+})\text{Mn}_2^{3+}\text{O}_4$ (Table 3.6), which suggests an overall Mn deficiency in the starting composition; this could arise from the excess hydration of the starting $\text{Mn}(\text{NO}_3)_2$ precursor (nominally tetrahydrate). Due to the low calcination temperature, the peaks are inherently broad and good fit could not be obtained.

Evidence for presence of this tetrahedral Mn^{2+} comes from the magnetic susceptibility data (Figure 3.8). In an ordered normal MgMn_2O_4 spinel, the tetragonal Jahn-Teller distortion of Mn^{3+} ions results in four nearest neighbour interactions J_1 along the a and b axes and two second nearest neighbour interactions J_2 along the c axis (Figure 3.1c). Despite the fact that these values are not straightforward to obtain from experiments without a good model for the magnetic exchange, we should expect a maximum below the magnetic ordering transition in the inverse susceptibility ($1/\chi$) versus temperature plot, since the exchange coupling in the octahedral sublattice is antiferromagnetic. Zero-field cooled susceptibility data, however, clearly shows presence of a ferrimagnetic component with a minimum in the plot. This behaviour is similar to Mn_3O_4 , where an antiferromagnetic coupling between the tetrahedral Mn^{2+} and octahedral Mn^{3+} causes ferrimagnetic ordering at low temperatures.[169] In addition, the fitted effective electron magnetic moment $\mu_{\text{eff}} = 5.93 \pm 0.06 \mu_B$ is clearly larger than the spin-only value of $4.90 \mu_B$ for the Mn^{3+} ion (d^4), suggesting the presence of Mn^{2+} ion (d^5). Calculated spin-only magnetic moment μ_{eff} of the $(\text{Mg}_{0.81}^{2+}\text{Mn}_{0.19}^{2+})\text{Mn}_2^{3+}\text{O}_4$ and $(\text{Mg}_{0.91}^{2+}\text{Mn}_{0.09}^{2+})\text{Mn}_2^{3+}\text{O}_4$ (determined from composition and refinement, respectively) are 5.00

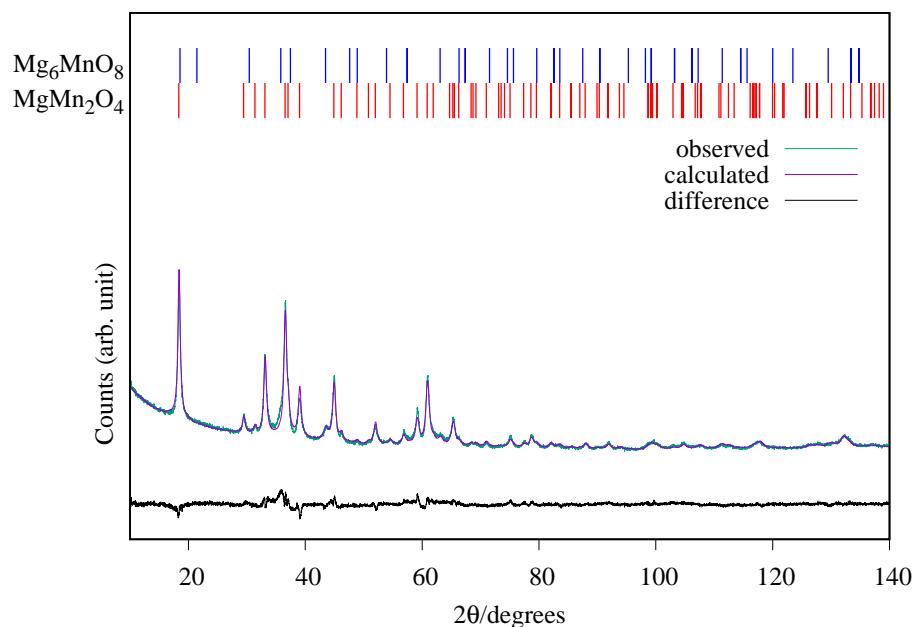


Fig. 3.7 X-ray powder diffraction pattern for MgMn_2O_4 . Collected data (red), refined data (black), and differences (lower panel) are shown. The positions of allowed reflections are indicated by the tick marks. 7.9 wt % of Mg_6MnO_8 phase was detected.

MgMn ₂ O ₄ 92.1(3) wt %					<i>I</i> ₄ ₁ / <i>amd</i> space group					
		<i>a</i> / Å	5.7274(2)	α / °	90					
		<i>b</i> / Å	5.7274(2)	β / °	90					
		<i>c</i> / Å	9.2660(5)	γ / °	90					
Atom	<i>x</i>	<i>y</i>	<i>z</i>	Occ						
Mg1 (4 <i>a</i>)	0	0.25	0.375	0.91(1)						
Mn1 (4 <i>a</i>)	0	0.25	0.375	0.09(1)						
Mn2 (8 <i>d</i>)	0	0	0	1.00(2)						
O1 (16 <i>h</i>)	0	0.51	0.2417(3)	1						
		<i>R</i> _{exp}			3.28					
		<i>R</i> _{wp}			5.43					
		χ^2			2.74					

Table 3.6 Rietveld refined parameters from the PXRD data of MgMn_2O_4 .

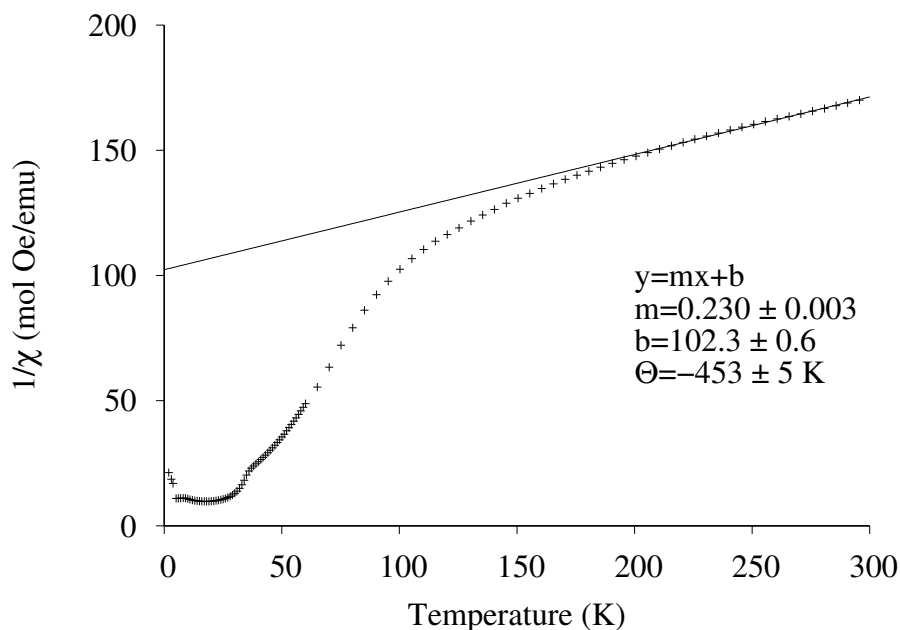


Fig. 3.8 Inverse magnetic susceptibility per mol Mn, $1/\chi$, as a function of temperature for MgMn_2O_4 .

and $4.95 \mu_B$. As for the MgCr_2O_4 case, the large discrepancy is likely due to the short-range fluctuations at $T < \Theta$.

The magnetic properties of the $(\text{Mg}_x\text{Mn}_{1-x})\text{Mn}_2\text{O}_4$ solid solution have previously been studied at $T < 60 \text{ K}$.^[169] The magnetic susceptibility is shown to be small ($< 0.1 \text{ emu/mol}$) and qualitatively similar for MgMn_2O_4 and $\text{Mg}_{0.75}\text{Mn}_{0.25}\text{Mn}_2\text{O}_4$ at 60 K. In this work we are interested in χ at 320 K (MAS frictional heating) and so will approximate our sample to MgMn_2O_4 . Finally, we note that the experimental Weiss constant $\Theta = -452.5 \text{ K}$ is consistent with a previously reported value of -500 K ,^[170] with the deviation between the two values potentially arising due to the excess Mn as discussed above. However, accurate numerical estimation of the moment from C is unlikely as the short-range ordering is still likely to exist at this temperature ($T \approx |T_N|$).

3.3.2 ^{25}Mg NMR

Mg_6MnO_8

The ^{25}Mg NMR spectrum of Mg_6MnO_8 is shown in Figure 3.9a, at 14 kHz MAS. To determine the isotropic shift, a MAT experiment was performed (Figure 3.9b) at 20 kHz MAS. The MAT spectrum (performed with the RAPT enhancement scheme as below) clearly

shows a single peak with $\delta_{iso} = 2960$ ppm in the isotropic dimension (ω_2). This clearly shows the applicability of RAPT-enhanced 2-dimensional experiments in paramagnetic systems with poor signal-to-noise ratio. RAPT-enhanced MAT experiments could be especially useful in determining isotropic resonances, since the conventional method of performing MAS experiments at two different spin rates (hence different degree of frictional heating) is not straightforward due to the strong temperature dependence of the shift tensor.

Determination of quadrupolar parameters from paramagnetic NMR spectra is considered to be difficult, as the characteristic quadrupolar patterns are often smeared out due to paramagnetic broadening of the spectra. We used the RAPT pulse sequence, which was previously used to estimate ^{27}Al quadrupolar parameters in diamagnetic samples,[137] to estimate the quadrupolar coupling constant, C_Q , of the Mg site in Mg_6MnO_8 . For optimum enhancement, the modulation frequency ν_m of saturating pulse trains alternating in phase ($+\pi/2$, $-\pi/2$) should match the value of $\nu_Q/2 = 3C_Q/40$ (for $I = 5/2$), where ν_Q is the quadrupolar frequency of the observed nucleus given by Equation 2.58.[135] By plotting the enhancement in integrated signal intensity versus the offset frequency, we see that the maximum enhancement occurs between $\nu = 250 - 300$ kHz (Figure 3.10a). This is consistent with the DFT prediction of $\nu = 277$ kHz, or the quadrupolar coupling constant $C_Q = 3.69$ MHz (Table 3.7).

Starting from these values of δ_{iso} and C_Q , a spectral fitting was performed with quadrupolar parameters fixed to the Hyb35 calculated values. The MAS lineshape could be fitted assuming a paramagnetic shift anisotropy and a quadrupolar interaction and the fitted parameters are shown in Table 3.7. Good fitting was obtained with the quadrupolar parameters from DFT calculations, and no further attempts were made to fit the quadrupolar parameters. The spectrum is dominated by the central transition (transition between spin levels $1/2 \leftrightarrow -1/2$), which is only affected in second-order by the quadrupolar coupling, and hence (other than the linewidth of the individual peaks within the spinning sideband manifold) is relatively insensitive to the size of the quadrupolar interaction. The paramagnetic shift anisotropy, arising from the dipolar coupling to the Mn^{4+} ions, which gives rise to a lineshape identical to that observed from the chemical shift anisotropy, is clearly visible. We note that the fitted $\delta_{iso} = 2994$ ppm is slightly larger than the $\delta_{iso} = 2960$ ppm obtained from the MAT experiment above. As the slower MAS rate results in lower sample temperatures, an increase in the paramagnetic shift is expected in the 14 kHz MAS case when compared to 20 kHz MAS spectrum (*i.e.* the MAT experiment).

From the RAPT pulse sequence, a maximum signal-to-noise enhancement by a factor of close to 2 is observed (Figure 3.10b). Under ideal conditions, the RAPT pulse sequence

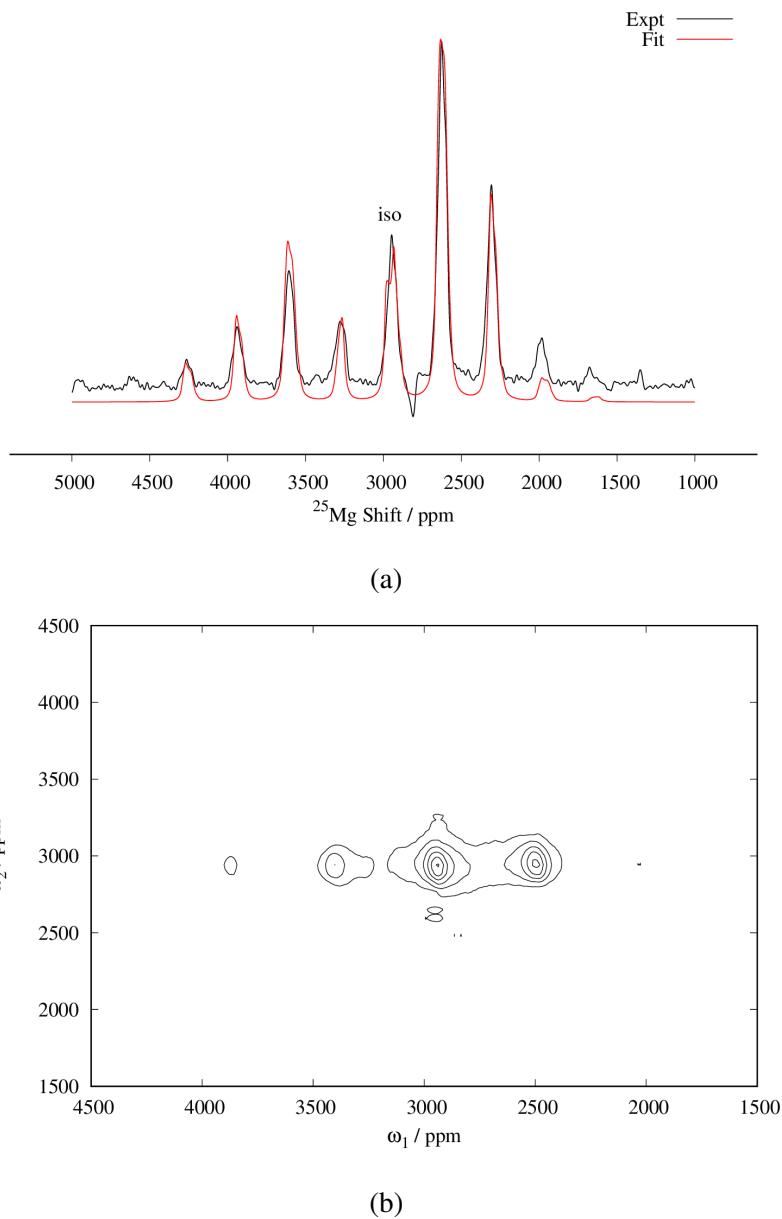
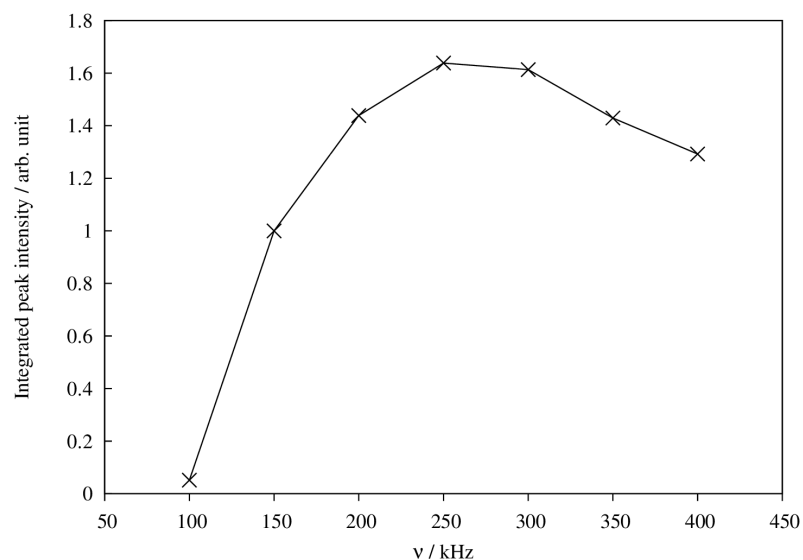
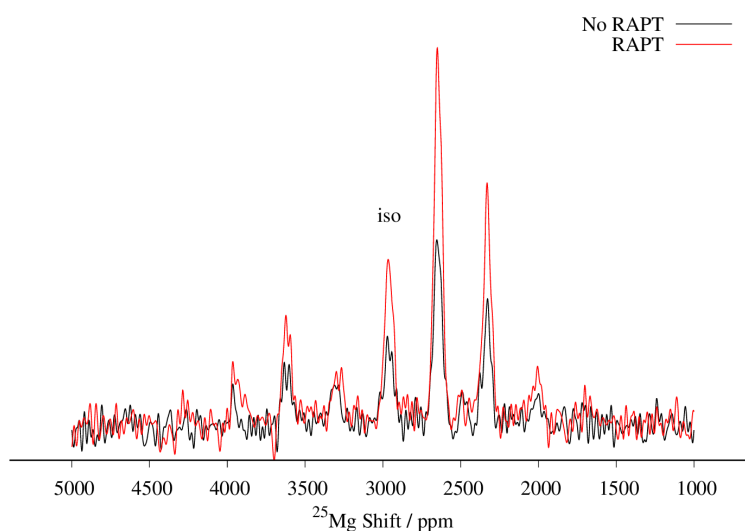


Fig. 3.9 (a) ^{25}Mg spin echo spectrum of Mg_6MnO_8 (14 kHz MAS, 81712 transients), with fitted central transition lineshape including contributions from both the paramagnetic shift anisotropy and the quadrupolar interaction (parameters are listed in Table 3.7). (b) Magic angle turning (MAT) spectrum of Mg_6MnO_8 (20 kHz MAS, 128 slices in the F1 dimension with $2.23 \mu\text{s}$ delay increment, 3072 transients acquired in each slice). RAPT pulses were applied before the MAT pulses to enhance the signal-to-noise ratio.



(a)



(b)

Fig. 3.10 (a) ^{25}Mg spin echo signal intensities of Mg_6MnO_8 with increasing offset frequency of the saturating pulse trains in the RAPT experiment. (b) Enhancement of spin echo signal intensity using the RAPT pulse. Saturating pulses were applied at a modulation frequency of 270 kHz. Both experiments were performed at MAS spin rate of 14 kHz. 1024 transients were acquired in each spectrum.

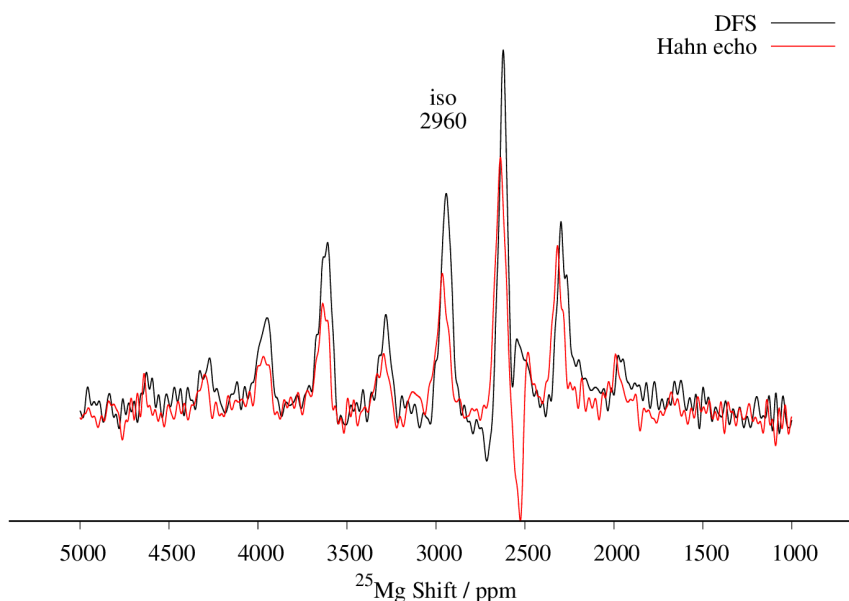


Fig. 3.11 ^{25}Mg NMR spectra of Mg_6MnO_8 , recorded with the rotor-synchronised Hahn echo and Double Frequency Sweep (DFS) pulse sequences. Signal-to-noise enhancement of around 1.5 is observed for the isotropic shift. A 36 kHz-strength DFS sweep pulse starting from an offset of 1000 kHz and ending at 100 kHz was applied for 2040 μs . 51200 transients were acquired in each case with recycle delays of 0.01 s.

should result in an enhancement factor of $I + 1/2 = 3$ for ^{25}Mg . However, due to the difficulty of saturating multiple satellite levels in a polycrystalline $I = 5/2$ system, it is not uncommon to observe enhancement factors lower than the theoretical maximum (for instance, an enhancement factor of 2 is reported for polycrystalline ^{27}Al ($I = 5/2$) spectrum in diamagnetic albite $\text{NaAlSi}_3\text{O}_8$). [135, 136] Despite the added difficulty of enhanced relaxation of the spin polarisation in paramagnetic materials, the observed enhancement factor of 2 clearly shows that the RAPT pulse sequence can be used for significant improvement in signal-to-noise ratio in paramagnetic materials.

In addition to the RAPT pulse sequence, we have also attempted a Double Frequency Sweep (DFS) enhancement scheme [138] also frequently used for quadrupolar nuclei. Only a signal-to-noise enhancement factor of around 1.5 is observed (Figure 3.11), as opposed to 2 times enhancement in RAPT. This could be explained in terms of faster paramagnetic relaxation effects present in the sample, as the DFS pulses are usually longer (around 2000 μs) to satisfy adiabaticity, whereas the RAPT pulses are shorter (around 110 μs optimised for Mg_6MnO_8).

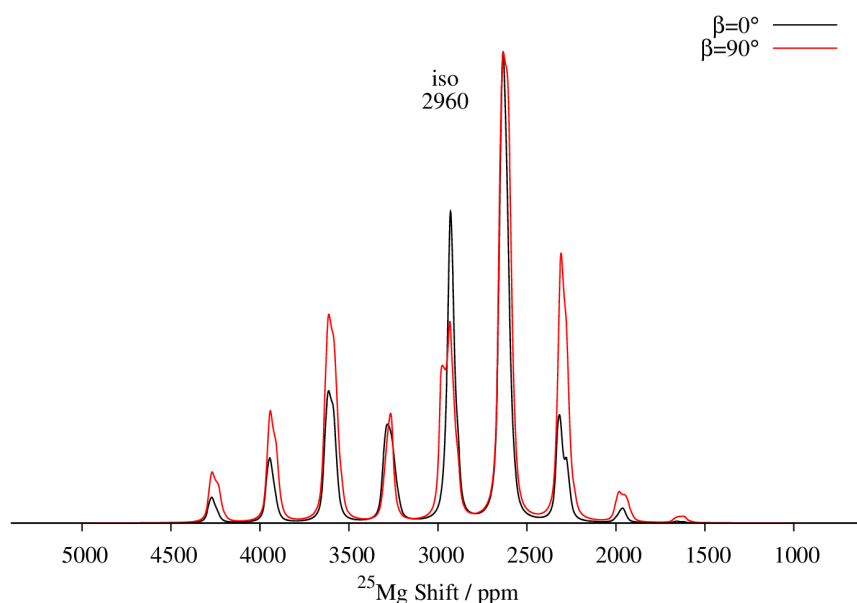


Fig. 3.12 Simulated ^{25}Mg NMR spectra of Mg_6MnO_8 , with different Euler angles β between the anisotropic hyperfine tensor and the EFG tensor in the simulation.

Based on the DFT (see below) and ^{25}Mg NMR results of Mg_6MnO_8 , we propose that Mg_6MnO_8 can be conveniently used as a model compound for paramagnetic ^{25}Mg NMR studies owing to a number of attractive properties: (1) it has six Mg atoms per formula unit and good NMR sensitivity, allowing signals to be observed with only 1024 scans at 16.4 T field; (2) it has nonvanishing quadrupolar coupling, meaning that we can study the quadrupolar behaviour of Mg atoms, which is likely to be the case for technologically important materials; (3) d^3 electron configuration of Mn^{4+} in octahedral environment eliminates the need to consider spin-orbit coupling effects in *ab initio* calculations to a good approximation; (4) the large distance (6 Å) between Mn atoms makes it a weak, well-defined paramagnet, which reduces the possible error in the paramagnetic scaling approach as taken in this work; (5) it is easy to prepare as a pure phase through solid-state reaction of corresponding oxides in air, although previous works have reported a sol-gel route [171] or calcination of carbonates under oxygen atmosphere [47]. It is also interesting to note that this compound was theoretically predicted to be a good carbon capture and storage material through a large-scale screening study.[172]

Finally, we note that the large magnitude not normally observed in shift anisotropy tensor (computational and experimental determination of chemical shift anisotropy in ^{25}Mg typically shows <100 ppm magnitude[42]) makes the relative orientation between the principle

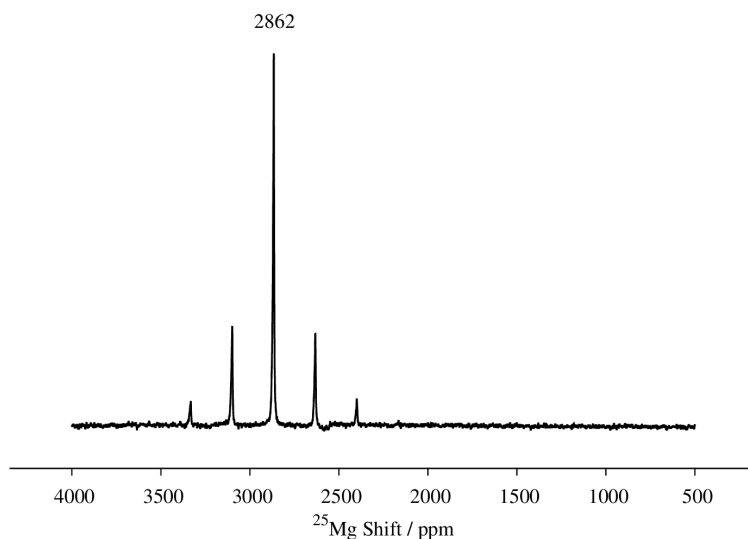


Fig. 3.13 ^{25}Mg spin echo spectrum of MgCr_2O_4 at a MAS spin rate of 10 kHz. 20480 transients were acquired. The broad feature seen around 2700 ppm is due to probe background.

components of the shift tensor and EFG tensor crucial. Figure 3.12 shows the effect of changing the Euler angle β (the angle between the largest shift and EFG principal components) on the simulated spectrum. As the paramagnetic contribution to the shift anisotropy is typically much larger than the corresponding CSA for many nuclei, determination of the Euler angles by DFT methods is crucial for accurate simulation/fitting of the spectra. This is also evidenced by a recent study of paramagnetic ^{17}O spectra of Li_2MnO_3 , where the observed and fitted spectra strongly depends on the two tensor orientations.[173]

MgCr_2O_4

MgCr_2O_4 adopts a cubic AB_2O_4 spinel-type structure with Mg atoms sitting on the tetrahedral ($8a$) site on the spinel lattice. Due to this tetrahedral coordination of Mg sites, the quadrupolar coupling constants C_Q are expected to be zero. The observed spectrum of MgCr_2O_4 is shown in Figure 3.13. Experimentally, the vanishingly small C_Q is confirmed by the sharp isotropic peak that does not exhibit typical quadrupolar lineshape under MAS conditions.

Tetrahedral coordination also dictates that the anisotropic (dipolar) electron-nuclear spin interaction be zero. Despite this, small nonvanishing dipolar interaction was observed ($\Omega = 840$ ppm). This discrepancy may be attributed to (i) bulk magnetic susceptibility effect which originates from inhomogeneous magnetic field due to random crystallite orientations,

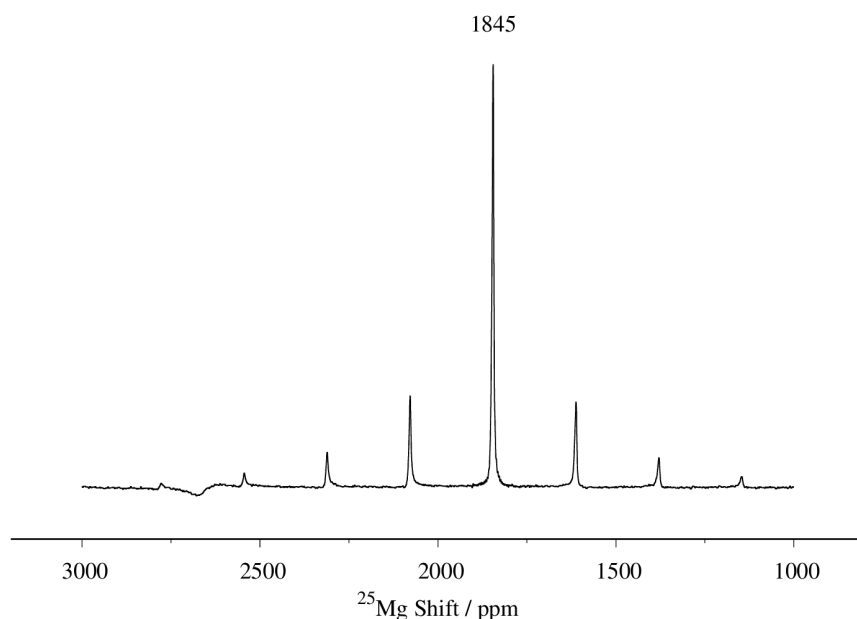


Fig. 3.14

Fig. 3.15 ^{25}Mg spin echo spectrum of SS- MgV_2O_4 (solid-state route) at MAS spin rate of 10 kHz. 505600 transients were acquired with recycle delays of 0.1 s.

as noted in previous paramagnetic MAS NMR works,[174, 175] or (ii) local defects present in the open spinel structure, resulting in breaking of the local symmetry. With the current data, it is difficult to ascertain which of these is going to be dominant; it is likely that both are responsible for the sideband intensities.

We note that Wustrow *et al.* have synthesised a MgCr_2S_4 thiospinel structure and reported the ^{25}Mg NMR resonance at 11220 ppm.[37] Variable temperature measurement indicates this shift is highly temperature dependent, which is characteristic of the Fermi contact shifts. This is clearly a large downfield shift from 2862 ppm resonance of MgCr_2O_4 , which clearly displays the more covalent nature of Cr–S–Mg bonding compared to Cr–O–Mg, which results in a larger transferred spin density and a larger hyperfine shift.

MgV_2O_4

MgV_2O_4 is isostructural with MgCr_2O_4 at room temperature, showing a cubic symmetry. Thus, the expectation for vanishing C_Q and hyperfine tensor anisotropy Ω should also hold true for MgV_2O_4 .

The observed spectrum for solid-state synthesised MgV_2O_4 (SS- MgV_2O_4), shown in Figure 3.15a, exhibits a sharp resonance at 1845 ppm, which demonstrates the small C_Q in this system. In line with the MgCr_2O_4 , nonvanishing shift anisotropy $\Omega = 672$ ppm is likely to arise from local defect or inhomogeneous magnetic fields around the crystallites.

MgMn_2O_4

The ^{25}Mg NMR spectrum of MgMn_2O_4 sample is shown in Figure 3.16a and the existence of the Mg_6MnO_8 secondary phase is clearly seen in the NMR spectrum. Fitted parameters (Table 3.7) reveal that nonzero anisotropic components in the hyperfine coupling tensor are present. As the tetragonal distortion reduces the tetrahedral symmetry of Mg sites, we should compare the anisotropy to the DFT value, which will be discussed in detail in the DFT section below. In addition, the RAPT enhancement scheme (Figure 3.16b) also shows around twicfold increase in intensity without any distortion to the sideband manifold, the offset used in the sequence again being chosen on the basis of the DFT-calculated C_Q value. This clearly demonstrates the utility of RAPT pulses to paramagnetic ^{25}Mg NMR experiments.

We now compare this result to the Kim *et al.*, who have recently reported a ^{25}Mg NMR spectrum of this compound.[30] Their reported NMR spectrum at a MAS frequency of 24 kHz shows two peaks at 2980 and 2850 ppm, which they assigned to MgMn_2O_4 , the two peaks being assigned to discontinuities of a second-order quadrupolar lineshape with a C_Q of 5.4 MHz. Considering the inverse temperature dependence of Fermi contact shifts (Equation 2.76), the MgMn_2O_4 resonance frequency should occur at higher shifts in the case of the 14 kHz MAS used here. For example, assuming representative rotor temperatures of 340 K and 320 K for 24 kHz and 14 kHz MAS, respectively, and using experimental value of Θ , our observed shift of $\delta_{iso} = 3128$ ppm at 14 kHz MAS translates to $\delta_{iso} = 3047$ ppm at 24 kHz MAS for our MAS probes. Thus, we assign their 2980 ppm peak to the Mg in MgMn_2O_4 structure, the lower shift originating from a lower sample temperature and/or slight differences in magnetic properties between samples. Considering the twicfold (*i.e.* the maximum attainable enhancement from the Mg_6MnO_8 case) enhancement in signal intensity using the RAPT pulse parameters calculated from $C_Q = 3.2$ MHz, the extra peak at 2850 ppm is not likely to arise from a MAS quadrupolar lineshape with C_Q of 5.4 MHz as suggested in their paper. Alternatively, we suggest that these peaks represent Mg sites in different coordination environments to the Mn in different oxidation states, arising from the antisite defect (Equation 1.5). We tentatively assign the peak at 2850 ppm to Mg neighbouring one Mn^{4+} and eleven Mn^{3+} , as opposed to the 2980 ppm peak where the Mg is neighbouring twelve Mn^{3+} .

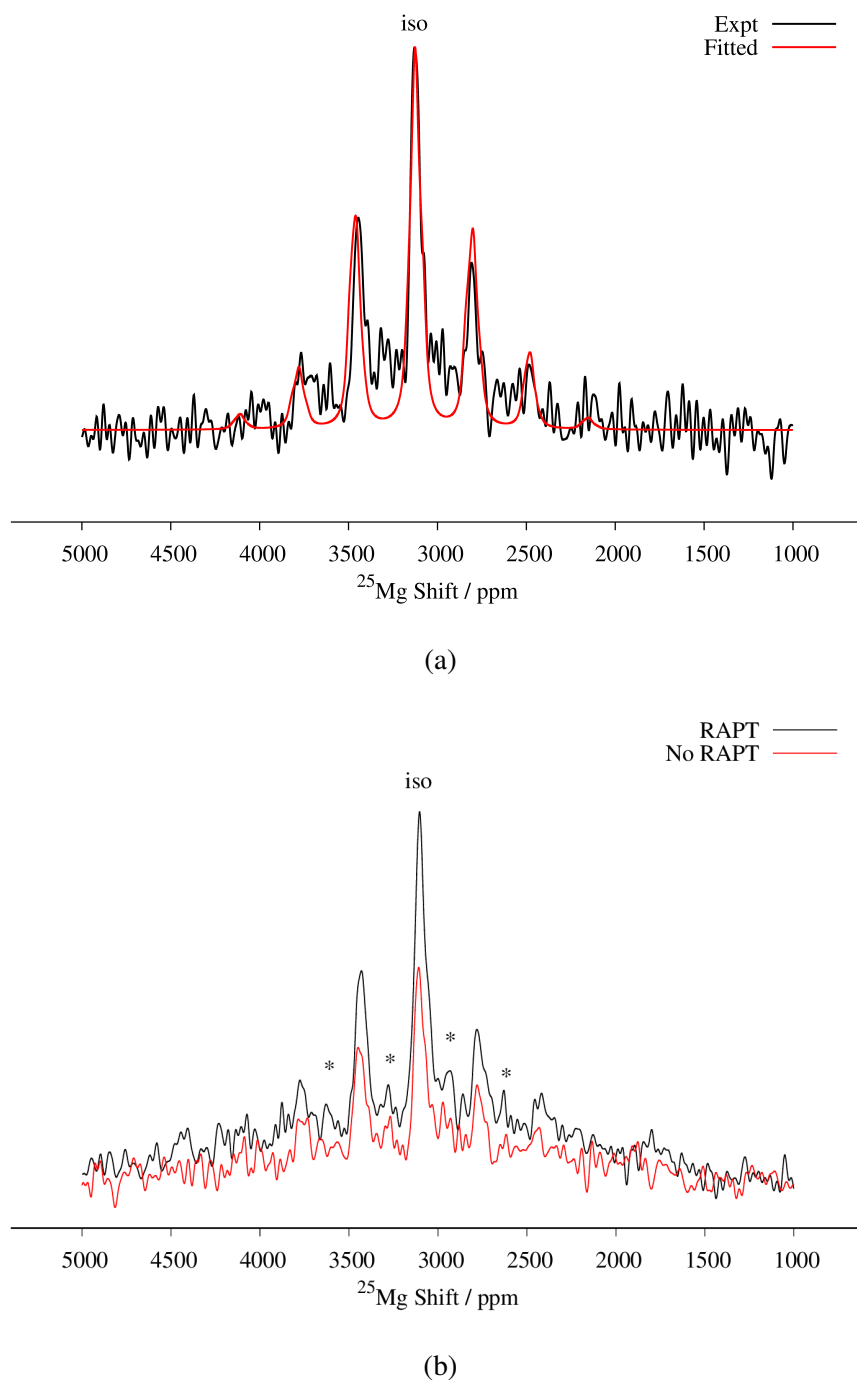


Fig. 3.16 ^{25}Mg spin echo spectrum of MgMn_2O_4 at MAS spin rate of 14 kHz. Mg_6MnO_8 secondary phase signals are shown with asterisks (*). 3550928 transients were acquired. (a) Comparison between experimental and fitted spectrum. Fitted parameters are listed in Table 3.7. (b) Enhancement of spin echo signal intensity with RAPT pulse sequence. RAPT modulation pulses were applied at 240 kHz. 1024000 transients were acquired in each spectrum.

	Mg ₆ MnO ₈		MgCr ₂ O ₄		MgV ₂ O ₄ (solid-state)		MgMn ₂ O ₄		
	Hyb20	Hyb35	Expt	Hyb20	Hyb35	Expt	Hyb20	Hyb35	Expt
Magn.									
J_1 / K	-0.7	-0.5	-0.7	-19.8	-14.8	-30.4	-45.0	-46.2	-
Θ / K	-22.5	-16.4	-21.9	-297.3	-222.2	-456.7	-448.3	-466.8	-452.5
$ \Psi_N^{\alpha-\beta} ^2 / 10^{-3} \times \text{Bohr}^{-3}$	19.5	17.4	17.0	40.4	34.1	37.9	41.2	36.1	36.1
$\Delta \Psi_N^{\alpha-\beta} ^2 / 10^{-3} \times \text{Bohr}^{-3}$	9.5	8.5	-	3.3	3.0	-	3.4	3.0	-
$\delta_{\text{iso}} / \text{ppm}$	3291	3152	2994	3842	3690	2862	2105	1840	1845
$\delta_{\text{FC}} / \text{ppm}$	3337	3199	3041	3842	3690	2862	2105	1840	1845
δ_Q / ppm	-46	-47	-47	0	0	0	0	0	0
Ω / ppm	2110	2297	1930	0	0	840	0	0	672
κ	-0.84	-0.82	-0.84	-	-	1.0	-	-	-0.75
C_Q / MHz	3.64	3.69	3.7*	0	0	0	0	0	0
η_Q	0.40	0.38	0.38*	-	-	-	-	-	-
α		270 ^{o*}		-	-	-	-	-	0 ^{o*}
β		90 ^{o*}		-	-	-	-	-	0 ^{o*}
γ		90 ^{o*}		-	-	-	-	-	42 ^{o*}

Table 3.7 *Ab-initio* calculated and experimentally fitted paramagnetic NMR parameters of Mg₆MnO₈, MgCr₂O₄, MgV₂O₄, and MgMn₂O₄. Hyb20 and Hyb35 refer to the degree of Hartree-Fock exchange energy (see methods). Values marked with asterisks (*) were fixed in the fitting. For MgV₂O₄, the experimental Weiss constant was obtained from literature.[164] EFG tensor eigenvalues and anisotropic hyperfine tensor components are near zero for MgV₂O₄ and MgCr₂O₄ and Euler angles are not reported for these systems. Detailed magnetic characterisation data are reported in Table 3.3.

3.3.3 DFT Calculation of NMR and Magnetic Parameters

We now discuss the *ab initio* results on the compounds studied above. DFT calculated values of magnetic parameters and paramagnetic NMR shifts are shown in Table 3.7.

Mg₆MnO₈

Good agreements between the *ab initio* values of NMR and magnetic parameters are seen, with the experimental shift lying between the Hyb20 and Hyb35 calculated values. In particular, the anisotropy parameter Ω and κ shows good agreement, despite the difficulties in obtaining good anisotropy parameters from powder MAS patterns in paramagnetic systems. Considering the possible origins of the discrepancies as discussed above, the dilute nature of paramagnetic spins in the Mg₆MnO₈ structure and close-packed rocksalt type structural arrangement are likely to be responsible for this good agreement.

MgCr₂O₄ and MgV₂O₄

The exchange coupling constant J_1 for MgCr₂O₄ determined from DFT (-19.8 K for Hyb20 and -14.8 K for Hyb35) and experiment (-30.4 K) shows that the magnitude of this exchange is strong and antiferromagnetic as expected. The experimentally measured and calculated J_1 values, while of the same order of magnitude, differ by around a factor of 2. The differences between the two values are ascribed to the difficulties in modelling the frustrated pyrochlore lattice with a simple Ising-type spin model at 0 K with DFT. A Heisenberg-type spin model would be more appropriate, but this is not supported by the current version of CRYSTAL. Consistent with this proposal, a previous plane-wave DFT calculation on this compound using the Heisenberg model has yielded a value close to the experimental value, $J_1 = -26.5$ K.[176] However, we note that the isotropic shift calculated using the DFT-predicted spin density $|\Psi_N^{\alpha-\beta}|^2$ and the experimental Weiss constant $\Theta = -456.7$ K is close to the *ab initio* value (3053 ppm, 2576 ppm, and 2862 ppm for Hyb20, Hyb35, and experimental, respectively). This shows that accurate determination of magnetism is key to *ab initio* calculation of paramagnetic shifts.

For MgV₂O₄, an *ab initio* prediction of magnetic parameters could not be made due to SCF instabilities in the supercell structure. However, a reasonable estimate of the paramagnetic shift could still be made from a previous experimental measurement of Weiss constant $\Theta = -600$ K.[164] Despite the fact that spin-orbit interactions at the d^2 center may influence the shift, calculations involving explicit spin-orbit coupling Hamiltonian could not be performed in the present version of CRYSTAL. Despite this limitation, the shift

values obtained without any correction for spin-orbit coupling shows a close match with the experimental result. Mulliken spin population analysis (Table 3.8) and the spin density map (Figure 3.17d) of the converged wavefunction shows equal occupation of the three t_{2g} orbitals d_{xy} , d_{yz} , and d_{zx} (which is expected, since we have preserved the cubic symmetry of the experimental cell). As discussed in the preceding section, this is likely to arise from the fact that the spin-orbit coupling is relatively weak for a V^{3+} ion (spin-orbit coupling constant $\lambda = 104 \text{ cm}^{-1}$ for free ion, 95 cm^{-1} when doped into Al_2O_3).^[177] Hence the energy levels split by spin-orbit coupling are equally occupied. It is thought that the *ab initio* result reflects this average occupation in effect, producing results close to the experimental values.

Finally, we note that in both cases DFT predicts zero paramagnetic shift anisotropy, which reflects the tetrahedral symmetry of Mg sites. As discussed above, this discrepancy is attributed to both the bulk susceptibility effect and local defects in the open spinel structures.

MgMn₂O₄

As values of J_1 and J_2 cannot be obtained from experiments without a good model to fit the susceptibility data, they were calculated from DFT. DFT Values of J_1 and J_2 for MgMn_2O_4 differ roughly by an order of magnitude ($J_1 = -45.0 \text{ K}$, $J_2 = -5.5 \text{ K}$ for Hyb20 and $J_1 = -46.2 \text{ K}$, $J_2 = -6.1 \text{ K}$ for Hyb35). As magnitudes of exchange interactions are known to be very sensitive to bond lengths, $|J_1| > |J_2|$ as expected. In this case, the tetragonal distortion effectively reduces the frustration and the main J_1 exchange occurs along the Mn chain (see Figure 3.17f), with J_2 perturbations between the chains. This explains the good agreement of DFT calculated Weiss constant Θ to the experimental value (-448.3 , -466.8 , and -452.5 K for Hyb20, Hyb35, and experimental, respectively)

Paramagnetic NMR shifts calculated using these values also show good match to the experimental value, where the experimental shift is between the Hyb20 and Hyb35 calculated values. However, again we see a discrepancy in the anisotropic shift parameter, similar to the result for other spinels MgCr_2O_4 and MgV_2O_4 . The discrepancy is also attributed to inhomogeneous magnetic field created by random crystallite orientations and local defects. These effects are more significant in the MgMn_2O_4 sample, as the low-temperature preparation condition results in (i) smaller crystallites, which increases the magnetic field inhomogeneity, and (ii) higher concentration of defects present in the sample.

3.3.4 Shift Mechanism and the Fermi Contact Pathways

We now turn our attention to the factors determining these large paramagnetic shifts and how they might be rationalised in terms of electronic structures. Paramagnetic NMR shifts in various Li transition metal oxides have been ascribed to the Fermi contact (FC) mechanism.[144] In this framework, a superexchange-like mechanism operates between the TM t_{2g}/e_g and the Li s orbital, resulting in small amounts of paramagnetic electron spins on the Li nucleus. As a similar kind of mechanism is expected to be responsible for paramagnetic Mg shifts, understanding the shift mechanism is important for rationalising both the sign and magnitude of shifts.

As shown in Equation 2.80, factors contributing to the Fermi contact shift can be separated into the spin density transfer $|\Psi_N^{\alpha-\beta}|^2$ (in units of Bohr $^{-3}$), and electron paramagnetism. Considering the expression for Θ , we can observe that metal ions with larger S are expected to give larger Fermi contact shifts, due to the μ_{eff} factor. This factor only depends on the formal spin of metal ions involved. On the other hand, Fermi contact spin density transfer depends heavily on the geometry of TM–O–Mg pathway. Here we can evaluate the contributions of each FC pathway P as $\Delta|\Psi_N^{\alpha-\beta}|^2$, which sums up to $|\Psi_N^{\alpha-\beta}|^2$. This is important since pathways with similar bond lengths and angles should contribute similar amounts of spin density to the observed nucleus. With sufficient amount of experimental and *ab initio* data, a database can be constructed which can give approximate shifts for novel structures without the need for further first principles calculations.

3-dimensional maps of electron spin density obtained from DFT wavefunctions are shown in Figure 3.17. From the spin density maps, it is clear that a delocalisation mechanism involving the t_{2g} orbitals is in operation for all four compounds, resulting in positive spin density $|\Psi_N^{\alpha-\beta}|^2$ on the nucleus. This is particularly evident in the Mg_6MnO_8 case, where a 95° interaction along the TM–O–Mg pathway (P_1 in Figure 3.1a) results in p orbitals with positive spin density pointing directly towards the Mg site (Figure 3.17a). We also note that p orbitals with negative spin density all point towards the vacancy site, which would result in a negative shift mediated by polarisation mechanism, had this site been occupied. Also large differences in spin densities are observed between the two crystallographically distinct oxygen sites O1 and O2, where essentially no spin is observed on the O2 site. This originates from the fact that O2 is only surrounded by Mg in its first coordination shell due to the ordered cation arrangements in the defect rocksalt structure (Figure 3.17b).

The situation in spinels is more complex, as the TM–O–Mg pathway is no longer near 90° . Here, both delocalisation ($t_{2g} - p_\pi - s$) and polarisation ($e_g - p_\sigma - s$) mechanisms are likely to operate along the P_1 pathway (Figure 3.1b), resulting in a transfer of positive and

	d_{xy}	d_{yz}	d_{zx}	$d_{x^2-y^2}$	d_z^2
MgV ₂ O ₄	0.625	0.625	0.625	0.056	0.056
MgMn ₂ O ₄	0.934	0.934	0.919	0.143	0.855

Table 3.8 Mulliken spin population analysis of transition metal d orbitals in selected spinel compounds.

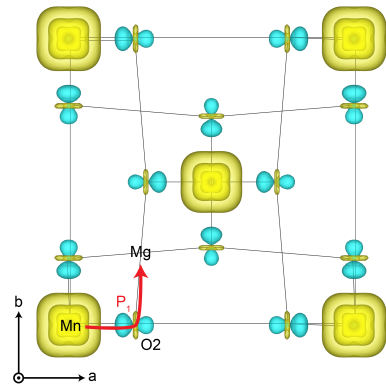
negative spins on Mg, respectively. Hybridisation of the oxygen orbital is evident, as the main lobe points towards the Mg atom in the case of cubic spinels MgCr₂O₄ and MgV₂O₄ (Figures 3.17c and 3.17d, respectively). In both cases where we have no ambiguity in the t_{2g} orbital occupation, it is clear that the delocalisation mechanism is dominant, resulting in positive spin density on Mg.

A similar analysis could be done for tetragonal spinel MgMn₂O₄ where we have a Jahn-Teller distorted Mn³⁺ ion (d^4), but the d orbital occupancies need to be determined. A close examination of the spin density map (Figures 3.17e and 3.17f) and Mulliken spin population analysis (Table 3.8) reveals that the valence electron configuration for Mn is $d_{xy}^1 d_{yz}^1 d_{zx}^1 d_z^2$, showing occupation typical of a positive Jahn-Teller elongation. This has important implications for the FC mechanism, as we have two distinct FC pathways P_1 and P_2 as a result of the Jahn-Teller distortion. P_1 lies on the crystallographic a, b -plane and P_2 points along the c -axis in the crystal structure (Figure 3.1c). In both cases, the occupied d_z^2 orbital on Mn³⁺ is likely to contribute a positive spin density to the oxygen along the c -axis (delocalisation), whereas the empty $d_{x^2-y^2}$ orbital will contribute negative spin density to the oxygen along the a -axis (polarisation). Again, examination of the spin density map reveals that the dominant shift mechanism is also the delocalisation mechanism in both cases, with the oxygen p_z orbital playing the most significant role. Large contribution from the $d_z^2 - p_\sigma - s$ pathway is evident. A noticeable negative spin density is observed on oxygen positions (resulting from polarisation along the $e_g - p_\sigma$ pathway), although this does not contribute significantly to the shift.

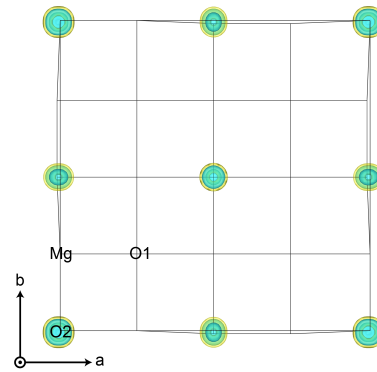
By obtaining the spin density contributions $\Delta|\Psi_N^{\alpha-\beta}|^2$ from each FC pathways (P), magnitudes of the observed shifts could be rationalised. Comparing the first-order contribution P_1 of two d^3 ions, Cr³⁺ in MgCr₂O₄ and Mn⁴⁺ in Mg₆MnO₈ (Table 3.7), a significant decrease in spin density transfer could be observed in the former case. In Mg₆MnO₈, each Mg atom is bonded to two Mn⁴⁺ ions *via* two 95° TM–O–Mg bonds. In terms of spin densities, pathway decomposition shows that each Mn⁴⁺ contributes approximately $P_1 = 9.5 \times 10^{-3}$ Bohr⁻³ (Hyb20) or 8.5×10^{-3} Bohr⁻³ (Hyb35) to Mg. In MgCr₂O₄ where each Mg is bonded to 12 Cr³⁺, each Cr³⁺ contributes approximately $P_1 = 3.3 \times 10^{-3}$ Bohr⁻³

(Hyb20) or $3.0 \times 10^{-3} \text{ Bohr}^{-3}$ (Hyb35). This is rationalised by the differences in bond angles: as shown by Carlier *et al.*, 90° interactions between the TM t_{2g} and observed nucleus result in positive spin transfer *via* a delocalisation mechanism, whereas 180° interactions result in negative spin transfer *via* a polarisation mechanism.[144] In Mg_6MnO_8 , near 90° interactions dictate that the delocalisation mechanism should be the dominant spin transfer mechanism, whereas in MgCr_2O_4 both delocalisation and polarisation mechanism should be in operation due to the 121° bond angle. The polarisation mechanism partially cancels the delocalisation mechanism, resulting in small spin density transfer in MgCr_2O_4 .

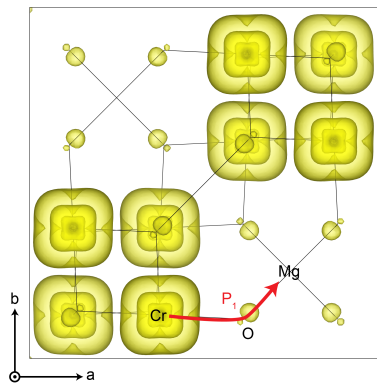
In MgMn_2O_4 , the Jahn-Teller elongation dictates that $a > c$. Due to the occupation of d_{z^2} orbital and bond elongation, we expect $P_1 > P_2$. Values of P_1 and P_2 cannot be gained from experiments and need to be determined *ab initio*. The DFT calculation shows that the first contribution is roughly 1.5 times larger in terms of spin density contribution ($P_1 = 4.0 \times 10^{-3}$ versus $P_2 = 2.6 \times 10^{-3} \text{ Bohr}^{-3}$ for Hyb20 and $P_1 = 3.3 \times 10^{-3}$ versus $P_2 = 1.8 \times 10^{-3} \text{ Bohr}^{-3}$ for Hyb35, respectively). As for the case of magnetic exchange coupling (see above), magnitude of the FC interaction is very sensitive to bond distances, which explains the difference.



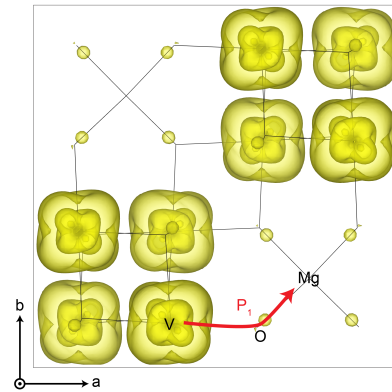
(a) Projections of the Mg_6MnO_8 (001) plane along the c -direction



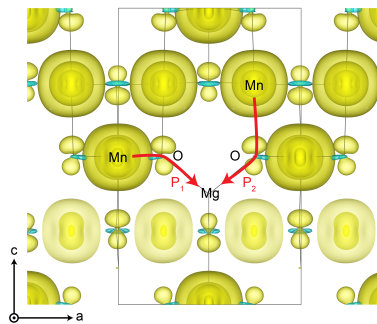
(b) Projections of the Mg_6MnO_8 $(00\frac{1}{4})$ plane along the c -direction



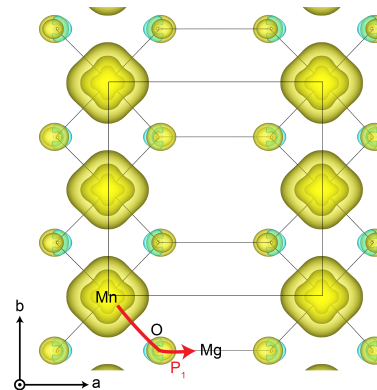
(c) Projections of the MgCr_2O_4 cubic cell along the c -direction.



(d) Projections of the MgV_2O_4 cubic cell along the c -direction.



(e) Projections of the MgMn_2O_4 tetragonal cell along the a -direction.



(f) Projections of the MgMn_2O_4 tetragonal cell along the c -direction.

Fig. 3.17 3-dimensional spin density maps. Yellow denotes positive spin; blue denotes negative spin. Bounding box refers to the unit cell and solid lines connecting atoms refer to the metal-oxygen bonds. Bond pathway contributions P to the spin density are shown in red.

3.4 Conclusion and Outlook

In this chapter, a combined DFT and experimental NMR approach to studying ^{25}Mg NMR spectra in paramagnetic TM oxides is demonstrated. Application of advanced NMR pulse sequences such as RAPT and MAT are also demonstrated to be viable for using in paramagnetic systems. Experimentally, it is shown that signal-to-noise enhancement is possible in paramagnetic Mg systems with RAPT pulses, allowing us to perform a 2-D MAT experiment on samples with natural ^{25}Mg abundances. While MAT is not strictly necessary to obtain the isotropic shift in the Mg_6MnO_8 case, we note that MAT experiments were used in the ^{23}Na NMR of related Na-ion battery materials to successfully deconvolute the complex spectra comprising multiple sites and sidebands.[93] DFT calculation of ^{25}Mg NMR parameters using the paramagnetic scaling approach is demonstrated with good agreement with the experiment. Comparison of the ^{25}Mg shifts in spinel and Mg_6MnO_8 compounds shows that TM-O-Mg 90° interaction results in stronger Fermi contact spin transfer, as expected from previous studies.

For spinel compounds MgCr_2O_4 and MgV_2O_4 , comparison of the experimental results (NMR, SQUID magnetometry) and DFT calculations show that NMR anisotropy parameters are difficult to determine from the experiments due to the bulk magnetic susceptibility effects. In addition, DFT prediction of magnetism is difficult due to the magnetic frustration of these structures. Despite these difficulties, we show that reasonable predictions of ^{25}Mg shifts can be made with the DFT values of spin density and the Weiss constant measured from SQUID magnetometry.

With the aid of DFT calculations and RAPT pulse sequence as shown above, it is possible to predict and acquire paramagnetic ^{25}Mg spectra with signal-to-noise enhancement factors of 2. Good agreements are observed between the DFT predicted values of magnetism and NMR shifts, with the exception of NMR anisotropy parameters. This approach enables us to record and interpret the paramagnetic ^{25}Mg spectra of other complex Mg compounds, which are more difficult to understand without the aid of DFT calculation.

Chapter 4

Carbothermal Synthesis and Characterisation of MgV_2O_5 , a Potential Mg-ion Battery Cathode Material

4.1 Introduction

As introduced in Chapter 1, computational works have identified $\delta\text{-MgV}_2\text{O}_5$ as a promising MIB cathode material with a relatively low migration barrier (0.6-0.8 eV) and high redox potential (>3 V). Two computational studies were reported on this compound which adopts a layered structure with potential 1-dimensional diffusion channels for the Mg^{2+} ions.[67, 68] This material is a natural extension from $\alpha\text{-V}_2\text{O}_5$, which previously showed reversible Mg insertion up to $\text{Mg}_{0.5}\text{V}_2\text{O}_5$ at a potential of 2.3 V vs Mg/Mg^{2+} .

Despite the promising computational predictions, no literature has been reported to date on the synthesis and cycling of $\delta\text{-MgV}_2\text{O}_5$ phase in Mg-ion cells. Apart from the evident challenges in obtaining suitable high-voltage electrolytes, this may be partly due to the difficulty in preparing a pure phase MgV_2O_5 : previous reported (impure) phases were prepared under a sealed quartz ampoule. This challenge, combined with the inherent unscalability of the sealed tube method, calls for a reliable approach for preparing these type of compounds.

In this regard, the present chapter attempts a comprehensive investigation of MgV_2O_5 , from synthesis to NMR, magnetic, and electrochemical characterisation. In the first part, a Hybrid eigenvector-following (HEF) approach is used to calculate the Mg migration barriers in MgV_2O_5 at various levels of theory to verify the previous results. Subsequently,

DFT-based computation of free energies are used to rationally design the synthetic steps leading to MgV₂O₅, using carbon as the reducing agent. An extension of this method to one other vanadate phase, MgV₂O₄, is also discussed. Characterisation of the product using X-ray diffraction and ²⁵Mg NMR spectroscopy follows the synthesis, combined with an initial electrochemical cycling data. Finally, *ab initio* prediction on the magnetic coupling and hyperfine NMR shift is presented. The chapter concludes with a discussion on the electrochemistry of MgV₂O₅ and prospects of extending this approach to other candidate cathodes for Mg-ion batteries.

4.2 Methods

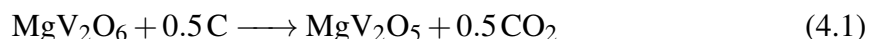
4.2.1 Materials Synthesis

Here we outline the steps toward the syntheses; detailed reasoning behind the reaction temperatures is presented in the Results section.

Syntheses of MgV₂O₅ and MgV₂O₄

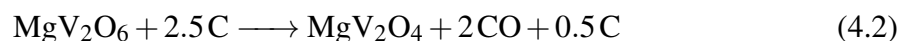
MgV₂O₆ precursor. Polycrystalline MgV₂O₅ and MgV₂O₄ samples were prepared by carbothermal reduction of microcrystalline MgV₂O₆ precursor (detailed rationale behind the synthetic procedure are discussed in the results section). MgV₂O₆ precursor was synthesised using a citrate sol-gel method. Mg(CH₃COO)₂ · 4H₂O (Sigma-Aldrich, 98 %), V₂O₅ (Sigma-Aldrich, 99.9 %), and anhydrous citric acid (Breckland Scientific, 99 %) were dissolved in a molar ratio of 1:1:4 in deionised water. After heating under stirring to remove acetic acid and water, the resulting gel was decomposed at 623 K for 6 hours. The collected ash was finally annealed at 873 K for 24 hours to yield MgV₂O₆ as a yellow powder.

MgV₂O₅. The above MgV₂O₆ precursor was mixed intimately with a stoichiometric quantity of high surface-area Super P carbon (Timcal) with the stoichiometry according to the following equation:



The mixture was then pressed into a pellet and placed in an alumina boat under an atmosphere of flowing Ar gas by means of a quartz tube. The pellet was subsequently heat-treated at 873 K for 24 hours followed by an additional annealing at 1173 K for 12 hours to yield MgV₂O₅. The obtained MgV₂O₅ powder was green, consistent with previous reports.[69, 178]

MgV₂O₄. The above MgV₂O₆ precursor was mixed with Super P carbon (Timcal) with the following reaction stoichiometry:



A 25 % excess carbon was used in this case to improve the conductivity of final product. The mixture was then pressed into a pellet and placed in an alumina boat under an atmosphere of flowing Ar gas. The pellet was subsequently heat-treated at 1173 K for 24 hours to yield MgV₂O₄. The obtained MgV₂O₄ powder was black, consistent with previous reports; [165, 166] however, presence of residual carbon may contribute to this colour. Synthesised samples were checked using a PANalytical Empyrean powder X-ray diffractometer (Cu K_{α} =1.5406 Å) and the structures were refined from their diffraction patterns by using the Rietveld method as implemented in the X'pert Highscore Plus software.

TGA measurements

A thermogravimetric analyser (TGA/DSC 1, Mettler Toledo) was used with a nitrogen flow of 80 mL/min and 5 K/min temperature ramping from the ambient temperature to 573 K. The sample was loaded in a 70 μ L alumina crucible.

4.2.2 Magnetic Measurements

Magnetisation measurements were performed on a Quantum Design Magnetic Property Measurement System (MPMS) with a SQUID magnetometer. Magnetic moments of zero field-cooled samples were measured at temperatures from 2 K up to 301 K in a field of 1000 Oe to obtain the dependence of magnetic susceptibility $\chi(T) = dM/dH \approx M/H$ (low-field approximation) on temperature.

4.2.3 ²⁵Mg NMR Spectroscopy

NMR experiments were performed on a 16.4 T Bruker Avance III spectrometer operating at a Larmor frequency of 42.9 MHz for ²⁵Mg with a Bruker 3.2mm triple resonance MAS probe. The pulse amplitude of 33.3 kHz was calibrated on solid MgO, which also served as a secondary shift reference of 26 ppm. CT-selective $\pi/6$ -pulses were used for the rotor-synchronised spin echo pulse sequence.

Rotor-assisted population transfer (RAPT) pulse sequence using a train of frequency-switched Gaussian pulses (FSG-RAPT) was used.[179] In total, 40 Gaussian pulses with

5 kHz amplitude and 16 μ s length were used to excite the satellite transitions; the number of Gaussian pulses and their offset frequencies were optimised for maximum enhancement. Spectrum fitting was performed with the Bruker Topspin 3.0 software.

4.2.4 Computational Methods

Free energy calculations

Cohesive energies of compounds MgV₂O₄, MgV₂O₅, and MgV₂O₆ were calculated with the CRYSTAL17 code. Standard B3LYP functional was used with POB-TZVP basis sets.[180] Cells were relaxed to the CRYSTAL default convergence criteria with a $4 \times 4 \times 4$ Monkhorst-Pack k -sampling,[181] 0.0003 a.u. root-mean-square gradient, and 10^{-6} hartree limit on electronic convergence. Temperature-dependent free energies of C, O₂, CO, and CO₂ were obtained from a published reference table.[182] We note that the entropic contribution to the free energy is expected to be significant, so simple formation energies cannot be used in these cases.

For carbon, free energies determined for the crystalline graphite were used; in practice, high surface area carbons such as Super P are noncrystalline and may deviate from the values determined for graphite. The difference in free energy, however, is expected to be minor compared to the energy scales (hundreds of kJ/mol) considered here: the enthalpy for a glassy (vitreous) carbon is measured to be only 0.4 kJ/mol higher than a graphite and the entropy at 0 K is estimated to be only 1-3 J/mol K.[183, 184]

Computation of NMR and magnetic parameters

Calculations were performed in CRYSTAL17 using a dual-basis set scheme as previously described.[185] A smaller basis set (BS-I) taken from works of Dovesi, Harrison, and Bredow[186, 187, 188] was used to relax the cell to CRYSTAL17 convergence limit with an electronic convergence criterion of 10^{-7} hartree. Spin-polarised B3LYP functional with 20 % and 35 % of Hartree-Fock exchange were used (Hyb20 and Hyb35, respectively). Monkhorst-Pack k -sampling[181] of $6 \times 2 \times 2$ was used. The resulting cell was expanded $3 \times 1 \times 1$ -times to generate a supercell for hyperfine and magnetic calculations.

Hyperfine and magnetic calculations were performed with more extensive BS-II sets taken from Mg (TZDP), V (DZP), and O (IGLO-III),[189, 190] consistent with previous studies on paramagnetic NMR of Mg TM oxides.[38] For magnetic exchange J calculations, a linear regression method was used on a set of energies calculated on different spin configurations.

Eight such configurations were used for the regression. The resulting values of J were used in a self-consistent mean-field theory code* to obtain the Curie-Weiss constant Θ .

Determination of the linear-response Hubbard- U parameter

To correct the self-interaction error in GGA-type functionals, we used the rotationally invariant Hubbard U correction by Dudarev *et al.*[80] We determined the $U_{\text{eff}} = U - J$ through the linear-response method of Cococcioni and de Gironcoli.[82, 75] Unit cell as determined by Millet *et al.*[69] was expanded $3 \times 1 \times 1$ -times to build a supercell onto which the perturbative potential α was applied. Twelve values of α were used to determine the changes in the d -orbital occupation.

Calculation of Mg-ion migration barrier

The hybrid eigenvector-following approach was used to locate the transition state as implemented in the OPTIM code.[113, 191] A low-memory Broyden-Fletcher-Goldfarb-Shannon scheme was used for finding the uphill path (root-mean-square gradient is less than 0.025 eV/\AA). Up to five LBFGS minimisation steps are performed in the tangent direction until the root-mean-square gradient $< 10^{-3} \text{ eV/\AA}$. The steepest descent pathway was found by displacing the moving atom (Mg) by 0.1 \AA from the transition state along the parallel and antiparallel directions to the eigenvector. Local minima were found by converging the energies to 10^{-3} eV .

VASP was used for the energy and force calculations. Spin-polarised PBE, PBE+ U ($U_{\text{eff}} = 3.55 \text{ eV}$ as fitted by a linear response method), vdW-DF2+ U (vdW-DF2), and HSE06 functionals were used.[192, 86, 193, 194] For the hybrid HSE06 calculations, only a few selected points along the reaction pathway were selected to sample the energies due to computation cost. We note that self-consistent vdW corrections such as vdW-DF2 are necessary to account for charge separation and transfer happening in these systems, as evidenced by Li migration in graphites.[195] Parametrised corrections based on point charges such as Grimme-D3 are significantly cheaper, but they do not account for the charge transfer.

A $3 \times 1 \times 1$ -expansion of MgV_2O_5 crystallographic cell was used to calculate the migration barrier. 520 eV plane-wave energy cutoff, $2 \times 2 \times 2$ Monkhorst-Pack k -sampling, and 10^{-6} eV convergence criterion of the energy were used. The cell was relaxed to 0.01 eV/\AA . Structures were plotted using the VESTA software.

*Provided by Dr Derek Middlemiss

4.2.5 Electrochemical Testing

Due to the aforementioned difficulties in cycling materials in a Mg-ion cell, the synthesised MgV_2O_5 compound were tested in Li-ion cells to investigate the de-magnesiumation capacity. The samples were mechanically milled to reduce the particle size in a high-energy shaker mill (SPEX SamplePrep 8000M) using a ZrO_2 jar and balls. The milling was conducted in an Ar atmosphere to prevent the possible oxidation of vanadium compounds. 5 minutes of milling was followed by 5 minutes of rest period to minimise heating effects. Six such cycles were performed. The resulting material was checked with SEM and XRD to confirm the reduction in particle sizes, and NMR was performed to check any changes in the sample (Appendix A).

Self-supporting films of active material were created from 72 wt % active material, 19 wt % poly(vinylene fluoride-*co*-hexafluoropropylene (PVDF-HFP, Kynar), 9 wt % Super P carbon (Timcal), and 6 drops of dibutylphthalate (DBP, Sigma-Aldrich) in acetone to create a slurry. After thorough mixing, the slurry was cast onto a glass surface and left to dry. The resulting film was subsequently punched, washed with diethyl ether (Sigma-Aldrich) to remove DBP, dried under vacuum at 100 °C overnight, and transferred into an Ar-filled glove box (MBraun) with H_2O and O_2 levels below 0.1 ppm.

2032-type coin cells (Cambridge Energy Solutions) were assembled inside an Ar-filled glove box using stainless steel current collectors. Li metal (LTS research, 99.95 %) and 1 M LiPF_6 in 1:1 ethylene carbonate:dimethyl carbonate electrolyte (Sigma-Aldrich, battery grade) solution were used as the counterelectrode and electrolyte, respectively. Electrochemical measurement was performed on a Lanhe battery cycler (Wuhan Land Electronics Co. Ltd.) with a charging cutoff of 4.4 V.

4.3 Results

This section is divided into three parts. We start by discussing the computational work on MgV_2O_5 , initially focusing on validating the previous report on Mg-ion migration barrier in this compound. Next, the carbothermal (CTR) synthetic approach (as introduced in Section 2.6) and rational design of the reaction conditions is presented based on the DFT-based thermodynamic energies. Following this, the prepared product is then characterised with X-ray diffraction and ^{25}Mg NMR. Electrochemical characterisation of the sample is then attempted. Finally, we also present a computational investigation on the magnetic and NMR property of this compound, aided with experimental measurements on the low-temperature

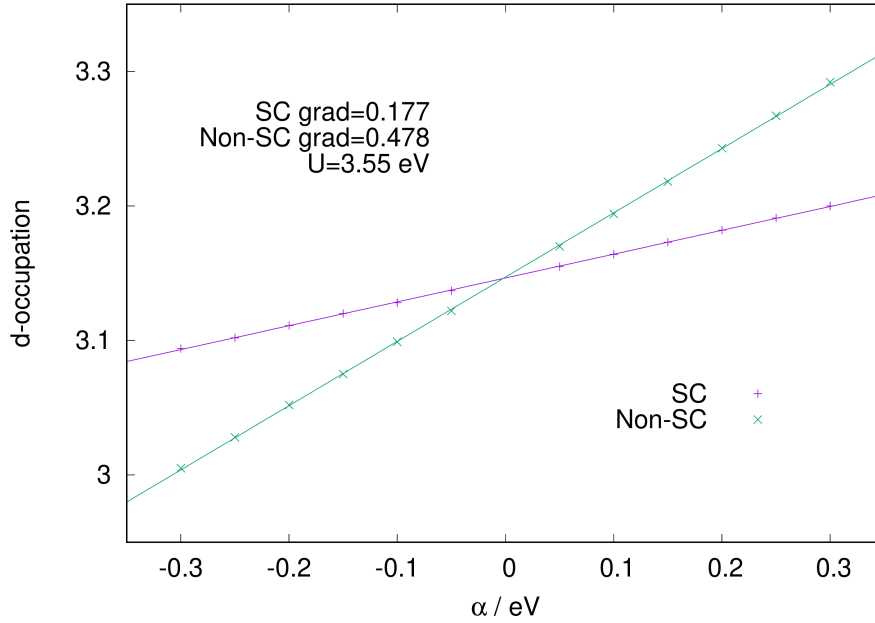


Fig. 4.1 Determination of rotationally invariant Hubbard U of V^{4+} in MgV_2O_5 by a linear response method by varying the site potential α . SC and non-SC refer to self-consistent and non-self-consistent calculations, respectively.

magnetism. We also briefly discuss the synthesis and characterisation (magnetic, NMR) of CTR-prepared MgV_2O_4 .

4.3.1 Calculation of Mg-ion Migration Barrier

Despite the previous work on MgV_2O_5 reporting a promising Mg-ion migration barrier, the authors have only used the PBE functional[67] which is known for its deficiency in accounting for the electron correlation. As charge hopping is also a crucial factor in determining the size of energy barriers involved in divalent ion diffusion,[196] calculations based on more advanced GGA+ U and hybrid functionals would be expected to give a more accurate picture of Mg-ion hopping in MgV_2O_5 . Therefore, we start by determining the U -parameter used in this approach.

Linear response determination of Hubbard U

Whereas a previous computation of the U -parameter in this system has been reported,[197] it was based on the Liechtenstein formulation of the U -correction[78] whereas we use the Dudarev formulation where only a single value U_{eff} .

Figure 4.1 shows the plot of changing the *d*-orbital occupation as a function of applied site potential α . This linear response approach yields a good linear regression of the self-consistent and non-self-consistent lines, resulting in a $U_{\text{eff}} = 3.55$ eV. This is in good agreement to the previously determined values of $U = 3.6$ eV by Korotin *et al.*[197] and is also close to the $U_{\text{eff}} = 3.1$ eV by Jain *et al.*, where an averaged value over multiple vanadium oxides were reported.[66] Hence, the determined $U_{\text{eff}} = 3.55$ eV was used for subsequent PBE+*U* calculations.

Migration of a Mg vacancy

As shown in Figure 1.4, δ -MgV₂O₅ has a 1-dimensional diffusion channel of Mg ions along the *c*-direction, which is in parallel with the direction of V₂O₅ ladder. Mg-ion diffusion in this structure has been shown to have a relatively low barrier of 0.6-0.8 eV, which is remarkable for a diffusion of divalent ions in an oxide structure. The following results attempts to validate this result using a single-ended transition state searching with considerations of coupled charge and ion hopping. We start with the fully discharged structure MgV₂O₅, in which a Mg vacancy diffuses through the cell.

Figure 4.2a shows the energy profile of a vacancy diffusion in a fully magnesiated phase. To evaluate the effect of functionals on the observed energy, a variety of functionals were investigated: hybrid HSE06, GGA PBE, Hubbard-*U* corrected PBE+*U*, and van der Waals (vdW) corrected vdW-DF2+*U*. The energy profiles of the latter GGA-based functionals show similar energy barriers between 0.6-0.8 eV. The range is in line with the previous study by Sai Gautam *et al.*, where only a PBE functional was used due to force instabilities.[67] Inclusion of Hubbard-*U* is shown to decrease the barrier height by approximately 0.1 eV, where inclusion of vdW correction further lowers the activation barrier when compared to the PBE+*U* case. Interestingly, the effect of this vdW correction is only significant for the barrier height (calculated by the energy difference between the transition state and the local energy minima) and does not affect the energies of both end minima significantly. Considering the crucial role of vdW interactions in maintaining the structures in layered materials, this point was further investigated as following.

A close examination of the PBE+*U*/vdW-DF2+*U* energy profiles (Figure 4.2a) indicate that they could be divided into three steps: (i) initial steep rise (-4 to -2 Å integrated path length), (ii) gradual plateau (-3 to 1 Å), and (iii) steep descent (1 to 3 Å). Structurally, steps (i) and (iii) correspond to the ‘rocking’ motion of the VO₅ octahedra with (partial) charge hopping only, whereas the actual Mg jump takes place in step (ii).

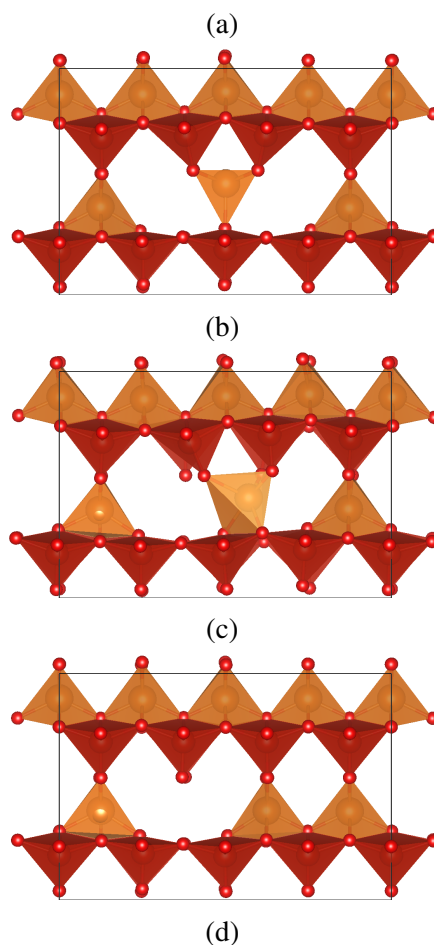
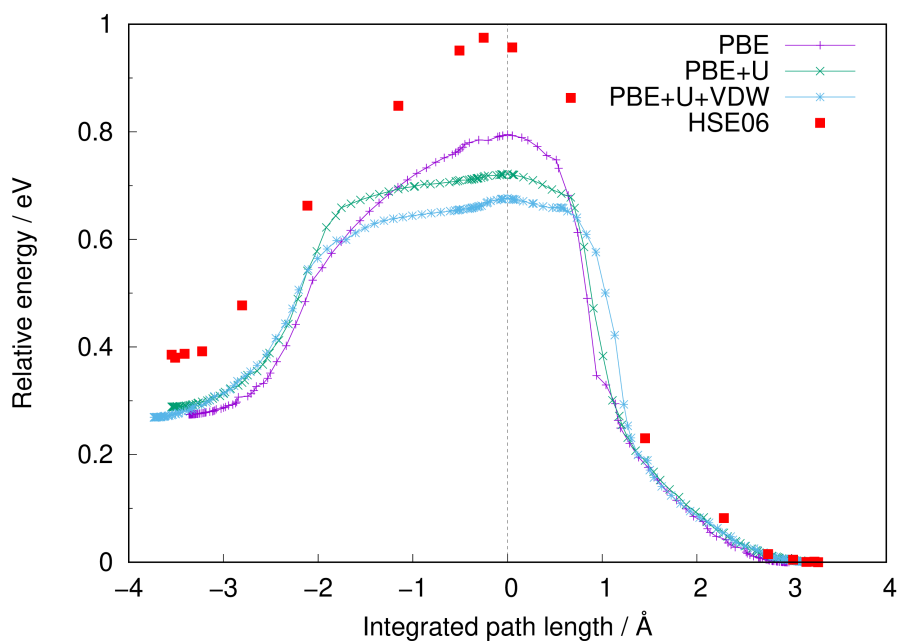


Fig. 4.2 (a) Energy profiles of a single Mg vacancy hop between 6-fold coordinated (stable) and 5-fold coordinated (metastable) sites. For the HSE06 calculations, only a handful of points along the PBE+U diffusion path was selected to calculate the single point energies. All energies are referenced to their lowest respective state. (b) Metastable 5-coordinated, (c) transition state, and (d) stable 6-coordinated Mg site along the diffusion pathway. Colour scheme: orange(Mg), red(V).

This behaviour is suggestive of a combined charge and ion hopping, as jump of a divalent Mg^{2+} ion to a nearby vacancy would result in a charge migration to satisfy the local charge balance. Pure PBE calculation does not exhibit this mid plateau-like region, which is more reminiscent of a simultaneous ion and electronic hop; this is expected from a delocalised electron cloud due to the lack of proper electron correlation. The fact that inclusion of vdW interaction only changes the energies of step (ii), the plateau, suggests that the rocking motion (related to the phonon modes) and charge hopping are less affected by the vdW correction, whereas the actual Mg migration is more heavily affected by so.

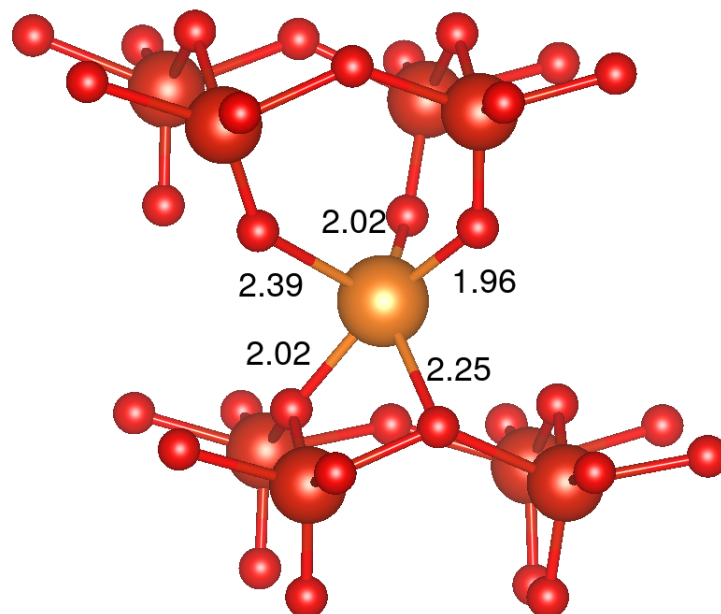
The same scenario with a hybrid HSE06 functional shows a much higher migration barrier of around 1 eV. However, a recent study on layered Li_xCoO_2 compounds has shown that several properties including the lithiation voltages, relative phase stabilities, and structural properties are better predicted with vdW-DF2+*U* approaches.[198] Hybrid methods tend to localise the electron density and this would result in a reduction of long-range diffuse interaction. As the vdW interactions are shown to be crucial in structures and insertion properties of layered oxides, it is likely that the actual activation barrier is closer to the vdW-DF2+*U* values of 0.6-0.8 eV.

Figures 4.2b–4.2d show the snapshots of the metastable 5-coordinated minimum (Figure 4.2b), 5-coordinated transition state (Figure 4.2c), and stable 6-coordinated minimum (Figure 4.2d). Analysis of the Mg–O bond lengths at the transition state (Figure 4.3a) shows that three slightly shorter (2.02, 2.02, 1.96 Å) bonds form a trigonal coordination, with two longer (2.39, 2.25 Å) bonds to ultimately form a 5-coordinated Mg transition state. Whereas Sai Gautam *et al.* fixed both local minima using a NEB method, they predicted a 3-fold coordinated transition state;[67] the NEB approach did not allow to predict the 5-coordinated transition state as found in this study. The overall Mg migration pathway would be therefore $6 \rightarrow 5' \rightarrow 5 \rightarrow 5' \rightarrow 6$, rather than $6 \rightarrow 3 \rightarrow 5 \rightarrow 3 \rightarrow 6$. The discovery of a 5-fold coordinated TS allows even smaller changes in coordination along the diffusion pathway and could be the driving force behind such low diffusion barrier of Mg.

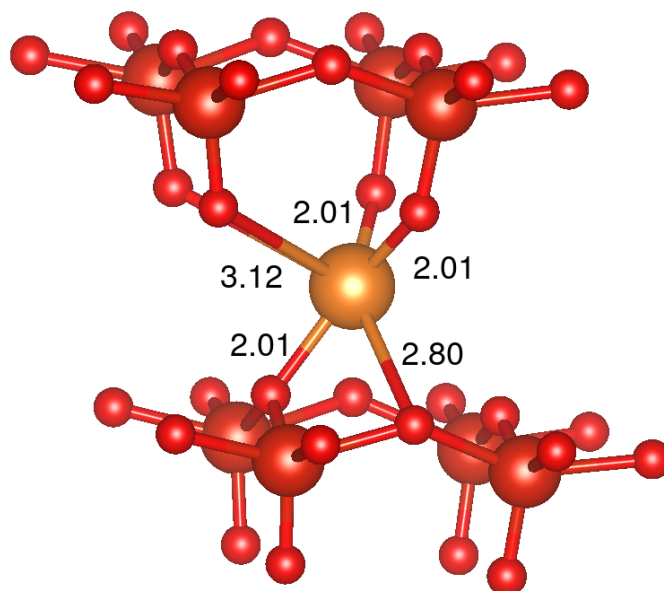
Migration of a Mg atom

As MgV_2O_5 is charged, demagnesiumation takes place to yield V_2O_5 . In terms of Mg diffusion, this is the another limiting case in which a single Mg ion moves through the lattice, unlike the vacancy diffusion above.

Figure 4.4a shows the energy profile for a single Mg diffusion. Since vanadium in a fully charged V_2O_5 is a $3d^0$ cation, PBE+*U* was not used for this system. The plot shows a more symmetrical migration profile, indicating a similarity in local minima between the metastable



(a)



(b)

Fig. 4.3 (a) Local geometry around the Mg in its transition state, fully magnesiated MgV_2O_5 . (b) Local geometry around the Mg in its transition state, fully demagnesiated V_2O_5 . All units are in Å. Mg–O bond distances closer than 3.2 Å are represented by a bond.

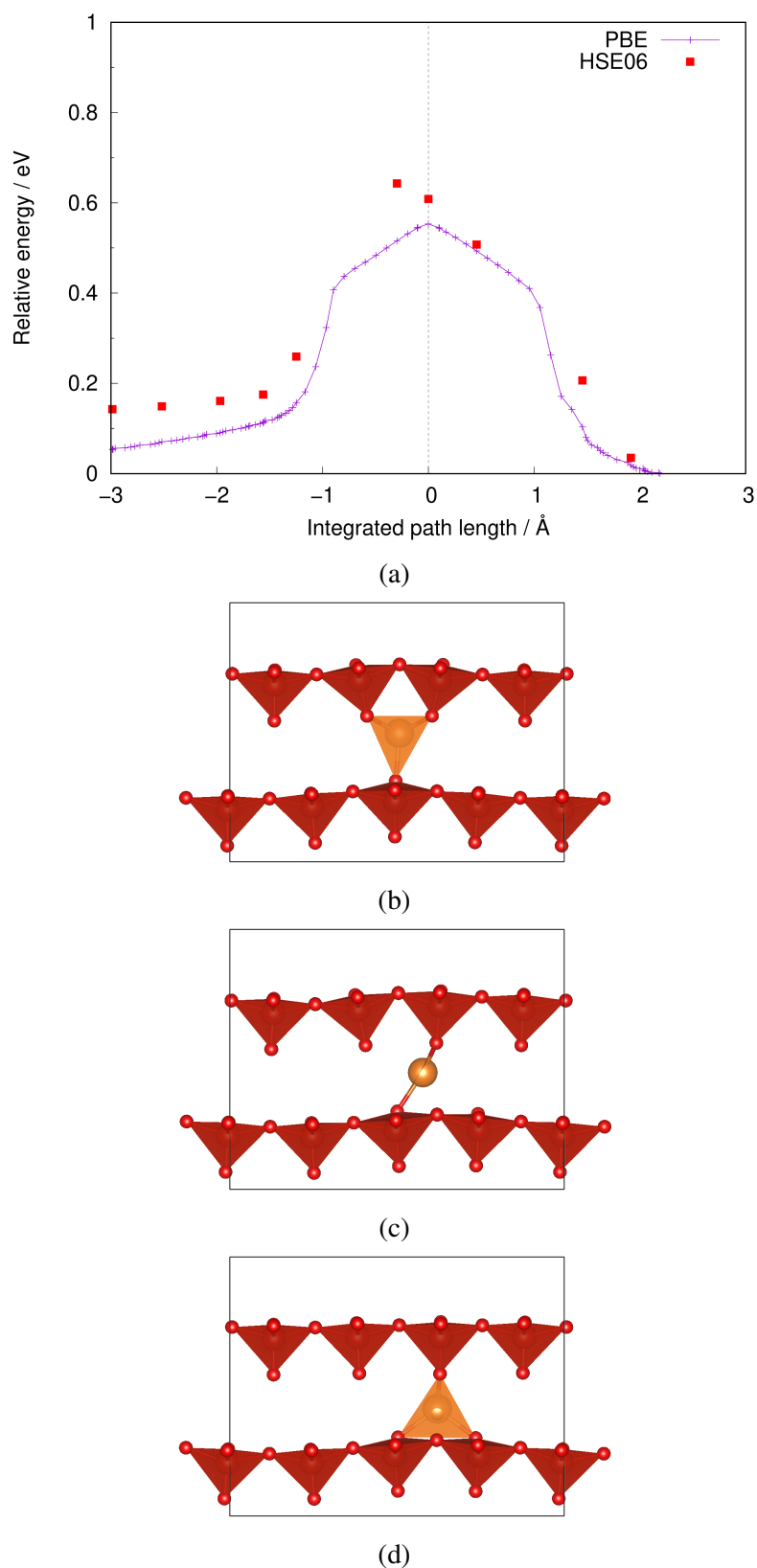


Fig. 4.4 (a) Energy profiles of a single Mg hop between 6-fold coordinated (stable) and 5-fold coordinated (metastable) sites. For HSE06 calculations, only a handful of points along the PBE+ U diffusion path was selected to calculate the single point energies. All energies are referenced to their lowest respective state. (b) Metastable 5-coordinated, (c) transition state, and (d) stable 6-coordinated Mg site along the diffusion pathway. Colour scheme: orange(Mg), red(V).

5-coordinated site and the 6-coordinated site. This is also reflected in the small difference between the end-point energies (0.05 eV), indicating a small energy penalty for such sites.

Perhaps the most surprising aspect of this plot is the agreement between the HSE06 and PBE results, which is distinct from the vacancy diffusion as seen above. The exact origin of this phenomenon is not yet clear; again coupled charge and ion migration may play a role. However, energy differences between the local minima also shows small formation energy (0.15 eV), again reinforcing the similarity argument in the PBE case.

Figures 4.4b–4.4d again show the snapshots of the metastable 5-coordinated minimum (Figure 4.4b), 3-coordinated transition state (Figure 4.4c), and stable 6-coordinated minimum (Figure 4.4d). In this case, a 3-fold coordination is predicted (Figure 4.3b), where the extra bonds show much longer Mg–O bond lengths (2.01 vs 3.12/2.80 Å). This gives an overall diffusion path of $6 \rightarrow 3 \rightarrow 5 \rightarrow 3 \rightarrow 6$, in agreement with previous report using a NEB approach.

Finally, we note that an accurate TS and its steepest descent energy profile could be constructed by virtue of TS searching using the HEF method. We note that this is a feature absent in a traditional NEB-type searching methodology, where the points along the band does not necessarily include the TS. Improved NEB methods such as the climbing image (CI)-NEB could be used to locate the accurate TS, but at the same time it is more expensive. Also, the HEF method allowed TS searching under the PBE+*U* and vdW functionals, which could show instabilities when used with the NEB method. The ability of this HEF approach to sample the diffusion pathway allows us to capture the subtle effects of the ion/charge migration on the calculated profile, allowing investigations of the detailed mechanism behind such migrations.

4.3.2 Rational Design of Synthetic Steps by DFT

Carbothermal synthesis: the motivation

Despite many previous reports on preparation and characterisation of complex AV_xO_y (A=Li, Na, Ca, Mg...)-type oxides, it is in general difficult to prepare stoichiometric compounds of alkaline vanadium oxides in reduced V^{3+} and V^{4+} oxidation states. This is evidenced by the subtle difference in stoichiometries of MgV_2O_4 samples synthesised under different partial pressures of H_2 in Ar.[166, 165] Clearly, a reliable way of preparing these complex oxides is needed.

As detailed in Chapter 2 (Section 2.6), *ab initio* methods could be used to calculate the free energy G of compounds under consideration. Under the approximation $G \approx U$, the

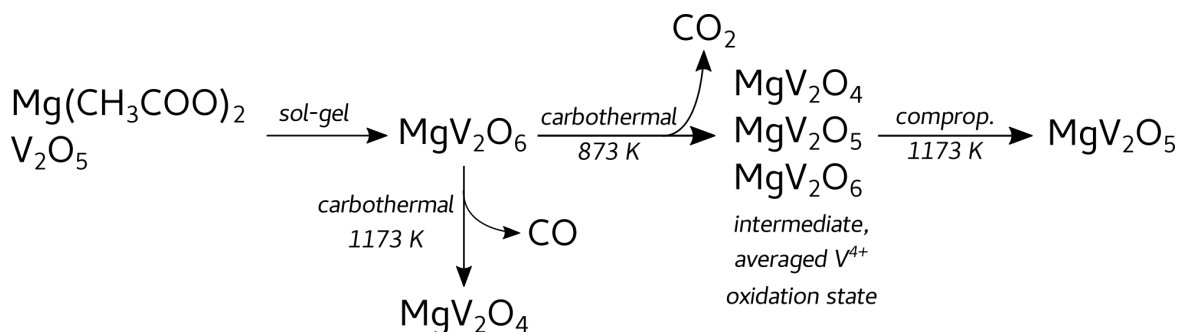


Fig. 4.5 Reaction scheme to synthesise MgV_2O_5 and MgV_2O_4 via the CTR approach.

cohesive, or formation, energy of any given structure could be calculated and the relevant ΔG obtained for any reaction using elemental carbon as the reducing agent. Using this approach, a synthesis scheme leading to MgV_2O_5 and a related compound MgV_2O_4 is presented in Figure 4.5, which we now discuss.

Free energy relations under standard conditions

Figure 4.6 shows the ΔG - T diagram of reactions involved in syntheses of MgV_2O_5 and MgV_2O_4 at standard pressures. Several important points could be noted from the diagram:

- The reactions involving magnesium vanadates



exhibit lines with similar positive gradients, as expected from the consumption of 1 mol gaseous O_2 in both reactions.

- Reduction of MgV_2O_6 to generate MgV_2O_5 (green line on Figure 4.6) is thermodynamically more favoured than forming MgV_2O_4 (purple line). This also means the MgV_2O_5 phase would be thermodynamically more stable than MgV_2O_4 under standard conditions.
- Oxidation of carbon has a sufficiently negative ΔG to allow formation of MgV_2O_5 and MgV_2O_4 . Below 973 K, the CO_2 reduction mechanism would be responsible; the CO mechanism takes place instead above this temperature.

These points clearly indicate that MgV_2O_5 could be prepared by a CTR reaction of the MgV_2O_6 precursor from thermodynamic considerations. However, it should be stressed that

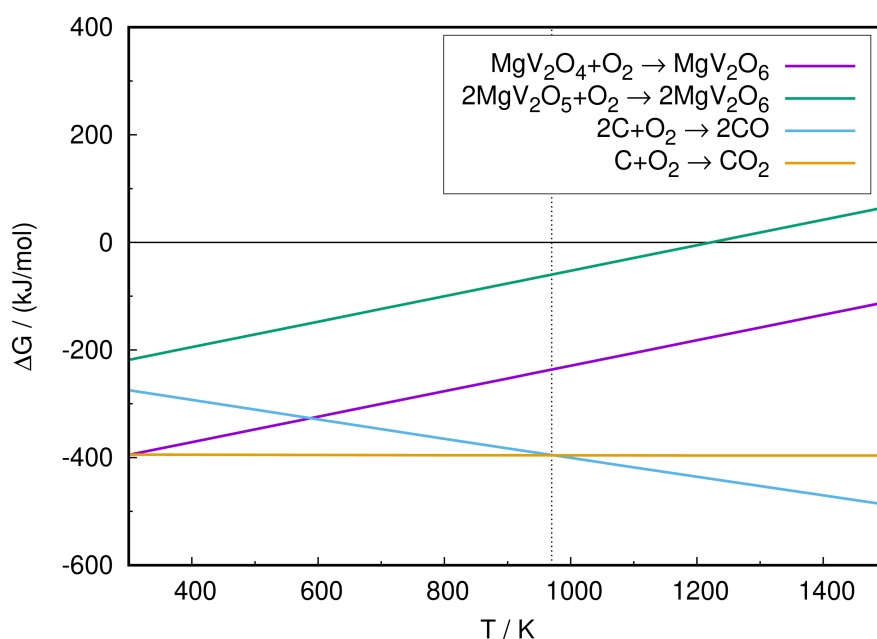


Fig. 4.6 Free energy ΔG vs. temperature T plot, or Ellingham diagram, of the various oxidation reactions involved in syntheses of MgV_2O_5 and MgV_2O_4 phases, calculated from DFT. All values are under standard 1 atm partial pressures. The two carbon lines cross at $T = 973$ K (700 °C). To allow a direct calculation of ΔG , the values are normalised with respect to 1 mol of O_2 .

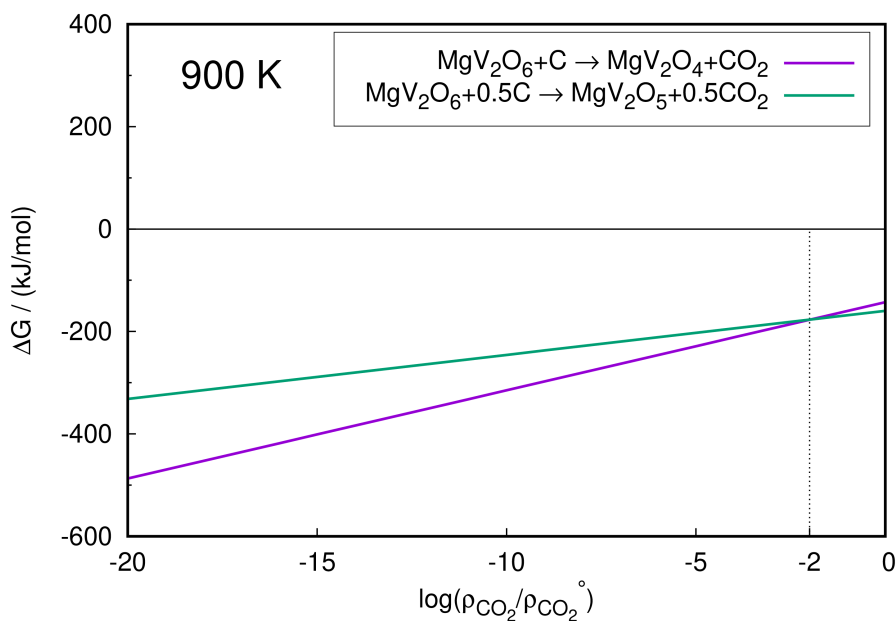


Fig. 4.7 DFT-based free energy ΔG of the CTR reactions to produce MgV_2O_5 and MgV_2O_4 phases at 900 K as a function of CO_2 partial pressure ρ_{CO_2} . The two lines cross at $\rho_{\text{CO}_2} = 10^{-2}$ atm. The values are normalised with respect to 1 mol of MgV_2O_6 .

these predictions are solely based on thermodynamic arguments concerning equilibria under 1 atm partial pressures. In practice, the reactions are conducted under a flowing Ar atmosphere where the oxygen partial pressure ρ_{O_2} is kept minimised to eliminate unwanted oxidation of products. Flowing Ar also ensures that the reaction goes to completion by continuous removal of CO_2/CO . To account for these reaction conditions, the same free energies must now be considered as a function of ρ_{CO_2} and ρ_{O_2} , which we now discuss.

Free energy relations under nonstandard conditions

Figure 4.7 shows the free energy plots of CTR reactions to produce MgV_2O_5 and MgV_2O_4 , now as a function of ρ_{CO_2} to simulate the continuous removal of CO_2 . The plot is created at 900 K to allow a stoichiometric CO_2 -reduction mechanism. As expected from the standard free energies, both $\Delta G < 0$, which becomes more negative as ρ_{CO_2} is reduced. However, below a CO_2 partial pressure of 10^{-2} atm, MgV_2O_4 becomes more favoured as a product, which arises from more CO_2 being produced in the reaction. In terms of the reaction, two cases are possible:

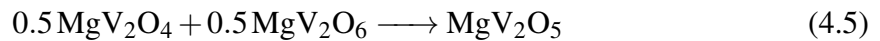
- Both MgV_2O_5 and MgV_2O_4 are likely to be produced around $\rho_{\text{CO}_2} = 10^{-2}$ atm since both reactions are close in free energy changes. This indicates that a selective reduction to MgV_2O_5 would be difficult under such circumstances.
- Under very low CO_2 partial pressures $\rho_{\text{CO}_2} \ll 10^{-2}$ atm, MgV_2O_4 is likely to be produced as the dominant reduction product. This could be a condition that is reached near the completion of the reaction, where the available amount of carbon is small.

These results indicate that a mixture of MgV_2O_4 and MgV_2O_5 would be the final product. It is difficult to accurately predict the final outcome based on purely thermodynamic considerations, especially since the kinetic contribution to the reaction is not taken into account. It is clear, however, that MgV_2O_4 is the more favoured product under strongly reducing conditions, and this phase would be exclusively produced in excess of added carbon (which is often done in CTR reactions to coat the particles with conductive carbon). Hence, MgV_2O_4 could be produced in a relatively straightforward fashion, where an excess (typically 25 %) of carbon is added and the precursor heated under Ar. The product could in addition be annealed at a higher temperature to improve crystallinity.

A two-step reaction leading to MgV_2O_5

Having established a potential reaction route to synthesise MgV_2O_4 , we turn our attention to the more challenging MgV_2O_5 synthesis. It is clear that a single-step CTR reaction cannot selectively produce this phase; a two-step process is then devised. In the first step, a *stoichiometric* CTR reduction is performed to yield an average vanadium oxidation state of 4+, and the whole mixture is annealed at a higher temperature to allow comproportionation of vanadium to form MgV_2O_5 .

Under standard 1 atm partial pressures, subtracting Equation 4.3 from Equation 4.4 yields the comproportionation equation to generate MgV_2O_5 :



which has a negative $\Delta G = -88$ kJ/mol at all temperatures, indicating a possibility for spontaneous comproportionation reaction of MgV_2O_4 and MgV_2O_6 to form MgV_2O_5 . This spontaneous reaction opens up a possibility for a new synthetic route to MgV_2O_5 : combined with the capacity for a stoichiometric reduction by the CTR method, the starting MgV_2O_6 precursor could in principle be reduced to $\text{MgV}_2\text{O}_4/\text{MgV}_2\text{O}_5/\text{MgV}_2\text{O}_6$ mixture with an average vanadium oxidation state of 4+, which would then be allowed to comproportionate

to give MgV₂O₅. This two-step process could be conducted in a one-pot setting in which the second annealing immediately follows the first reduction step in the same setup, *i.e.* without any intermediate grinding or change in ρ_{CO_2} .

In terms of determining the appropriate reaction conditions for this two-step process to prepare MgV₂O₅, several points need to be considered:

- As the one-pot reaction needs a stoichiometric reduction to yield the correct oxidation state for vanadium, a CO₂, rather than CO, reduction needs to be performed. This sets an upper bound for the reduction temperature to below 973 K, but the temperature still needs to be sufficiently high to overcome the kinetic barrier. For this reason, the reduction step is performed at 873 K (600 °C).
- The second comproportionation step could be performed at a higher temperature, as long as the MgV₂O₅ product is thermally stable in Ar. MgV₂O₅ is known to decompose above 1223 K,[178] so the annealing is performed at 1173 K (900 °C).
- However, designing this reaction also requires a careful consideration of the oxygen partial pressure ρ_{O_2} involved in the reaction, as the inevitable presence of oxygen in the Ar flow can oxidise/reduce the mixture depending on the free energies.

Intuitively, one would expect MgV₂O₄ to be more stable under a strongly reducing (low ρ_{O_2}) condition due to its lower oxidation state. During the second annealing step, this could result in MgV₂O₄ being formed instead if ρ_{O_2} is sufficiently low. In an attempt to control the ρ_{O_2} , the whole crucible was wrapped with a Cu foil, with additional Cu foils placed before the crucible to catch the O₂. Since both foils are kept at the same temperature as the reaction mixture, we can now investigate the equilibrium ρ_{O_2} of the oxidation reaction



of this ‘sacrificial’ Cu close to the comproportionation temperature (1173 K). Referring to the Ellingham diagram in Chapter 2 (Figure 2.4), this reaction has an equilibrium $\rho_{\text{O}_2} \approx 10^{-8}$ atm at 1200 K; this is assumed to be the lower limit of ρ_{O_2} for the reaction atmosphere, as oxidation of copper would take place above this oxygen pressure.

Figure 4.8 shows the free energy ΔG of the oxidation reactions involving MgV₂O₅ and MgV₂O₄ phases as a function of ρ_{O_2} at 1200 K. At $\rho_{\text{O}_2} = 10^{-8}$ atm, the reduction reaction to form MgV₂O₅ would be thermodynamically more favourable than the corresponding reaction to form MgV₂O₄, although both are energetically allowed. As this is the lower bound for the oxygen partial pressure (based on Cu oxidation), the diagram also indicates

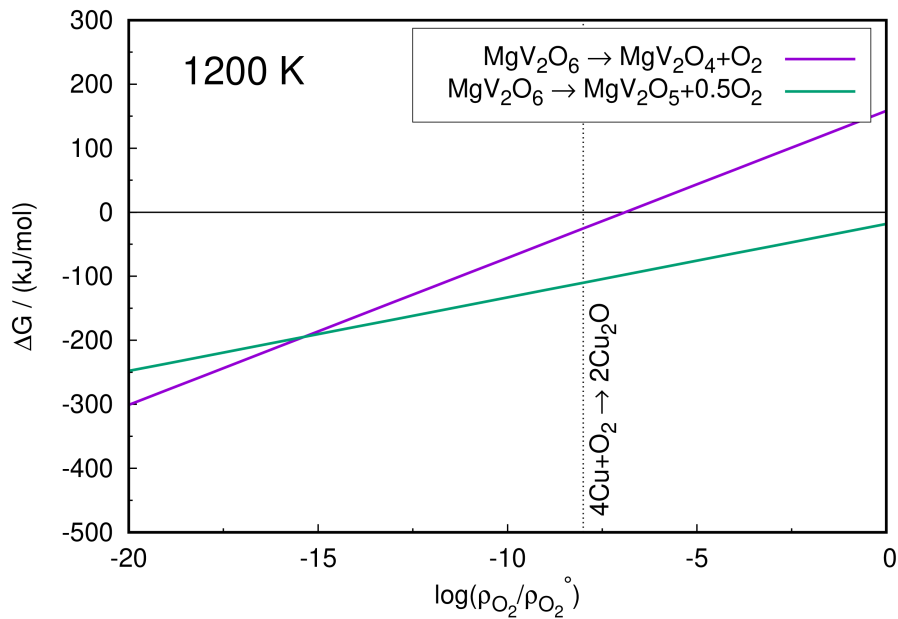


Fig. 4.8 DFT-based free energy ΔG of the oxidation reactions involving MgV_2O_5 and MgV_2O_4 phases at 1200 K as a function of O_2 partial pressure ρ_{O_2} . Equilibrium ρ_{O_2} of Cu oxidation is also shown as a dashed line at 10^{-8} atm. The values are normalised with respect to 1 mol of MgV_2O_6 .

that formation of MgV_2O_5 is thermodynamically allowed at least until 1 atm ρ_{O_2} at this temperature. Hence, the annealing step could be predicted to result in MgV_2O_5 , the product we aimed for, rather than MgV_2O_4 .

Based on these considerations, the reaction scheme to produce MgV_2O_4 and MgV_2O_5 could be finalised and is summarised in Figure 4.5 (*vide supra*). A final note on the precursor: as CTR reactions happen at the particle surface, both the precursor and carbon need to be small particles with high surface areas. This is most easily achieved by sol-gel or co-precipitation methods to prepare the precursor, or alternatively a bulk sample could be prepared initially and ball-milled to reduce the particle size. Commercial high surface area carbon such as Super P could be used as the reducing agent.

4.3.3 Characterisation of MgV_2O_5

Powder X-ray diffraction

Figure 4.9 presents the powder X-ray diffraction data of MgV_2O_5 (5 g batch) prepared by the CTR approach developed above. Rietveld refinement results are also shown in Table 4.1.

Apart from a minor VO₂ impurity (1 wt %), XRD identifies the product as MgV₂O₅. This clearly shows the success of the rational design strategy; it also highlights the scalable nature of CTR method. Excess VO₂ phase is likely to be present due to the hydrated magnesium acetate precursor (nominally tetrahydrate).

To elucidate the origin of excess VO₂ present in the final MgV₂O₅ sample, a thermogravimetric analysis (TGA) of the starting magnesium acetate precursor was performed. The resulting TGA data is shown in Figure 4.10. At 573 K, complete dehydration of the hydrated magnesium acetate results in a plateau.[199] From this the stoichiometry of initial precursor is estimated to be Mg(CH₃CO₂)₂ · 4.22H₂O, whereas the sample is nominally a tetrahydrate; this would result in approximately 2 mol % of magnesium deficiency. Considering the presence of around 1 wt % (equivalent to 2.5 mol %) of VO₂ detected on PXRD, this excess hydration is likely to be the reason behind the VO₂ secondary phase.

It should be stressed that the CTR reaction is selective for vanadium reduction (more stable MgO reduction requires a much higher reaction temperature), so this vanadium excess does not have an influence on the carbon stoichiometry. This is evidenced by the formation of VO₂, which is likely to be a reduction product of excess V₂O₅. It also indicates the possibility of using the CTR approach to prepare VO₂, a phase which has been shown to exhibit electrolyte gating behaviour on top of the metal-insulator transition at 340 K.[200] This phase has wide potential applications in ‘smart’ windows, Mott transistors, and memory devices.[201, 200]

²⁵Mg NMR: signal enhancements using RAPT

Having obtained a sample of MgV₂O₅ through the CTR method, we now turn our attention to the ²⁵Mg NMR spectrum of this compound. Figure 4.11a shows the ²⁵Mg spectrum of the as-synthesised compound. Fitting of this spectrum gives $\delta_{\text{iso}} = 1763$ ppm, together with the $C_Q = 5.3$ MHz and $\eta_Q = 0$. The spectrum is in good agreement to previously reported ²⁵Mg spectrum of this compound,[34, 35] although no detailed NMR characterisation was presented in these works. As expected from a distorted 6-fold Mg coordination environment, the resonance shows a distinct MAS quadrupolar lineshape with a $C_Q = 5.3$ MHz. This is by far the largest C_Q measured in paramagnetic Mg environments, despite the fact that quadrupolar coupling in paramagnetic solids is often difficult to measure due to the large line broadening and loss of resolution. In MgV₂O₅, however, the small electron spin moment of V⁴⁺ ($S = 1/2$) is likely to reduce the nuclear relaxation rate ($1/T_1 \propto S(S+1)$ from the Solomon-Bloembergen-Morgan Equation[142]) and thus result in an improved resolution.

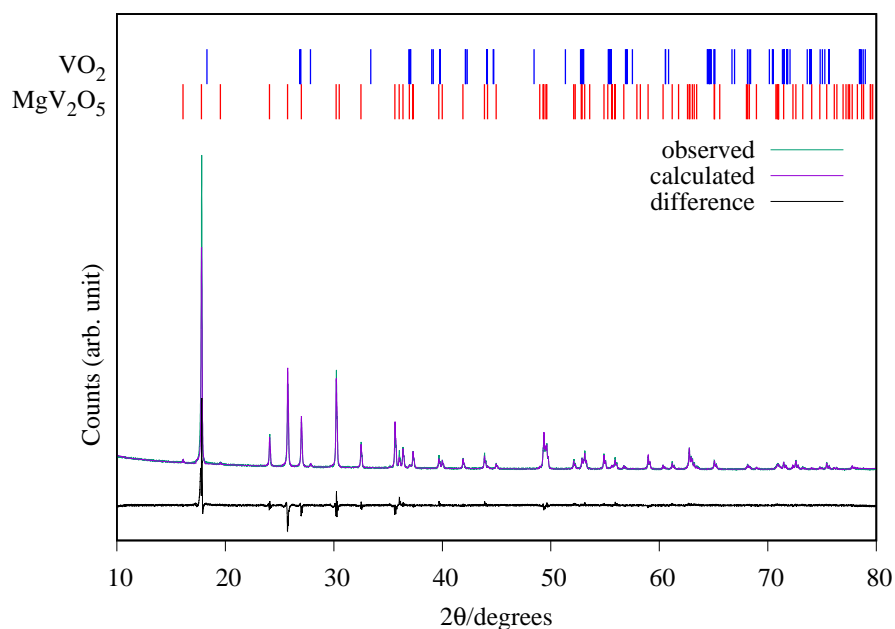


Fig. 4.9 Refined powder X-ray diffraction data of MgV₂O₅ as prepared by the CTR method. Refined parameters are shown in Table 4.1. Reflections for MgV₂O₅ (50979) and VO₂ (34033) are taken from the ICSD.

MgV ₂ O ₅ 99 wt %		<i>Cmcm</i> space group	
$a / \text{Å}$	3.69050(4)	$\alpha / ^\circ$	90
$b / \text{Å}$	9.97075(1)	$\beta / ^\circ$	90
$c / \text{Å}$	11.01735(1)	$\gamma / ^\circ$	90
Atom	x	y	z
Mg1 (4 <i>c</i>)	0	0.8801(2)	0.25
V1 (8 <i>f</i>)	0	0.2050(1)	0.0959(1)
O1 (8 <i>f</i>)	0	0.0440(4)	0.1298(3)
O2 (8 <i>f</i>)	0	0.2401(3)	0.5794(3)
O3 (4 <i>c</i>)	0	0.2983(6)	0.25

Table 4.1 Rietveld refined parameters from the PXRD data of MgV₂O₅ as prepared by the CTR method.

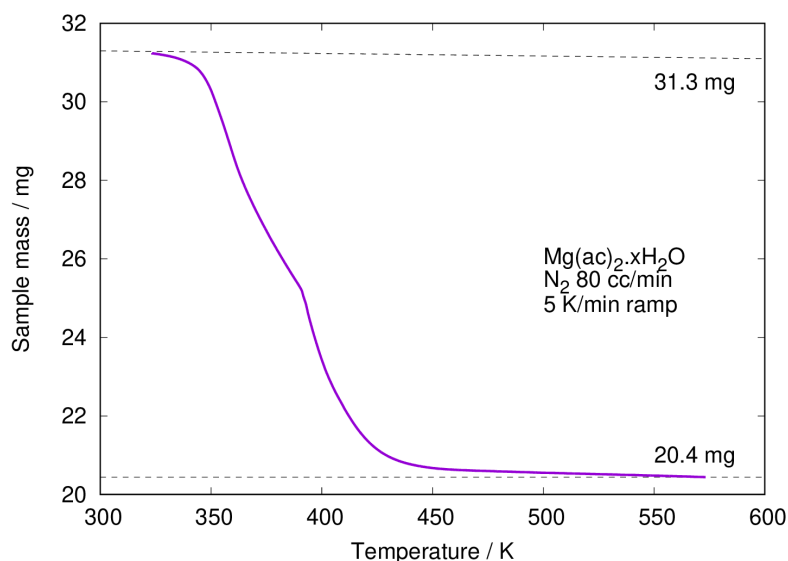
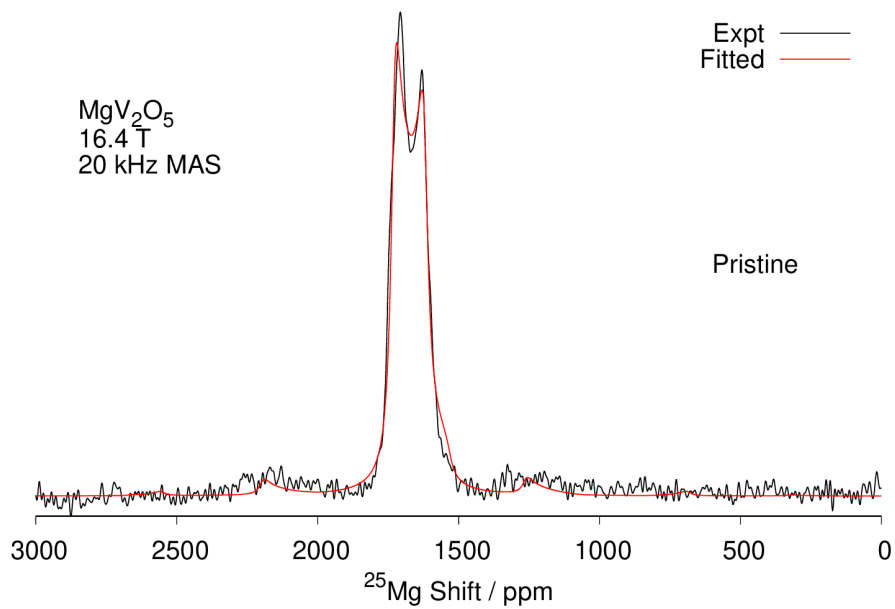


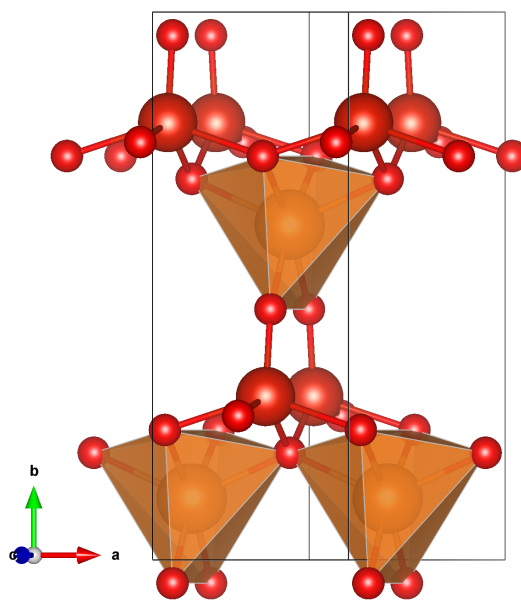
Fig. 4.10 Thermogravimetric data of the magnesium acetate (nominally tetrahydrate) precursor used in the synthesis of MgV_2O_6 .

Having measured the NMR parameters and especially the C_Q , we can now apply the RAPT pulse sequence to this sample, as used in the previous chapter for signal enhancements in paramagnetic ^{25}Mg spectra. In terms of the experiment, the large quadrupolar coupling observed in this material poses a significant challenge due to two reasons:[179, 202]

- Large quadrupolar coupling necessitates the use of faster spinning to deconvolute the spinning sidebands from the broad second-order CT lineshape. The individual ST isochromat in RAPT experiments should ‘sweep’ through the alternating Gaussian pulses at a fixed frequency, so faster spinning would result in less efficient saturation of ST populations and thus lower enhancements.
- The STs are located at frequencies far apart from the CT resonance, such that the saturating Gaussian pulses should also have large offsets from the CT frequency. This is problematic in terms of the limited bandwidth of NMR probe circuitry, and one would expect a rapidly decreasing enhancement when the offset is increased beyond the available probe bandwidth. For low- γ nuclei such as ^{25}Mg , the narrower bandwidth at lower frequencies makes this extra challenging. Referring to the theoretical description in Chapter 2, this also means that offset at the excitation edge (Equation 2.68), where the signal enhancement is expected to return to 1, cannot be recorded accurately. Instead, the C_Q should be estimated from the offset at maximum enhancement (Equation 2.69).



(a)



(b)

Fig. 4.11 (a) ²⁵Mg spin echo spectrum of the as-synthesised MgV₂O₅, measured under 20 kHz MAS and a 0.1 s recycle delay. Fitted parameters are shown in Table 4.3. (b) Structure of MgV₂O₅, showing the 6-fold Mg coordination environment as polyhedra.

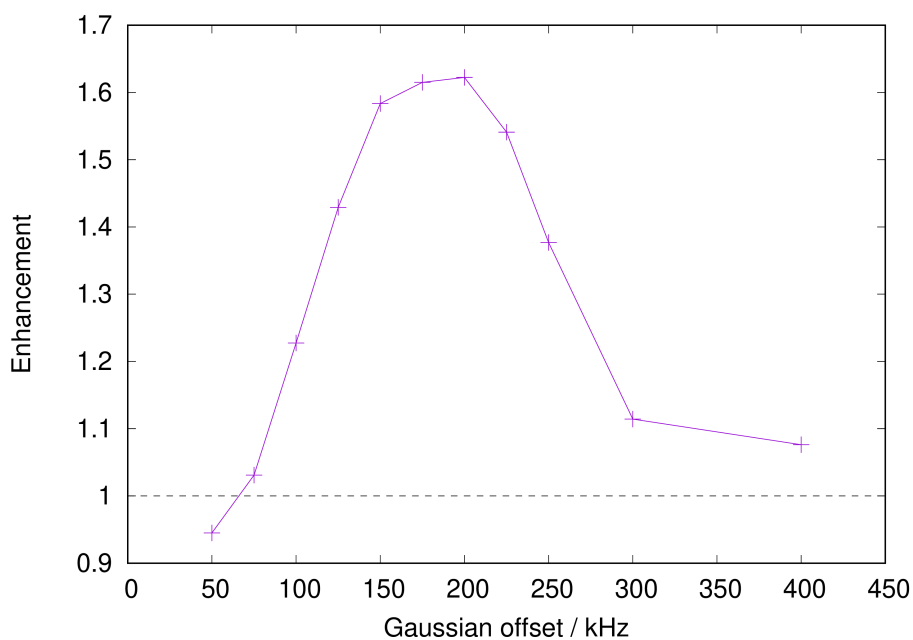


Fig. 4.12 Enhancement profile of the integrated signal intensity in MgV_2O_5 using the RAPT pulse sequence, as a function of the Gaussian offset ν_{off} . All samples were measured under 20 kHz MAS and a 0.1 s recycle delay.

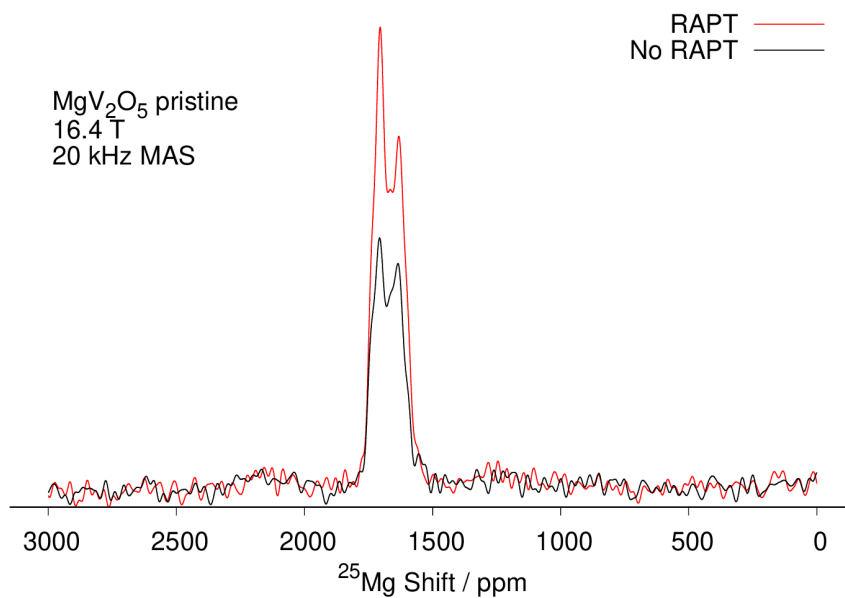


Fig. 4.13 ^{25}Mg spectra of as-synthesised MgV_2O_5 , measured with a normal spin echo and a RAPT-spin echo pulse sequences. Both were measured under 20 kHz MAS and 0.1 s recycle delay.

In this regard, Figure 4.12 shows a full enhancement profile over a range of offset frequencies recorded on MgV_2O_5 . As predicted in Equation 2.69, a maximum enhancement of 3 should occur at $\nu_{\text{off}} = 400$ kHz ($C_Q = 5.3$ MHz). The experimental enhancement profile displays a maximum enhancement of 1.6 around $\nu_{\text{off}} = 200$ kHz, a clear indication of inefficient ST saturation under this challenging condition.

Examination of the enhancement profile could also give information on the asymmetry parameter η_Q . Fitting of the MgV_2O_5 spectrum (Table 4.3) shows a well-defined $\eta_Q = 0$, which would be expected to result in a ‘tailing off’ slow decline in the enhancement profile. Figure 4.12, however, shows a rather steep decline in intensity near $\nu_{\text{off}} = 250$ kHz, a feature characteristic of systems with large η_Q close to unity. This discrepancy is likely to be a direct consequence of the limited probe bandwidth at this low frequency (42.5 MHz at 16.4 T), which also contributes to the lower enhancement factor compared to the expected factor of 3.

Despite these challenges, Figure 4.13 demonstrates a maximum enhancement of around 1.6 using the RAPT pulse sequence. It is also seen that the lineshape distortion is minimal upon RAPT enhancement, which further confirms the applicability of RAPT in quadrupolar NMR of paramagnetic species.

^{25}Mg NMR of the ball-milled MgV_2O_5

Having established the RAPT methodology for the pristine, as-synthesised sample, we now turn our attention to a mechanically milled sample with a reduced particle size. As typical Mg-ion battery electrodes are prepared in reduced particle sizes with a ball-milling step, this provides us with the sample in a similar condition to those in a cycled Mg-ion battery. Figure 4.14 shows the ^{25}Mg spectrum of ball-milled MgV_2O_5 sample as analysed in Appendix A. The spectrum shows a similar shift as the pristine sample at 1763 ppm, supporting the XRD data that the sample has not degraded. The characteristic CT lineshape, however, has now completely disappeared, possibly due to the reduced crystalline sizes and/or presence of defects as created by the milling. As the quadrupolar coupling interaction is local to each spin, which results from a local coordination environment and not the overall crystallinity, the RAPT pulse sequence is still expected to enhance the ^{25}Mg signals regardless of the milling. Under these conditions, application of the RAPT pulse sequence to this material still displays an overall enhancement factor of 1.5, illustrating the powerful sensitivity of the RAPT pulse sequence (and NMR in general) to the local environment around the spin.

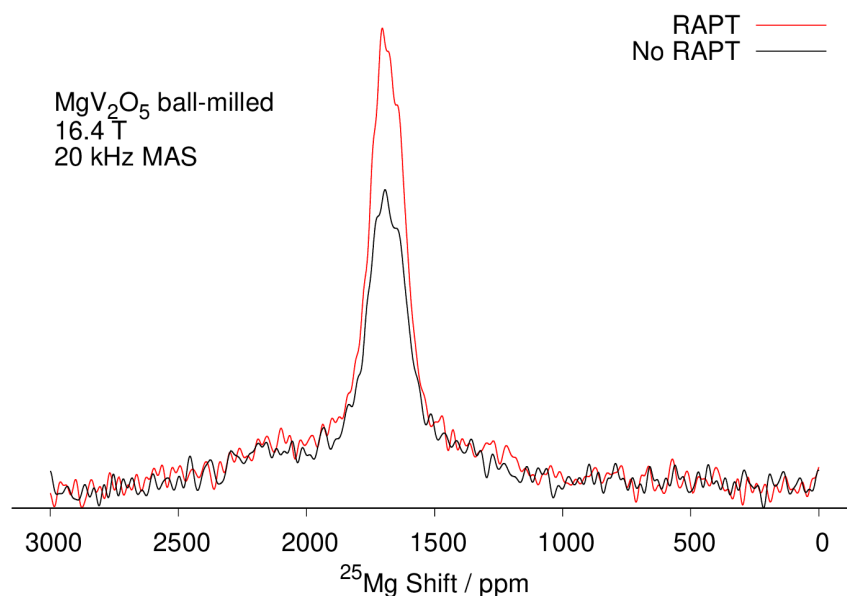


Fig. 4.14 ^{25}Mg spectra of ball-milled MgV_2O_5 , measured under normal spin echo and RAPT-spin echo. Both were measured under 20 kHz MAS and a 0.1 s recycle delay.

4.3.4 Electrochemical Cycling of MgV_2O_5

Based on the computational discussion above, Mg diffusion in the MgV_2O_5 host would have a relatively low Mg diffusion barrier. Combined with the work on NMR detection of this compound, electrochemically cycled sample could be measured to confirm the reversible magnesiation behaviour of this material. In this section the initial cycling data are presented.

Charging behaviour of MgV_2O_5

To confirm the demagnesiation of MgV_2O_5 , the compound was charged in a standard Li-ion half-cell with Li metal counterelectrode and standard LP30 electrolyte. Ball-milled MgV_2O_5 was used to reduce the particle size to enhance diffusion, and the sample was checked for structural integrity post ball-mill with powder XRD and NMR (Figures A.2 and 4.14). SEM images indicate that the particle size is reduced to a sub-micron level (Figure A.1).

Electrochemical response for the galvanostatic charging step (C/50-rate) is presented in Figure 4.15a. The curve displays an initial plateau at 3.8 V and shows a gradual increase in potential until about 4.2 V, after which it displays a ‘wiggle’-like behaviour. Previous computation on this compound predicted a potential of 2.56 V vs Mg metal, which corresponds to 2.9 V vs Li metal (using the standard electrode potentials). This agrees with the observed

open circuit voltage (OCV) of 3 V, but a significant overpotential of about 0.8 V is observed on charging.

The onset of this wiggle happened at about 250 mAh/g capacity, close to the theoretical capacity of 260 mAh/g (assuming a full demagnesiumation of MgV_2O_5). The cell clearly was charged beyond its theoretical capacity, which could arise from an electrolyte decomposition or a structural failure. As electrolyte decomposition typically happens at a flat potential, structural disintegration, possibly involving vanadium dissolution, was suspected.

Postmortem examination of charged cell (Figure 4.15b) revealed that the lithium metal counterelectrode was covered in a black species and the glass fibre separator was in green colour. Upon charging, vanadium (either from the VO_2 or $(\text{Mg})\text{V}_2\text{O}_5$) could dissolve into the electrolyte giving a green hue for the separator, which could then plate on the lithium counterelectrode. Possible origins for this behaviour are discussed in the next section.

XRD pattern of the charged cathode film was measured and is given in Figure 4.15c. Almost all MgV_2O_5 reflections have disappeared with appearance of $\alpha\text{-V}_2\text{O}_5$ reflections, confirming the charging step. Several relatively narrow reflections arising from uncycled MgV_2O_5 still survive ($2\theta = 20, 25, 27, 30$ degrees). However, the broad $\alpha\text{-V}_2\text{O}_5$ reflection indicates possible particle amorphisation upon cycling and irreversibility; further work needs to be done with this compound to confirm this. A detailed study on cycling this compound was not attempted due to an absence of high-voltage electrolytes and the problem of vanadium dissolution (see below).

Vanadium dissolution of VO_2

Previous XRD analysis revealed presence of VO_2 in this batch of MgV_2O_5 (Figure 4.9). As VO_2 becomes metallic above 340 K (70 °C), the possibility of a facilitated vanadium dissolution arising from VO_2 was investigated by charging a pristine VO_2 sample.

Figure 4.16a shows the charging curve of a VO_2 self-standing film in a Li-ion cell. An abrupt increase in potential is observed above 3.4 V, which plateaus out at 4 V. Postmortem examination of the Li counterelectrode is also black, confirming the vanadium dissolution from VO_2 . XRD analysis shows the presence of significant amount of V_6O_{13} , equally written $\text{V}_{12/13}\text{O}_2$, which would have resulted from an oxidation reaction as described in the Discussion section (Section 4.4.2); what is clear however is the formation of V_6O_{13} as an oxidation product of VO_2 upon charging, as evidenced by the XRD pattern.

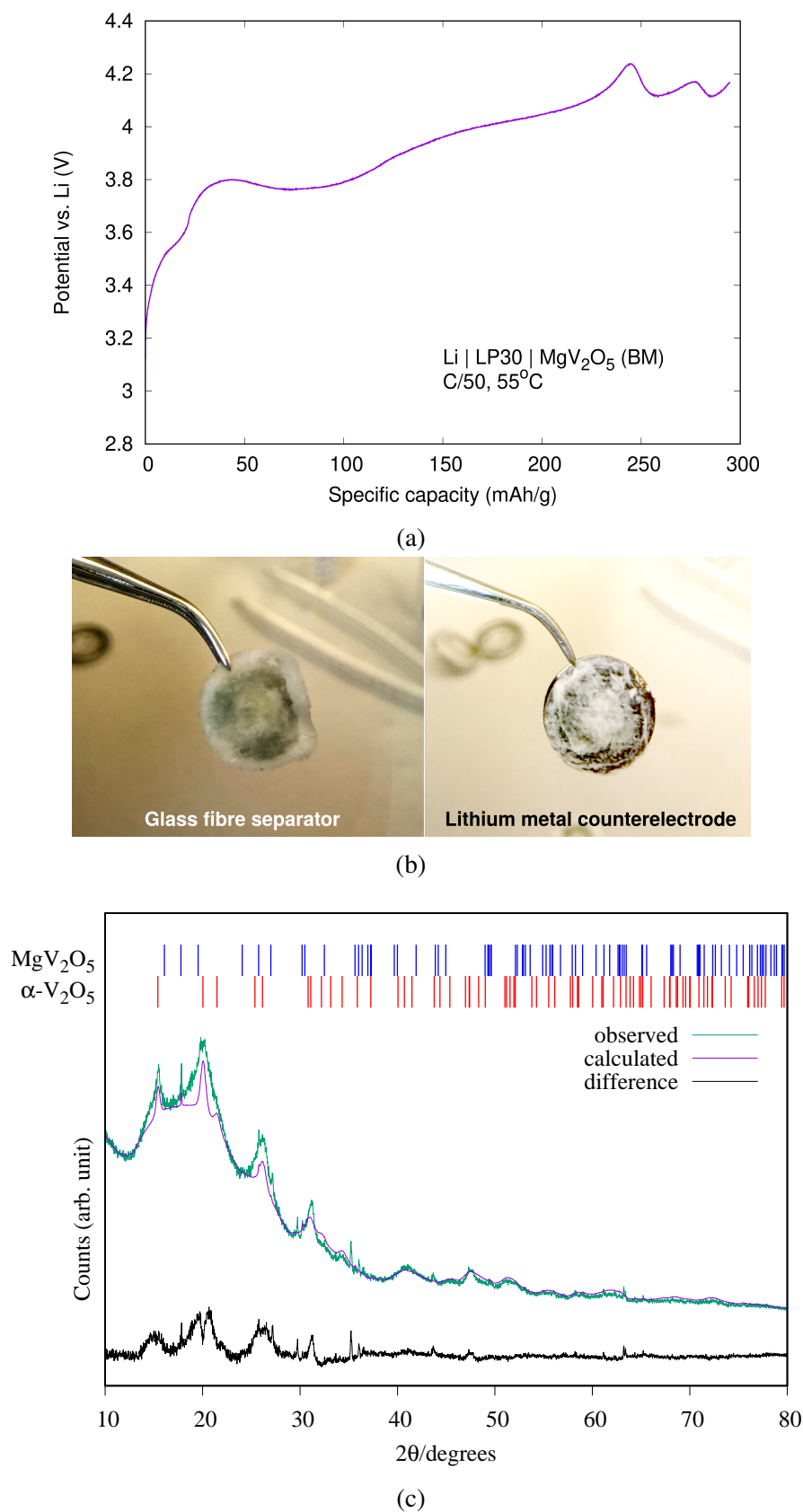
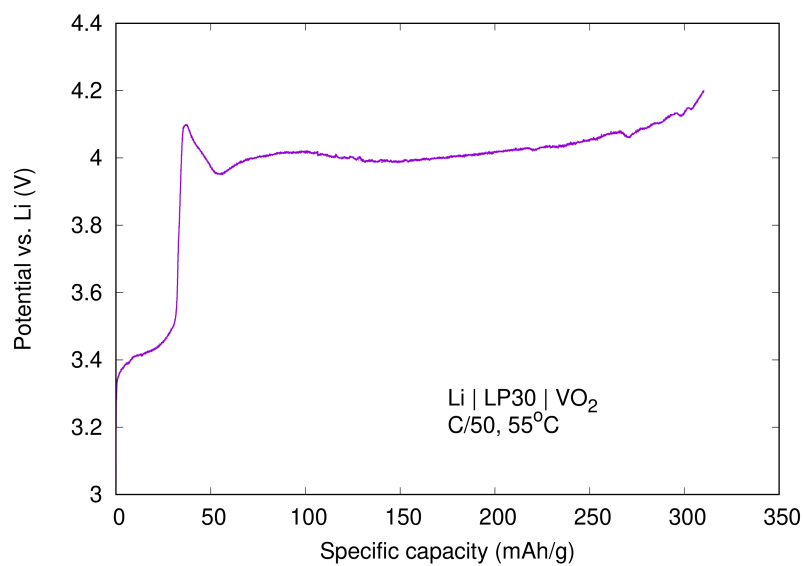
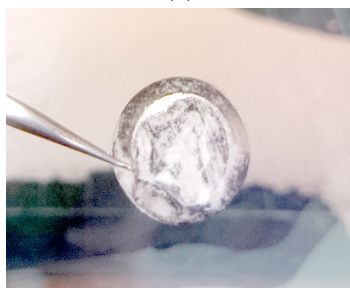


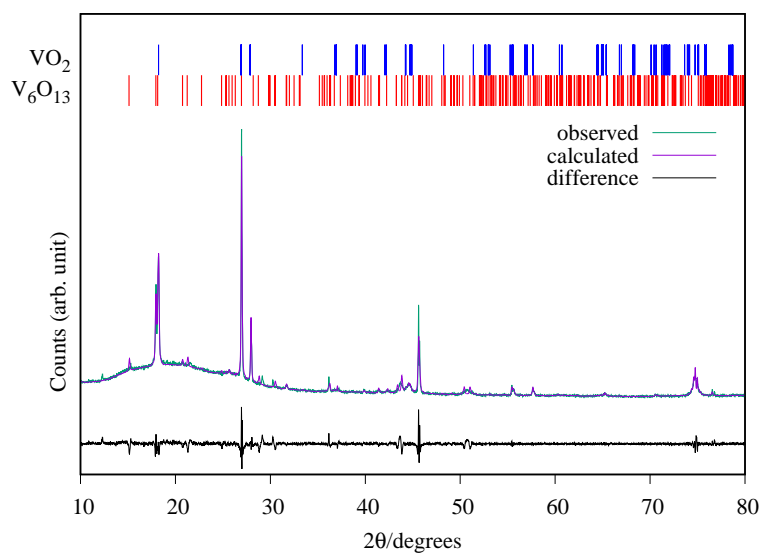
Fig. 4.15 (a) Electrochemical cycling data of ball-milled MgV_2O_5 , charged vs Li. (b) Glass fibre separator and lithium disc after disassembly of the coin cell shown in (a). (c) Powder X-ray diffraction data of charged cathode. Broad background at 20° is due to Kapton sample holder.



(a)



(b)



(c)

Fig. 4.16 (a) Electrochemical cycling data of VO₂, charged vs Li. (b) Lithium disc after disassembly of the coin cell. (c) Powder X-ray diffraction data and Le Bail fit of charged VO₂. Broad background at 20° is due to Kapton sample holder. Self-standing films were provided by Michael Hope.

	This work			Reported			
	Expt	PBE+ <i>U</i>	Hyb20	Hyb35	Korotin[197]	Millet[203]	Onoda[178]
J_1 / K	-	62	25	16	-30	-100	-
J_2 / K	-	-55	-55	-40	-46	-282	-
J_3 / K	-	-57	-74	-58	-72	-	-
J_4 / K	-	-	-	-	-9	-	-
Θ / K	-277	-22	-77	-62	-339	-307	-174

Table 4.2 Magnetic parameters of MgV₂O₅ determined by experiment and DFT calculations. Experimental parameters were determined by SQUID magnetometer (Figure 4.17); J-couplings are as denoted on Figure 4.18a.

4.3.5 Computation of Magnetic and NMR Parameters

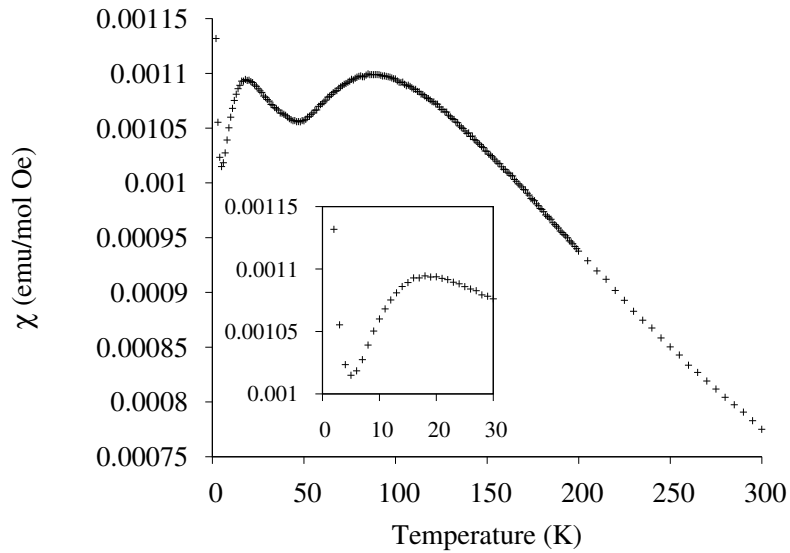
Now we turn our attention to the *ab initio* computation of the magnetic and ²⁵Mg NMR parameters for MgV₂O₅. The magnetic parameters are of interest since the previous magnetic measurements on this compound have reported a magnetic response characteristic of a system with reduced dimensionality. Since the hyperfine NMR parameters also intimately depend on the magnetism, we attempt to measure and predict the magnetism present in MgV₂O₅.

Magnetic interactions

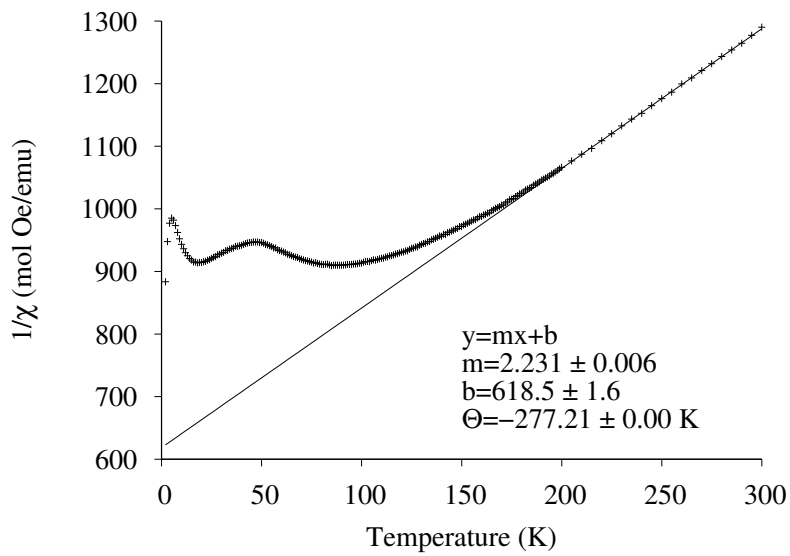
The plot showing the experimentally measured magnetic susceptibility χ is displayed in Figure 4.17a. The low-temperature data presented in figure inset is in good agreement to the previous report by Millet *et al.* where a fall and then rapid rise in χ was attributed to the reduced dimensionality of the system.[203]

Our value for the Curie-Weiss constant, $\Theta = -277 \text{ K}$, determined from the inverse susceptibility plot (Figure 4.17b) also shows good agreement to experimental values determined by Korotin and Millet *et al.* Onoda *et al.* reported a slightly smaller $\Theta = -174 \text{ K}$; it is likely their sample was highly nonstoichiometric (residual VO₂ was visually observed) which would have contributed to the error. However, further work on preparing a better quality sample with no detectable impurity on the XRD must be carried out.

Table 4.2 shows the *ab initio* computed exchange coupling parameters J_n as determined by the linear regression method. Literature values are also shown, where available. The largest discrepancy is observed in the sign and magnitude of J_1 , the nearest neighbouring interaction along the edge sharing square pyramids. PBE+*U* and both hybrids (20 % and 35 % Hartree-fock exchange) consistently show a positive (ferromagnetic) exchange for this



(a)



(b)

Fig. 4.17 (a) Zero field cooled molar susceptibility χ and (b) Zero field cooled inverse molar susceptibility $1/\chi$ of MgV_2O_5 as measured by SQUID magnetometry. Linear fitting was performed from 200 K to 300 K.

interaction, whereas reported values using the Linear Muffin-Tin Orbital method with the LDA+*U* functional show a negative (antiferromagnetic) exchange.[197]

To explain this discrepancy, we need to understand the underlying orbital overlap. MgV₂O₅ is a $S = 1/2$ system with a $3d^1$ state, with the d_{xy} orbital being the lowest in energy.[197] This orbital lies in the pyramidal plane avoiding the oxygen, as illustrated in Figure 4.18a. Two competing interactions are present in the case of J_1 : a direct exchange between the $3d_{xy}$ orbitals lead to an antiferromagnetic coupling, whereas a superexchange *via* an O²⁻ leads to a ferromagnetic correlation superexchange. It is thought that the DFT-based methods ‘over-bind’ the electrons to underestimate the direct exchange and overestimate the superexchange, resulting in an overall ferromagnetic interaction. The relatively diffuse nature of vanadium orbitals make the overlaps very sensitive to bond lengths and angles; further investigation is necessary using different structures and functionals. This discrepancy is most likely to be the reason behind the significantly smaller values of the Curie-Weiss constant Θ (simulated values range from -22 to -77 K *versus* the experimental -277 K) when compared to the experiment and other reported values.

The $J_{2,3}$ couplings arise mostly from a superexchange mediated by an O²⁻, and a delocalisation superexchange mechanism successfully explains the antiferromagnetic nature of these two interactions. These couplings also show good agreement to the Linear Muffin-tin Orbital (LMTO) method results by Korotin *et al.*[197] Results by Millet *et al.*[203] were estimated from the structural parameters by use of empirical relationships between the J and bond length/angles, so they are likely to be less accurate when compared to first principles methods. Onoda *et al.* did not report any values for J . [178]

NMR parameters

Hyperfine and quadrupolar parameters determined from experiment and DFT computations are shown in Table 4.3. Both Hyb20 and Hyb35 results consistently overestimate the shifts. DFT predictions in other Li-, Na-, and Mg-oxides have consistently shown an overestimation of Hyb20 and an underestimation for Hyb35, thus defining a boundary of the experimental shift; [38, 204, 205, 185] this is clearly not the case for MgV₂O₅.

A major source of this error comes from the *ab initio* determination of the magnetism. The shift δ_{iso} depends inversely on the Θ : $\delta_{iso} \propto \frac{1}{T-\Theta}$. As seen in the previous section, DFT predicts a ferromagnetic interaction for the J_1 , which gives a significantly less negative value of Θ and overestimates the shifts.

An additional error comes from the electronic structure itself; it is likely that the hyperfine coupling constant A_{iso} (or equally, spin density at nuclear positions $|\Psi_N^{\alpha-\beta}|^2$) is also

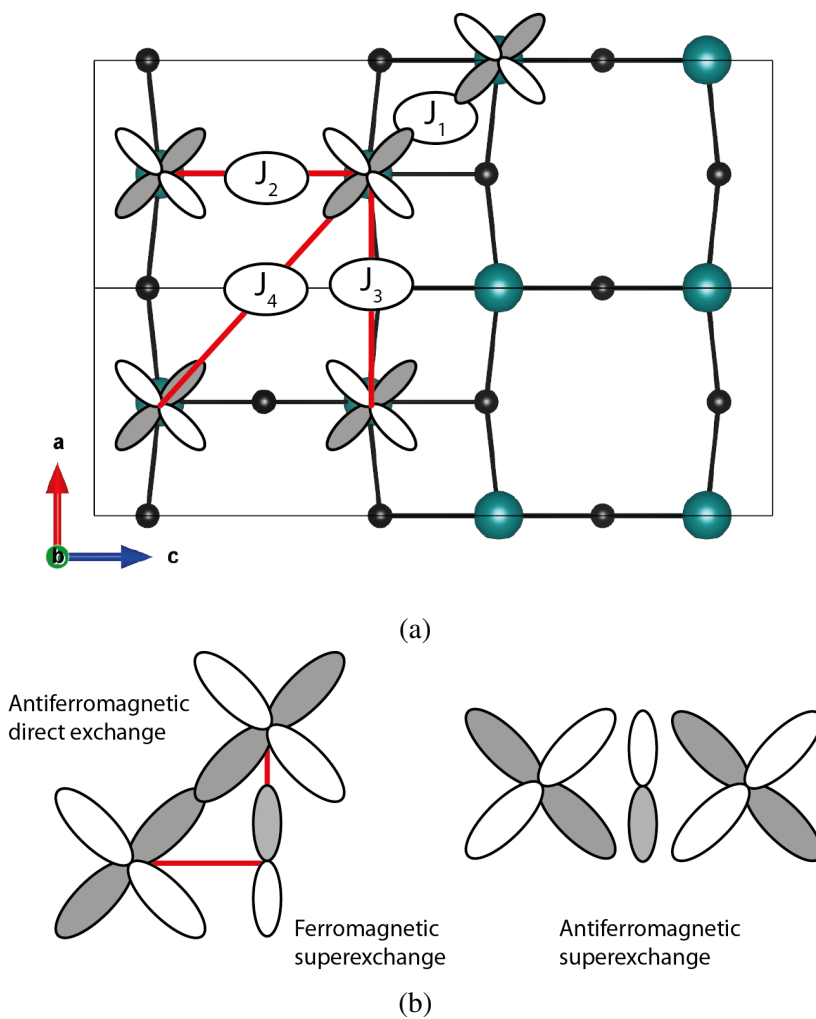


Fig. 4.18 (a) Illustration of the V–V exchange interactions J_n up to the fourth nearest neighbour in MgV_2O_5 . Dark blue colour refers to vanadium. (b) Dominant exchange mechanisms for the J_1 (left) and $J_{2,3}$ (right).

	Hyb20	Hyb35	Expt
δ_{iso} / ppm	2329	1991	1763
Ω	4329	4164	-
κ	-0.23	-0.34	-
C_Q / MHz	4.3	4.3	5.3
η_Q	0.0	0.0	0.0

Table 4.3 NMR parameters of MgV_2O_5 determined by experiment and DFT calculations. Experimental parameters are fitted from the spectrum in Figure 4.11a (anisotropies could not be determined from the spectrum). Herzfeld-Berger convention is used for the shift anisotropy.

underestimated due to the over-binding of hybrid methods, in a manner similar to the J_1 interaction. Using the experimentally determined $\Theta = -277$ K, Hyb20 and Hyb35 gives $\delta_{iso} = 1478$ and 1217 ppm, respectively. This confirms the over-binding of hybrid methods, as the discrepancy in this case should come from the hyperfine coupling itself.

Hence, determination of accurate magnetism is the most crucial component of the hyperfine shift calculations in vanadium compounds; this behaviour is observed in other Mg-compounds (Chapter 3, Section 3.3.3) as well. The diffuse nature of vanadium makes the prediction particularly challenging; more advanced functionals such as the meta-GGA functional combined with plane-wave basis sets could be used for such purposes.

The computed quadrupolar parameters show a value of $C_Q = 4.3$ MHz for both Hyb20 and Hyb35, which is smaller than the fitted value of 5.3 MHz. This result is also consistent with the observation of over-binding of hybrid methods in this case.

4.3.6 Characterisation of MgV_2O_4 Prepared Through the CTR method

As shown previously in Figure 4.5, the CTR method could also provide a novel way to prepare a spinel-type magnesium vanadate, MgV_2O_4 . In Chapter 3, this compound was prepared *via* a solid-state route (with the resulting sample containing V_2O_3 secondary phases) and characterised with ^{25}Mg NMR spectroscopy; hence we exploit this opportunity to briefly demonstrate the applicability of the CTR method to synthesise MgV_2O_4 and present the initial magnetic and ^{25}Mg NMR characterisation of this compound.

Powder X-ray diffraction

Powder X-ray diffraction data and the Rietveld refinement of the resulting MgV_2O_4 prepared through the CTR method (denoted CTR- MgV_2O_4) is shown in Figure 4.19 and Table 4.4).

The diffraction pattern shows a predominant MgV_2O_4 phase without noticeable V_2O_3 impurity, clearly demonstrating the utility of CTR method in preparing various magnesium vanadate compounds. SS- MgV_2O_4 sample exhibits broader reflections compared to the CTR- MgV_2O_4 , which may reflect the smaller particle size/increased degree of disorder for this sample.

However, X-ray diffraction was insufficient to conclude any nonstoichiometry (arising due to the hydrated magnesium acetate; see Section 4.3.3), where the refinement indicated no significant partial occupancies (within the experimental limits of laboratory X-ray diffraction) in both Mg and V sites (0.991(2) and 0.983(2), respectively).

Magnetic characterisation

As the CTR- MgV_2O_4 sample is phase-pure in contrast to the SS- MgV_2O_4 sample prepared in Chapter 3, SQUID magnetometry was performed on the CTR- MgV_2O_4 to determine the magnetism and possible site disorder present in this material. The resulting inverse susceptibility plot is shown in Figure 4.20. Upon cooling under a zero magnetic field, the cubic to tetragonal transition occurs at $T_s = 60$ K, followed by an antiferromagnetic ordering at $T_N = 34$ K (Néel temperature). These values are in slight disagreement to the previous reports of $T_s = 65$ K and $T_N = 42$ K; [165, 164] the discrepancy could originate from the V^{4+} in the system, arising from the slight Mg deficiency expected in the composition as explained below.

The electron magnetic moment per mol V (from the ‘elevated’-temperature regime of 200–300 K) of $\mu_{\text{eff}} = 3.60 \pm 0.02 \mu_B$ was determined for the CTR- MgV_2O_4 , whereas the spin-only moment is expected to be $\mu_{\text{eff}} = 2.83 \mu_B$ (Table 3.3). This inconsistency could again be ascribed to the short-range fluctuations as for the case of MgCr_2O_4 ; our result is consistent with the report by Mamiya *et al.* where a value of $\mu_{\text{eff}} = 3.35 \mu_B$ was measured for a temperature range of 100–200 K. [164] At a higher temperature range of 450–600 K, the reported value of μ_{eff} decreased to $2.97 \mu_B$ (similar to the spin-only value of $2.83 \mu_B$), which clearly indicates a near complete suppression of this short-range fluctuation.

When analysing the magnetic data, we should make note that the preparation of CTR- MgV_2O_4 starts from a MgV_2O_6 precursor made under ambient air, and the Mg understoichiometry of approximately 2 mol % (arising from the acetate precursor as described in Section 4.3.3) should still be present in this precursor. In MgV_2O_6 , the Mg deficiency should be compensated by oxygen vacancies to form a $\text{Mg}_{0.98}\text{V}_2\text{O}_{5.98}$ phase (no extra V_xO_y -type secondary phases were observed in the precursor). This translates to a Mg-deficient phase of $\text{Mg}_{0.98}\text{V}_{1.96}^{3+}\text{V}_{0.04}^{4+}\text{O}_4$ after the reduction step. This was not readily observed with

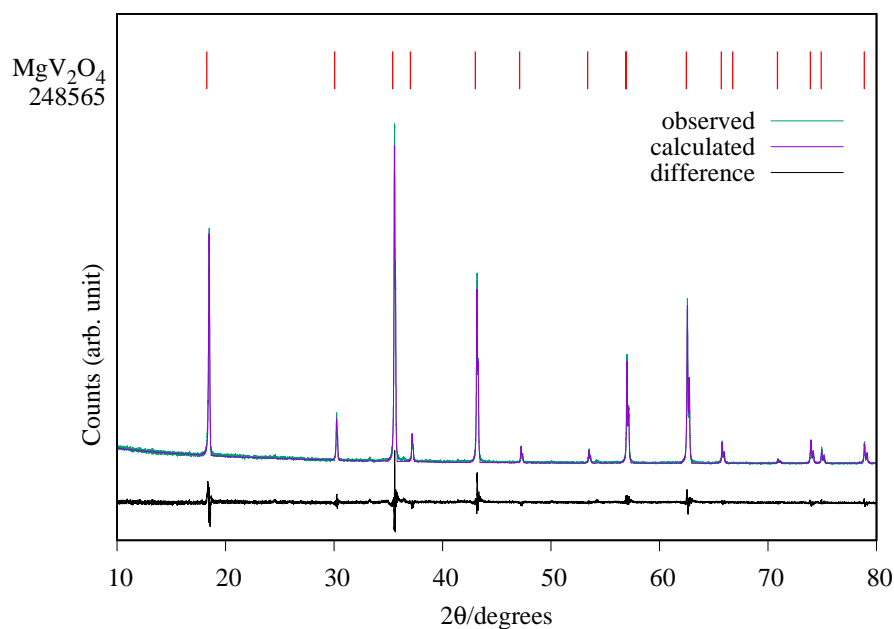


Fig. 4.19 X-ray powder diffraction pattern for CTR- MgV_2O_4 (carbothermal route). The positions of allowed reflections are indicated by the tick marks.

MgV ₂ O ₄ 100 wt %			<i>Fd</i> $\bar{3}$ <i>m</i> space group	
	<i>a</i> / Å	8.41499(7)	α / °	90
	<i>b</i> / Å	8.41499(7)	α / °	90
	<i>c</i> / Å	8.41499(7)	α / °	90
Atom	<i>x</i>	<i>y</i>	<i>z</i>	Occ
Mg1 (8 <i>b</i>)	0.375	0.375	0.375	0.991(2)
V1 (16 <i>d</i>)	0	0	0	0.983(2)
O1 (32 <i>e</i>)	0.2419(1)	0.2419(1)	0.2419(1)	1
	<i>R</i> _{exp}		7.43	
	<i>R</i> _{wp}		12.26	
	χ^2		1.65	

Table 4.4 Rietveld refined parameters from the PXRD data of MgV_2O_4 prepared *via* a carbothermal method (CTR- MgV_2O_4).

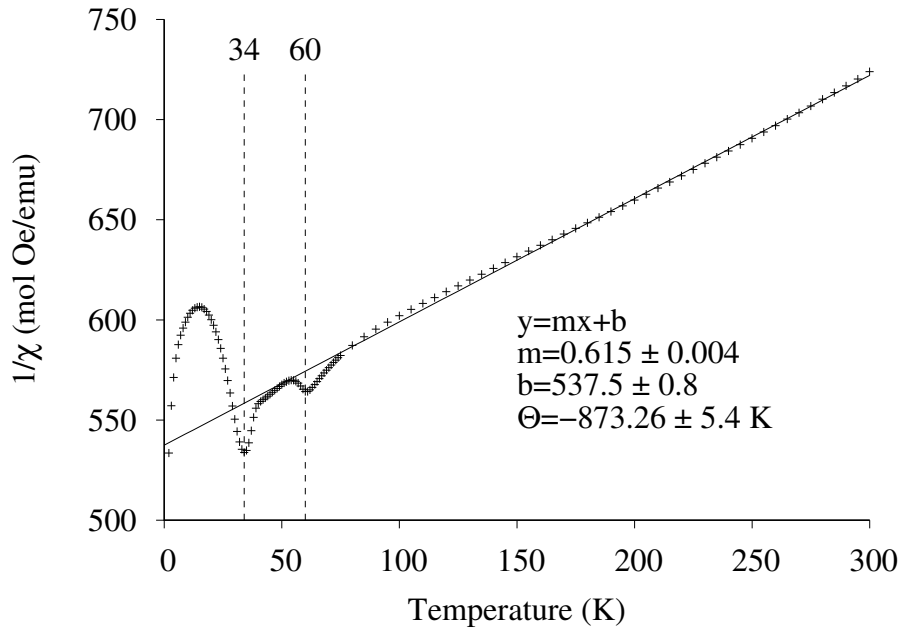


Fig. 4.20 Inverse magnetic susceptibility per mol V, $1/\chi$, as a function of temperature for the CTR-MgV₂O₄ sample prepared *via* a carbothermal route.

XRD (refined site occupancies correspond to a composition of Mg_{0.99}V_{1.97}O₄) but could be detected with magnetic measurements and ²⁵Mg NMR (*vide infra*).

The nonstoichiometry argument is also consistent with a previous observation of variation in T_s and T_N along the growth direction of a single crystal by Islam *et al.*[165] In their study, 3 mol % of excess V₂O₃ was added to the crystal flux to allow a homogeneous composition. The lower part of this single crystal exhibited $T_s = 55$ K and $T_N = 38$ K, which are lower than the corresponding $T_s = 65$ K and $T_N = 42$ K measured from the middle part of the crystal. Our values of $T_s = 60$ K and $T_N = 34$ K are in agreement to this lowering of both transition temperatures.

What is also clear in our measurement is the absence of clear spin-glass like transition at low temperatures, which has been previously demonstrated for a *site-disordered* MgV₂O₄ with excess Mg (~3 %) on octahedral sites.[165] The presence of clear structural (T_s) and magnetic (T_N) transitions may indicate the absence of a *site* disorder in this compound.

In addition, the Weiss constant $\Theta = -873.3 \pm 5.4$ K and the nearest-neighbour magnetic interaction $J_1 = -109.6 \pm 0.7$ K (determined from Θ by use of the relation 2.73) is also significantly larger than the reported values of $\Theta = -600$ K and $J_1 = -75$ K, which would be consistent with the large observed value of μ_{eff} arising from the short-range fluctuations.

Mamiya *et al.* again reported values of $\Theta = -760$ K (100–200 K) and -600 K (450–600 K);[164] our value agrees better with their 100–200 K data.

^{25}Mg NMR

The ^{25}Mg MAS spectrum of the carbothermally prepared CTR- MgV_2O_4 is shown in Figure 4.21. It is noticeably different from the spectrum of the solid-state synthesised SS- MgV_2O_4 sample (Figure 3.15): first of all, three peaks are observed at 1861, 1783, and 1713 ppm, where the 1783 ppm peak is the dominant resonance; they are also significantly broadened compared to the SS- MgV_2O_4 case. Whereas a full DFT calculation of the individual sites could not be performed due to SCF instabilities, approximate insights into the nature of these resonance could be gained by considering the bond pathway contribution (similar to that considered in Section 3.3.4) in MgCr_2O_4 and SS- MgV_2O_4 . Taking into account that each A-site Mg is neighbouring twelve B-site TMs, the contribution of each Cr in MgCr_2O_4 approximates to 238.5 ppm per Cr^{3+} ion or 79.5 ppm per *d*-electron. Mg in SS- MgV_2O_4 , on the other hand, resonates at 1845 ppm, which gives 153.8 ppm per V^{3+} ion or 76.9 ppm per *d*-electron. Hence, we can estimate that the contribution of a *single d*-electron on the cubic spinel B sublattice is around 75-80 ppm. As the V^{4+} cations have only one *d*-electron compared to two of V^{3+} , we can expect a smaller shift for the Mg neighbouring a V^{4+} . Assuming that a single *d*-electron contributes 77 ppm to the total hyperfine shift of a Mg site, the hyperfine shifts of Mg atoms neighbouring two and one V^{4+} ions could be estimated as 1768 and 1691 ppm, respectively. These values are close to the observed shifts of 1783 and 1713 ppm, which suggests the presence of V^{4+} on the vanadium lattice. The results are summarised in Table 4.5.

One can also predict the relative intensities of these resonances by assuming a random distribution of the Mg vacancy- V^{4+} pair. As each Mg site is bonded to twelve V sites, a composition of $\text{Mg}_{0.98}\text{V}_{1.96}^{3+}\text{V}_{0.04}^{4+}\text{O}_4$ (determined from the starting Mg/V ratio) should result in a relative intensity ratio of 39:9.5:1 for the resonances at 1861, 1783, and 1713 ppm, respectively. The experimental intensities, however, show a ratio of 0.9:7.7:1; this initial investigation shows that the random model of V^{4+} distribution is not valid for this sample and may point towards a higher concentration of the V^{4+} ions contained in the lattice, coupled with some degree of ion ordering.

Lastly, the peak broadening observed for the CTR- MgV_2O_4 could come from a lack of sintering present in this sample, as the pellet was pressed with carbon which ultimately gets oxidised to leave an empty space in the pellet; it could also arise from a small degree of quadrupolar coupling introduced by an uneven distribution of electrons due to the arrange-

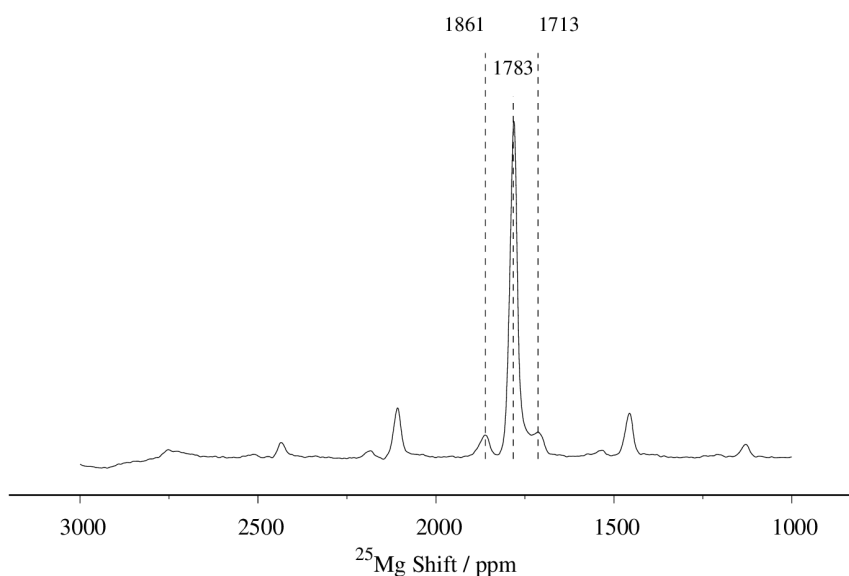


Fig. 4.21 ^{25}Mg spin echo spectrum of CTR- MgV_2O_4 (carbothermal route) at MAS spin rate of 10 kHz. Positions of the isotropic resonances are indicated. 628400 transients were acquired with recycle delays of 0.1 s.

Coordination	12V^{3+}	$11\text{V}^{3+}, 1\text{V}^{4+}$	$10\text{V}^{3+}, 2\text{V}^{4+}$	Remarks
$\delta_{\text{expt}} / \text{ppm}$	1861	1783	1713	Experimental
$\delta_{\text{est,SS}} / \text{ppm}$	1845	1768	1691	Referenced to 1845 ppm of SS- MgV_2O_4
$\delta_{\text{est,CTR}} / \text{ppm}$	1861	1784	1707	Referenced to 1861 ppm of CTR- MgV_2O_4
I_{expt}	0.9	7.7	1	Experimental
I_{random}	39	9.5	1	Random distribution

Table 4.5 Estimated hyperfine shifts and the intensity ratio for the Mg ions in the MgV_2O_4 spinel structure neighbouring V^{3+} and V^{4+} ions. The shifts ‘referenced’ from the 1845 ppm (SS- MgV_2O_4) or 1861 ppm (CTR- MgV_2O_4) are shown. Integrated relative intensities are shown for the experimental spectrum and also calculated assuming a random distribution of the V^{4+} ions.

ments of $\text{V}^{3+}/\text{V}^{4+}$ around the Mg positions. Without DFT calculations, however, quantitative estimations on the magnitude of quadrupolar coupling parameters could not be made.

4.4 Discussion

4.4.1 Implications of the CTR Method for Other Oxides

Many of the potential high-voltage cathode materials for Mg-ion batteries, including $\text{Mg}_3\text{Nb}_6\text{O}_{11}$ and $\text{Mg}_2\text{Mo}_3\text{O}_8$, [206] have unconventional TM oxidation states that are difficult to prepare. The conventional way of preparing these compounds would be a comproportionation of precursors, or a (partial) reduction under a reducing gas such as H_2/Ar . The comproportionation route often requires a crucible inside an evacuated quartz ampoule (MgO reacts with SiO_2 at elevated temperatures), which poses a moderate experimental difficulty. The reduction route under H_2 cannot, in general, be used to easily control the final oxidation state of the product as the reaction is not stoichiometric. This is most easily evidenced by the fact that MgV_2O_5 , a V^{4+} compound, is prepared *via* the first route; reduction under H_2 would result in a V^{3+} compound, as previously mentioned.

As an alternative route, the CTR method could potentially be used to make products with these unusual oxidation states as it provides a way for stoichiometric reduction starting from a stable precursor such as V^{5+} . When combined with computational predictions of the thermodynamic parameters involved, the reaction scheme could be designed in a rational manner. This approach is in principle completely general and it could potentially be a powerful method to prepare many of these complex Li, Na, Mg, and Ca TM oxides which may have technological importance. In addition, it could also be a valuable tool in exploring the complex magnetism in TM oxides, as many of these compounds exhibit unusual magnetic structures at low temperatures. The CTR method can be easily used to prepare large batches of samples for neutron diffraction to probe the magnetic order. This could be an advantage over the quartz ampoule route, where the amount of a single batch is determined by the size of ampoules used. Further work is also in progress regarding the low-temperature magnetic behaviour of $S = 1/2$ compounds MgV_2O_5 and MgVO_3 prepared by the CTR method.

4.4.2 Discussion on the Initial MgV_2O_5 Electrochemistry

Vanadium dissolution

Upon charging/de-magnesiumation of the MgV_2O_5 sample with a VO_2 impurity, it is evident that a vanadium dissolution takes place on the cathode, which is then replated on the lithium anode. Whereas we have shown that VO_2 can give vanadium to become oxidised to V_6O_{13} , possible involvement of $(\text{Mg})\text{V}_2\text{O}_5$ should not be ruled out.

Vanadium dissolution in metal vanadates during an electrochemical cycling has been reported before, mostly for lithium vanadates. For instance, Jouanneau *et al.* reported dissolution of a V³⁺ species upon lithiation of Li_{1.1}V₃O₈, which takes place *via* a Li–V site exchange, or an O²⁻ loss.[207] As our observation of the dissolution takes place upon charging, however, the dissolution must take place *via* an oxidation of the sample. This oxidation could happen alongside an electrolyte degradation (ethylene carbonate and dimethyl carbonate both contain oxygen in the structure) caused by the high applied potential; either or both VO₂ and MgV₂O₅ may exhibit such dissolution.

Assuming an oxidised V⁵⁺ species is present as a VO₄³⁻, a potential oxidation equation could be written for VO₂ as:



where [O] denotes an oxygen generated from the electrolyte degradation. However, a similar oxidation on the MgV₂O₅ again should not be ruled out, which will become evident when a pure-phase sample is prepared and tested.

This vanadium dissolution poses problems for a proper analysis of MgV₂O₅ electrochemistry displayed on Figure 4.15a, for at least three reasons.

- Some of the observed capacity could come from an electrolyte decomposition, which cannot be ruled out. This could be solved by using better electrolytes such as ionic liquids to achieve a higher stability window.
- Vanadium plating on lithium will change the observed cell potential (standard potential for V²⁺ \rightleftharpoons V is –1.13 V *vs* SHE), thus masking the real potential. A three-electrode cell, with the reference, working, and counter electrodes, could be used to deconvolute the effect of Li counterelectrode.
- However, there is no way of distinguishing between the VO₂ dissolution and MgV₂O₅ demagnesiation in terms of voltage, as both are likely to happen in a cell. Obviously, the only solution to this problem is to prepare a sample without VO₂.

However, we note that a full oxidation of VO₂ up to 4.2 V would give 60 mAh/g (based on the amount present in the sample). This is clearly smaller than the observed ‘capacity’ of 250 mAh/g (the tailing ‘wiggles’ excluded); the rest of the capacity is expected to arise from MgV₂O₅, which is also evidenced by the V₂O₅ reflections on the diffraction pattern. Hence, further work with a phase-pure MgV₂O₅ would clarify this electrochemical activity.

The origin of the observed capacity and electrochemical activity

In our electrochemical cycling, a full ‘capacity’ of 250 mAh/g (the tailing ‘wiggles’ excluded) was observed, whereas the material is expected to have a theoretical capacity of 260 mAh/g. While this observed capacity could arise from a combination of the real capacity, electrolyte degradation, and possible vanadium dissolution, we note the possibility of electrochemical activity being present upon charging, as evidenced from the V_2O_5 reflections on the powder diffraction of the charged sample.

We also note that a full demagnesiumation of δ - MgV_2O_5 have resulted in a structural transformation from the AB-type stacking of the V_2O_5 layers in δ - MgV_2O_5 to the AA-type stacking in α - V_2O_5 . This is in direct contrast to the computational result predicted by Sai Gautam *et al.*, where the δ - V_2O_5 type AB-stacking was expected to be metastable over a wide Mg stoichiometry.[67] However, the application of a significant overpotential upon charging (0.8 V in our case) may serve as the driving force for this $\delta \rightarrow \alpha$ phase transformation; in addition, the ‘wiggles’ that extend beyond this theoretical capacity (Figure 4.15a) may be characteristic of this phase transition.

Based on these considerations, further work on preparing and cycling a pure-phase MgV_2O_5 needs to be carried out. Fortunately, the potential source of this excess VO_2 has already been identified: the MgV_2O_6 CTR precursor was prepared by a sol-gel chemistry using a magnesium acetate precursor (nominally tetrahydrate). It is likely that the precursor was further hydrated beyond tetrahydrate, which would result in a Mg deficiency and thus excess vanadium, as evidenced by the TGA measurement. Thus, VO_2 formation could be circumvented by using a stoichiometric amount of the acetate precursor. Alternatively, MgV_2O_6 could be prepared *via* a solid-state route by reacting MgO and V_2O_5 , and subsequently ball-milled to reduce the particle size for the CTR reaction.

4.4.3 MgV_2O_4 : Sample Dependence on the Preparation Method

In this Chapter, we have also demonstrated the applicability of this rational design approach to prepare MgV_2O_4 , a material previously only synthesised through conventional solid-state methods. Starting from the same MgV_2O_6 precursor, it is clear that the reaction conditions (carbon stoichiometry, reaction temperature) could have a direct control over the final product formed (MgV_2O_4 , MgV_2O_5).

^{25}Mg NMR spectrum of the CTR- MgV_2O_4 showed a remarkable difference from the spectrum of SS- MgV_2O_4 , where additional Mg sites were observed as two extra resonances. The starting Mg/V composition and the paramagnetic shifts of these additional resonances

indicate the possible presence of V^{4+} on the lattice arising from the Mg deficiency. This warrants a further work using X-ray spectroscopic techniques such as XANES experiments to confirm the distribution of oxidation states; also, new samples using stoichiometric quantities of precursors must be prepared to rule out the effects of magnesium nonstoichiometry. However, we do note that this also opens up a potential opportunity to perform a systematic study on the overall magnetism (using a SQUID magnetometry) and the local distribution of this V^{4+} sites (as probed with ^{25}Mg NMR) by varying the level of Mg deficiency present in the precursor. This would not only clarify the nature and distribution of the V^{4+} sites, but also help to explain the intensity ratios of the three ^{25}Mg resonances which do not agree with the scenario of random distribution.

4.5 Conclusion and Further Work

In this chapter, a comprehensive investigation was performed on the synthesis, characterisation, and electrochemical cycling of MgV_2O_5 . It was shown that the carbothermal reduction (CTR) method could be used to prepare complex vanadium oxides which are difficult to prepare with conventional methods; computational prediction of the thermodynamic parameters allowed a rational design of reaction conditions leading to this compound, which was experimentally demonstrated. This would open a potential way for large-scale battery applications since many of Li-, Na-, Mg-, and Ca-transition metal oxides are shown to be promising battery electrodes; in addition, large quantities of samples could be easily prepared for neutron diffraction, a technique to probe the long- and short-range magnetic order in these materials. Work is being carried out on extension of this methodology to other interesting oxide materials.

The prepared compound was characterised with advanced NMR techniques. In particular, application of the RAPT pulse sequence allowed a signal enhancement by a factor of 1.6, which would afford a 2.5-fold reduction in acquisition time. The fitted NMR parameters showed good agreement to the DFT-predicted values.

Transition state searching on Mg-ion migration showed that the barrier is indeed low for a divalent ion, 0.6–0.8 eV, which is further reduced by the van der Waals interaction. Interplay of charge and cation migration plays a crucial role in Mg-ion migration for this compound. In particular, doping the system with other cations to investigate the changes in electronic and ionic conductivity would be a natural extension from this work.

Finally, the attempted cycling of MgV_2O_5 in a Li-ion cell showed some evidences for demagnesiumation capacity, despite the VO_2 dissolution; further work will be carried out on cycling a pure-phase sample to confirm reversible cycling.

Chapter 5

An Investigation on the Electronic Structure, Defect Energetics, and Magnesium Kinetics in Mg_3Bi_2

5.1 Introduction

Despite the extensive research conducted in the MIB field, it still remains extremely challenging to identify an electrolyte that is suitable for use with both high voltage cathodes and Mg metal.[10] Whereas the previous chapters have primarily focused on developing ^{25}Mg NMR techniques for cathode materials, the ultimate aim of producing a working MIB system cannot be achieved with the anode counterelectrode and electrolytes. This incompatibility of electrolytes that are suitable for high voltage cathodes with Mg metal and *vice versa* has been a major problem in developing a working MIB system. Hence, a number of studies have focused on using an alternative anode material other than Mg to bypass this problem.[19] In this respect, bismuth metal is a promising anode material with a low discharge voltage of 0.2 V *versus* Mg metal.[208, 209, 210] Bismuth alloys with magnesium to form an intermetallic Mg_3Bi_2 phase, resulting in a theoretical capacity of 385 mAh/g. However, the most interesting feature of bismuth anode is that it displays fast Mg ion insertion and de-insertion, a feature not present in most other Mg-ion electrodes.[211, 208] ^{25}Mg NMR, being an optimal technique to study local ionic motion in solid systems, thus is a promising technique that can be applied to study bismuth system.

As ion dynamics are properties intimately related to the defect chemistry (which in turn depends heavily on the preparation conditions) and ultimately the electronic structure, an

in-depth *ab initio* investigation on the Mg₃Bi₂ system, the end product of discharge process, is presented. This chapter is divided into four sections: in the first section, the structural characteristics of Mg₃Bi₂ is discussed, identifying the possible Mg diffusion pathways. Next, electronic structures and defect energetics are described. Due to the well known problem of band gap underestimation in semilocal DFT, we use three different methods (PBE, HSE06, and G_0W_0) to calculate the electronic structure. In particular, the Greens function based G_0W_0 method is used to give the most accurate value for the minimum band gap, overcoming the band gap problem in semilocal DFT.

Bismuth is a heavy element where relativistic spin-orbit coupling is expected to have a significant influence on the properties relevant to battery chemistry, as shown for lead in a recent *ab initio* study of the lead-acid battery.[212] Thus, calculations were performed with and without the explicit spin-orbit coupling Hamiltonian. Inclusion of spin-orbit coupling was found to reduce the band gap, defect formation energies, and also the Mg migration barrier which was calculated using the hybrid eigenvector-following approach. In addition, inclusion of scalar relativistic effects was shown to significantly influence the lattice structure and calculated NMR shifts.

Finally, previous data on variable-temperature ²⁵Mg NMR data on discharged Mg₃Bi₂ is compared to the *ab initio* data. Using these results one is able to reconcile and rationalise the previous reports on the Mg mobility in Mg₃Bi₂, in which very different Mg mobilities were assumed to occur due to the different concentrations of Mg vacancies in the samples. We also demonstrate that the hybrid eigenvector-following method can be a very efficient approach for locating transition states in systems where spin-orbit coupling is likely to play an important role.

5.2 Methodology

5.2.1 Computational Details

All Density Functional Theory (DFT) calculations were performed with the VASP code[213, 214] employing the projector-augmented wave (PAW) method[215]. Spin-polarized Perdew-Burke-Ernzerhof (PBE) and Heyd-Scuseria-Ernzerhof (HSE06) exchange-correlation functionals were adopted.[216, 86] For the energy and force calculations, PAW pseudopotentials treating the Mg $3s^2$ and Bi $5d^{10}6s^26p^3$ as valence states were used, with a plane-wave basis cutoff of 350 eV. All lattice relaxations were performed with 1.3 times the ENMAX value as defined in the pseudopotential file. In addition, additional support grid was used for the

evaluation of augmented charges (ADDGRID=.TRUE.). Self-consistent field (SCF) cycles were converged with an energy tolerance of 10^{-4} eV. Monkhorst-Pack k -point sampling of $< 0.05 \text{ \AA}^{-1}$ was used in the Brillouin zone. For the density of states and band structure calculations, Mg $2p$ states were also treated as valence states in the PAW potential and an increased cutoff of 550 eV was used. Cellular relaxations SCF cycles were converged to a 10^{-6} eV limit. Γ -centered k -point sampling of $< 0.03 \text{ \AA}^{-1}$ was used.

Single-shot G_0W_0 calculations* were performed with 250 frequency grid points and a 360 eV plane-wave cutoff for the response function calculations. HSE06 wavefunctions were used as starting wavefunctions for the G_0W_0 calculations. Band gap convergence with respect to the number of frequency grid points, number of empty bands, and plane-wave cutoffs were checked. Quasiparticle energy iterations were converged to a 10^{-8} eV limit.

Relativistic corrections to the electronic structure were taken into account through two levels of theory: a ‘scalar relativistic’ correction which only includes the mass-velocity and Darwin terms of the relativistic Hamiltonian, as implemented in VASP; (see Section 2.2 and [217]) and a ‘full relativistic’ correction that explicitly includes the spin-orbit coupling term alongside the scalar relativistic correction.

The initial structure of Mg_3Bi_2 was fully relaxed until the energy differences between the subsequent steps are converged to 10^{-5} eV per cell and the forces are $< 0.05 \text{ eV/\AA}^{-1}$. For the defect calculations, two supercells each containing 40 atoms (16 Mg, 24 Bi) and 120 atoms (48 Mg, 72 Bi) were created and again relaxed to the above criteria. Defect notations follow that of Kroger and Vink, with charge superscripts omitted for clarity (*e.g.* $\text{Bi}_{\text{Mg}(\text{oct})}$ denotes a neutral Bi sitting on an octahedral Mg site).[218] All defect energies were referenced to the respective bulk metals (Mg, Bi) at the same level of theory as the defect calculations. Only the neutral defects are considered since the system has a vanishing band gap under the PBE level of theory, with the metallic behaviour enhanced under the inclusion of spin-orbit coupling. Whereas the formation energies under the HSE06 level of theory (where a finite band gap was observed) could give a chemical potential dependence, this was not possible due to the computational resources available.

5.2.2 Calculation of NMR Parameters

NMR parameters of Mg_3Bi_2 using the Gauge Including Projector-Augmented Wave (GI-PAW) method was calculated with the CASTEP 16.11 code.[219, 97, 220] Experimental cell structures were fully relaxed (under symmetry constraints) to $< 0.03 \text{ eV/\AA}^{-1}$ limit under

*Performed by Dr Bartomeu Monserrat (Cavendish Laboratory, University of Cambridge)

three different conditions: (i) nonrelativistic (NR), with the core electrons treated with only Schrödinger Equation; (ii) scalar relativistic (SR), with the Zeroth-order regular approximation (ZORA) to the core electrons; (iii) full relativistic (FR), with full inclusion of spin-orbit coupling in the Hamiltonian. CASTEP keywords `RELATIVISTIC_TREATMENT=Schroedinger/ZORA` were used to generate the on-the-fly pseudopotentials for the first two, whereas a j -dependent pseudopotential available from the CASTEP developers were used for the FR calculations. Monkhorst-Pack k -point sampling of $< 0.03 \text{ \AA}^{-1}$ was used in the Brillouin zone with a plane-wave cutoff of 700 eV and SCF convergence of 10^{-5} eV. NMR parameters were only calculated for the NR and SR case, as CASTEP does not support a FR Hamiltonian in GIPAW calculations. The calculated shielding σ_{iso} were converted to the shift δ_{iso} with reference to solid MgO (26 ppm).

5.2.3 Transition State Searching

Transition state and steepest-descent pathway were found using the hybrid eigenvector-following approach as implemented in the OPTIM code.[221, 113, 191] In brief, this method finds the smallest eigenvalue of the Hessian matrix without calculating the full matrix, by minimizing the Rayleigh-Ritz ratio. Here we use a low-memory Broyden-Fletcher-Goldfarb-Shannon (LBFGS) scheme to minimize this ratio on a given point to find the uphill path. The minimization was deemed to have occurred when the root-mean-square gradient is smaller than $0.025 \text{ eV \AA}^{-1}$. Then up to five LBFGS minimization steps are performed in the tangent space until the root-mean-square gradient is smaller than $10^{-3} \text{ eV \AA}^{-1}$. Initial guesses of the transition state structure were produced by removing a nearby Mg atom and putting the migrating Mg atom in the middle of the proposed diffusion path. The steepest descent pathway from the transition state is found by displacing the atoms by 0.1 \AA from the transition state in the parallel and antiparallel directions to the eigenvector. Local minima are then found by the LBFGS algorithm with energy convergence of 10^{-3} eV .

We note that the transition state geometry and eigenvectors obtained from the significantly cheaper scalar relativistic calculations could be re-used as an initial guess for the fully relativistic calculations. We have observed that only < 5 force evaluations are typically needed for the relativistic calculations when this approach is taken, which significantly reduces the computational requirement. In addition, unlike the classical nudged elastic band (NEB) method where only a few points along the pathway are sampled, HEF method can sample the path at an arbitrary step size. This allows us to capture the finer details of the energy variance along the pathway.

5.3 Results and Discussion

5.3.1 Crystal Structure

Mg_3Bi_2 is the last in a series of magnesium pnictide compounds Mg_3X_2 ($\text{X}=\text{P}, \text{As}, \text{Sb}, \text{Bi}$) and is a Zintl-type compound with closed shell ions with formal charges of Mg^{2+} and Bi^{3-} . It adopts an anti- La_2O_3 type structure with hexagonal $P\bar{3}m1$ space-group symmetry.[222] The structure is schematically illustrated in Figure 5.1. In terms of ion arrangements, Mg_3Bi_2 incorporates two alternating layers: layer A consists of tetrahedrally coordinated Mg^{2+} cations (denoted $\text{Mg}(\text{tet})$) and octahedral interstitial sites forming ‘covalent’ $\text{Mg}_2\text{Bi}_2^{2-}$ sheets whereas layer B consists of octahedrally coordinated Mg^{2+} cations (denoted $\text{Mg}(\text{oct})$) and tetrahedral interstitial sites. These interstitial sites are expected to play an important role in ionic diffusion[223] as discussed further below.

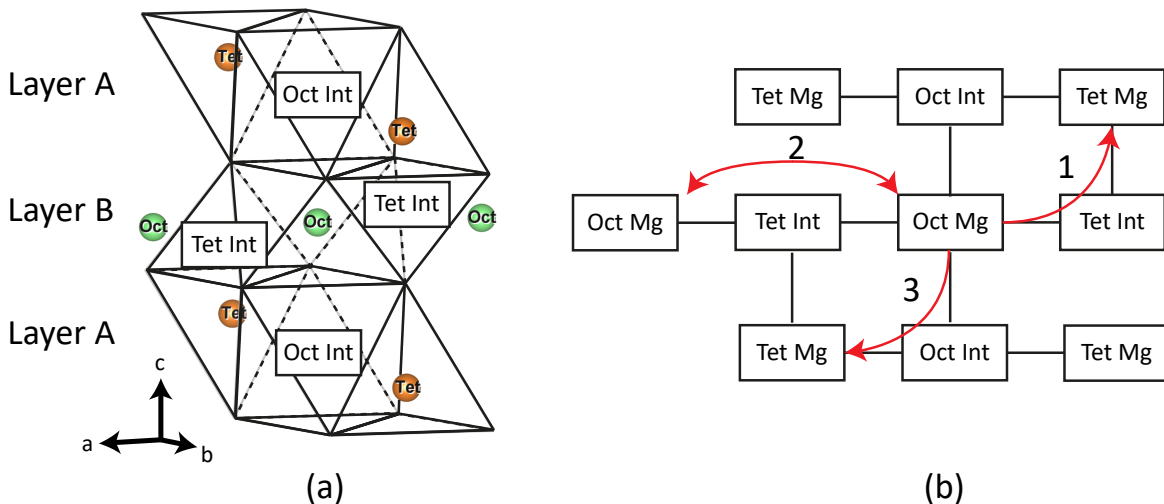


Fig. 5.1 (a) Crystal structure of Mg_3Bi_2 . Positions of tetrahedrally coordinated Mg (orange sphere, Tet) and octahedrally coordinated Mg (green sphere, Oct) are shown. Bismuth atoms sit on the line vertices (not shown for clarity). (b) Schematic illustration of the Mg_3Bi_2 structure (on the left) showing the possible diffusion pathways involving the tetrahedral and the octahedral interstitial sites (‘Tet Int’ and ‘Oct Int’).

From DFT-based lattice relaxation, we can see that the PBE functional (both on CASTEP and VASP) consistently overestimates the experimentally determined a cell parameter[224] at both the scalar relativistic and full relativistic levels of theory, whereas it marginally underestimates the c parameter at the scalar relativistic level, and overestimates it at the full relativistic level (Table 5.1). Fully nonrelativistic calculations, however, result in a distortion in the a/c ratio; the effect of this is discussed in Section 5.3.3. The HSE06 functional again

overestimates the a lattice parameter, although to a smaller extent than PBE, whereas it underestimates the c lattice parameter. Finally, inclusion of SOC results in slight expansion of the cell which may arise from reduced electrostatic interactions (see below).

	PBE) (CASTEP)			PBE (VASP)		HSE06 (VASP)		Expt
	NR	SR	FR	SR	FR	SR	FR	
$a / \text{\AA}$	4.96	4.70	4.72	4.71	4.72	4.65	4.66	4.62
$c / \text{\AA}$	6.50	7.46	7.48	7.40	7.44	7.35	7.36	7.41

Table 5.1 DFT-predicted cell parameters of Mg₃Bi₂ using the PBE and HSE06 exchange-correlation functionals using CASTEP and VASP. NR, SR and FR refer to nonrelativistic, scalar relativistic, and full relativistic (i.e. explicit spin-orbit coupling) calculations, respectively. ZORA method was used for SR calculation on CASTEP. Experimental lattice constants are from Lazarev *et al.*[224]

Finally, we note that Mg₃Bi₂ undergoes a phase transition above 703 °C to a defective body-centered cubic structure similar to AgI, with excess Mg cations as the tetrahedral interstitials, resulting in Mg_{1.5}Bi.[225] As expected from the AgI structure, it shows superionic conduction of Mg²⁺ cations as determined through neutron diffraction.[226] In this study, however, we restrict the investigation to the room-temperature hexagonal phase which is more relevant to Mg-ion batteries.

5.3.2 Electronic Structure

Despite being first reported in 1933 by Zintl[222], the precise electronic structure and the band gap (E_g) of Mg₃Bi₂ has not been conclusively determined with either experiment or theoretical calculations. In a series of work, Ferrier and co-workers have speculated that Mg₃Bi₂ is semimetallic based on a conductivity-composition plot;[227, 228] Lazarev *et al.* have assumed Mg₃Bi₂ is semiconducting with $E_g = 0.1$ eV;[224] Watson *et al.* obtained $E_g = 0.5$ eV from Mg X-ray emission spectra.[229] Work on the amorphous Mg₃Bi₂ alloy have shown from conductivity measurements that it is semiconducting with a band gap of 0.15 eV.[230] These varying results may arise from the difficulty in preparing these materials stoichiometrically, due to the high vapour pressure of Mg. Previous literature describing electronic structure calculations is also sparse: Sedighi *et al.* concluded Mg₃Bi₂ is a semiconductor with $E_g = 0.25$ eV based on Engel-Vosko Generalized Gradient Approximation (EV-GGA),[231] whereas Imai *et al.*, Xu *et al.*, and Zhang *et al.* concluded it is a semimetal based on pure GGA calculations.[232, 233, 234] However, all these works except the last

one did not consider explicit spin-orbit coupling (SOC), which has been shown to play an important role in the electronic structure of compounds involving heavy atoms such as bismuth.[235, 236]; in addition, the well known problem of band gap underestimation in semilocal DFT necessitates the use of a higher level of theory to predict the accurate electronic structure of this material. Hence, we revisit the electronic structure of this compound using state-of-the-art electronic structure methods such as hybrid functionals and many-body perturbation theory in the G_0W_0 approximation, and also consider the effects of spin-orbit coupling.

First we look at the Bader charges of Mg and Bi in the structure, shown in Table 5.2. The HSE06 functional results in an increased ionicity in the system compared to the semilocal PBE values. In all cases, inclusion of SOC resulted in decreased ionicity which is consistent with the density of states data shown below.

	Bi	Mg _{oct}	Mg _{tet}
PBE SR	-2.10	+1.42	+1.39
PBE FR	-2.06	+1.39	+1.37
HSE06 SR	-2.21	+1.51	+1.45
HSE06 FR	-2.18	+1.48	+1.44

Table 5.2 Scalar relativistic (SR) and full relativistic (FR) Bader charge analysis of Mg_3Bi_2 using the Perdew-Burke-Ernzerhof (PBE) and Heyd-Scuseria-Ernzerhof (HSE06) exchange-correlation functionals. Only the valence charge is calculated.

Figure 5.2 shows the density of states (DOS) plots obtained for Mg_3Bi_2 using DFT within the semilocal PBE and hybrid HSE06 approximations. Both methods show the same trend comparing the results with and without SOC. As expected from the charge distribution of Mg_3Bi_2 , the top of valence band is strongly dominated by the bismuth $6p$ contribution down to around -5 eV from the Fermi level and has a negligible Mg contribution. As expected from the literature, the relativistic contraction of the bismuth $6s$ states around -12 eV from the Fermi level results in a relatively large separation of around 5 eV between the top of $6s$ and the bottom of $6p$ states, which makes it chemically inactive (the so-called inert-pair effect).[237]. The downshift in $6s$ energy by adding the full relativistic effect is around -0.15 eV; effects of similar magnitudes were observed in PbO_2 , an important active material in lead-acid batteries.[212]

Figure 5.3 shows the band structure of Mg_3Bi_2 using DFT within the semilocal PBE and hybrid HSE06 approximations, with and without the spin-orbit interaction. At the PBE level, Mg_3Bi_2 exhibits semimetallic behaviour, consistent with the earlier reports of a type-II nodal line semimetal at this level of theory.[234] The inclusion of spin-orbit coupling opens

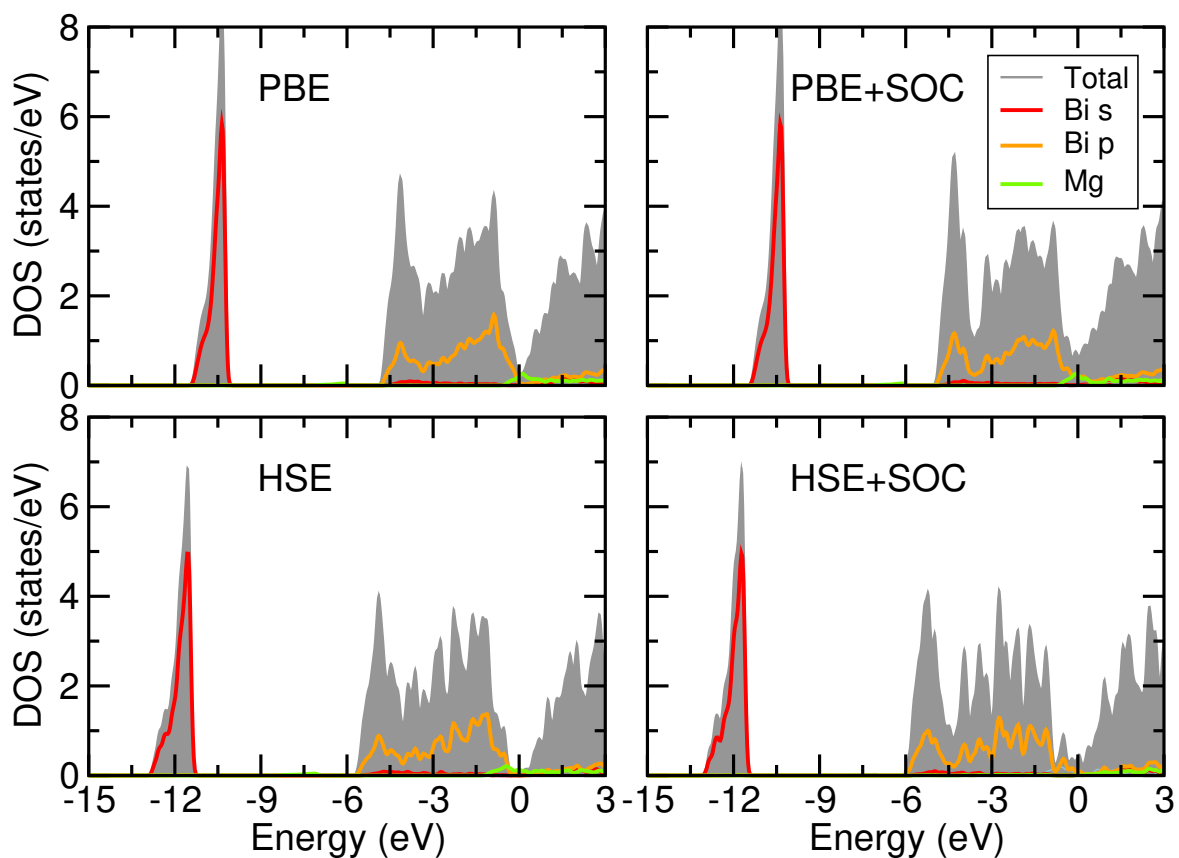


Fig. 5.2 Density of states plot of Mg_3Bi_2 using the PBE and HSE06 exchange-correlation functionals. Local atomic DOS projections inside the sphere defined by the Wigner-Seitz radii (1.63 and 1.52 Å for Bi and Mg, respectively) are also shown. All energies were referenced to the highest occupied state.

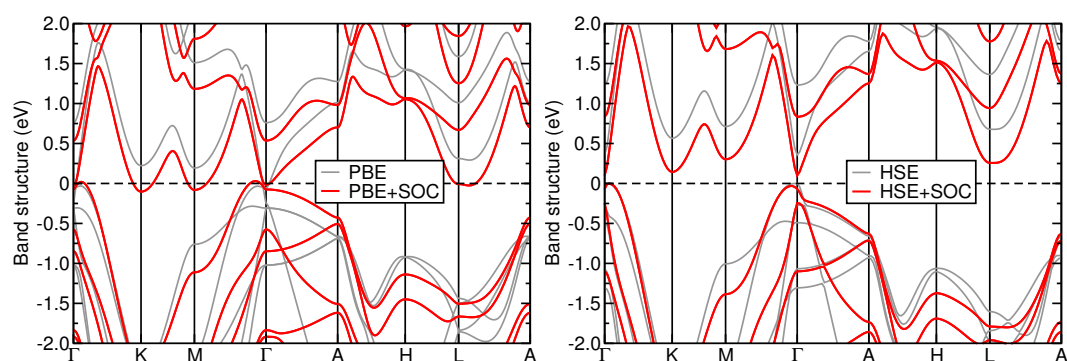


Fig. 5.3 Band structure plots of Mg_3Bi_2 using the PBE (left) and HSE06 (right) exchange-correlation functionals without (grey) and with (red) spin-orbit coupling (SOC). The Fermi level is located at the zero of energy.

a small gap in the nodal line, but the system remains semimetallic. At the HSE06 level, Mg_3Bi_2 is a semiconductor with the minimum band gap of 0.36 eV located at the Γ point. The inclusion of spin-orbit coupling reduces the band gap to 0.17 eV, but the system remains semiconducting. The G_0W_0 calculations show that the Γ -point band gap increases to 0.58 eV without spin-orbit coupling. We expect that spin-orbit coupling would reduce the band gap by an amount similar to that observed in HSE06, and thus Mg_3Bi_2 is also semiconducting at the G_0W_0 level of theory.

We note that inclusion of SOC results in a reduced band gap and increased dispersion of the Bi $6p$ states. Previous reports on binary Sb and Te compounds have attributed this phenomenon to spin-orbit coupling in the anion p -orbitals: energy splitting of the degenerate p -states result in the $j = 3/2$ state being split upward in energy, and the $j = 1/2$ state being split downward in energy.[238] The net effect of this splitting is a reduction in the band gap.

5.3.3 Calculation of the ^{25}Mg NMR Shifts

With a full understanding of the relativistic SOC on the electronic structure of Mg_3Bi_2 , DFT-based NMR parameter calculations were also performed on the Mg_3Bi_2 structure to confirm the assignment and to evaluate the effect of SOC. Calculations using the CASTEP code is shown in Table 5.3. The corresponding DOS plot in Figure 5.4 show a result consistent with the VASP result in Figure 5.2. While the relativistic contribution of the heavy bismuth atoms is significant for the electronic structure and ultimately the chemical shielding, fully relativistic calculation of chemical shielding is not yet supported in this version of CASTEP. Indeed, the chemical shifts δ_{iso} using the scalar relativistic Zeroth-Order Regular Approximation (ZORA) method show a poor match to the experimentally observed shifts, showing errors on the order of hundreds of ppm. However, it is seen that the ZORA method gives a qualitatively correct prediction on the relative magnitudes of the chemical shielding: Mg(oct) environment is more shielded (down-shifted) relative to the Mg(tet) environment, which supports our NMR assignment. The error is likely to arise from the (i) relativistic contribution to the chemical shift and (ii) semimetallic behaviour of Mg_3Bi_2 at the PBE level of theory, which creates small partial occupancies of bands close to the Fermi level.

On the other hand, a fully nonrelativistic calculation using the on-the-fly pseudopotential on CASTEP shows the partial extent of relativistic SOC effects for chemical shifts in Mg_3Bi_2 , where the errors are on the order of thousands of ppm. This extreme increase in chemical shift of both Mg ions are likely to come again from the fact that the relativistic contraction of Bi s -orbitals make the Bi ions ‘softer’ by screening the $6p$ -orbitals (i.e. make the bonding

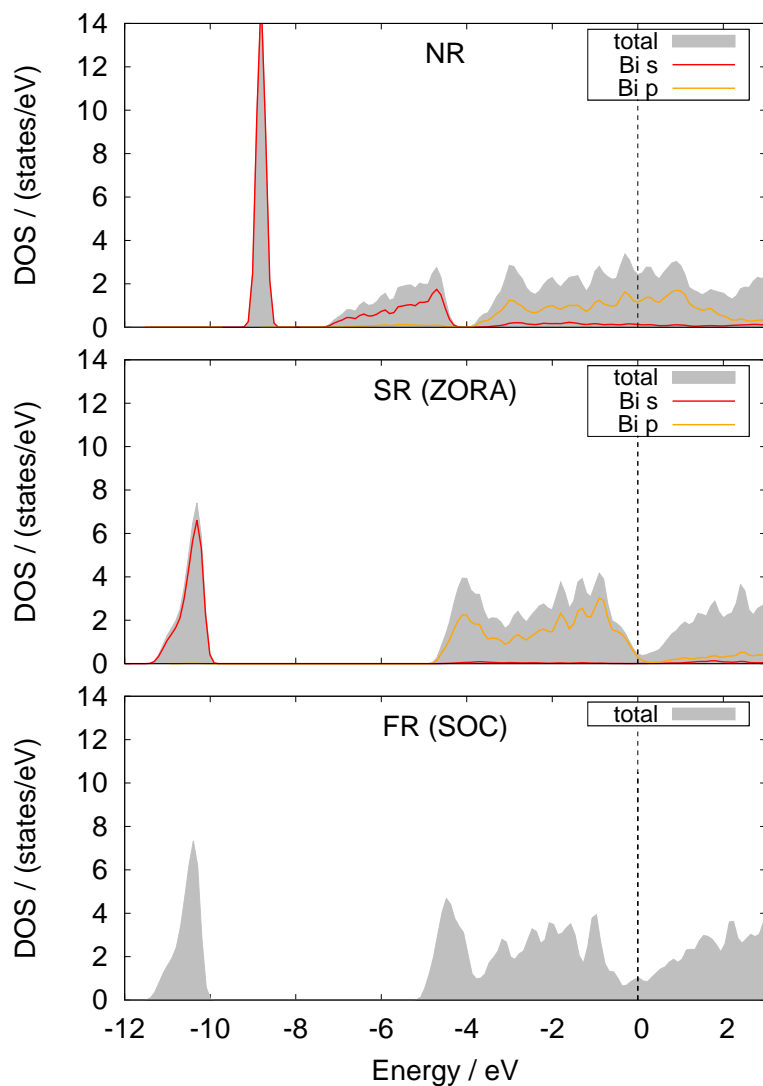


Fig. 5.4 Density-of-states (DOS) plot for Mg_3Bi_2 , generated using CASTEP. Three cases are considered: nonrelativistic (NR), scalar relativistic (SR) using the ZORA method, and full relativistic (FR) including the SOC. All energies were referenced to the highest occupied state. Site- and orbital-decomposed DOS under SOC is not supported in the version of CASTEP used.

Site	Level	δ_{iso} / ppm	Ω / ppm	κ	C_Q / MHz	η
Mg(oct)	Expt	-306	-	-	-	-
	SR	64.9	204.2	-0.96	-1.23	0.0
	NR	2145.7	3920.3	-0.49	3.44	0.0
Mg(tet)	Expt	-6	-	-	-	-
	SR	169.6	166.5	-0.96	-2.47	0.0
	NR	2157.8	2522.7	-0.51	-0.15	0.0

Table 5.3 Calculated NMR parameters of the two Mg sites (octahedral and tetrahedral) in Mg_3Bi_2 using the GIPAW method. Core electrons are treated with two levels of theory: scalar relativistic (SR) ZORA and nonrelativistic (NR) Schrödinger. δ_{iso} , Ω , and η refer to the chemical shift tensor expressed in the Herzfeld-Berger convention. C_Q and η refer to the quadrupolar coupling parameter and asymmetry, respectively.

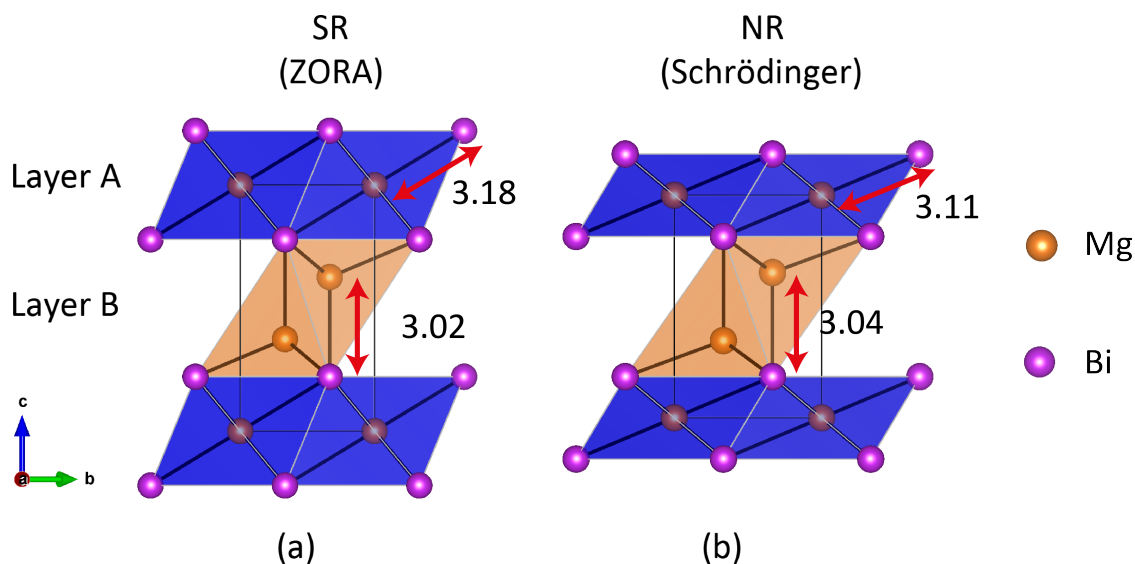


Fig. 5.5 Relaxed cell structures using the (a) scalar relativistic ZORA approximation, and (b) nonrelativistic Schrödinger equation, projected along the a -direction. Here, Mg(oct) sits on layer A and Mg(tet) sits on layer B.

less ionic). However, it must also be stressed that the system is properly metallic under this level of theory, with a significant density of states at the Fermi level (Figure 5.4); this would likely render the calculated chemical shift to be unphysical.

EFG components show only a variation on the same magnitude between the ZORA and Schrödinger methods. This is expected as EFG tensors are quantities more dependent on the local atomic arrangements and less dependent on the core electron distribution compared to the chemical shielding. Previous determination of ²³Na EFG tensors in oxides have also reported a qualitative agreement of the EFG values obtained by use of a *classical* point charge approximation.[239]

However, a reduction of -94 % in the EFG tensor is observed for the Mg(tet), from 2.47 MHz (ZORA) to 0.15 MHz (Schrödinger). Such negative variation is not observed for the Mg(oct), where the rate of change is larger and positive (1.23 MHz to 3.44 MHz; 227 %). To better understand such different changes in the EFG tensor, the structural aspects need to be taken into account. Figure 5.5 shows the dramatic difference in the local Mg coordination between the relaxed cell structures using the ZORA and Schrödinger approximations. As shown in Table 5.1, nonrelativistic Schrödinger calculations result in a large contraction of the *c*-lattice parameter and slight expansion of the *a*-lattice parameter. The net effect of this is a ‘squeezing’ of the cell, as shown in Figure 5.5. Due to this effect, the local coordination around Mg is drastically changed, and the coordination octahedron around the Mg(oct) is distorted significantly; this results in an increased C_Q , but keeps $\eta = 0$ due to the axial symmetry present from the lattice symmetry. The effect of relativistic SOC on Mg(tet) is less obvious, but the contraction of *c* and elongation of *a* simultaneously result in a spherically more symmetric environment, resulting in a significantly reduced C_Q .

5.3.4 Defect Energetics

To investigate the possibility of different types of defects present in the Mg₃Bi₂ sample, formation energies ΔE_f of various stoichiometric and non-stoichiometric point defects were calculated *ab initio*. The results outlined in Table 5.4 are separated into three categories: antisite defects, Frenkel defects, and vacancy defects, which we discuss in sequence. Nonstoichiometric antisite and vacancy defects were created by removing or inserting relevant atoms from the stoichiometric cell while retaining the charge neutrality of the cell due to Mg₃Bi₂ being a semimetal at the PBE level of theory (*i.e.* charged defects are not possible under such a situation). For instance, a Mg vacancy defect would involve removal of a neutral Mg atom resulting in a composition of Mg₂₃Bi₁₆ (for a 40-atom supercell) and two electron holes on

the Fermi level; similarly, a Mg substitutional defect would involve a Bi atom replaced for a Mg atom, resulting in $\text{Mg}_{25}\text{Bi}_{15}$ (again for a 40-atom supercell) and five excess electrons on the Fermi level. Charge neutrality is automatically maintained in the antisite and Frenkel defects since they are stoichiometric.

First, the formation of antisite defects are energetically unfavorable, with the Mg on a Bi site having the highest formation energy of 2.92 eV. This is most likely due to the large difference between their ionic radii. Despite the fact that no ionic radius for the Bi^{3-} ion is reported, the trend can still be explained in terms of the corresponding atomic radii of Mg and Bi (Mg 1.50 Å; Bi 1.60 Å), the difference being expected to get even larger as Mg is oxidized and Bi is reduced. This is also supported from the Mg–Bi bond lengths in Mg_3Bi_2 crystal: $\text{Mg}_{\text{oct}}\text{–Bi}$ 3.21 Å *versus* $\text{Mg}_{\text{tet}}\text{–Bi}$ 2.92 Å. Using the Shannon radii of 0.72 and 0.57 Å for Mg_{oct} and Mg_{tet} , respectively,[18] Bi^{3-} radii of 2.49 and 2.35 Å are obtained in each case. In addition, the unfavourable electrostatic interaction between the ions of same charge (Mg occupying the Bi lattice site is coordinated by Mg ions, and vice versa) reinforces the high energy cost in forming these types of defects.

The ΔE_f of Frenkel-type defects (creation of a vacancy plus an interstitial) are also shown to be relatively high for both nearby and separated vacancy–interstitial pairs; around 0.8-1.2 eV is required for their formation. However, performing structural relaxation on some of the starting guesses with the defect Mg ion sitting on an interstitial site that is adjacent (in the first coordination shell) to a Mg vacancy (specifically, the $V_{\text{Mg}(\text{oct})} + \text{Mg}_{\text{i}(\text{tet})}(\text{nn})$, $V_{\text{Mg}(\text{tet})} + \text{Mg}_{\text{i}(\text{tet})}(\text{nn})$, and $V_{\text{Mg}(\text{tet})} + \text{Mg}_{\text{i}(\text{tet})}(\text{nn})$ cases) resulted in the structure reverting back to that of the pristine cell, with no defects. This indicates that these defects are energetically unstable and they would revert back to the original structure, if formed at all. These sites, as we will see later, may play an important role as energy maximum transition state sites in Mg-ion diffusion.

Perhaps the most surprising results are the energies of the vacancy defects: while Mg vacancy defects have around the same ΔE_f as Frenkel defects without SOC, their magnitudes are reduced significantly when SOC is included in the Hamiltonian. From the fully relativistic calculation on the 120-atom supercell with SOC included, ΔE_f of octahedral vacancies $V_{\text{Mg}(\text{oct})}$ is found to be as low as 0.33 eV, with a slightly higher value of 0.42 eV for tetrahedral vacancies $V_{\text{Mg}(\text{tet})}$. This effect is likely to be connected to the enhanced shielding of Bi 6*p*-levels due to the SOC effect as explained above: as formation of a neutral Mg vacancy should involve loss of electrons from the Bi, this deshielding should result in a significant reduction of the formation energy. Hence, considering their low formation

energies, we conclude that vacancy defects are the dominant type of defects present in Mg₃Bi₂.

5.3.5 Mg Migration Kinetics

Having established the defect chemistry in Mg₃Bi₂, we now turn our attention to the Mg diffusion in this structure and study the migration barriers.

As Mg vacancies were shown to have low formation energy, especially with SOC included, we attempt to simulate the effect of vacancy diffusion following the creation of one octahedral Mg vacancy $V_{\text{Mg}(\text{oct})}$. This has lower ΔE_f than the tetrahedral vacancy $V_{\text{Mg}(\text{tet})}$ as illustrated in the previous section. Then, a nearby tetrahedral Mg atom is removed from its original position and placed on the guessed ‘transition state’. Finally, a hybrid eigenvector-following approach is used to find the transition state, followed by the search for a steepest descent path connecting the two corresponding minima.

The result presented in Figure 5.6 clearly shows a small diffusion barrier of hopping between the Mg_{oct} and Mg_{tet} (Path 1 on Figure 5.1b), with 0.34 eV for the fully relativistic calculation and 0.43 eV for the scalar relativistic calculation. In contrast, the Mg_{oct} – Mg_{oct} diffusion barrier (Path 2 on Figure 5.1b) is around twice that of the Mg_{oct} – Mg_{tet} diffusion barrier, indicating that the Mg diffusion must occur *via* octahedral-tetrahedral exchange. This is in line with the conclusion from ²⁵Mg NMR studies of Liu *et al.*[40] An alternative exchange mechanism involving Path 3 on Figure 5.1b was also investigated, but the transition structure searching resulted in the same transition state as for the Path 1, clearly indicating the absence of a diffusion pathway along this line.

With the *ab initio* calculations of the defect creation and activation energies, we now compare our results with available experimental data. As reported in the literature, bismuth can be cycled reversibly to form Mg₃Bi₂ in a Mg-ion battery.[208] Previous work on magnesium ion conduction in bismuth anodes either used the Galvanostatic Intermittent Titration Technique (GITT) on an electrochemical cell, or *ex-situ* variable-temperature (VT) ²⁵Mg NMR spectroscopy to probe Mg transport.[211, 40] In this work, however, we restrict the discussion to the latter NMR result, due to the following limitation of GITT experiments: in the GITT measurement, the voltage response (resulting from the relaxation) of the cell after the application of a short current pulse is modelled with the diffusion equation to extract the diffusion coefficient D under the assumption that the (de)insertion reaction occurs *via* a solid solution (*i.e.* the relaxation of the potential after the current pulse is a measure of ionic transport through a *single* phase). In-situ X-ray diffraction results, however, have clearly shown

	ΔE_f			
	40-atom Supercell		120-atom Supercell	
	SR	FR	SR	FR
Antisite defects				
$\text{Bi}_{\text{Mg}(\text{oct})}$	1.84			
$\text{Bi}_{\text{Mg}(\text{tet})}$	2.01			
Mg_{Bi}	2.92			
$\text{Bi}_{\text{Mg}(\text{oct})} + \text{Mg}_{\text{Bi}}$	2.51	2.27		
$\text{Bi}_{\text{Mg}(\text{tet})} + \text{Mg}_{\text{Bi}}$	1.17	1.15		
Frenkel defects				
$\text{V}_{\text{Mg}(\text{oct})} + \text{Mg}_{\text{i}(\text{oct})}$ (nn)	0.87	0.79	0.89	
$\text{V}_{\text{Mg}(\text{oct})} + \text{Mg}_{\text{i}(\text{oct})}$ (far)	0.89	0.81	1.04	
$\text{V}_{\text{Mg}(\text{oct})} + \text{Mg}_{\text{i}(\text{tet})}$ (nn)	*	*	*	*
$\text{V}_{\text{Mg}(\text{oct})} + \text{Mg}_{\text{i}(\text{tet})}$ (far)	1.49	1.41	1.55	
$\text{V}_{\text{Mg}(\text{tet})} + \text{Mg}_{\text{i}(\text{oct})}$ (nn)	*	*	*	*
$\text{V}_{\text{Mg}(\text{tet})} + \text{Mg}_{\text{i}(\text{oct})}$ (far)	1.07	0.98	1.10	
$\text{V}_{\text{Mg}(\text{tet})} + \text{Mg}_{\text{i}(\text{tet})}$ (nn)	*	*	*	*
$\text{V}_{\text{Mg}(\text{tet})} + \text{Mg}_{\text{i}(\text{tet})}$ (far)	1.17	1.15	1.61	
Vacancy defects				
$\text{V}_{\text{Mg}(\text{oct})}$	1.09	0.40	1.03	0.33
$\text{V}_{\text{Mg}(\text{tet})}$	1.17	0.50	1.12	0.42
V_{Bi}	1.88	2.02		

Table 5.4 Scalar relativistic (SR) and full relativistic (FR) *ab initio* formation energies ΔE_f of various stoichiometric and non-stoichiometric defects in Mg_3Bi_2 using the PBE functional. Defect notations follow the convention of Kroger and Vink with neutral sign omitted for clarity.[218] All calculations assumed non-charged defects (see text) with cell dimensions fixed to simulate a dilute limit. Vacancy defect energies are referenced to the respective metals. For Frenkel defects, two scenarios where the Mg sits on a nearby (nn) or far interstitial sites were considered. Asterisks(*) indicate that the resulting structure was unstable and reverted back to the starting structure. All values are quoted in electron-volts. Only some of the calculations were performed under the 120-atom supercell condition after an initial screening with the 40-atom supercell.

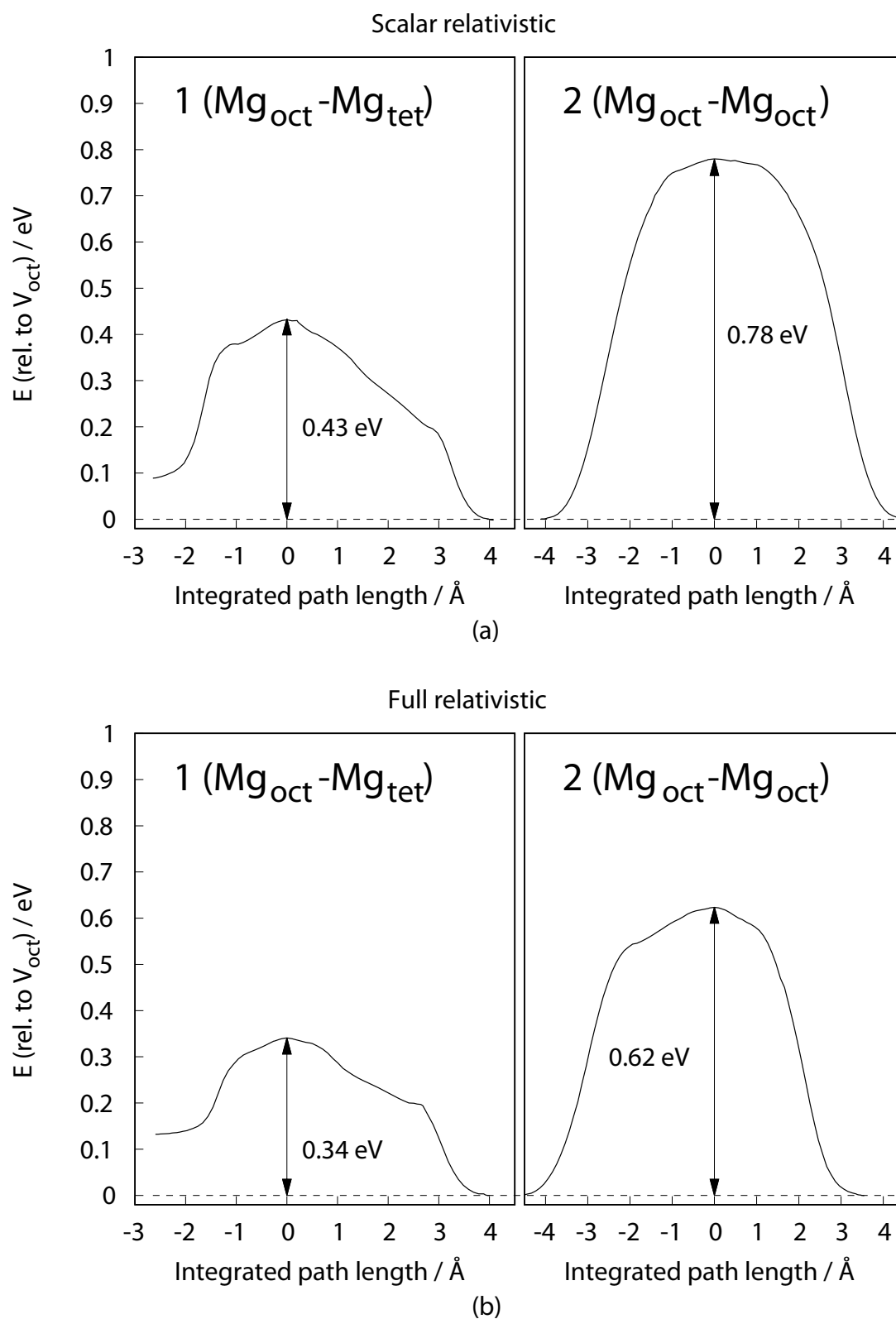


Fig. 5.6 Diffusion profile of Mg ion for selected pathways as illustrated in Figure 5.1b. (a) Scalar relativistic, (b) full relativistic, with SOC included. Energies are referenced to the bulk energy of each 120-atom supercell with one V_{oct} defect.

that magnesianation occurs *via* a two-phase reaction between Bi and Mg_3Bi_2 .^[40] Thus the diffusion coefficients extracted from GITT measurements must be treated with caution, since the relaxation phenomena under these conditions may include multiple contributions such as (i) redistribution of Mg ions due to the formation of metastable (possibly non-stoichiometric solid solution) phases formed under operating conditions (and on application of an over-potential), and (ii) redistribution of phase boundaries to minimise the interfacial energies, etc.

We now consider transport in two cases, the first in a completely stoichiometric material where we need to consider the energy associated with defect formation. In this case, substitutional and vacancy defects are not relevant because they result in stoichiometry changes. The second case explores diffusion in off-stoichiometry materials $\text{Mg}_{3-x}\text{Bi}_2$ and $\text{Mg}_3\text{Bi}_{2+y}$, representing Mg vacancy and (excess) Bi substitutional defects, respectively. As no extrinsic Mg vacancies are expected in the stoichiometric Mg_3Bi_2 compound, the diffusion in this case must occur *via* a vacancy diffusion mechanism involving thermally generated Mg vacancies; hence the observed D would be the diffusion coefficient of Mg vacancies. In the latter case, nonstoichiometry dictates that extrinsic Mg vacancies must exist in the compound.

Table 5.5 compares the effective activation barriers E_a^{eff} obtained experimentally *versus* the E_a^{eff} estimated from the *ab initio* calculations using the scalar relativistic (SR) and full relativistic (FR) treatments. Looking at the SR case first, a large variation in E_a^{eff} is observed where a significantly lower barrier is predicted for the Mg jumps with an existing nearby extrinsic vacancy defect (i.e. Case 2, $\text{Mg}_{3-x}\text{Bi}_2$ SR): 0.43 eV. In Case 1 (stoichiometric Mg_3Bi_2), where generation of a thermal Mg vacancy is required for diffusion, the effective diffusion barrier E_a^{eff} should now include this formation of vacancy. Naturally, we would expect an increase in E_a^{eff} due to this inclusion of vacancy formation energy: depending on the vacant site (tetrahedral or octahedral Mg vacancy), the E_a^{eff} is estimated to be 1.46 eV (octahedral) or 1.55 eV (tetrahedral).

We also observe that inclusion of spin-orbit coupling enhances the diffusion noticeably in all three cases, where a reduction of effective activation barrier is seen (e.g. for Case 1, SR with V_{oct} 1.46 eV *versus* FR V_{oct} 0.67 eV. This is mainly due to the vacancy formation energy, where the FR case results in a dramatically lowered formation energy.

Comparing these results to the experiment, the effective activation barrier E_a^{eff} in the fully relativistic case ignoring the vacancy creation (Case 2) agrees with the E_a^{eff} of the ball-milled sample, determined through VT NMR. On the other hand, E_a^{eff} obtained for the electrochemically prepared samples (VT NMR Echem) agree well with the E_a^{eff} assuming a Mg vacancy creation plus Mg diffusion (Case 1). Hence, we conclude that the primary

diffusion mechanism in electrochemically prepared samples (measured *ex-situ*, i.e. not during battery operating conditions) should involve vacancy creation, whereas the mechanism in mechanically prepared samples only involves the vacancy diffusion. This could be explained by method of sample preparation: the electrochemical Mg insertion process in this case produced samples closer to the thermodynamic equilibrium creating fewer vacancies, whereas mechanical milling is largely a high energy process resulting in more vacancies (for instance, vacancy formation in ZnO through milling was previously observed with HRTEM studies[240]). This is also a known phenomenon in the synthesis of intermetallic phases: mechanical milling can provide excess energy to the material, which can be stored in the sample as atomistic disorders of which vacancies are one example.[241] Furthermore, as discussed above, Mg deficiency is likely due to preferential Mg sticking to the ball-mill components (jar, balls). The already present vacancies in mechanically prepared samples act as potential diffusion sites for adjacent Mg ions, enhancing their diffusion.

Extending this result to a battery under operating conditions, it is important to stress that the Mg_{3-x}Bi₂ phases formed *in-situ* may not be stoichiometric. The kinetics of Bi (de)magnesiumation will depend on a number of factors which include the interfacial energies between the Bi and Mg₃Bi₂ phases, and transport of Mg in Bi, Mg₃Bi₂, and at the various interfaces. In particular, the mechanism of demagnesiumation will depend strongly on the ease of vacancy formation in Mg₃Bi₂. By analogy with previous work on *e.g.* lithium silicides[242] and CuTi₂S₄,[243]) this energy of vacancy formation may even be responsible for setting (or strongly influencing) the overpotential observed on charge.

Finally, we note that Zintl-type A₃B₂ materials to which Mg₃Bi₂ belongs have been identified as potentially promising thermoelectric materials.[244, 245] Mg mobility in these materials could have important implications on the thermoelectric power generation, and work is in progress on doping other atoms into this structure to enhance, or suppress, this mobility.

Case	Diffusion process	$E_a^{\text{eff}} / \text{eV}$	
		SR	FR
DFT			
Case 1	formation and diffusion of V_{oct}	1.46	0.67
Case 1	formation and diffusion of V_{tet}	1.55	0.76
Case 2	pre-formed vacancy diffusion	0.43	0.34
Experiment			
	VT NMR Echem	0.71	
	VT NMR Ball-mill	0.19	

Table 5.5 Effective migration barriers E_a^{eff} estimated through DFT and VT NMR techniques. VT NMR data are taken from Liu *et al.*[40] For the NMR measurements, Mg_3Bi_2 prepared through electrochemical insertion and mechanical milling were considered. SR and FR refer to scalar relativistic and full relativistic calculations, as described in the text.

5.4 Conclusion

In conclusion, advanced electronic structure calculations show that spin-orbit coupling plays an important role in structure and dynamics of Mg_3Bi_2 , a promising Mg-ion battery anode material. Inclusion of relativistic spin-orbit coupling also significantly changes the electronic structure and the calculated NMR parameters of this material. It also lowers the formation energies of Mg vacancy defects, which is crucial to the apparent low Mg-ion diffusion barrier. Using an efficient single-ended hybrid eigenvector-following approach, we have calculated the Mg migration barriers involving relativistic spin-orbit coupling which are as low as 0.34 eV for the octahedral to tetrahedral diffusion. The calculated activation barriers are in good agreement with the previous experimental report using variable temperature ^{25}Mg NMR experiments for materials prepared electrochemically and *via* ball-milling. Stoichiometric materials show higher activation energies, since the activation energy involves both the cost of vacancy generation and transport. An understanding of Mg transport and the energetics of vacancy formation are important in understanding the mechanisms for demagnesiumation of Mg_3Bi_2 . Further work needs to be carried out on improving the Mg diffusion in similar materials such as Sn, which have been shown to have good capacity but poor rate performance in Mg-ion batteries.[246]

Chapter 6

Conclusion and Further Work

The primary objective of this thesis has been to develop a combined experimental and computational approach to studying potential Mg-ion battery (MIB) electrodes using ^{25}Mg NMR spectroscopy. Due to the challenging nature of solid-state ^{25}Mg NMR, particular focus was put on *ab initio* prediction of various NMR parameters to (i) aid the experimental acquisition and interpretation and to (ii) enhance the sensitivity and resolution of resulting spectra. Also, due to the inherent magnetism present in paramagnetic TM oxides, a secondary objective of this thesis has been on investigating the magnetism of these compounds.

In Chapter 3, this combined approach was developed and validated on a series of paramagnetic TM oxides (Mg_6MnO_8 , MgV_2O_4 , MgCr_2O_4 , MgMn_2O_4). *Ab initio* predictions of ^{25}Mg NMR parameters (hyperfine shifts, quadrupolar coupling) yield reliable results which are verified with the ^{25}Mg NMR experiments. In particular, the Rotor-Assisted Population Transfer (RAPT) pulse sequence was successfully used, for the first time, to (i) enhance the central transition intensity in quadrupoles under paramagnetic environments, and (ii) estimate the quadrupolar coupling parameter in such paramagnetic systems where a direct fitting is likely to be difficult due to broad lineshapes.

With the baseline set in Chapter 3 on paramagnetic ^{25}Mg NMR, this method was applied to MgV_2O_5 in Chapter 4 to observe and interpret the NMR spectra of this potential MIB cathode material. In particular, use of the RAPT-echo pulse sequence was investigated to yield an enhancement of 1.6 over a simple echo, which amounts to a 2.5-fold reduction in acquisition time. More importantly, ball-milling of the sample was shown not to affect the RAPT enhancement significantly, which shows the possibility of applying this methodology to studying real cycled systems. Attempted cycling of this compound, however, exhibited vanadium dissolution from the VO_2 impurity phase. Possible source of this phase was

identified as the hydrated Mg precursor; clearly a fresh sample in absence of this impurity phase needs to be prepared and the electrochemistry tested.

In Chapter 5, the focus was shifted towards understanding the Mg dynamics in an MIB anode material Mg_3Bi_2 . By advanced electronic structure calculations, this material was predicted to be a small band-gap semiconductor, in line with previous experimental reports. DFT-based calculations on the defect creation energies indicate that the energy of defect formation takes a significant portion of the observed activation energy; combined with the Mg-ion migration barrier obtained through a hybrid eigenvector following method, the dramatic differences between the mechanochemically and electrochemically prepared samples are explained. In particular it is observed that the relativistic spin-orbit coupling in heavy bismuth is important for fast Mg-ion conduction, a factor which is likely to be relevant for anodes with heavy atoms (*e.g.* Sn, Pb). Investigations on similar systems (Mg_2Sn , Mg_3Sb_2) using this methodology is needed to assess the full extent of this effect.

This work also contained substantial investigations on the magnetism of these TM oxide compounds, many of which are not straightforward to prepare and are expected to show interesting low-temperature magnetism. In Chapter 3, we have validated the weakly coupled magnetism present in Mg_6MnO_8 through a DFT-based calculation of the electron J -coupling and low-temperature measurement of magnetism. Calculated magnetic coupling in a magnetically frustrated MgCr_2O_4 spinel is compared to experiments to yield a good agreement. Also, Mg–Mn inversion in another spinel MgMn_2O_4 was shown experimentally through a combined refinement of the X-ray data and magnetic measurements. Finally, the magnetism of MgV_2O_5 was investigated with DFT methods and SQUID magnetometry. The system showed magnetic responses characteristic of one-dimensional magnetism; DFT calculations indicate the subtle nature of V–V magnetic interactions which depend heavily on the computational parameters used.

In this regard, initial further work must be focused on obtaining a pure-phase MgV_2O_5 starting from stoichiometric quantities of precursors. The sample would then be subjected to neutron diffraction to explore the low-temperature magnetism of this material; neutron diffraction on this sample has not been reported before. This work could also be extended to preparing other TM oxides (*e.g.* MgTi_2O_4 , MgVO_3 , $\text{Mg}_3\text{Nb}_6\text{O}_{11}$) and systematically investigating their magnetic and NMR properties. With the aid of *ab initio* predictions on the carbothermal synthesis conditions taken in Chapter 4 for MgV_2O_5 , many TM oxides previously difficult to access could be prepared in large quantities in a straightforward manner.

This thesis, overall, sets a baseline for preparing and investigating Mg-ion battery electrodes by solid-state ^{25}Mg NMR spectroscopy and *ab initio* calculations. The methodology presented in this work is general and can be expected to be applied to real battery systems for studying the local structure, confirming reversible insertion, elucidating failure mechanisms, and investigating Mg-ion dynamics. This provides us with a new tool to study Mg-ion batteries, which are promising systems for future green energies.

References

- (1) Huggins, R. A., *Advanced Batteries: Materials Science Aspects*; Springer-Verlag: 2009.
- (2) Greenwood, N. N.; Earnshaw, A., *Chemistry of the Elements*, 2nd Ed.; Butterworth-Heinemann: 1997.
- (3) Olivetti, E. A.; Ceder, G.; Gaustad, G. G.; Fu, X. *Joule* **2017**, *1*, 229–243.
- (4) Aurbach, D.; Zinigrad, E.; Cohen, Y.; Teller, H. *Solid State Ionics* **2002**, *148*, 405–416.
- (5) Larcher, D.; Beattie, S.; Morcrette, M.; Edström, K.; Jumas, J.-C.; Tarascon, J.-M. *J. Mater. Chem.* **2007**, *17*, 3759–3772.
- (6) Van Noorden, R. *Nature* **2014**, *507*, 26.
- (7) Kim, S.-W.; Seo, D.-H.; Ma, X.; Ceder, G.; Kang, K. *Advanced Energy Materials* **2012**, *2*, 710–721.
- (8) Dunn, B.; Kamath, H.; Tarascon, J.-M. *Science* **2011**, *334*, 928–935.
- (9) Larcher, D.; Tarascon, J.-M. *Nature chemistry* **2015**, *7*, 19.
- (10) Canepa, P.; Sai Gautam, G.; Hannah, D. C.; Malik, R.; Liu, M.; Gallagher, K. G.; Persson, K. A.; Ceder, G. *Chemical Reviews* **2017**, *117*, 4287–4341.
- (11) Jäckle, M.; Groß, A. *The Journal of Chemical Physics* **2014**, *141*, 174710.
- (12) Ding, M. S.; Diemant, T.; Behm, R. J.; Passerini, S.; Giffin, G. A. *Journal of The Electrochemical Society* **2018**, *165*, A1983–A1990.
- (13) Hebié, S.; Ngo, H. P. K.; Leprêtre, J.-C.; Iojoiu, C.; Cointeaux, L.; Berthelot, R.; Alloin, F. *ACS Applied Materials & Interfaces* **2017**, *9*, 28377–28385.
- (14) Hebié, S.; Alloin, F.; Iojoiu, C.; Berthelot, R.; Leprêtre, J.-C. *ACS Applied Materials & Interfaces* **2018**, *10*, 5527–5533.
- (15) Aurbach, D.; Gofer, Y.; Lu, Z.; Schechter, A.; Chusid, O.; Gizbar, H.; Cohen, Y.; Ashkenazi, V.; Moshkovich, M.; Turgeman, R. *Journal of Power Sources* **2001**, *97-98*, 28.
- (16) Aurbach, D.; Lu, Z.; Schechter, A.; Gofer, Y.; Gizbar, H.; Turgeman, R.; Cohen, Y.; Moshkovich, M.; Levi, E. *Nature* **2000**, *407*, 724–727.
- (17) Muldoon, J.; Bucur, C. B.; Gregory, T. *Angewandte Chemie International Edition* **2017**, *56*, 12064–12084.
- (18) Shannon, R. D. *Acta Crystallographica A* **1976**, *32*, 751–767.
- (19) Mohtadi, R.; Mizuno, F. *Beilstein Journal of Nanotechnology* **2014**, *5*, 1291–1311.

- (20) Canepa, P.; Bo, S.-H.; Gautam, G. S.; Key, B.; Richards, W. D.; Shi, T.; Tian, Y.; Wang, Y.; Li, J.; Ceder, G. *Nature Communications* **2017**, *8*.
- (21) Bonnicksen, P.; Blanc, L.; Vajargah, S. H.; Lee, C.-W.; Sun, X.; Balasubramanian, M.; Nazar, L. F. *Chemistry of Materials* **2018**, *30*, 4683–4693.
- (22) Pecher, O.; Carretero-González, J.; Griffith, K. J.; Grey, C. P. *Chemistry of Materials* **2017**, *29*, 213–242.
- (23) Grey, C. P.; Dupré, N. *Chemical Reviews* **2004**, *104*, 4493.
- (24) Freitas, J. C. C.; Smith, M. E. *Annual Reports on NMR Spectroscopy* **2012**, *75*, 25.
- (25) Dupree, R.; Smith, M. E. *Journal of the Chemical Society, Chemical Communications* **1988**, 1483.
- (26) Moudrakovski, I. L. *Annual Reports on NMR Spectroscopy* **2013**, *79*, ed. by Webb, G., 129.
- (27) Larsen, F. H.; Jakobsen, H. J.; Ellis, P. D.; Nielsen, N. C. *Journal of Magnetic Resonance* **1998**, *131*, 144–147.
- (28) Sideris, P. J.; Nielsen, U. G.; Gan, Z.; Grey, C. P. *Science* **2008**, *321*, 113–117.
- (29) Griffin, J. M.; Berry, A. J.; Ashbrook, S. E. *Solid State Nuclear Magnetic Resonance* **2011**, *40*, 91–99.
- (30) Kim, C.; Phillips, P. J.; Key, B.; Yi, T.; Nordlund, D.; Yu, Y.-s.; Bayliss, R. D.; Han, S.-d.; He, M.; Zhang, Z.; Burrell, A. K.; Klie, R. F.; Cabana, J. *Advanced Materials* **2015**, *27*, 3377.
- (31) Sai Gautam, G.; Canepa, P.; Richards, W. D.; Malik, R.; Ceder, G. *Nano Letters* **2016**, *16*, 2426–2431.
- (32) Sa, N.; Wang, H.; Proffit, D. L.; Lipson, A. L.; Key, B.; Liu, M.; Feng, Z.; Fister, T. T.; Ren, Y.; Sun, C.-J.; Vaughey, J. T.; Fenter, P. A.; Persson, K. A.; Burrell, A. K. *Journal of Power Sources* **2016**, *323*, 44–50.
- (33) Nam, K. W. et al. *Nano Letters* **2015**, *15*, 4071–4079.
- (34) Sa, N.; Kinnibrugh, T. L.; Wang, H.; Sai Gautam, G.; Chapman, K. W.; Vaughey, J. T.; Key, B.; Fister, T. T.; Freeland, J. W.; Proffit, D. L.; Chupas, P. J.; Ceder, G.; Barenko, J. G.; Bloom, I. D.; Burrell, A. K. *Chemistry of Materials* **2016**, *28*, 2962–2969.
- (35) Wang, H.; Senguttuvan, P.; Proffit, D. L.; Pan, B.; Liao, C.; Burrell, A. K.; Vaughey, J. T.; Key, B. *ECS Electrochemistry Letters* **2015**, *4*, A90–A93.
- (36) Incorvati, J. T.; Wan, L. F.; Key, B.; Zhou, D.; Liao, C.; Fuoco, L.; Holland, M.; Wang, H.; Prendergast, D.; Poeppelmeier, K. R.; Vaughey, J. T. *Chemistry of Materials* **2016**, *28*, 17–20.
- (37) Wustrow, A.; Key, B.; Phillips, P. J.; Sa, N.; Lipton, A. S.; Klie, R. F.; Vaughey, J. T.; Poeppelmeier, K. R. *Inorganic Chemistry* **2018**, *57*, 8634–8638.
- (38) Lee, J.; Seymour, I. D.; Pell, A. J.; Dutton, S. E.; Grey, C. P. *Physical Chemistry Chemical Physics* **2017**, *19*, 613–625.
- (39) Keyzer, E. N.; Lee, J.; Liu, Z.; Bond, A. D.; Wright, D. S.; Grey, C. P. *J. Mater. Chem. A* **2019**, *7*, 2677–2685.

- (40) Liu, Z.; Lee, J.; Xiang, G.; Glass, H. F. J.; Keyzer, E. N.; Dutton, S. E.; Grey, C. P. *Chemical Communications* **2017**, *53*, 743–746.
- (41) Murgia, F.; Laurencin, D.; Weldekidan, E. T.; Stievano, L.; Monconduit, L.; Doublet, M.-L.; Berthelot, R. *Electrochimica Acta* **2018**, *259*, 276–283.
- (42) Pallister, P. J.; Moudrakovski, I. L.; Ripmeester, J. A. *Physical Chemistry Chemical Physics* **2009**, *11*, 11487.
- (43) Azevedo, L. J.; Schirber, J. E.; Switendick, A. C.; Baughman, R. J.; Morosin, B. *Journal of Physics F: Metal Physics* **1981**, *11*, 1521–1530.
- (44) Bastow, T.; Celotto, S. *Solid State Nuclear Magnetic Resonance* **2009**, *35*, 217–222.
- (45) Rong, Z.; Malik, R.; Canepa, P.; Sai Gautam, G.; Liu, M.; Jain, A.; Persson, K.; Ceder, G. *Chemistry of Materials* **2015**, *27*, 6016–6021.
- (46) Xia, Y.; Yoshio, M. In *Lithium Batteries: Science and Technology*, Nazri, G.-A., Pistoia, G., Eds.; Springer US: Boston, MA, 2003, pp 361–380.
- (47) Kasper, J. S.; Prener, J. S. *Acta Crystallographica* **1954**, *7*, 246.
- (48) Winkler, B.; Chall, M.; Pickard, C. J.; Milman, V.; White, J. *Acta Crystallographica Section B* **2000**, *56*, 22–26.
- (49) Shannon, R. D. *Acta Crystallographica A* **1976**, *32*, 751.
- (50) Lu, J.; Lee, K. S. *Materials Technology* **2016**, *31*, 628–641.
- (51) O’Neill, H.; Navrotsky, A. *American Mineralogist* **1983**, *68*, 181–194.
- (52) Navrotsky, A.; Kleppa, O. *Journal of Inorganic and Nuclear Chemistry* **1967**, *29*, 2701.
- (53) Sickafus, K. E.; Wills, J. M.; Grimes, N. W. *Journal of the American Ceramic Society* **1999**, *82*, 3279.
- (54) Verwey, E. J. W.; Heilmann, E. L. *Journal of Chemical Physics* **1947**, *15*, 174.
- (55) Burdett, J. K.; Price, G. D.; Price, S. L. *Journal of the American Chemical Society* **1982**, *104*, 92–95.
- (56) Winter, M., *D-block Chemistry*; Oxford University Press: 2015.
- (57) McClure, D. S. *Journal of Physics and Chemistry of Solids* **1957**, *3*, 311–317.
- (58) Dunitz, J.; Orgel, L. *Journal of Physics and Chemistry of Solids* **1957**, *3*, 20–29.
- (59) Manaila, R.; Pausescu, P. *Physica Status Solidi B* **1964**, *6*, 101.
- (60) Manaila, R.; Pausescu, P. *Physica Status Solidi B* **1965**, *9*, 385.
- (61) Irani, K. S.; Sina, A. P. B.; Biswas, A. B. *Journal of Physics and Chemistry of Solids* **1962**, *23*, 711–727.
- (62) Sai Gautam, G.; Canepa, P.; Urban, A.; Bo, S.-H.; Ceder, G. *Chemistry of Materials* **2017**, *29*, 7918–7930.
- (63) Ropp, R., *Encyclopedia of the Alkaline Earth Compounds*; Elsevier: 2012.
- (64) Wang, Q.; Xu, J.; Zhang, W.; Mao, M.; Wei, Z.; Wang, L.; Cui, C.; Zhu, Y.; Ma, J. *Journal of Materials Chemistry A* **2018**, *6*, 8815–8838.

- (65) Jain, A.; Ong, S. P.; Hautier, G.; Chen, W.; Richards, W. D.; Dacek, S.; Cholia, S.; Gunter, D.; Skinner, D.; Ceder, G.; Persson, K. A. *APL Materials* **2013**, *1*, 011002.
- (66) Jain, A.; Hautier, G.; Ong, S. P.; Moore, C. J.; Fischer, C. C.; Persson, K. A.; Ceder, G. *Physical Review B* **2011**, *84*, 045115.
- (67) Sai Gautam, G.; Canepa, P.; Abdellahi, A.; Urban, A.; Malik, R.; Ceder, G. *Chemistry of Materials* **2015**, *27*, 3733–3742.
- (68) Zhou, B.; Shi, H.; Cao, R.; Zhang, X.; Jiang, Z. *Physical Chemistry Chemical Physics* **2014**, *16*, 18578–18585.
- (69) Millet, P.; Satto, C.; Sciau, P.; Galy, J. *Journal of Solid State Chemistry* **1998**, *136*, 56–62.
- (70) Szabo, A.; Ostlund, N., *Modern Quantum Chemistry: Introduction to Advanced Electronic Structure Theory*; Dover Publications: 1996.
- (71) Koch, W.; Holthausen, M., *A Chemist's Guide to Density Functional Theory*; Wiley-VCH: 2000.
- (72) Hohenberg, P.; Kohn, W. *Physical Review* **1964**, *136*, B864–B871.
- (73) Kohn, W.; Sham, L. J. *Physical Review* **1965**, *140*, A1133–A1138.
- (74) Mardirossian, N.; Head-Gordon, M. *Molecular Physics* **2017**, *115*, 2315–2372.
- (75) Himmetoglu, B.; Floris, A.; de Gironcoli, S.; Cococcioni, M. *International Journal of Quantum Chemistry* **2014**, *114*, 14–49.
- (76) Hubbard, J.; Flowers, B. H. *Proceedings of the Royal Society of London. Series A. Mathematical and Physical Sciences* **1963**, *276*, 238–257.
- (77) Khomskii, D., *Transition Metal Compounds*; Cambridge University Press: 2014.
- (78) Liechtenstein, A. I.; Anisimov, V. I.; Zaanen, J. *Physical Review B* **1995**, *52*, R5467–R5470.
- (79) Anisimov, V.; Korotin, M.; Zöfl, M.; Pruschke, T.; Le Hur, K.; Rice, T. *Physical Review Letters* **1999**, *83*, 364–367.
- (80) Dudarev, S. L.; Botton, G. A.; Savrasov, S. Y.; Humphreys, C. J.; Sutton, A. P. *Physical Review B* **1998**, *57*, 1505–1509.
- (81) Cococcioni, M. In *Correlated Electrons: From Models to Materials Modeling and Simulation*; Verlag des Forschungszentrum Jülich: Jülich, Germany, 2012.
- (82) Cococcioni, M.; de Gironcoli, S. *Physical Review B* **2005**, *71*, 035105.
- (83) Becke, A. D. *Journal of Chemical Physics* **1993**, *98*, 5648.
- (84) Kim, K.; Jordan, K. D. *The Journal of Physical Chemistry* **1994**, *98*, 10089–10094.
- (85) Adamo, C.; Barone, V. *The Journal of Chemical Physics* **1999**, *110*, 6158–6170.
- (86) Heyd, J.; Scuseria, G. E.; Ernzerhof, M. *The Journal of Chemical Physics* **2006**, *124*, 219906.
- (87) Becke, A. D. *Physical Review A* **1988**, *38*, 3098–3100.
- (88) Lee, C.; Yang, W.; Parr, R. G. *Physical Review B* **1988**, *37*, 785–789.

- (89) Corà, F.; Alfredsson, M.; Mallia, G.; Middlemiss, D. S.; Mackrodt, W. C.; Dovesi, R.; Orlando, R. In *Principles and Applications of Density Functional Theory in Inorganic Chemistry II*; Springer Berlin Heidelberg: Berlin, Heidelberg, 2004, pp 171–232.
- (90) Feng, X.; Harrison, N. *Physical Review B* **2004**, *70*, 092402.
- (91) de P. R. Moreira, I.; Illas, F.; Martin, R. *Physical Review B* **2002**, *65*, 155102.
- (92) Kim, J.; Middlemiss, D. S.; Chernova, N. A.; Zhu, B. Y. X.; Masquelier, C.; Grey, C. P. *Journal of the American Chemical Society*. **2010**, *132*, 16825.
- (93) Clément, R. J.; Pell, A. J.; Middlemiss, D. S.; Strobridge, F. C.; Miller, J. K.; Whittingham, M. S.; Emsley, L.; Grey, C. P.; Pintacuda, G. *Journal of the American Chemical Society*. **2012**, *134*, 17178.
- (94) Middlemiss, D. S.; Ilott, A. J.; Clément, R. J.; Strobridge, F. C.; Grey, C. P. *Chemistry of Materials* **2013**, *25*, 1723.
- (95) Boys, S. F. *Proceedings of the Royal Society A: Mathematical, Physical and Engineering Sciences* **1950**, *200*, 542–554.
- (96) Payne, C.; York, N. *Reviews of Modern Physics* **1992**, *64*, 1045–1097.
- (97) Pickard, C. J.; Mauri, F. *Physical Review B* **2001**, *63*, 245101.
- (98) Kaxiras, E., *Atomic and Electronic Structure of Solids*; Cambridge University Press: 2003.
- (99) *Quantum-Mechanical Ab-initio Calculation of the Properties of Crystalline Materials*; Berthier, G., Fischer, H., Fukui, K., Hall, G. G., Hinze, J., Jortner, J., Kutzelnigg, W., Ruedenberg, K., Tomasi, J., Eds.; Lecture Notes in Chemistry, Vol. 67; Springer Berlin Heidelberg: Berlin, Heidelberg, 1996.
- (100) Dirac, P. A. M., *The Principles of Quantum Mechanics*; Clarendon Press: Oxford, 1930.
- (101) Schwabl, F., *Quantum mechanics*, 4th ed; Springer: Berlin ; New York, 2007; 424 pp.
- (102) Farazdel, A.; Smith, V. H. *International Journal of Quantum Chemistry* **1986**, *29*, 311–314.
- (103) Jameson, C. J.; De Dios, A. C. In *Nuclear Magnetic Resonance*, Webb, G. A., Ed.; Royal Society of Chemistry: Cambridge, 2007; Vol. 34, pp 57–86.
- (104) Chang, C.; Pelissier, M.; Durand, P. *Physica Scripta* **1986**, *34*, 394–404.
- (105) Heully, J. L. *Journal of Physics B: Atomic and Molecular Physics* **1982**, *15*, 4079–4091.
- (106) Van Lenthe, E.; Snijders, J. G.; Baerends, E. J. *The Journal of Chemical Physics* **1996**, *105*, 6505–6516.
- (107) Yates, J. R.; Pickard, C. J.; Payne, M. C.; Mauri, F. *The Journal of Chemical Physics* **2003**, *118*, 5746–5753.
- (108) Hamaed, H.; Laschuk, M. W.; Terskikh, V. V.; Schurko, R. W. *Journal of the American Chemical Society* **2009**, *131*, 8271–8279.
- (109) Widdifield, C. M.; Bryce, D. L. *The Journal of Physical Chemistry A* **2010**, *114*, 10810–10823.
- (110) Grabowski, B.; Hickel, T.; Neugebauer, J. *Physical Review B* **2007**, *76*, 024309.

- (111) Steiner, S.; Khmelevskiy, S.; Marsmann, M.; Kresse, G. *Physical Review B* **2016**, *93*, 224425.
- (112) Wales, D. J., *Energy Landscapes: Applications to Clusters, Biomolecules and Glasses*; Cambridge University Press: 2003.
- (113) Munro, L. J.; Wales, D. J. *Physical Review B* **1999**, *59*, 3969–3980.
- (114) Kumeda, Y.; Wales, D. J.; Munro, L. J. *Chemical Physics Letters* **2001**, *341*, 185–194.
- (115) Keeler, J., *Understanding NMR Spectroscopy*; Wiley: 2011.
- (116) Harris, R. K.; Becker, E. D.; Cabral De Menezes, S. M.; Granger, P.; Hoffman, R. E.; Zilm, K. W. *Solid State Nuclear Magnetic Resonance* **2008**, *33*, 41–56.
- (117) Duer, M., *Introduction to Solid-State NMR Spectroscopy*; Wiley: 2005.
- (118) Herzfeld, J.; Berger, A. E. *Journal of Chemical Physics* **1980**, *73*, 6021.
- (119) Mehring, M., *Principles of High Resolution NMR in Solids*; Springer Berlin Heidelberg: 2012.
- (120) Widdifield, C. M.; Bain, A. D.; Bryce, D. L. *Physical Chemistry Chemical Physics* **2011**, *13*, 12413.
- (121) Perras, F. A.; Widdifield, C. M.; Bryce, D. L. *Solid State Nuclear Magnetic Resonance* **2012**, *45-46*, 36–44.
- (122) Freude, D.; Haase, J. In *Special Applications*, Pfeifer, H., Barker, P., Eds.; Springer Berlin Heidelberg: Berlin, Heidelberg, 1993, pp 1–90.
- (123) Man, P. P. In *Encyclopedia of Analytical Chemistry*, Meyers, R. A., Ed.; John Wiley & Sons, Ltd: Chichester, UK, 2006.
- (124) Freude, D. In *Encyclopedia of Analytical Chemistry*, Meyers, R. A., Ed.; John Wiley & Sons, Ltd: Chichester, UK, 2006.
- (125) Andrew, E. R. *Philosophical Transactions of the Royal Society of London. Series A, Mathematical and Physical Sciences* **1981**, *299*, 505–520.
- (126) Lowe, I. J. *Phys. Rev. Lett.* **1959**, *2*, 285–287.
- (127) Gan, Z.; Gor'kov, P.; Cross, T. A.; Samoson, A.; Massiot, D. *Journal of the American Chemical Society* **2002**, *124*, 5634–5635.
- (128) Haase, J.; Eckert, D.; Siegel, H.; Eschrig, H.; Müller, K.-H.; Steglich, F. *Concepts in Magnetic Resonance Part B: Magnetic Resonance Engineering* **2003**, *19B*, 9–13.
- (129) Samoson, A.; Lippmaa, E.; Pines, A. *Molecular Physics* **1988**, *65*, 1013–1018.
- (130) Mueller, K.; Sun, B.; Chingas, G.; Zwanziger, J.; Terao, T.; Pines, A. *Journal of Magnetic Resonance* **1990**, *86*, 470–487.
- (131) Medek, A.; Harwood, J. S.; Frydman, L. *Journal of the American Chemical Society* **1995**, *117*, 12779–12787.
- (132) Gan, Z. *Journal of the American Chemical Society* **2000**, *122*, 3242–3243.
- (133) Hahn, E. L. *Physical Review* **1950**, *80*, 580–594.
- (134) Perras, F. A.; Viger-Gravel, J.; Burgess, K. M.; Bryce, D. L. *Solid State Nuclear Magnetic Resonance* **2013**, *51-52*, 1–15.

- (135) Yao, Z.; Kwak, H.-T.; Sakellariou, D.; Emsley, L.; Grandinetti, P. J. *Chemical Physics Letters* **2000**, *327*, 85.
- (136) Kwak, H. T.; Prasad, S.; Clark, T.; Grandinetti, P. J. *Solid State Nuclear Magnetic Resonance* **2003**, *24*, 71.
- (137) Prasad, S.; Kwak, H.-T.; Clark, T.; Grandinetti, P. J. *Journal of the American Chemical Society* **2002**, *124*, 4964.
- (138) Kentgens, A.; Verhagen, R. *Chemical Physics Letters* **1999**, *300*, 435.
- (139) Hung, I.; Gan, Z. *Chemical Physics Letters* **2010**, *496*, 162.
- (140) Blundell, S., *Magnetism in Condensed Matter*; Oxford Master Series in Condensed Matter Physics 4; OUP Oxford: 2001.
- (141) Köhler, F. H. In *Magnetism: Molecules to Materials I*; John Wiley & Sons, Ltd: 2003; Chapter 12, pp 379–430.
- (142) Pell, A. J.; Pintacuda, G.; Grey, C. P. *Progress in Nuclear Magnetic Resonance Spectroscopy* **2019**, *111*, 1–271.
- (143) Kurland, R. J.; McGarvey, B. R. *Journal of Magnetic Resonance* **1970**, *2*, 286–301.
- (144) Carlier, D.; Ménétrier, M.; Grey, C.; Delmas, C.; Ceder, G. *Physical Review B* **2003**, *67*, 174103.
- (145) Ellingham, H. J. T. *Journal of the Society of Chemical Industry* **1944**, *63*, 125–160.
- (146) Chevrier, V. L.; Ong, S. P.; Armiento, R.; Chan, M. K. Y.; Ceder, G. *Physical Review B* **2010**, *82*, 075122.
- (147) Rietveld, H. M. *Journal of Applied Crystallography* **1969**, *2*, 65.
- (148) Levi, E.; Gofer, Y.; Aurbach, D. *Chemistry of Materials* **2010**, *22*, 860.
- (149) Novák, P.; Imhof, R.; Haas, O. *Electrochimica Acta* **1999**, *45*, 351.
- (150) D'Alessandro, D. M.; Smit, B.; Long, J. R. *Angewandte Chemie International Edition* **2010**, *49*, 6058.
- (151) Garg, N.; Menaka; Ramanujachary, K. V.; Lofland, S. E.; Ganguli, A. K. *Journal of Solid State Chemistry* **2013**, *197*, 392.
- (152) Maitra, U.; Naidu, B. S.; Govindaraj, A.; Rao, C. N. R. *Proceedings of the National Academy of USA* **2013**, *110*, 11704.
- (153) Mackenzie, K. J. D.; Smith, M. E., *Multinuclear Solid-State NMR of Inorganic Materials*; Pergamon Materials Series, Vol. 6; Elsevier: 2002, pp 461–532.
- (154) Catti, M.; Valerio, G.; Dovesi, R.; Causa, M. *Physical Review B* **1994**, *49*, 179.
- (155) Catti, M.; Sandrone, G.; Valerio, G.; Dovesi, R. *Journal of the Physics and Chemistry of Solids* **1996**, *57*, 1735.
- (156) Catti, M.; Sandrone, G.; Dovesi, R. *Physical Review B* **1997**, *55*, 16122.
- (157) Kutzelnigg, W.; Fleischer, U.; Schindler, M. In *NMR-Basic Principles and Progress*; Springer-Verlag: 1990, p 165.
- (158) Stephens, P. J.; Devlin, F. J.; Chabalowski, C. F.; Frisch, M. J. *Journal of Physical Chemistry* **1994**, *98*, 11623.

- (159) Monkhorst, H. J.; Pack, J. D. *Physical Review B* **1976**, *13*, 5188.
- (160) Pallister, P. J.; Moudrakovski, I. L.; Ripmeester, J. A. *Physical Chemistry Chemical Physics* **2009**, *11*, 11487.
- (161) Goodenough, J., *Magnetism and the Chemical Bond*; Wiley: 1963.
- (162) Porta, P.; Valigi, M. *Journal of Solid State Chemistry* **1973**, *6*, 344.
- (163) Dutton, S. E.; Huang, Q.; Tchernyshyov, O.; Broholm, C. L.; Cava, R. J. *Physical Review B* **2011**, *83*, 064407.
- (164) Mamiya, H.; Onoda, M. *Solid State Communications* **1995**, *95*, 217.
- (165) Islam, A. T. M. N.; Wheeler, E. M.; Reehuis, M.; Siemensmeyer, K.; Tovar, M.; Klemke, B.; Kiefer, K.; Hill, A. H.; Lake, B. *Physical Review B* **2012**, *85*.
- (166) Wheeler, E. M.; Lake, B.; Islam, A. T. M. N.; Reehuis, M.; Steffens, P.; Guidi, T.; Hill, A. H. *Physical Review B* **2010**, *82*.
- (167) Yagi, S.; Ichikawa, Y.; Yamada, I.; Doi, T.; Ichitsubo, T.; Matsubara, E. *Japanese Journal of Applied Physics* **2013**, *52*, 025501.
- (168) Cabello, M.; Alcantara, R.; Nacimiento, F.; Ortiz, G.; Lavela, P.; Tirado, J. L. *CrysiEngComm* **2015**, *17*, 8728.
- (169) Ghigna, P.; De Renzi, R.; Mozzati, M.; Lascialfari, A.; Allodi, G.; Bimbi, M.; Mazzoli, C.; Malavasi, L.; Azzoni, C. *Physical Review B* **2006**, *73*, 184402.
- (170) Muramori, K.; Miyahara, S. *Journal of the Physical Society of Japan* **1960**, *15*, 1906.
- (171) Taguchi, H.; Nagao, M. *Journal of Materials Science Letters* **1991**, *10*, 658.
- (172) Dunstan, M. T.; Jain, A.; Liu, W.; Ong, S. P.; Liu, T.; Lee, J.; Persson, K. A.; Scott, S. A.; Dennis, J. S.; Grey, C. P. *Energy & Environmental Science* **2016**, *9*, 1346.
- (173) Seymour, I. D.; Middlemiss, D. S.; Halat, D. M.; Trease, N. M.; Pell, A. J.; Grey, C. P. *Journal of the American Chemical Society* **2016**, *138*, 9405–9408.
- (174) Grey, C. P.; Dobson, C. M.; Cheetham, A. K. *Journal of Magnetic Resonance* **1992**, *98*, 414.
- (175) Stoll, M.; Majors, T. *Journal of Magnetic Resonance* **1982**, *46*, 283.
- (176) Xiang, H. J.; Kan, E. J.; Wei, S.-H.; Whangbo, M.-H.; Gong, X. G. *Physical Review B* **2011**, *84*, 224429.
- (177) Brumage, W. H.; Quade, C. R.; Dorman, C. F. *Physical Review B* **1995**, *52*, 4256–4262.
- (178) Onoda, M.; Ohyama, A. *Journal of Physics: Condensed Matter* **1998**, *10*, 1229–1236.
- (179) Prasad, S.; Kwak, H.-T.; Clark, T.; Grandinetti, P. J. *Journal of the American Chemical Society* **2002**, *124*, 4964–4965.
- (180) Peintinger, M. F.; Oliveira, D. V.; Bredow, T. *Journal of Computational Chemistry* **2013**, *34*, 451–459.
- (181) Monkhorst, H. J.; Pack, J. D. *Physical Review B* **1976**, *13*, 5188–5192.
- (182) Barin, I.; Platzki, G., *Thermochemical data of pure substances*, 3rd ed; VCH: Weinheim ; New York, 1995.

- (183) Lewis, J.; Murdoch, R.; Moul, A. *Nature* **1969**, *221*, 1137.
- (184) Das, S.; Hucke, E. *Carbon* **1975**, *13*, 33–42.
- (185) Kim, J.; Middlemiss, D. S.; Chernova, N. A.; Zhu, B. Y. X.; Masquelier, C.; Grey, C. P. *Journal of the American Chemical Society* **2010**, *132*, 16825–16840.
- (186) Valenzano, L.; Noël, Y.; Orlando, R.; Zicovich-Wilson, C. M.; Ferrero, M.; Dovesi, R. *Theoretical Chemistry Accounts* **2007**, *117*, 991–1000.
- (187) Ruiz, E.; Llunell, M.; Alemany, P. *Journal of Solid State Chemistry* **2003**, *176*, 400–411.
- (188) Bredow, T.; Jug, K.; Evarestov, R. A. *Physica Status Solidi B* **2006**, *243*, R10–R12.
- (189) Schäfer, A.; Horn, H.; Ahlrichs, R. *The Journal of Chemical Physics* **1992**, *97*, 2571–2577.
- (190) Kutzelnigg, W.; Fleischer, U.; Schindler, M. In *NMR-Basic Principles and Progress*; Springer-Verlag: 1990, p 165.
- (191) Kumeda, Y.; Wales, D. J.; Munro, L. J. *Chemical Physics Letters* **2001**, *341*, 185–194.
- (192) Perdew, J. P.; Ruzsinszky, A.; Csonka, G. I.; Vydrov, O. A.; Scuseria, G. E.; Constantin, L. A.; Zhou, X.; Burke, K. *Physical Review Letters* **2008**, *100*.
- (193) Klimeš, J.; Bowler, D. R.; Michaelides, A. *Physical Review B* **2011**, *83*.
- (194) Lee, K.; Murray, E. D.; Kong, L.; Lundqvist, B. I.; Langreth, D. C. *Physical Review B* **2010**, *82*.
- (195) Ganesh, P.; Kim, J.; Park, C.; Yoon, M.; Reboredo, F. A.; Kent, P. R. C. *Journal of Chemical Theory and Computation* **2014**, *10*, 5318–5323.
- (196) Levi, E.; Levi, M. D.; Chasid, O.; Aurbach, D. *Journal of Electroceramics* **2009**, *22*, 13–19.
- (197) Korotin, M. A.; Anisimov, V. I.; Saha-Dasgupta, T.; Dasgupta, I. *Journal of Physics: Condensed Matter* **2000**, *12*, 113–124.
- (198) Aykol, M.; Kim, S.; Wolverton, C. *The Journal of Physical Chemistry C* **2015**, *119*, 19053–19058.
- (199) Koga, N.; Suzuki, Y.; Tatsuoka, T. *The Journal of Physical Chemistry B* **2012**, *116*, 14477–14486.
- (200) Jeong, J.; Aetukuri, N.; Graf, T.; Schladt, T. D.; Samant, M. G.; Parkin, S. S. P. *Science* **2013**, *339*, 1402–1405.
- (201) Granqvist, C. *Thin Solid Films* **1990**, *193-194*, 730–741.
- (202) Yao, Z.; Kwak, H.-T.; Sakellariou, D.; Emsley, L.; Grandinetti, P. J. *Chemical Physics Letters* **2000**, *327*, 85–90.
- (203) Millet, P.; Satto, C.; Bonvoisin, J.; Normand, B.; Penc, K.; Albrecht, M.; Mila, F. *Physical Review B* **1998**, *57*, 5005–5008.
- (204) Middlemiss, D. S.; Ilott, A. J.; Clément, R. J.; Strobridge, F. C.; Grey, C. P. *Chemistry of Materials* **2013**, *25*, 1723–1734.
- (205) Clément, R. J.; Middlemiss, D. S.; Seymour, I. D.; Ilott, A. J.; Grey, C. P. *Chemistry of Materials* **2016**, *28*, 8228–8239.

- (206) Gautam, G. S.; Sun, X.; Duffort, V.; Nazar, L. F.; Ceder, G. *Journal of Materials Chemistry A* **2016**, *4*, 17643–17648.
- (207) Jouanneau, S.; Le Gal La Salle, A.; Verbaere, A.; Guyomard, D. *Journal of The Electrochemical Society* **2005**, *152*, A1660–A1667.
- (208) Shao, Y.; Gu, M.; Li, X.; Nie, Z.; Zuo, P.; Li, G.; Liu, T.; Xiao, J.; Cheng, Y.; Wang, C.; Zhang, J.-G.; Liu, J. *Nano Letters* **2014**, *14*, 255–260.
- (209) Arthur, T. S.; Singh, N.; Matsui, M. *Electrochemistry Communications* **2012**, *16*, 103–106.
- (210) Murgia, F.; Stievano, L.; Monconduit, L.; Berthelot, R. *Journal of Materials Chemistry A* **2015**, *3*, 16478–16485.
- (211) Ramanathan, M.; Benmayza, A.; Prakash, J.; Singh, N.; Mizuno, F. *Journal of The Electrochemical Society* **2016**, *163*, A477–A487.
- (212) Ahuja, R.; Blomqvist, A.; Larsson, P.; Pyykkö, P.; Zaleski-Ejgierd, P. *Physical Review Letters* **2011**, *106*, 018301.
- (213) Kresse, G.; Hafner, J. *Physical Review B* **1993**, *47*, 558–561.
- (214) Kresse, G.; Joubert, D. *Physical Review B* **1999**, *59*, 1758–1775.
- (215) Blöchl, P. E. *Physical Review B* **1994**, *50*, 17953–17979.
- (216) Perdew, J. P.; Burke, K.; Ernzerhof, M. *Physical Review Letters* **1996**, *77*, 3865–3868.
- (217) Hafner, J. *Journal of Computational Chemistry* **2008**, *29*, 2044–2078.
- (218) Kröger, F.; Vink, H. In *Solid State Physics*; Elsevier: 1956; Vol. 3, pp 307–435.
- (219) Clark, S. J.; Segall, M. D.; Pickard, C. J.; Hasnip, P. J.; Probert, M. J.; Refson, K.; Payne, M. Z. *Kristall*. **2005**, *220*, 567–570.
- (220) Yates, J. R.; Pickard, C. J.; Mauri, F. *Phys. Rev. B* **2007**, *76*, 024401.
- (221) Seymour, I. D.; Chakraborty, S.; Middlemiss, D. S.; Wales, D. J.; Grey, C. P. *Chemistry of Materials* **2015**, *27*, 5550–5561.
- (222) Zintl, E.; Husemann, E. *Zeitschrift für Physikalische Chemie* **1933**, *21*, 138–155.
- (223) Elliott, S. R., *The Physics and Chemistry of Solids*; Wiley: 1998.
- (224) Lazarev, V. B.; Marenkin, S. F.; Shevchenko, V. Y.; Goncharenko, G. I. *Neorganicheskie Materialy* **1974**, *10*, 1615–1616.
- (225) Barnes, A. C.; Guo, C.; Howells, W. S. *Journal of Physics: Condensed Matter* **1994**, *6*, L467.
- (226) Howells, W.; Barnes, A.; Hamilton, M. *Physica B: Condensed Matter* **1999**, *266*, 97–99.
- (227) Ferrier, R. P.; Herrell, D. J. *Philosophical Magazine* **1969**, *19*, 853–868.
- (228) Ferrier, R. P.; Herrell, D. J. *Journal of Non-Crystalline Solids* **1970**, *2*, 278–283.
- (229) Watson, L. M.; Marshall, C. A. W.; Cardoso, C. P. *Journal of Physics F: Metal Physics* **1984**, *14*, 113.
- (230) Sutton, C. *Solid State Communications* **1975**, *16*, 327–330.

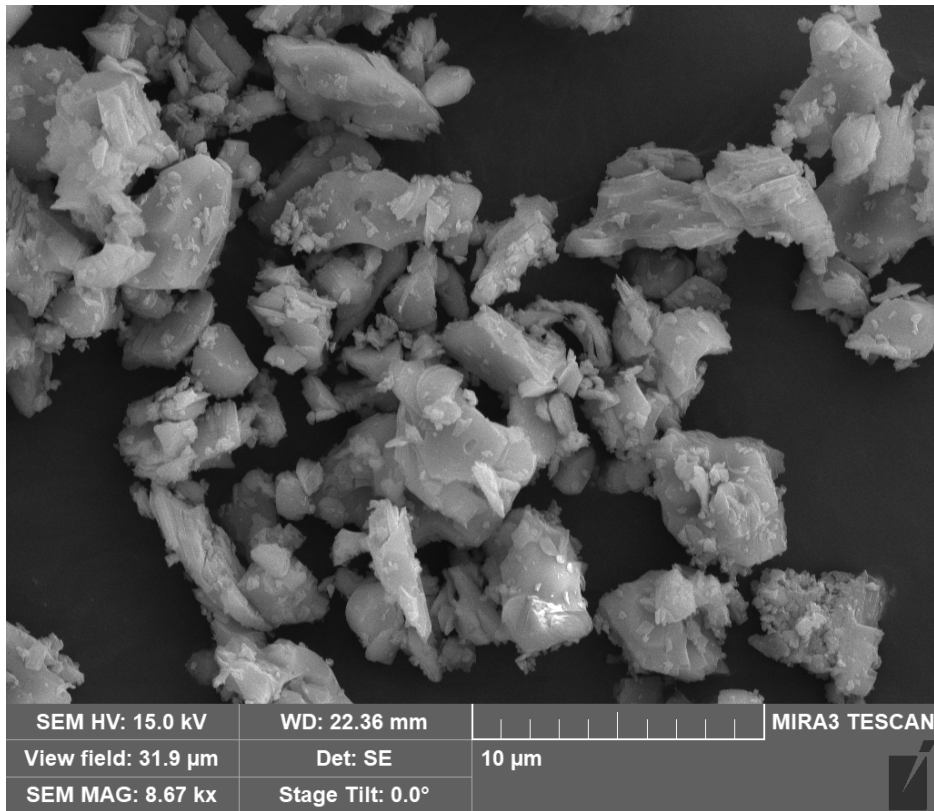
- (231) Sedighi, M.; Arghavani Nia, B.; Zarringhalam, H.; Moradian, R. *The European Physical Journal Applied Physics* **2013**, *61*, 10103.
- (232) Imai, Y.; Watanabe, A. *Journal of Materials Science* **2006**, *41*, 2435–2441.
- (233) Xu, R.; de Groot, R. A.; van der Lugt, W. *Journal of Physics: Condensed Matter* **1993**, *5*, 7551–7562.
- (234) Zhang, X.; Jin, L.; Dai, X.; Liu, G. *The Journal of Physical Chemistry Letters* **2017**, *8*, PMID: 28927265, 4814–4819.
- (235) Shao, D. F.; Luo, X.; Lu, W. J.; Hu, L.; Zhu, X. D.; Song, W. H.; Zhu, X. B.; Sun, Y. P. *Scientific Reports* **2016**, *6*, 21484.
- (236) Noh, H.-J.; Koh, H.; Oh, S.-J.; Park, J.-H.; Kim, H.-D.; Rameau, J. D.; Valla, T.; Kidd, T. E.; Johnson, P. D.; Hu, Y.; Li, Q. *Europhysics Letters* **2008**, *81*, 57006.
- (237) Yatsimirskii, K. B. *Theoretical and Experimental Chemistry* **1995**, *31*, 153–168.
- (238) Crowley, J. M.; Tahir-Kheli, J.; Goddard, W. A. *The Journal of Physical Chemistry Letters* **2016**, *7*, 1198–1203.
- (239) Koller, H.; Engelhardt, G.; Kentgens, A. P.; Sauer, J. *The Journal of Physical Chemistry* **1994**, *98*, 1544–1551.
- (240) Chen, D.; Wang, Z.; Ren, T.; Ding, H.; Yao, W.; Zong, R.; Zhu, Y. *The Journal of Physical Chemistry C* **2014**, *118*, 15300–15307.
- (241) Suryanarayana, C. In *Pergamon Materials Series*; Elsevier: 1999; Vol. 2, pp 49–85.
- (242) Ogata, K.; Salager, E.; Kerr, C.; Fraser, A.; Ducati, C.; Morris, A.; Hofmann, S.; Grey, C. *Nature Communications* **2014**, *5*, 3217–3228.
- (243) Yu, H.-C.; Ling, C.; Bhattacharya, J.; Thomas, J. C.; Thornton, K.; Van der Ven, A. *Energy & Environmental Science* **2014**, *7*, 1760–1768.
- (244) Ponnambalam, V.; Morelli, D. T. *Journal of Electronic Materials* **2013**, *42*, 1307–1312.
- (245) Sun, J.; Singh, D. J. *Journal of Materials Chemistry A* **2017**, *5*, 8499–8509.
- (246) Singh, N.; Arthur, T. S.; Ling, C.; Matsui, M.; Mizuno, F. *Chemical Communications* **2013**, *49*, 149–151.

Appendix A

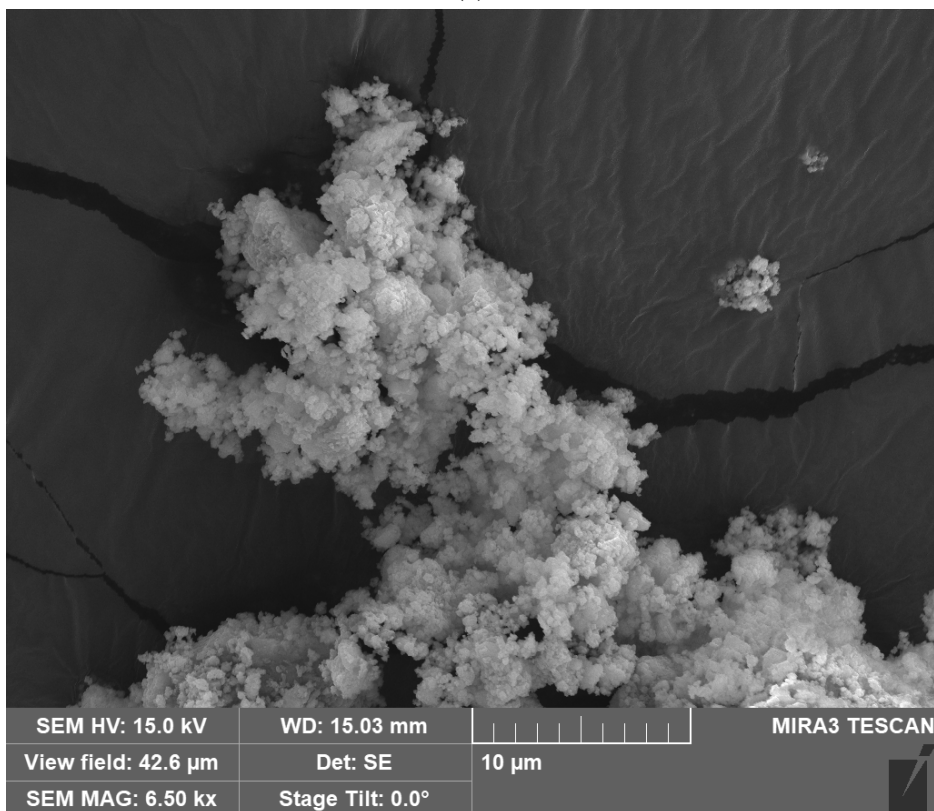
Post ball-mill analysis of MgV_2O_5

A.1 SEM

SEM images were taken with TESCAN MIRA3 FEG-SEM with a secondary electron detector. Acceleration voltage of 15 kV was used for both images.



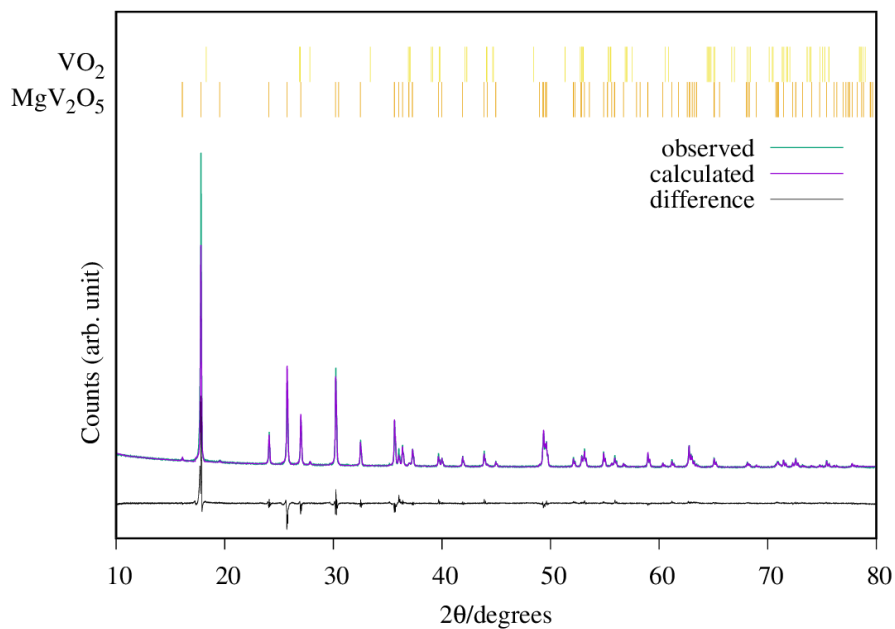
(a)



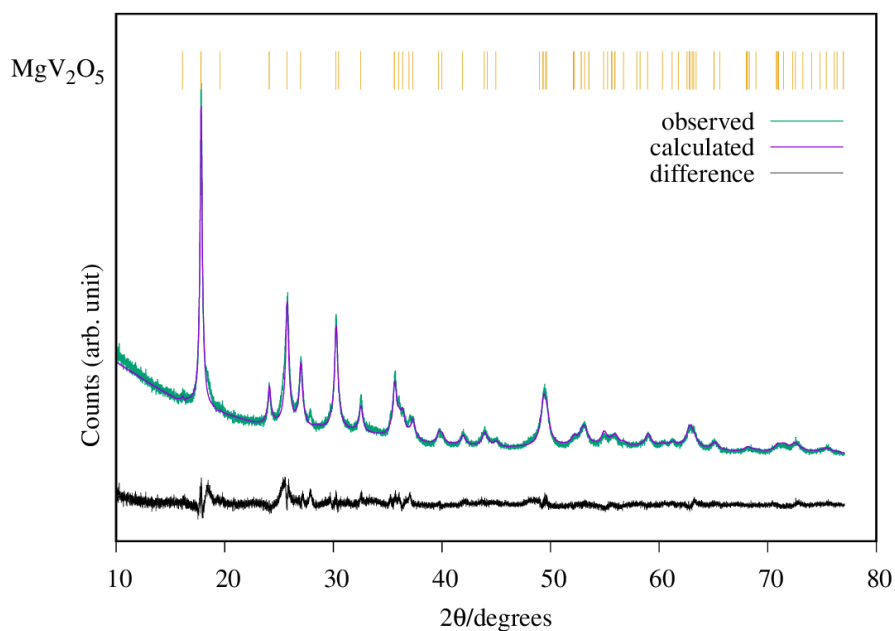
(b)

Fig. A.1 (a) SEM image of pristine MgV_2O_5 before ball-milling. (b) SEM image of MgV_2O_5 after ball-milling.

A.2 XRD



(a)



(b)

Fig. A.2 (a) XRD pattern of pristine MgV_2O_5 before ball-milling. (b) XRD pattern of MgV_2O_5 after ball-milling.

Appendix B

EDX data of lithium counterelectrode from charged VO₂ cell

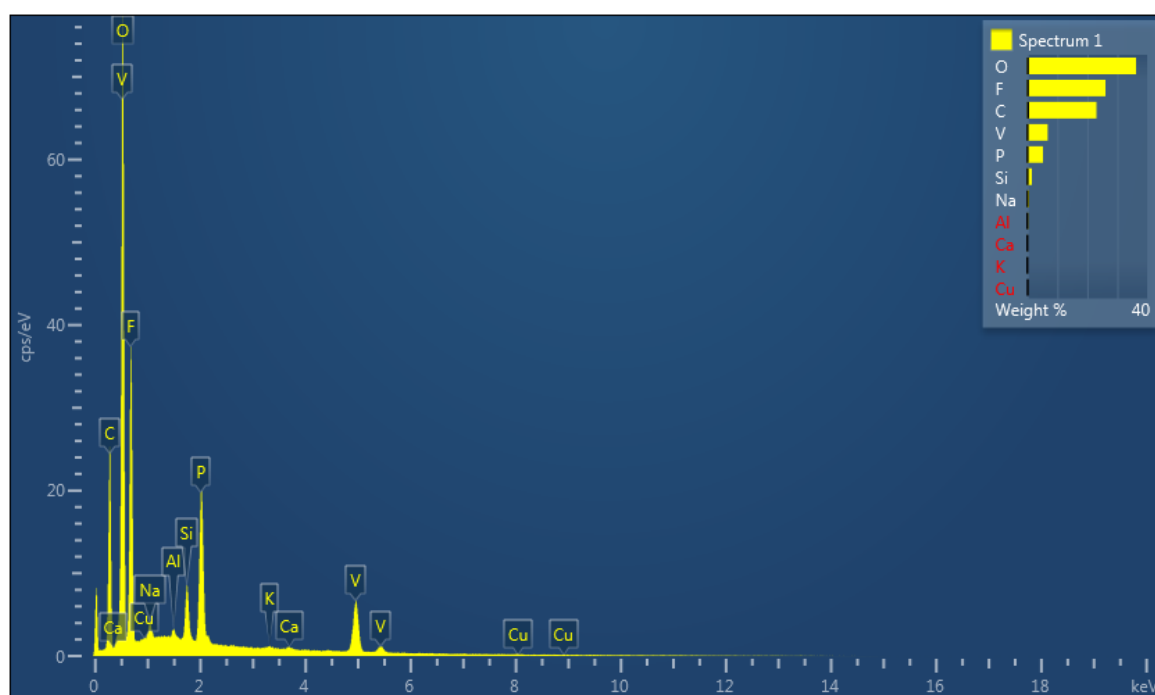


Fig. B.1 EDX data of the lithium disc from the coin cell after charging of VO₂.

